

Technical developments for quantitative and motion resolved MR-guided radiotherapy

Tom Bruijnen

Colophon

The cover is an edited image of the MR-linac system (Image courtesy of Elekta), where the gear spanner on the laptop indicates the focus on software improvements. The back book cover highlights the intrinsic struggle, within this thesis, of using Cartesian or non-Cartesian k-space trajectories for the data acquisition process.

Cover design and layout by Tom Bruijnen.

Technical developments for quantitative and motion resolved MR-guided radiotherapy

PhD thesis, Utrecht University, the Netherlands

All rights reserved. No part of this publication may be reproduced, distributed, or transmitted in any form or by any means without the prior written permission from the author. The copyright of the papers that have been published or have been accepted for publication has been transferred to the respective journals.

Manuscript

Layout:	T. Bruijnen
Typeset in:	L ^A T _E X
Printed by:	Proefschrift Maken
ISBN:	978-94-6423-349-0

Copyright

©Tom Bruijnen
©Elsevier (Chapter 2)
©Wiley (Chapter 3 and 6)
©IOP publishing Ltd (Chapter 4 and 7)

Technical developments for quantitative and motion resolved MR-guided radiotherapy

Technische ontwikkelingen in kwantitatieve and
bewegingsgecorrigeerde MRI-gestuurde radiotherapy
(met een samenvatting in het Nederlands)

Proefschrift

ter verkrijging van de graad van doctor aan de Universiteit Utrecht op gezag
van de rector magnificus, prof.dr. H.R.B.M. Kummeling, ingevolge het besluit
van het college voor promoties in het openbaar te verdedigen op donderdag 2
september 2021 des middags te 4.15 uur

door

Tom Bruijnen

geboren op 17 july 1992 te Beringe

Promotor: Prof.dr.ir. J.J.W. Lagendijk
Prof.dr.ir. C.A.T. van den Berg

Copromotoren: Dr.ir. H.N. Tijssen
Dr. A. Sbrizzi

This research is supported by the Dutch Technology Foundation STW, which is part of the Netherlands Organisation for Scientific Research (NWO) and partly funded by the Ministry of Economic Affairs (15354).

Obstacles are those frightful things you see when you take your eyes off your goal.

- Henry Ford

Contents

List of Acronyms	ix
1 General introduction	1
2 Quantifying head-and-neck tumor motion using 2D cine MRI	21
3 GIRF-based RF phase cycling to reduce eddy currents in bSSFP	35
4 Multiresolution radial MRI in pre-beam imaging (MR-RIDDLE)	53
5 Free-breathing 3D T2-weighted turbo spin-echo body MRI	69
6 Non-rigid 3D motion estimation using low-rank MR-MOTUS	85
7 Magnetic Resonance Fingerprinting on a 1.5T MRI-Linac	107
8 Summary and Discussion	121
9 Samenvatting	137
Bibliography	141
List of Publications	157
Acknowledgements	163
Curriculum vitae	167

List of Acronyms

ART	Adaptive Radiotherapy
bSSFP	balanced Steady-State Free Precession
CBCT	Cone-Beam Computed Tomography
CS	Compressed Sensing
CS2Dt	Compressed Sensing 2D+t reconstruction
CT	Computed Tomography
CTV	Clinical Target Volume
DCE	Dynamic Contrast Enhanced
DVF	Deformation Vector Field
DWI	Diffusion Weighted Imaging
DNA	Deoxyribonucleic Acid
EBRT	External Beam Radiation Therapy
FFT	Fast Fourier Transform
FID	Free-Induction Decay
FOV	Field-Of-View
g-factor	Geometry factor
GRAPPA	Generalized Autocalibrating Partially Parallel Acquisitions
GTV	Gross Tumor Volume
HU	Hounsfield Unit
IGRT	Image-Guided Radiotherapy
IMRT	Intensity Modulated Radiation Therapy
ITV	Internal Target Volume
kV	kilo Voltage
Linac	Linear Accelerator
LTI	Linear and Time-Invariant
MCIR	Motion Compensated Image Reconstruction
MLC	Multi-Leaf Collimator
MRCP	Magnetic Resonance Cholangio-Pancreatography
MRF	Magnetic Resonance Fingerprinting
MRI	Magnetic Resonance Imaging
MRL	Magnetic Resonance Linear Accelerator
MR-MOTUS	Model-based Reconstruction of MOTion from Undersampled Signals
MS	Multi-Slice

MV	Mega Voltage
NUFFT	Non-Uniform Fast Fourier Transform
OAR	Organ At Risk
PET	Positron Emission Tomography
PI	Parallel Imaging
PTV	Planning Target Volume
QMS	Quality Management System
REN	Relative error norm
rCASPR	Rewinded Cartesian Acquisition with SPiral Profile ordering
RF	Radio Frequency
SBRT	Stereotactic Body Radiation Therapy
SENSE	Sensitivity Encoding
SNR	Signal-to-Noise Ratio
SPECT	Single-Photon Emission Computed Tomography
TCP	Tumor Control Probability
TSE	Turbo Spin Echo
TV	Total Variation
VMAT	Volumetric Arc Therapy

General introduction

1.1 Radiotherapy

1.1.1 A brief overview of Radiotherapy in Oncology

In approximately half of the yearly diagnosed cancer patients radiotherapy will be a crucial component of the treatment [1,2]. Radiotherapy is a non-invasive treatment modality that uses high-energy ionizing radiation to sterilize the tumor [3,4]. The amount of deposited energy (dose) to the tumor is directly correlated to the desired therapeutic effect of local tumor control. The optimal tumor dose to maximize this therapeutic effect is in theory as high as possible [5], but is in practice limited by the collateral damage to healthy tissue (toxicity). In particular, the dose to the healthy tissues that are crucial for physiological function, called organs at risk (OAR), needs to be minimized to prevent severe toxicity [6]. Therefore, many innovations in the field of radiotherapy have been driven by the promise to minimize the dose to the OAR while maximizing the dose to the tumor, which is often referred to as conformal radiotherapy [7]. The remainder of Section 1.1 provides a brief summary on the three parallel innovations tracks that have improved the dose conformality over the last couple of decades.

1.1.2 Radiotherapy delivery

To improve the treatment conformality, one major line of innovation has been the optimization of the physical delivery of the radiation. The radiation is often delivered in the form of external beam radiotherapy using linear accelerators. Linear accelerators (linacs) generate directional X-rays, which induce scattered electrons that locally deposit the radiation. The linac's system properties are nowadays carefully characterized and modelled, which enables precise predictions of the delivered dose given a set of machine configurations (forward planning) [8]. These precise predictions of the system response in combination with advances

in inverse computing [9, 10] have enabled inverse radiotherapy planning [11, 12], which finds the optimal configurations of the linac to maximize the dose conformity. The concept of inverse planning in conjunction with the implementation of multi leaf collimators (MLCs) [13], an additional configurable directionality filter for the X-rays, has led to the modern day radiotherapy delivery modes of intensity modulated radiotherapy (IMRT) [14, 15] and volumetric arc therapy (VMAT) [16]. IMRT and VMAT are advanced radiotherapy planning techniques that provide a controlled distribution of the dose over the tumor and healthy tissue. The high precision of these radiotherapy delivery modes accentuates the importance of precise imaging to prepare the treatment, as small geometric errors in the tumor position translate to relatively large losses in the delivered dose [17].

1.1.3 Imaging for treatment simulation

Parallel to the advances in the physical delivery of the radiation, technological innovations have integrated imaging technology for the localization of the tumor into the radiotherapy treatment planning workflow (treatment simulation). The use of imaging has been primarily driven by computed tomography (CT), which captures the spatial distribution of the X-ray attenuation, expressed in Hounsfield Units (HU), which can be converted into a relative electron densities using a look-up table [18]. The electron density is subsequently used in two distinct ways: 1) the electron density describes how the radiation beam interacts with the tissue (required for treatment planning); 2) the electron density provides image contrast for the radiation oncologist to locate the gross target volume (GTV) and the OARs. The delineation of the GTV is a key step during treatment simulation, where any geometric error in the simulation model will persist throughout the complete course of the radiotherapy treatment. To account for potential microscopic tumor infiltration that is not visible on the imaging, the GTV is expanded with an additional safety margin termed the clinical treatment volume (CTV).

The radiotherapy treatment typically consists of 3-35 fractions distributed over a period of 1-7 weeks. For each treatment fraction, the patient's simulation model (position) needs to be accurately reproduced. However, the assumption of a reproducible patient anatomy is inherently flawed, as limited positioning accuracy and physiological processes impose geometrical uncertainties. These physiological processes include relaxation of muscular tissue, peristalsis in the gastrointestinal tract, filling of the bladder/rectum and respiratory/cardiac motion. These physiological processes are often distinguished based on the time-constant of how the anatomy is altered. Processes which change the anatomy between fractions cause interfraction motion, while processes that change the anatomy within a fraction cause intrafraction motion. The total geometric uncertainty imposed by the delineation uncertainty, the physiological processes and the limited positioning accuracy are covered in the so called planned target volume (PTV) [19, 20]. The PTV's are volumetric expansions of the CTV and GTV, that ensures that the CTV and GTV receives the intended dose and is currently determined by population-based averages [21]. Expansion of the CTV and GTV (into the PTV)

leads to larger treatment volumes, which in the case of a homogeneous dose distribution, vastly increases the total delivered dose. However, the dose distribution is not required to be uniform over the PTV, instead tumor probability control (TCP) models indicate that the dose distribution should approximately follow the density of the tumor cells [22]. The tumor cell density is difficult to estimate with current imaging methods, but the density can be assumed to be lower in the CTV than the GTV. Therefore, the dose to the CTV is typically lower than the dose to the GTV. However, the expansion of the GTV to CTV is typically less than 5 mm and therefore relies on accurate positioning.

1.1.4 Image guided-radiotherapy (IGRT)

In response to the successful integration of imaging into the treatment simulation, technical innovations have also directly integrated imaging technology onto the linacs, which is referred to as image guided radiotherapy (IGRT) [23]. The primary function of IGRT is the (daily) localization of the tumor and OAR, while the patient is on the treatment table, to accurately reproduce the patient positioning as in the simulation model. In other words, IGRT has to minimize the expansion of the PTV margin by measuring the position of the patient *prior to* (pre-beam imaging) and *during* (beam-on imaging) the radiotherapy delivery. Modern day linacs are equipped with megavoltage planar (MV) or cone beam computed tomography (CBCT) imaging modalities. These imaging modalities typically acquire images with relatively poor soft-tissue contrast, but provide valuable information to localize the interfaces between air, bone and soft-tissue. As a consequence, the primary use of IGRT is the daily positioning of the patient's bony landmarks with respect to the simulation model, while potential internal soft-tissue deformations, both prior to and during the treatment, are not captured. These internal soft-tissue deformations lead to residual treatment uncertainties, which expand the PTV and therefore reduce the treatment conformality. Note that recent innovations in CBCT technology are improving soft-tissue visualization [24], however the image quality is still considerably poorer than CT. The combined clinical workflow of creating a static patient model in conjunction with accurate daily patient positioning using MV or CBCT is currently the standard of care in radiotherapy.

An illustrative overview of the three innovations tracks that have improved treatment conformality is shown in Figure 1.1.

1.2 MRI in radiotherapy

1.2.1 Rationale

Over the last decade the use of CT in radiotherapy has been augmented with other imaging modalities such as positron emission tomography (PET) and magnetic resonance imaging (MRI) [26,27]. The MRI and PET images are fused with the

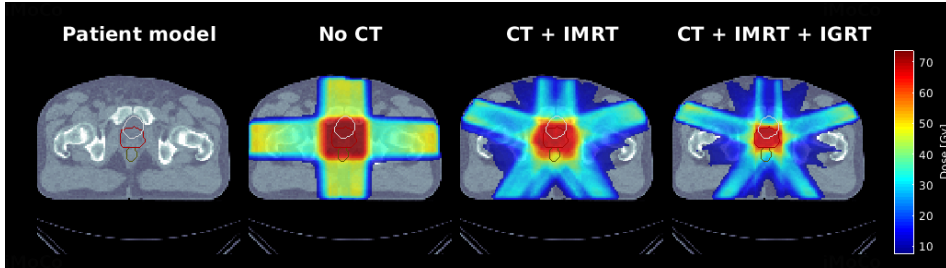


Figure 1.1: An overview of the improvements in treatment conformality using CT imaging, IMRT and IGRT. **A)** The CT scan of a patient with a prostate tumor (red) and the bladder (white) and rectum (green) as the primary OAR. **B)** Radiotherapy without a CT scan requires a large PTV, which leads to high dose regions in the bladder/rectum. **C)** Radiotherapy with the CT scan and IMRT reduces the high dose regions in the bladder/rectum. **D)** Radiotherapy with CT + IMRT + IGRT further reduces the dose to the heart and provides the most conformal therapy. Dose calculations were performed using the open-source dose calculation and optimization toolkit matRad [25].

CT images to provide additional anatomical, functional or metabolic information to provide multiple illuminations of the GTV and OARs. In particular, MRI is an especially versatile imaging modality that is capable to encode multiple tissue properties, ranging from the diffusivity of water molecules, to estimates of the (relative) proton density, to the physical properties such as T_1 and T_2 relaxation (Figure 1.2). The inclusion of these additional imaging modalities enables comprehensive soft-tissue characterization and is the primary motivation for the use of MRI in radiotherapy [28].

The secondary advantages of MRI in radiotherapy include: the 3D visualization of the anatomy in any desired orientation, the measurement of physiological motion such as cardiac, respiratory and peristaltic motion, the non-ionising nature of the imaging that enables precise and repeated examinations [29]. The exact mechanisms through which the motion measurements can be incorporated in the treatment planning will be discussed in Section 1.2.2. All these three advantages improve the characterization of the tissue during treatment planning, which ultimately contribute to improved conformality of the therapy.

1.2.2 MRI for treatment simulation

The primary use of MRI in the radiotherapy treatment simulation is the generation of multi-contrast MR images, which typically consist of the tissue properties shown in Figure 1.2. Note that these specific multi-contrast scans are often further tailored to a specific organ such that the contrast between the tumor and native tissues is maximized. The multi-contrast images are then used by the radiation oncologist, along with the CT images, to precisely delineate the GTV and the OAR.

While MRI provides considerable theoretical advantages in terms of image contrast, MRI comes with additional challenges related to image artefacts that

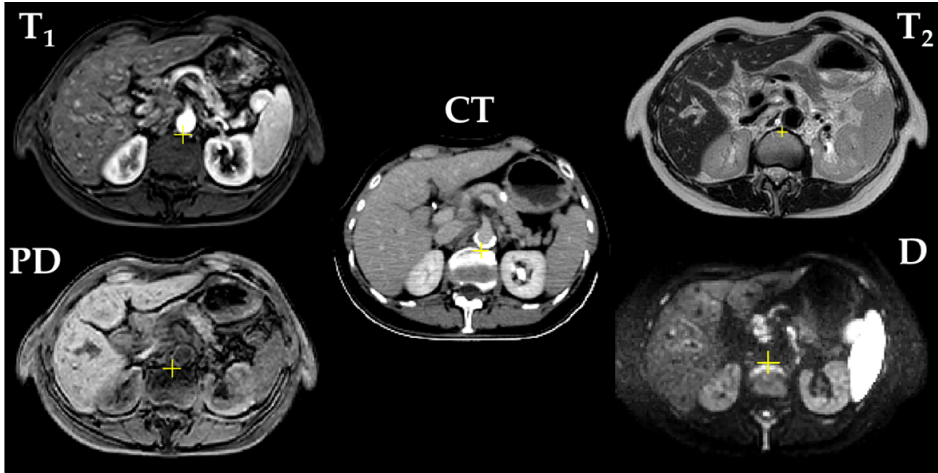


Figure 1.2: Versatility of MR image contrast in comparison with CT in a patient with pancreas cancer. Sequential MRI scans that encode different tissue properties into the image, while CT only encodes the relative electron density. The MR derived tissue properties shown are longitudinal relaxation (T_1), transverse relaxation (T_2), proton density (PD) and the diffusivity (D). Note that both the CT scan and the T_1 scan are acquired with administration of contrast agent.

degrade image quality. Image artefacts are especially pronounced in the abdominothoracic region, where the artefacts often originate from physiological motion (Figure 1.3-A) [30]. The physiological motion is often controlled for during acquisition, by using breath-hold scans or respiratory triggered/gated scans (Figure 1.3-B) [31, 32]. While these motion synchronization techniques are effective for mitigating motion-induced image artefacts, these techniques often fail in uncooperative patients that are unable to suspend their breath or are unable to breath in a controlled pattern [33].

Instead of using imaging techniques that control the respiratory motion, free-breathing techniques can be used that resolve the motion. These techniques are often referred to as respiratory correlated 4D-MRI [34, 35], which provide means to both correct for the motion in the images [36] (Figure 1.3-C) and to quantify the time-averaged respiratory motion. The respiratory motion quantification is of particular interest to radiotherapy, because the motion provides information on the uncertainty of the GTV delineation, which is subsequently included in the PTV margin (Figure 1.3-D). However, not all MRI vendors provide commercial solutions for 4D-MRI scans [35] and the ones that do provide these solutions require very specific MRI scans. In conclusion, a robust and generic solution for respiratory correlated 4D-MRI remains an unsolved problem, but is key for radiotherapy treatment planning in the abdomen/thorax.

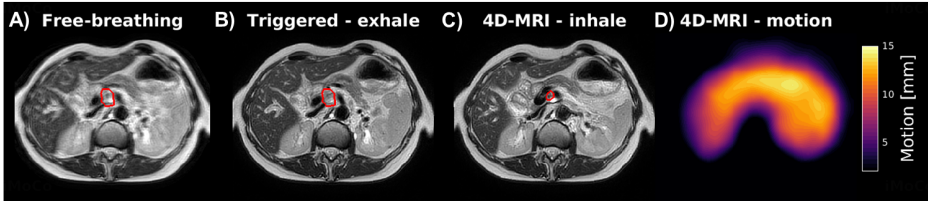


Figure 1.3: An overview of respiratory motion compensation methods for abdominal imaging in radiotherapy. **A)** Free-breathing standard MR scans results into considerable loss of resolution and artefacts. **B)** Respiratory triggered MR scans only acquire data during exhale, which restores the loss of resolution. **C)** 4D-MR scans acquire data during free-breathing, which restores the loss of resolution for all respiratory phases. **D)** The respiratory phases can be aligned to estimate the average respiratory motion across the MR scan. GTV is shown with the red contour.

1.2.3 MR-linac for MR-guided radiotherapy

In response to the advantages of using MRI in radiotherapy treatment planning, the conceptualization of using MRI for online image-guided radiotherapy was first proposed in 1999 [37]. The key idea was that MRI provides the optimal imaging to localize the GTV and OARs *prior to* and *during* the radiotherapy delivery. The idea of hybrid MR-linacs was implemented in a proof-of-concept in 2009 by the UMCU [38] and subsequently industrialized by multiple health technology companies. The two MR-linac systems that are currently clinically certified are: The 0.35T MRIdian system (ViewRay, Mountain View, CA, United States), which has been used clinically as of 2014 [39, 40]; The 1.5T Elekta Unity (Elekta AB, Stockholm, Sweden), which has been used clinically as of 2017 [41–43]. The Elekta Unity system is installed at the UMCU and the system design will be discussed in more detail in the next subsection 1.2.4.

The clinical availability of these hybrid MR-linac systems allow daily online (pre-beam + beam-on) MR imaging during radiotherapy, which provides much more informative imaging in comparison to MV and CBCT. The online MR imaging could be used to improve the daily positioning, based on soft-tissue landmarks, to reduce the PTV. However, the majority of the geometric error in the PTV margin resides in the intrafraction and interfraction motion of the anatomy with respect to the static patient simulation model. Instead, the online MR imaging should be used to adapt the patient simulation model as a response to interfraction and intrafraction motion. This adaptation presents a radically new approach to account for geometric errors in radiotherapy, with the potential to eliminate a large part of the PTV. For example, the interfraction motion could be corrected for by replanning the radiotherapy treatment on-the-fly (online replanning) [44]. Another example could be to act upon excessive internal organ motion during the radiation delivery by pausing the radiation beam (beam-gating) [45]. The complete set of all these possible interventions to modify the treatment plan in response to the imaging during the treatment is called adaptive radiotherapy (ART) [46]. ART is fundamentally different from the conventional radiotherapy workflow, as discussed in Section 1.1, which relies upon the precise reproduction of

the static patient model that is built during the radiotherapy simulation. The ultimate promise of ART is to deliver the most precise radiotherapy treatment with the smallest possible PTV. However, optimal implementation of ART requires high performance MR imaging techniques that necessitate complete system control over the MR-linac scanner. The requirements of the high performance MR imaging are discussed later in Section 1.3 and an overview of the MR-linac system design adjustments that affect the imaging are discussed in the next Section 1.2.4.

1.2.4 MR-linac system design

The Elekta Unity MR-linac system combines a whole-body 1.5T cylindrical diagnostic MRI scanner (Ingenia, Philips, Best, the Netherlands), with a 7 MV linac (Elekta, AB, Stockholm, Sweden), which is mounted on a ring-shaped gantry. The MR-linac system design required considerable hardware adjustments such that the magnetic interaction between the two systems was minimized. The first major adjustment was the modification of the active shielding of the MRI's main magnet [47, 48], such that the gun of the linear accelerator and the MRI are magnetically decoupled (Figure 1.4).

The second major adjustment was the adjustment of the superconducting wires of the main magnet (15 cm gap) and the design of a split gradient coil (20 cm gap) to accommodate a (nearly) attenuation-free passage of the radiation beam. The split magnet design reduces the main magnetic field uniformity, which can largely be corrected for by installing additional passive shim gantry shims [49–51]. The split gradient coil design has considerable impact on the imposed linear magnetic fields (gradients) used in MRI, which increases gradient system imperfections. To mitigate the impact of the system imperfections the clinical certification of the system constrains the software to a maximum gradient strength of 15.0 mT/m (instead of 34.0 mT/m) and to a maximum slew rate of 65 T/m/s (instead of 120 T/m/s) [52]. The constraint configuration mitigates the impact of eddy currents sufficiently in the center of the field-of-view [53], while substantial residual effects remain in the periphery [54, 55].

The third major adjustment was the use of a 2x4 channel radiolucent receive coil that displaced all attenuating components outside of the radiation window. These receive coils provide reduced signal-to-noise ratio and parallel imaging performance compared to diagnostic quality receive coils [56, 57].

1.3 Adaptive MR-guided radiotherapy: an imaging perspective

1.3.1 A conceptual introduction to adaptive radiotherapy

Section 1.1 and Section 1.2 have described the process of conventional radiotherapy and have explained how deeply (MR) imaging is intertwined in the workflow. The conventional radiotherapy workflow can be summarized as a static process consisting of three building blocks, a single simulation phase, repeated radiotherapy delivery and finally tumor response monitoring after the complete treatment.

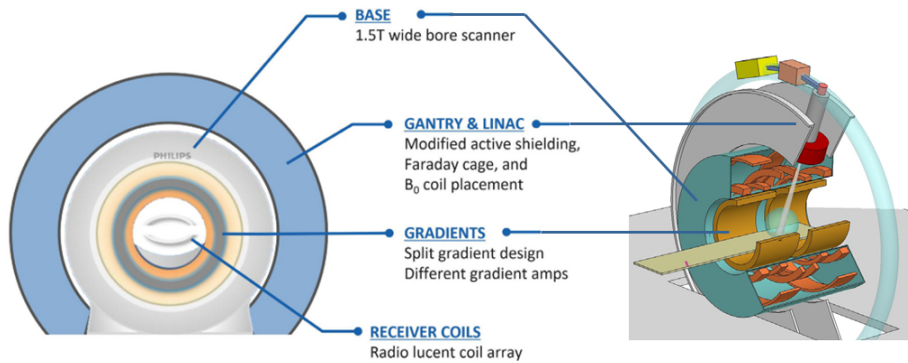


Figure 1.4: Overview of the modified MR-linac hardware components. Left side shows a schematic front view of the arrangement of hardware components. The right side shows a 3D rendered side view of the same system. Figures are adapted from [49, 50].

The static simulation model of the patient limits the precision of radiotherapy treatment, as interfraction and intrafraction processes impose geometric uncertainties. These geometric uncertainties can be resolved by using an adaptive radiotherapy workflow on the MR-linac, as already briefly hinted on in Section 1.2.3. The adaptive radiotherapy workflow consists of multiple sequentially connected static workflows (Figure 1.5). These multiple static workflows can be cycled on different time-scales, ranging from once over the course of the entire treatment to multiple times per second. The temporal resolution of the cycling speed is, to a large extent, dictated by the MR imaging required to support the three workflow building blocks.

The optimal cycling speed for ART heavily depends on the type of geometric uncertainty that needs to be resolved. A convenient classification of the types of geometric uncertainties is obtained by distinguishing between interfraction and intrafraction processes, as described in Section 1.1.3. The uncertainties induced by interfraction processes are addressed with ART by online replanning, which includes recontouring of the GTV/OAR on the daily anatomy. The imaging required to support the recontouring is referred to as pre-beam imaging and is on the time-scale of minutes. The uncertainties induced by the intrafraction processes are addressed with ART by online motion management [58], which involves real-time adjustments to the radiation delivery. The imaging required to support the real-time adjustments is referred to as beam-on imaging and is on the time-scale of subseconds. The third building block of the radiotherapy workflow is the tumor response monitoring. Tumor response monitoring in ART is, unlike the simulation and delivery, not used to reduce geometric uncertainties. Instead, tumor response monitoring is used to assess whether the on-going therapy is efficacious or not, with the ultimate promise to alter the entire treatment strategy (e.g. to increase the dose or to completely stop the radiotherapy). The imaging required to support the tumor response monitoring is referred to as beam-off imaging and is on the time-scale of days.

The introduction of this section has provided a very coarse description of ART and explained that different types of MR imaging are required to optimally guide the individual building blocks. A detailed discussion on these image requirements will follow in Sections 1.3.2-1.3.4 below.

MR-linac ART

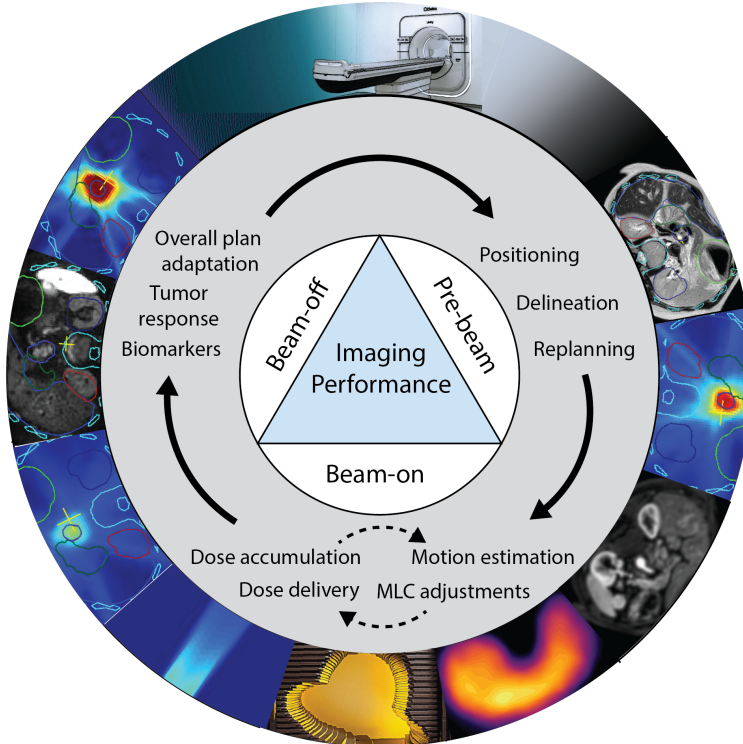


Figure 1.5: Overview of adaptive radiotherapy on an MR-linac. The ART workflow triangle, which consists of three building blocks. The first block is the online treatment setup, which consists of patient positioning, tumor delineation and online replanning and is supported with pre-beam imaging. The second block is the real-time guided dose delivery, which consists of motion estimation, MLC adjustments, dose delivery and dose accumulation and is supported with beam-on imaging. This cycle is repeated many times within a single treatment fraction. The third block is the therapy response monitoring, which consists of functional/quantitative imaging to derive the tumor response followed by a change in the treatment plan and is supported with beam-off imaging.

1.3.2 Pre-beam imaging

The primary objective of pre-beam imaging is to provide a high resolution 3D and large field-of-view volume that visualizes the daily anatomy. The current clini-

cal practice of pre-beam imaging uses accelerated free-breathing 3D MR scans derived from MR simulation protocols. These pre-beam scans provide decent image quality, but are not optimized with respect to the clinical workflow. The clinical workflow consists of deformable image registration of the pre-beam images to the pretreatment CT, followed by precise recontouring of the GTV/OAR for online replanning. Therefore, the pre-beam images should be acquired and reconstructed with minimal latency to initialize the online replanning in order to facilitate a fast clinical workflow. An acceptable acquisition + reconstruction time for the pre-beam scans is less than 5 minutes. The pre-beam imaging has to be robust to imaging artefacts, because rescanning is not a practical scenario. The secondary objective of pre-beam imaging is to quantify the organ motion, derived from the 4D-MRI, to determine adequate PTV margins. In case of abdominothoracic tumors, the motion can also be used to reconstruct the images in the desired respiratory phase (i.e. exhale or mid-position) [59, 60]. The 4D-MRI can also be used to aid beam-on imaging to quantify time-resolved 4D motion, which will be discussed in more detail in the next Section 1.3.3.

1.3.3 Beam-on imaging

The primary objective of beam-on imaging is to quantify the time-resolved 4D motion in the entire radiation window with high spatiotemporal resolution for real-time gating/tracking. The current clinical practice of beam-on imaging is the acquisition of 3D MR scans (± 2 mm spatial resolution and ± 10 s temporal resolution), which are not yet used to adapt the therapy. This spatiotemporal resolution is sufficient for anatomical sites that are not affected by respiratory/cardiac motion such as the pelvis and rectum. However, the abdominothoracic sites require a temporal resolution of ± 200 ms. The required spatial resolution varies for different anatomical sites, but is often reduced with respect to diagnostic imaging, as deformable image registration can quantify the motion with sub-voxel accuracy. A spatial resolution of ± 3 -4 mm is likely to be sufficient for many cases [61]. The combined requirements of the moderate spatial + high temporal resolution is not feasible for conventional 3D imaging techniques as these require at least an order of magnitude longer scan time. Novel time-resolved 4D imaging techniques have been proposed in literature to speed-up the acquisition. These methods are based on compressed sensing techniques that will be discussed later in Section 1.4.1. However, compressed sensing based techniques require long reconstruction time that make them impractical for real-time gating and tracking. Alternatively, hybrid time-resolved 4D imaging techniques have been proposed that relate 2D beam-on imaging to the respiratory correlated pre-beam 4D-MRI and infer the time-resolved 4D motion from the relationship. These methods do provide sufficient spatiotemporal resolution, but rely on strong assumptions in the consistency of the internal anatomy. In conclusion, a robust and generic solution for real-time time resolved 4D-MRI is still an unsolved problem, but is key for MR-guided ART.

The secondary objective of beam-on imaging is to quantify the time-resolved 4D motion with high spatiotemporal resolution for retrospective dose accumulation. Dose accumulation couples the time-resolved motion estimates with the linac's

machine output to calculate the delivered dose for the fraction. The delivered dose is then compared with the planned dose and possible underdosage or overdosage can then be corrected in the next fraction. Retrospective dose accumulation has relaxed requirements regarding the imaging latency, as the motion estimation does not have to be available in real-time. The relaxed requirements on the temporal resolution opens up this application for novel time-resolved 4D imaging techniques with long reconstruction times.

1.3.4 Tumor response monitoring

The primary objective of tumor response monitoring is to assess early radiation-induced tissue changes. These changes could potentially be used to distinguish responders from non-responders or to intensify or reduce the (local) radiation during the radiotherapy treatment [62]. The current clinical practice of response monitoring is limited to qualitative MR scans, which could be used to derive macroscopic biomarkers such as the tumor size. However, these biomarkers are not used yet to adapt the therapy, because the correlation with respect to local tumor control is not well established. Alternatively, quantitative MR scans could be used to derive functional biomarkers such as the T1, T2 or the diffusivity. The biomarkers derived from quantitative MRI could be more sensitive to radiation-induced tissue changes and are increasingly being used in the pre-treatment setting for tumor staging [63–65]. Quantitative MR scans typically require long acquisition times, which pose a considerable practical challenge as the patient on table time is almost completely filled with anatomical imaging (pre-beam + beam-on). Typical MR-linac treatment fractions have at most a couple of minutes of free imaging time available such that it does not interfere with the clinical workflow [43]. Therefore, fast and precise quantitative MR scans are required for a practical implementation of online tumor response monitoring.

1.3.5 The case for Non-Cartesian readouts

The three building blocks for ART need varying type of image guidance, which differ considerably in terms of spatiotemporal resolution (imaging performance). However, the one requirement that these imaging techniques do have in common is the need for fast and motion-robust scans. These two properties are in part dictated by the selected k-space readout, which is therefore a crucial lever in the sequence design. Conventional MR sequences are mostly sampled using Cartesian readouts with varying phase encode view-ordering schemes, which control the imaging speed through incoherent sampling patterns [66, 67] and control the motion robustness through repetitively sampling of the low frequencies [68]. However, the imaging speed and motion robustness of Cartesian scans is inherently limited, because the readout orientation is fixed and therefore can only provide additional encoding in this single direction. Contrarily, non-Cartesian readouts continuously rotate the readout direction and therefore provide improved spatiotemporal encoding. Commonly used non-Cartesian readouts include golden angle stack-of-stars [69], golden angle stack-of-spirals [70], golden mean kooshball [71] and golden mean hybrid radial cones [72] (Fig 1.6). From left to right

these trajectories provide improved spatiotemporal encoding, but are counter-balanced by an increased sensitivity to measurement imperfections [73]. These measurement imperfections include off-resonances, concomitant gradient field effects [74] and gradient system imperfections [75]. The measurement imperfections must be adequately addressed in the image reconstruction to effectively capitalize on the advantages of these non-Cartesian readouts, which considerably increases the implementational complexity. This thesis focuses on the characterization of the gradient systems imperfections for non-Cartesian MRI, which will be further discussed in the next Section 1.3.6.

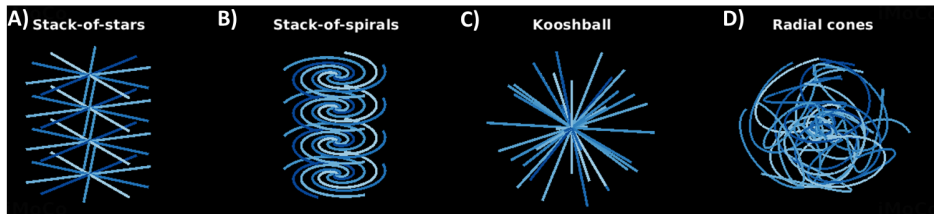


Figure 1.6: Commonly used non-Cartesian trajectories for rapid and motion robust imaging. **A)** Stack-of-stars trajectory that samples radial lines on Cartesian planes. **B)** Stack-of spiral trajectory that samples spiral interleaves on Cartesian planes. **C)** Kooshball trajectory that samples radial lines in a 3D sphere. **D)** Hybrid radial cones that samples spirals in a 3D sphere.

1.3.6 MR gradient system characterization

Non-Cartesian trajectories rely on fast time-varying magnetic fields (gradient) and the resulting image quality rapidly degrades when deviations of the gradients occur. In practice, the imposed gradients significantly differ from the actual produced gradients due to system imperfections. The dominant system imperfections are thermal variation in hardware components, bandwidth limitations of the gradient amplifiers, mechanical vibrations caused by gradient switching and eddy currents induced in the gradient coil and other conducting structures [76]. Most of these effects are expected to be more severe in the MR-linac system, in comparison to the diagnostic system, due to the split gradient coil and magnet design (Figure 1.3). Therefore, a comprehensive characterization of the gradient system of the MR-linac is crucial for implementation of advanced non-Cartesian MR imaging techniques for ART.

1.4 Advancements in MRI physics

The optimal implementation of MRI in radiotherapy requires advanced MR imaging techniques that generate images with high quality. The image quality is a combination of both the image acquisition and image reconstruction technique. While innovations in MR imaging have historically been driven by advancements on the image acquisition side, the current wave of innovation is clearly driven

by advancements in image reconstruction. The switch from the focus on the acquisition to the reconstruction was guided by the realization that any type of prior knowledge on the imaging process, such as image structure or model errors (e.g. motion or system imperfections), could be included in an inverse problem reconstruction formulation. The inclusion of the prior knowledge into the reconstruction speed-ups the imaging and reduces the sensitivity to artefacts. The inclusion of prior knowledge is especially alluring for the repeated imaging in adaptive radiotherapy. The work presented in this thesis follows this philosophy and therefore the remainder of Section 1.4 provides the reader with the basic principles on inverse image reconstruction in order to understand the concepts and methods developed in this thesis. A detailed and comprehensive review of the complete image acquisition and reconstruction theory can be found in these works [77, 78].

1.4.1 A brief overview of MR image reconstruction

Consider an MR acquisition that uses the gradients for spatial encoding to sample k-space points of the steady-state transverse magnetization (\mathbf{m}). The k-space coordinates (\vec{k}) represent specific spatial frequencies in 3D that are connected to the object through the Fourier transform. Therefore, an MR system is, in essence, a machine that performs an analogue Fourier transform of the object and samples discrete spatial frequencies. The sampled signal $y^c(t)$ at the receive coil (c) is given by the following forward model (Eq 1.1):

$$y^c(t) = \int_{\Omega} m(\vec{r}) s^c(\vec{r}) e^{-2\pi i \vec{k}(t) \cdot \vec{r}} d\vec{r} \quad 1 \leq c \leq N_c \quad (1.1)$$

With $s^c(\vec{r})$ as the complex receive coil sensitivity at spatial position \vec{r} and N_c as the total number of coils. The forward model can be described with matrix-vector notation for all measurements and coils in compact notation (Eq 1.2):

$$\mathbf{y} = F S \mathbf{m} \quad (1.2)$$

With $\mathbf{y} \in \mathbb{C}^{N_c N \times 1}$, $\mathbf{m} \in \mathbb{C}^{M \times 1}$, $S \in \mathbb{C}^{(N_c M) \times (M)}$ as the coil sensitivities and $F \in \mathbb{C}^{(N_c N) \times (N_c M)}$ as the discrete Fourier transform operator. Here M is the number of pixels in the image and N as the number of k-space samples. Now for the special case where we have sampled all k-space coordinates ($N \geq M$) the image can be reconstructed with the adjoint model (Eq 1.3):

$$\mathbf{m} = S^H F^H \mathbf{y} \quad (1.3)$$

However, in practical scenarios we have limited sampling time ($N < M$) and the corresponding evaluation of the adjoint model reconstructs images with artefacts, often referred to as aliasing. To restore the aliasing in the images the additional spatial encoding of the parallel receive coils can be included in the reconstruction

with a technique called parallel imaging. Parallel imaging can be included in the image reconstruction with a least square problem formulation (Eq 1.4):

$$\mathbf{m}^* = \arg \min_{\mathbf{m}} \|FS\mathbf{m} - \mathbf{y}\|_2^2 \quad (1.4)$$

An intuitive explanation for parallel imaging is the following: each coil multiplies the image with a smooth function $s_c(\vec{r})$ with wide support, which is equivalent to convolution in k-space with a compact kernel. Therefore, the sampling function of a each coil is not a delta function, but provides information on a small neighborhood surrounding the k-space coordinate. This additional information can be used to infer missing samples in k-space from the multicoil data. The imaging acceleration performance of parallel imaging can be further enhanced by adding prior information on the image structure in the reconstruction formulation in the form of regularization. A particular case of regularization is the l_1 norm in combination with a sparsifying transformation, which is referred to as compressed sensing. Compressed sensing transforms the image to a sparse domain, where less coefficients are required to represent the image, which effectively reduces the size of M and therefore requires less samples N for reconstruction (Eq 1.5):

$$\mathbf{m}^* = \arg \min_{\mathbf{m}} \|FS\mathbf{m} - \mathbf{y}\|_2^2 + \lambda \|\Psi\mathbf{m}\|_1 \quad (1.5)$$

Here Ψ is the sparsifying transform and λ the regularization parameters that regulates the trade-off between the image consistency and regularization term. Compressed sensing is increasingly being used in clinical MR scans and is currently the standard for highly accelerated MR imaging.

1.4.2 Gradient system imperfections in image reconstruction

The previous Section 1.4.1 described the theoretical forward signal model (Eq 1.1) and explained how this forward model was inverted in the image reconstruction. However, the forward model is not fully accurate in practical imaging scenarios where gradient system imperfections cause considerable deviations. These deviations can be interpreted as additional space-time magnetic fields $\xi(\vec{r}, t)$ that modulate the measured signal (1.6):

$$y^c(t) = \int_{\Omega} \xi(\vec{r}, t) m(\vec{r}) s^c(\vec{r}) e^{-2\pi i \vec{k}(t) \cdot \vec{r}} d\vec{r} \quad (1.6)$$

With $|\xi(\vec{r}, t)| = 1$, such that gradient system imperfections only modulate the phase of the complex magnetization $m(\vec{r})$. These additional spatio-temporal magnetic fields are fully dependent on the input gradient waveforms $\vec{G}(t)$ and can be modeled as a linear and time-invariant system (LTI) [76]. LTI systems allow the gradient impulse response function (GIRF) to map $\vec{G}(t)$ to the gradient-induced space-time magnetic fields $\xi(\vec{r}, t)$. The GIRF $H(\vec{r}, t)$ can be characterized using

specialized magnetic field probes or customized MR scans that directly measure $\xi(\vec{r}, t)$ given $\vec{G}(t)$. However, accurate estimation of $H(\vec{r}, t)$ is difficult and very time-consuming. Therefore, in practice $H(\vec{r}, t)$ is often approximated using Laplace's spherical harmonic functions with order l and phase m ($\tilde{H}_{lm}(t)$) and corresponding expansion coefficients ω_{lm} .

$$\angle \xi(\vec{r}, t) = \int_0^t \vec{G}(t) * H(\vec{r}, t) dt \approx \int_0^t \vec{G}(t) * \sum_{l=0}^L \sum_{m=-l}^l \omega_{lm} \tilde{H}_{lm}(t) \quad (1.7)$$

The neat property of the spherical harmonic decomposition is that specific l and m combinations provide a simple physical interpretation. For example, $l = 0$ and $m = 0$ describe the space-time field modulations that are uniform over space, i.e. $\Delta B_0(t)$, which can be corrected for in k-space with a global phase demodulation. Another example, $l = 1$ and $m = -1, 0, 1$ describe the space-time field modulations that vary linearly over space, i.e. deviations of $\vec{G}(t)$, which can be corrected for by modifying $\vec{k}(t)$ in the image reconstruction. Therefore, corrections for zeroth and first order gradient imperfections effectively reduce Eq 1.6 to Eq 1.1, which again allows conventional image reconstruction as outlined in Section 1.4.1. However, higher order terms do not have these quick-fixes and can only be corrected for by inclusion in the forward model, which requires the inversion of a very large (modified) signal model [79]. The quantification of the higher order terms and the subsequent adjustments in the image reconstruction were not considered in this thesis, because these currently do not provide practical use for MRI in radiotherapy.

While $\xi(\vec{r}, t)$ only affected the phase of $m(\vec{r})$, gradient system imperfections can also lead to magnitude deviations. Deviations in magnitude are often referred to as steady-state disruptions and are induced by residual phase errors at the end of the repetition time $\phi_{tr}(\vec{r})$:

$$\phi_{tr}(\vec{r}) = \int_{TR \cdot (tr-1)}^{TR \cdot tr} \xi(\vec{r}, t) dt \quad (1.8)$$

Here lowercase tr refers to the readout number and capital TR refers to the repetition interval. The impact of $\phi_{tr}(\vec{r})$, at a specific readout (tr), on the $|m(\vec{r})|$ depends on the tissue-specific properties $T_{1,2}$, which is described with the Bloch equations. As a consequence, the modulation of $|m_{tr}(\vec{r})|$ at readout number tr depends on the entire sequence history $\phi_{1,2..tr}(\vec{r})$:

$$y_{tr}^c(t) = \int_{\Omega} \xi_{tr}(\vec{r}, t) m_{tr}(\vec{r}, \phi_{1,2..tr}(\vec{r})) s^c(\vec{r}) e^{-2\pi i \vec{k}_{tr}(t) \cdot \vec{r}} d\vec{r} \quad (1.9)$$

Eq 1.9 provides the complete forward model of the MR signal, which includes the linear part of the gradient system imperfections. The use of the GIRF to correct for zeroth and first order space-time magnetic fields is currently the state-of-the-art in clinical MR scans.

1.4.3 Modelling motion in image reconstruction

Another source of error in the forward signal model is the movement of the subject during the MR scan. The origin of the subject motion was already discussed in Section 1.2.2 and therefore the current Section focuses on the mathematical description of motion for image reconstruction. Motion is often modelled using deformation vector fields (DVF) that describe a warping operation from a reference state to another motion state. The warping operation can be included in the forward signal model to relate the measured signal at the second motion state to the reference state:

$$y^c(t) = \int_{\Omega} m(V(\vec{r})) s^c(\vec{r}) e^{-2\pi i \vec{k}(t) \cdot \vec{r}} d\vec{r} \quad (1.10)$$

Here $V(\vec{r})$ is the warping operation, where we assumed that the total mass is conserved, i.e. $\det \nabla V(\vec{r}) = 1$. The new forward model can also be described in matrix form and reconstructed using compressed sensing (Eq 1.11):

$$\mathbf{m}^* = \arg \min_{\mathbf{m}} \|FSU\mathbf{m} - \mathbf{y}\|_2^2 + \lambda \|\Psi\mathbf{m}\|_1 \quad (1.11)$$

With $U \in \mathbb{R}^{M \times M}$ as the linear operator of $V(\vec{r})$. Now that the motion can be accurately modelled in the image reconstruction the challenge is the estimation of the deformation vector fields V . The concept of considering U as a warping operator in image space leads to a difficult conundrum, namely to accurately estimate U multiple images \mathbf{m} for different motion states are required in image space. However, U is required to accurately estimate a high quality image \mathbf{m} . Therefore, most approaches that estimate U select parts of the data \mathbf{y} to reconstruct low-quality images \mathbf{m} . These low-quality images are subsequently registered with deformable image registration algorithms that are robust to image artefacts to obtain the motion fields. This approach is inherently limited by the amount of data required for the Fourier transform to reconstruct \mathbf{m} with sufficient quality for deformable image registration.

Another strategy to estimate U is to rewrite the forward model from a k-space perspective:

$$y^c(t) = \int_{\Omega} m(\vec{r}) s^c(\vec{r}) e^{-2\pi i \vec{k}(t) \cdot V^{-1}(\vec{r})} d\vec{r} \quad (1.12)$$

Here V^{-1} is the inverse of the warping operator, which appears in the exponential function that encodes the k-space. Therefore, V effectuates a change of coordinates of \vec{r} . From this perspective it is possible to invert Eq 1.12 to solve for $V(\vec{r})$ given an adequate image \mathbf{m} . The advantages of this approach is that it is not limited by the amount of data required for the Fourier transform, but is limited by the amount of data required to sufficiently encode the motion. Image

reconstruction using Eq 1.10 is currently gaining popularity and inverting Eq 1.11 is the state-of-the-art in a research setting and will be further explored in this thesis.

1.5 Scientific contributions and thesis outline

MRI is going to disrupt the field of radiotherapy in the next decade through real-time image guidance and frequent tumor response monitoring to optimize the treatment. The development of advanced MR imaging techniques that are specifically tailored for these adaptive radiotherapy applications are going to be crucial. This thesis focuses on the development of these MR techniques along/throughout the whole imaging spectrum in the radiotherapy workflow, including treatment simulation (Chapter 2-3), pre-beam imaging (Chapter 4-5), beam-on imaging (Chapter 6) and tumor response monitoring (Chapter 7).

Chapter 2 quantifies the typical tumor motion in patients with head-and-neck cancer to determine PTV margins for treatment simulation. Standard available available (spoiled) 2D cine MR scans were acquired in 100 patients and the motion was estimated using non-rigid image registration. The motion estimates were used to determine population-based PTV margins, which were significantly smaller than the current clinically used PTV margins, therefore the clinical protocol was adjusted in response to these findings. In addition to the PTV margins, the imaging data provided insight on the soft-tissue motion dynamics and the limitations of currently available MR imaging techniques for motion estimation in more challenging anatomical regions.

Balanced steady-state free precession (bSSFP) scans offer shorter repetition times and higher signal-to-noise efficiency compared to spoiled scans and therefore are highly useful for real-time beam on imaging. However, bSSFP scans are susceptible to image artefacts arising from gradient system imperfections. These gradient system imperfections are characterized in **Chapter 3** by measuring the GIRF. We show that the GIRF provides the information to accurately model the bSSFP image artefacts and we provide a novel method to correct for these artefacts. The measured GIRFs are subsequently used to enable robust non-Cartesian imaging in Chapters 4,6-7.

Chapter 4 focuses on the design of a novel pre-beam MR-linac scan (MR-RIDDLE) that optimally integrates with the online radiotherapy workflow. MR-RIDDLE uses non-Cartesian golden angle radial data sampling to reconstruct multiple resolution images during the acquisition. Low-resolution images are available after a very short acquisition window, after which the data collection continues for subsequent high-resolution image updates. We anticipate that this novel concept of parallelising the MR imaging and the clinical tasks has the potential to considerably speed-up and streamline the online MR-guided radiotherapy workflow.

Chapter 5 focuses on the design of a generic free-breathing imaging technique that simultaneously quantifies and corrects for the respiratory motion. We propose a novel rewinded Cartesian Acquisition with spiral profile ordering (rCASPR)

sampling scheme, which provides similar image contrast to conventional clinically used T2-w scans, while enabling the self-navigation and robustness to motion artefacts required to reconstruct the 4D-MRI. The 4D-MRI is used to estimate the motion, which is subsequently used for the motion compensated image reconstruction. The key philosophy of this technique is that clinically used motion-triggered scans can easily be replaced by free-breathing rCASPR implementations without loss of image contrast or an increase in scan time. Therefore, rCASPR could be a robust and generic solution for pre-treatment and pre-beam imaging to obtain high resolution images for GTV delineation.

Chapter 6 focuses on the implementation of a novel beam-on imaging framework to retrospectively reconstruct time-resolved non-rigid motion-fields with very high spatiotemporal resolution (> 10 Hz for 3D). Here, we build upon a previously (theoretically) described motion estimation framework called MR-MOTUS [80] and expand the method with a low-rank signal model and develop a prospective implementation. Low-rank MR-MOTUS exploits spatiotemporal correlations in internal body motion with a low-rank motion model, and inverts a signal model that relates motion-fields directly to a reference image and k-space data. The time-resolved motion-fields are required for retrospective dose accumulation and could form the basis for prospective real-time motion estimation for real-time gating/tracking. Note that my contribution to this work primarily consisted of the k-space trajectory development, the prospective scanner implementation and the signal preprocessing of low-rank MR-MOTUS on the MR systems.

Chapter 7 investigates the technical feasibility of magnetic resonance fingerprinting (MRF) for daily tumor response monitoring for MR-linac. MRF is a rapid multiparametric quantitative MRI technique that relies on adequate control over system imperfections, such as eddy currents and B_1^+ , which differ significantly on MR-linac scanners compared to diagnostic scanners. We investigate whether MRF is feasible on MR-linac systems and conclude that the precision and accuracy of the parametric maps are sufficient for further investigation of the clinical utility of MRF for online quantitatively MRI-guided radiotherapy.

Lastly, **Chapter 8** summarizes the most important findings of this thesis, critically reflects on the individual chapters and speculates on the potential impact for MRI in radiotherapy. Finally, I will provide my perspective on the future of MRI in radiotherapy and how the technologies described in this thesis fit into this narrative.

He who thinks great thoughts, often makes great errors.

- Martin Heidegger

Quantifying head-and-neck tumor motion using 2D cine MRI

Bruijnen, Tom
Stenkens, Bjorn
Terhaard, Chris
Legendijk, Jan J.W.
Raaijmakers, Cornelis P.J.
Tijssen, Rob H.N.

The following chapter is based on:

Intrafraction motion quantification and planning target volume margin determination of head-and-neck tumors using cine magnetic resonance imaging, 2019, *Radiotherapy and Oncology*; **91**: 571-578

Abstract

Purpose: To quantify intrafractional motion to determine population-based radiotherapy treatment margin determination for head-and-neck tumors.

Methods: Cine MR imaging was performed in 100 patients with head-and-neck cancer on a 3T scanner in a radiotherapy treatment setup. MR images were analyzed using deformable image registration (optical flow algorithm) and changes in tumor contour position were used to calculate the tumor motion. The tumor motion was used together with patient setup errors (450 patients) to calculate population-based PTV margins.

Results: Tumor motion was quantified in 84 patients (12/43/29 nasopharynx/oropharynx/larynx, 16 excluded). The mean maximum (95th percentile) tumor motion (swallowing excluded) was: 2.3 mm in superior, 2.4 mm in inferior, 1.8 mm in anterior and 1.7 mm in posterior direction. PTV margins were: 2.8 mm isotropic for nasopharyngeal tumors, 3.2 mm isotropic for oropharyngeal tumors and 4.3 mm in inferior-superior and 3.2 mm in anterior-posterior for laryngeal tumors, for our institution.

Conclusions: Intrafractional head-and-neck tumor motion was quantified and population-based PTV margins were calculated. Although the average tumor motion was small (95th percentile motion <3.0 mm), tumor motion varied considerably between patients (0.1-12.0 mm). The intrafraction motion expanded the CTV-to-PTV with 1.7 mm for laryngeal tumors, 0.6 mm for oropharyngeal tumors and 0.2 mm for nasopharyngeal tumors.

Keywords: Intrafraction motion, head-and-neck cancer, MRI, radiotherapy, margins

2.1 Introduction

Radiotherapy is used as a primary or secondary treatment in up to 75% of patients with head-and-neck cancer [81]. Head-and-neck tumors are often in close vicinity of multiple organs at risk and therefore require highly conformal treatment plans. These treatment plans are characterized by steep dose gradients that minimize the dose to the organs at risk while maintaining an adequate tumor dose. These steep dose gradients generate effective treatment plans in theory, but rely heavily on accurate geometrical dose delivery.

To deliver the dose with high geometric accuracy, the treatment needs to be set up precisely and the intrafractional and interfractional tumor motion needs to be accounted for. Treatment setup is improved using immobilization devices such as thermoplastic masks and a personalized head support [82–84]. The residual interfractional motion is accounted for by adding an uncertainty margin that expands the clinical target, called the planning target volume (PTV), which accounts for setup errors [85, 86] patient weight loss and tumor shrinkage [87, 88]. Intrafractional motion is accounted for by either a personalized margin or a population-based margin that is included in the PTV. Intrafractional motion could be defined as the internal motion; that is, the result of respiration, swallowing, tongue movements and slow motions induced by organ relaxation. These movements must be accurately quantified either to determine population-based margins or personalized margins to account for the internal motion. For head-and-neck tumors this margin is not explicitly reported but generally an additional margin is used for laryngeal tumors. In our institute an additional margin of 5 mm is added to the standard PTV margin [89].

Thus far, the quantification of the intrafractional motion has primarily focused on the impact of swallowing on the accumulated dose. Swallowing-induced motion of head-and-neck tumors or surrogate structures such as the larynx was in the range of 15–29 mm [90–96]. Although the tumor motion is large, the incidence and total duration of swallowing was 1% of the irradiation time. In addition, the tumor is only at the maximum position during a small part of the complete swallowing event. Therefore, the sole effect of swallowing on the accumulated tumor dose was considered small [91, 92, 95].

Non-swallowing induced tumor motion, on the other hand, could have a larger effect on the accumulated dose and has been investigated in three studies. Prevost et al. used video fluoroscopy in 15 patients to track platinum markers, as a surrogate for tumor motion, and concluded that the motion was insignificant for clinical practice [92]. Bradley et al. used 2D cine MRI in 11 patients to quantify intrafraction tumor motion and concluded that the tumor motion required a PTV expansion [95]. Gurney-Champion et al. used dynamic contrast enhanced MRI in 56 patients to quantify intrafractional tumor motion in 3D and concluded that the tumor motion required a PTV expansion [97].

Although these studies analyzed patients with head-and-neck cancer in radiotherapy treatment setup, the extent of the quantified (non-swallowing) tumor motion

varied a lot. The variation could be due to differences in imaging setup and patient population, but we believe that the different imaging methods are the main cause. In particular, the temporal resolution of the imaging method determines the sensitivity to measure fast occurring motions such as respiration. While the 3D method [97] is superior to quantify slower shifts throughout the treatment, the method lacks the temporal resolution (0.34 Hz) to accurately quantify respiratory-induced tumor motion. This hypothesis is supported by the lower respiratory-induced tumor motion found with the 3D method compared to the 2D methods by Bradley et al. That study, however, had a limited sample size (11 patients) and too short imaging window (15 s) to describe the respiratory-induced tumor motion on a population-based level.

In this study we quantify the intrafractional motion to calculate PTV margins of head-and-neck tumors in supine radiotherapy treatment position. We quantify tumor motion using 2D cine MRI and deformable image registration. We show that respiratory-induced tumor motion varies considerably among patients (larger than 10 mm) and we calculate population-based PTV margins for nasopharyngeal, oropharyngeal and laryngeal tumors.

2.2 Methods

2.2.1 Study population

Cine MR scans were acquired in 100 consecutive patients with head-and-neck cancer that were selected for radiotherapy treatment in our department between June 2016 and July 2017. From the 100 selected patients, 16 were excluded due to one of three reasons: image quality was insufficient for analysis (2 patients), the 2D image was not positioned correctly (7 patients), or the patient was retracted from the treatment (7 patients). The patient characteristics are described in Supplementary information I. MR scans were acquired during pretreatment imaging for which the requirement to obtain informed consent was waived by the institutional review board.

2.2.2 MR image acquisition

The patients underwent CT and MRI scans prior to the first week of treatment. The scans were acquired in radiotherapy treatment setup, which consisted of a custom-fit five-point thermoplastic immobilization mask and an individualized head support (Civco Radiotherapy, Reeuwijk, the Netherlands). The MRI scans were acquired on a 3T MR scanner (Ingenia, Philips, Best, the Netherlands) with two flexible surface coils and an integrated posterior coil for signal reception (Fig. 2.1-A).

Two 2D cine MR scans of 60 s were added to the clinical protocol, which were acquired approximately 5 and 13 min after the start of the MR examination. The time between the two cine scans was 8.8 ± 1.5 min and the range was 4–11 min. The cine MR scans were acquired in the sagittal plane because the motion in the left–right direction was found to be small [95,97]. Since the tumor position is not

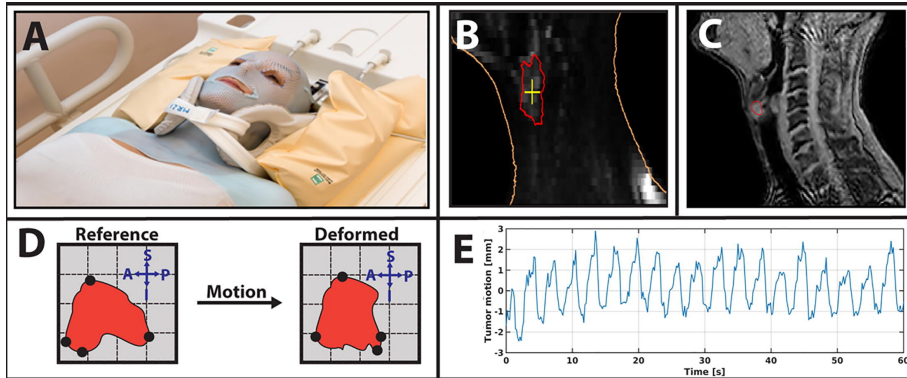


Figure 2.1: Methods used to quantify the tumor motion. (A) Imaging setup including the immobilization mask, personalized head support and surface receiver coils. (B) Diffusion weighted image used to estimate tumor position. (C) RF and gradient spoiled gradient echo image from a cine MR scan. (D) Method to calculate the tumor motion by comparing maximum contour coordinates (black dots) between time-points. (E) Applying the method of (D) for each time-point yields motion profiles that can be evaluated over time.

delineated prior to pretreatment imaging, the radiotherapy technicians used the diffusion weighted image (Fig. 2.1-B) along with the localizer images to estimate the slice position such that it was placed through the center of the tumor. From 84 scanned patients, 17 did not receive a second cine MR scan due to logistical reasons.

The cine MR scans were acquired using a 2D spoiled gradient echo sequence with the following sequence parameters: field of view = $250 \times 250 \text{ mm}^2$, slice thickness = 10 mm, flip angle = 5° , echo time = 1.45 ms and repetition time = 3.16 ms. The scans were accelerated using partial Fourier sampling of 70% and parallel imaging ($R = 2.3$) to increase the temporal resolution to 158 ms with 1.5 mm in-plane spatial resolution (Fig. 2.1-C). We did not give the patients any instructions regarding breathing patterns or swallowing behavior prior to the exam.

2.2.3 MR image analysis

As part of the clinical workflow, the radiation oncologist delineated the gross target volume (GTV) using the MRI and CT scans. The GTV was transferred onto a single image (reference) of the cine MR scan using a 2D-to-3D rigid normalized mutual information registration in Volumetool (an in-house built software package) [98]. The other images of the cine MR scan were then registered to the reference image using the RealTITracker [99]. The RealTITracker uses an optical flow algorithm to estimate deformable tissue motion and the algorithm returns pixel-wise deformation vector fields (DVF). The RealTITracker has been validated for cine MR scans in multiple anatomical locations and for multiple image contrasts [100].

First, the two cine MR scans were analyzed separately to quantify the tumor motion within the one minute scan. The images were registered using the Re-

alTITracker to obtain DVFs for the entire field-of-view. The DVFs were used to propagate the GTV to the next time-point and were used to calculate the outermost contour position of the GTV for each direction. The outermost GTV contour position was then compared to the contour positions of the reference image (Fig. 2.1-D). The differences in the contour positions were used to quantify the tumor motion and will be referred to as motion profiles $x(t)$ (Fig. 2.1-E). To investigate whether the first and second scans showed significant systematic differences a paired t-test was performed between the motion profiles. Second, for both cine MR scans the average GTV contour positions (\vec{x}_{cine}) were calculated and then the difference was used to quantify the tumor shift between the scans.

To investigate the contribution of respiration to the tumor motion, the maximum tumor displacement was calculated for both the cine MR scans. In the calculation we excluded the images that were affected by swallowing motion or tongue motion. Swallowing was identified according to the definition of Matsuo et al. [101] and we discarded these frames from the analyses to calculate the maximum tumor motion. We did not discard the frames in the analysis for the PTV margin determination.

2.2.4 PTV margin determination

The measured tumor motion was used together with the treatment setup errors to calculate a population-based PTV (expansion from clinical target volume (CTV)). The tumor motion within and between the cine MR scans, which included swallowing motion and tongue motion, was separated into systematic errors (Σ_{motion}) and random errors (σ_{motion}). The different components of the systematic and random errors were added in quadrature, i.e. $\Sigma_{motion} = \sqrt{(\Sigma_{shift}^2 + \Sigma_{resp}^2)}$ and $\sigma_{motion} = \sigma_{resp}$. The tumor shift between the scans was described as a linear occurring translation such that $\Sigma_{shift} = SD(\vec{x}_{cine1} - \vec{x}_{cine2})$, with SD as the standard deviation over the patients. The tumor motion within the scans was calculated as $\Sigma_{resp} = \sigma_{resp} = \sqrt{(1/N \Sigma(0.5SD(\vec{x}_{cine1}) + 0.5SD(\vec{x}_{cine2}))^2)}$ with N is the number of patients. The Σ_{resp} was used to account for the mismatch between the planning CT and the treatment setup cone beam CT [102].

The treatment setup errors were calculated from positioning verification data in 450 patients with head-and-neck cancer treated in the last two years at our institute. Note that the 100 patients selected for the cine imaging are a subgroup of the 450 patients used for the position verification data. The treatment followed an extended no action level (eNAL) protocol [103], in which imaging was performed for the first three fractions and subsequently once per week. We calculated the setup errors by registering the on board cone beam CT images to the reference CT. The images were registered in XVI using bone matching with a clipping box. All the patients received thermoplastic masks and all the registration were performed by the radiotherapy technicians. We then calculated Σ_{resp} by taking the standard deviation of the mean systematic error over all the patients and σ_{setup} as the mean of all the average standard deviations over all the fractions.

The tumor motion errors and the treatment setup errors were then applied in the margin recipe of van Herk et al. ($PTV = 2.5\sqrt{(\Sigma_{motion}^2 + \Sigma_{setup}^2)} + 0.7\sqrt{(\sigma_{motion}^2 + \sigma_{setup}^2)}$)

σ_{setup}^2)) to calculate the population-based PTV [20,21].

2.3 Results

2.3.1 Tumor motion quantification

The maximum tumor motion (swallowing excluded) was more pronounced in laryngeal tumors than in oropharyngeal and nasopharyngeal tumors (Fig. 2.2). Typical motion profiles for tumors that move due to respiration, swallowing or do not move at all are shown in Fig. 2.3. Furthermore, tumor motion was most pronounced in the superior and inferior direction and was significantly different between all directions and anatomical locations (repeated factorial ANOVA). Tumor motion varied considerably between patients and some large tumor displacements were detected (Supplementary information II). The mean maximum tumor motion was 2.3 (range: 0.3–12.0) mm in superior, 2.4 (range: 0.3–7.8) mm in inferior, 1.8 (range: 0.2–5.2) mm in anterior and 1.7 (range: 0.3–4.1) mm in posterior direction (Table. 1). The measured maximum tumor displacements of the first and second MR scans did not differ significantly ($p < 0.05$).

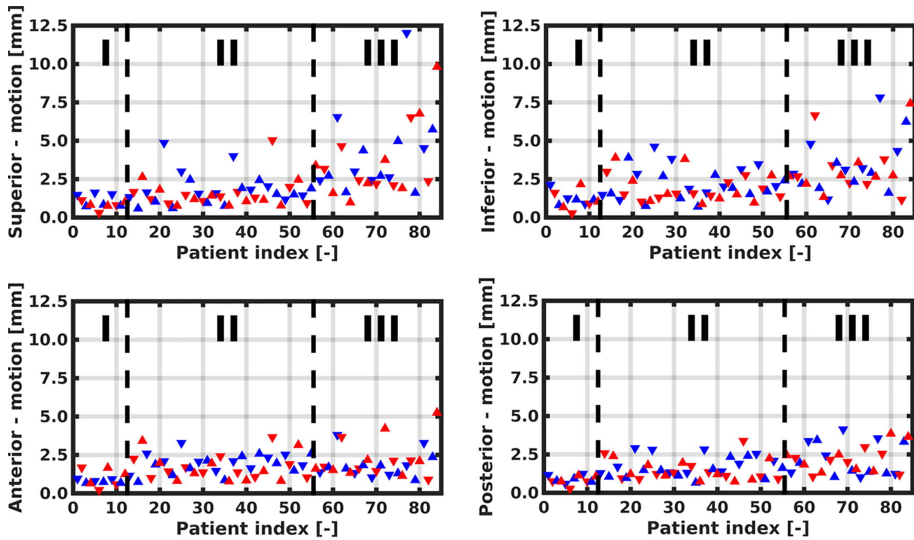


Figure 2.2: Maximum (95th percentile) tumor motion (swallowing excluded) over the cine MR scans. Patients are arranged according to the anatomical position of the tumor, with I denoting the nasopharyngeal tumors, II the oropharyngeal tumors and III the laryngeal tumors. The different colors and shapes are used to distinguish neighboring points.

2.3.2 PTV margin determination

To determine the systematic motion errors and the random motion errors the standard deviation of the tumor motion profiles was calculated for all patients (Fig. 2.4). The Σ_{motion} over all patients was 0.9 mm in superior, 0.7 mm in inferior, 0.6 mm in anterior and 0.6 mm in posterior direction. The standard

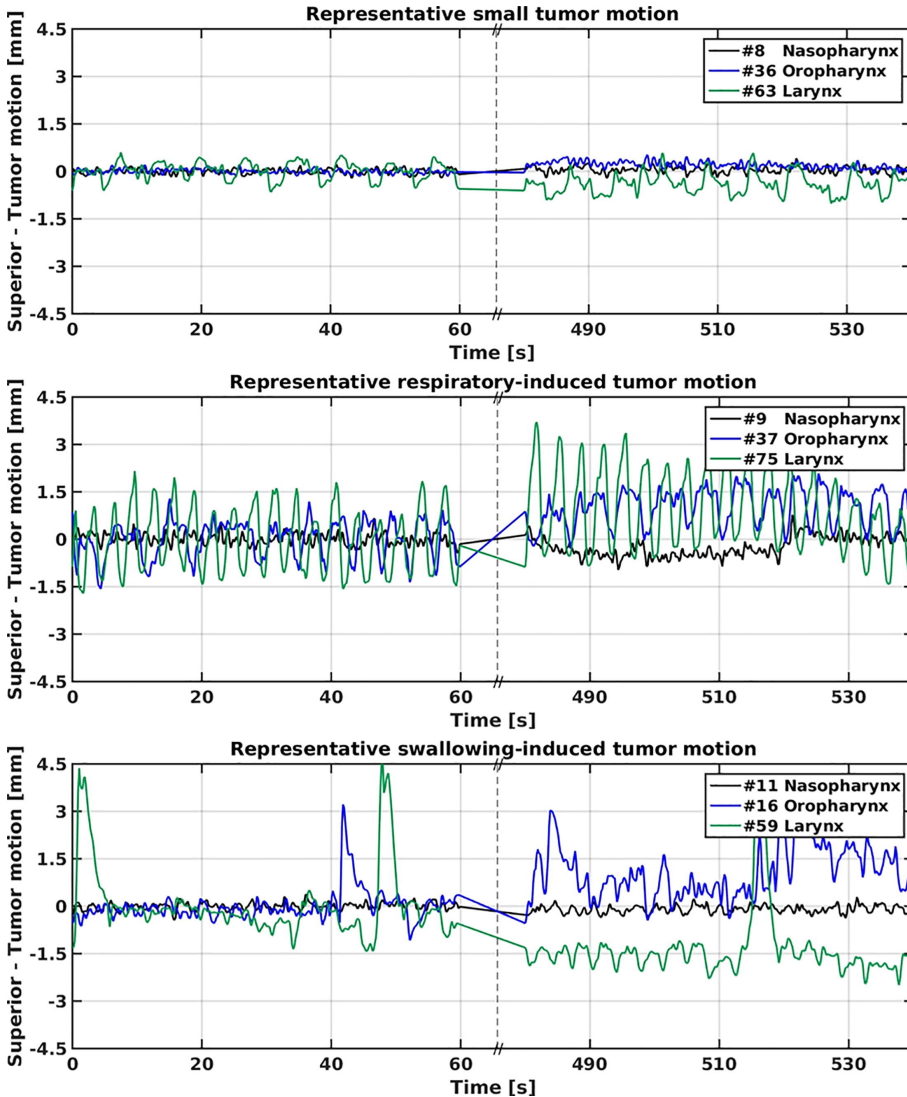


Figure 2.3: Examples of motion in the superior direction for tumors that showed almost no motion, for tumors that showed respiratory-induced motion and tumors that showed swallowing-induced motion. The graphs have a break on the horizontal axis to differentiate the data from the two different cine MR scans.

deviation (σ_{motion}) over all the patients was 0.8 mm in superior, 0.7 mm in inferior, 0.5 mm in anterior and 0.5 mm in posterior direction. The Σ_{motion} and σ_{motion} for all the directions and anatomical subsites are shown in Supplementary information III.

The systematic setup errors, calculated from positioning verification data in 450 patients, were 0.7 mm in the anterior and posterior direction and 0.7 mm in the superior and inferior direction. The random setup errors were 1.6 mm in the

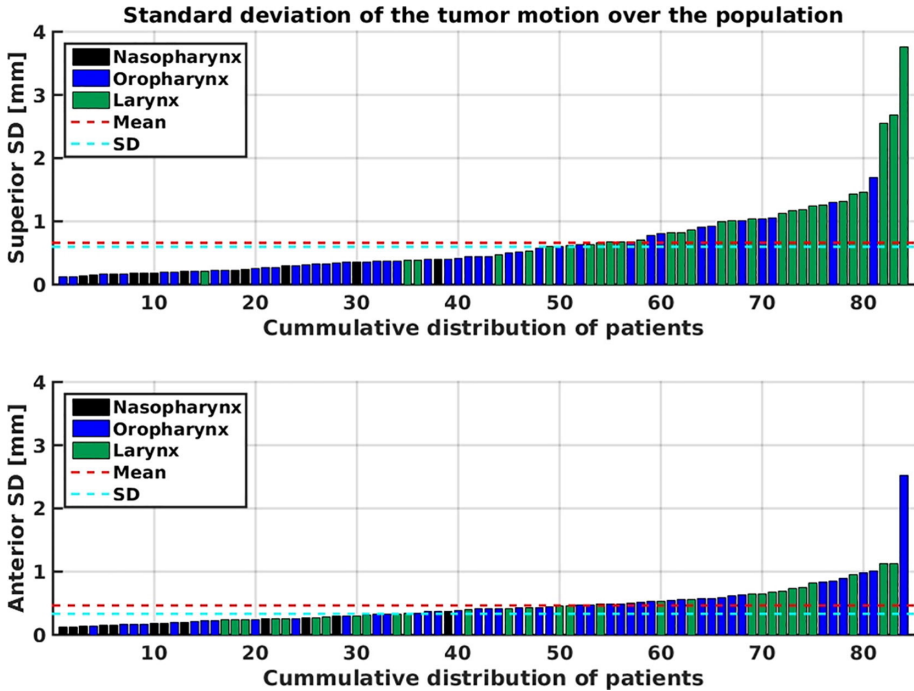


Figure 2.4: Sorted distribution of the standard deviation of the tumor motion profiles and colored by the anatomical location.

anterior and posterior direction and 1.4 mm in the superior and inferior direction. Note that these setup errors are institution specific and therefore require separate validation in other clinics.

The setup errors (450 patients) and the motion errors (84 patients) were used to calculate PTV margins according to the recipe of van Herk et al. (Table. 2). In general, the tumor motion expanded the CTV-PTV margin for nasopharyngeal tumors with <0.2 mm (compared to the static case). The PTV margin for oropharyngeal tumors was isotropically expanded with about 0.6 mm. The PTV margin for laryngeal tumors was expanded with 1.7 mm expansion in the superior and inferior direction and 0.7 mm expansion in the anterior and posterior direction.

2.4 Discussion

We quantified the 2D intrafractional tumor motion in 84 patients using cine MRI and deformable image registration. The maximum tumor motion (swallowing excluded) was small on average, with 2.8 mm in the superior–inferior direction and 2.1 mm in the anterior–posterior direction. However, we found that some laryngeal tumors showed respiratory-induced tumor motion larger than 10 mm in the superior–inferior direction. The intrafractional tumor motion (swallowing included), together with treatment setup errors, was used to calculate population-

based PTV margins for nasopharyngeal, oropharyngeal and laryngeal tumors.

Head-and-neck tumor motion was quantified in three studies before: Prevost et al. used videofluoroscopy (10 Hz) to measure 2D tumor motion (swallowing excluded) in 15 patients with oropharyngeal cancer over 20 s and found mean maximum motion of 1.4 mm (range: 0.4–3.1) in superior–inferior and 1.3 mm (range: 0.4–3.4) in anterior–posterior [92]. Bradley et al. used cine MRI (6.5 Hz) to measure 2D tumor motion (swallowing excluded) in 11 patients (4 oropharyngeal and 7 laryngeal cancer), over 15 s and found mean maximum motion of 3.1 mm (range: 0.0–8.2) in superior–inferior and 1.8 mm (range: 0.0–6.0) in anterior–posterior [95]. Gurney-Champion et al. used dynamic contrast MRI (0.34 Hz) to measure 3D tumor motion in 56 patients (48 oropharyngeal and 8 laryngeal cancer) over 223 s and found 95th percentile systematic tumor motion of 0.6 mm in anterior–posterior and 1.1 mm in superior–inferior [97]. These studies did not have sufficient data to report the tumor motion separate for the anatomical subsites, however our findings indicate that the motion depends considerably on the anatomical subsite and therefore requires comparison accordingly. Here we will compare the motion reported in the aforementioned studies versus our study and discuss the resulting PTV margins. Nasopharyngeal tumors are in practice considered as non-moving tissue and thus no margin is added to account for the internal motion. The mean maximum tumor motion was approximately 1 mm and expanded the PTV with less than 0.2 mm. Therefore, our findings support the clinical practice of not adding a margin to account for the internal motion for nasopharyngeal tumors. Oropharyngeal tumors showed mean maximum motion of 2.0 mm in superior–inferior direction and 1.7 mm in anterior–posterior direction. While the average tumor motion was small, some patients had respiratory patterns that involved a structural component of tongue displacement that resulted into increased tumor motion (Video: Supplementary information IV). The tumor motion in our study slightly differed from Prevost et al. and Bradley et al. which is presumably due to the difference in imaging time and difference in patient population. However, the tumor motion reported by Gurney-Champion et al. was considerably smaller than the 95th percentile systematic motion found in our study, which was 1.5 mm in anterior–posterior and 2.0 mm in superior–inferior. The clinically used PTV for oropharyngeal tumors is typically between 3 and 5 mm depending on the availability of daily image guided radiotherapy [104]. Our findings suggest that a isotropic 0.7 mm PTV expansion is required to account for the internal motion for oropharyngeal tumors. Laryngeal tumors showed mean maximum motion of 3.8 mm in superior–inferior direction and 2.2 mm in anterior–posterior direction. While the average tumor motion was small, some patients had tumors that moved more than 10 mm due to respiration (Video: Supplementary information IV). The tumor motion in our study is larger than reported by Bradley et al. which was presumably due to the longer period of imaging that was considered. Our findings suggest that a 2.0 mm PTV expansion in superior–inferior and a 0.7 mm in anterior–posterior is required to account for the internal motion for laryngeal tumors. Here we want to emphasize that relatively small margins of 2.0 mm in superior–inferior are sufficient to account for the large displacements of up to 12 mm.

Tumor motion was quantified using cine MRI in combination with deformable image registration. While deformable image registration is widely used [105], a general geometric validation in the radiotherapy setting remains difficult [106]. The accuracy of deformable image registration is dependent on both the parametrization of the algorithm and the contrast of the images. In this work we validated the deformable image registration algorithm by tracking local landmarks (epiglottis, posterior oral cavity) in a small number of patients and adjusted the parametrization such that the best match was obtained. In addition, we subtracted the deformation vector field from each image and inspected the residual motion to ensure that the registration fully resolved the motion around the tumor. Deformable image registration was used to quantify tumor with sub-voxel precision. Sub-voxel precision of the specific algorithm used in this work was demonstrated to detect deformations at approximately $1/3$ of the pixel size [61].

Tumor motion was quantified over a 8 min period approximately 5 and 13 min after the patient entered the MR scanner. While these times correspond with typical step-and-shoot intensity modulated radiotherapy (IMRT) treatment at our institute, typical volumetric modulated arc therapy treatment times are approximately half [107]. For the volumetric modulated arc therapy (VMAT) treatment times we calculated the PTV margins by halving the tumor shift between the two cine MR scans (Supplementary information V). Note that VMAT and hypofractionation will counterbalance the assumption that swallowing has a relatively low contribution to total accumulated dose. However, ultimately it is the percentage of time per fraction that the person is swallowing which is important, which does not differ between VMAT or IMRT.

The motion analysis provides a representative overview of the tumor motion in a large group of patients with head-and-neck cancer, however the analysis has some inherent limitations: (1) Left–right (through-plane) motion can affect the image registration, however previous studies reported the motion to be small compared to slice thickness of 10 mm used in our acquisition [97]. (2) The tumor motion between the two cine MR scans was processed as a linear trend. This assumption is not completely valid but it is the most reasonable approach for the presented data [20]. (3) The persistence of the tumor motion over a prolonged period of treatment is unclear. For example, swallowing incidence is known to vary over the course of the treatment [91].

Intrafractional tumor motion was quantified in 84 patients using cine MRI with deformable image registration and population-based PTV margins were calculated for patients with head-and-neck tumors. Although the average tumor motion was small (95th percentile motion <3.0 mm), tumor motion varied considerably between patients (0.1–12.0 mm). Incorporating the tumor motion in the margin recipe expanded the CTV to PTV with 0.2 mm for nasopharyngeal tumors, with 0.6 mm for oropharyngeal tumors and with 1.7 mm for laryngeal tumors.

Acknowledgments

This work is part of the research programme HTSM with project number 15354, which is financed by the Netherlands Organisation for Scientific Research (NWO) and Philips Healthcare (Best, the Netherlands).

We are what we repeatedly do. Excellence, then, is not an act, but a habit.

- Aristotle

GIRF-based RF phase cycling to reduce eddy currents in bSSFP

Bruijnen, Tom
Stenkens, Bjorn
van den Berg, Cornelis A.T.
Tijssen, Rob H.N.

The following chapter is based on:
Prospective GIRF-based RF phase cycling to reduce eddy current-induced steady-state disruption in bSSFP imaging, 2019, *Magnetic Resonance in Medicine*; **84**(1): 115-127

Abstract

Purpose: To propose an explicit bSSFP signal model that predicts eddy current-induced steady-state disruptions and to provide a prospective, practical and general eddy current compensation method.

Theory and Methods: Gradient impulse response functions (GIRF) were used to simulate trajectory-specific eddy current-induced phase errors at the end of a repetition block. These phase errors were included in bloch simulations to establish a bSSFP signal model to predict steady-state disruptions and their corresponding image artefacts. The signal model was embedded in the MR system and used to compensate the phase errors by prospectively modifying the phase cycling scheme of the RF pulse. The signal model and eddy current compensation method were validated in phantom and *in vivo* experiments. In addition, the signal model was used to analyze pre-existing eddy current mitigation methods, such as 2D tiny golden angle radial and 3D paired phase encoded Cartesian acquisitions.

Results: The signal model predicted eddy current-induced image artefacts, with the zeroth order GIRF being the primary factor to predict the steady-state disruption. Prospective RF phase cycling schemes were automatically computed online and considerably reduced eddy current-induced image artefacts. The signal model provides a direct relationship for the smoothness of k-space trajectories, which explains the effectiveness of phase encode pairing and tiny golden angle trajectory.

Conclusion: The proposed signal model can accurately predict eddy current-induced steady-state disruptions for bSSFP imaging. The signal model can be used to derive the eddy current-induced phase errors required for trajectory specific RF phase cycling schemes, which considerably reduce eddy current-induced image artefacts.

Keywords: MRI, Eddy current, bSSFP, GIRF, RF phase cycling, non-Cartesian

3.1 Introduction

Balanced steady-state free precession (bSSFP) sequences offer the highest signal-to-noise ratio (SNR) [108–110] and encode multiple physical parameters into the signal [111, 112]. However, the sequence is prone to eddy current-induced steady-state disruptions that can severely compromise image quality or the physical parameter quantification [113, 114]. These eddy currents are a direct consequence of the gradients used for the spatial encoding [115, 116]. In particular, the gradients that change dynamically over repetition blocks disrupt the steady-state (e.g. phase encode gradient), while the static gradients do not (e.g. slice-selection gradient). Here a repetition block is defined as the pulse sequence diagram with length of one repetition time. These eddy current effects alter the signal evolution and therefore have to be corrected prospectively. One strategy to reduce the impact of the eddy currents is to select an encoding scheme that smoothly varies the gradient waveforms across sequential repetition blocks. This strategy has been applied to reduce the impact of eddy currents in Cartesian bSSFP imaging using phase encode rearranging [114, 116, 117], phase encode grouping [115, 118] or phase encode averaging [119]. Similar developments were reported in non-Cartesian bSSFP imaging that primarily aim to minimize angular increments while maintaining incoherent aliasing properties and robustness to motion artefacts [120–122].

While these smoothly varying encoding schemes are effective at reducing eddy current artefacts, they considerably constrain the k-space trajectory design parameter space, leading to sub-optimal encoding efficiency. Further, the effectiveness of these smoothly varying encoding schemes is dependent on sequence parameters, such as the resolution, and therefore do not provide a general solution. A second, and more general, proposed strategy is to annihilate the eddy current effect through partial slice dephasing (through-slice equilibration) [115]. However, this method requires modification of the slice select gradient and is therefore not applicable to 3D acquisitions. A third proposed method is to monitor the eddy current-induced magnetic field perturbations during a calibration scan using a dynamic field camera [123] and to subsequently correct the corresponding phase errors by prospectively inserting small gradients and adjusting the RF phase cycling (RF-PC) scheme of the excitation pulse [124]. While these "run-time" adjustments require only minor sequence modifications and provide a direct and effective compensation method, they require additional hardware and a calibration scan, which considerably reduces the practicality for clinical implementation. From these observations it is evident that there is a clear need for a deterministic signal model that can relate system-dependent eddy current properties to sequence specific steady-state disruptions and subsequently to bSSFP image artefacts. Such a general signal model could be taken into account for numerical or empirical sequence optimization or could be used for the direct compensation method [124].

Recently, the Gradient Impulse Response Function (GIRF) has been proposed as a comprehensive method to characterize the linear and time-invariant behaviour of the entire gradient system [76]. This characterization includes the eddy current

behavior and therefore we hypothesize that the GIRF should contain all the information required to describe the steady-state disruptions in bSSFP acquisitions. In this work we show that these eddy current effects are indeed deterministic and can be predicted given the gradient waveform and the system-specific GIRF. We propose an explicit bSSFP signal model, based on the GIRF, that predicts the impact of the eddy currents on the steady-state. First we use this signal model to show that the largest component in the steady-state disruption originates from the zeroth order eddy currents. Second, we show with phantom experiments that the proposed signal model can accurately predict eddy current image artefacts for both Cartesian and non-Cartesian acquisitions. Third, we revisit the prospective compensation method that adjusts the phase of the excitation pulse and we derive the input for RF-PC directly from the GIRF. We demonstrate that GIRF-based RF-PC counteracts the eddy current effects and therefore reduces steady-state disruptions. Finally, we show that the proposed method works for 2D/3D Cartesian and non-Cartesian sequences and is in principle applicable to any MRI trajectory.

3.2 Theory

3.2.1 Eddy currents and bSSFP signal model

Balanced steady-state free precession sequences converge to a steady-state if the following three conditions are met: 1) $TR \ll T_2$; 2) The gradients must be zeroth moment nulled; 3) The total phase accumulation (ϕ) due to B_0 , gradient waveforms ($G(t)$) and RF-pulses must be constant over repetition block n . Bieri et al. showed that eddy currents can violate condition 3) and therefore disrupt the steady-state [110, 115]. The effect of steady-state disruption can be directly related to eddy current-induced time-varying magnetic fields that accumulate additional phase $\Delta\phi(n)$ in the transverse magnetization (m_{xy}). This $\Delta\phi(n)$ can be decomposed in spatially uniform (0^{th} order), spatially linear varying (1^{st} order) and higher order (n^{th} order) magnetic field components. In this work we refer to these components as $\Delta B_0(n, t)$ that induces $\Delta\phi^0(n)$ and $\Delta G(n, t)$ that induce $\Delta\phi^1(n)$ with total phase error $\Delta\phi(n, r) = \Delta\phi^0(n) + \Delta\phi^1(n, r)$. Fischer et al. showed that higher order field contributions are unlikely to exhibit a considerable effect on these phase errors and therefore they are ignored in the signal model [124]. Note that $\Delta\phi^1(n, r)$ is a function of distance r from isocenter. The $\Delta\phi(n, r)$ over the entire repetition block can then be described as Eq.3.1.

$$\Delta\phi(n, r) = \sum_{ax \in x, y, z} \gamma \int_0^{TR} [\Delta B_{0,ax}(n, t) + \Delta G_{ax}(n, t) r] dt \quad (3.1)$$

Here γ is the gyromagnetic ratio and ax are the x,y,z axes of the physical gradient coils. The eddy current-induced time-varying magnetic fields ΔG_{ax} and $\Delta B_{0,ax}$ are a function of the gradient waveforms $G_{ax}(t)$. The relationship between these fields and $G(t)$ can be approximated using the zeroth and first order Gradient Impulse Response Functions ($GIRF^{0,1}$) [76]. The zeroth order GIRF ($GIRF^0$) describes the spatially uniform field modulations and the first order

GIRF ($GIRF^1$) describes the spatially linear field modulations. The GIRFs can be used to express Eq.3.1 in terms of the known quantity $G(t)$ Eq.3.2.

$$\Delta\phi(n, r) = \sum_{ax \in x, y, z} \gamma \int_0^{TR} [GIRF_{ax}^0 * G_{ax}(n, t) + GIRF_{ax}^1 * G_{ax}(n, t) r] dt \quad (3.2)$$

The process of computing $\Delta\phi(n, r)$ for a standard 2D Cartesian gradient echo sequence is illustrated in Figure 3.1. Note that Figure 3.1 shows actually measured field responses where $\Delta\phi^1$ is calculated at $r = 10$ cm (off iso-center). Eq.3.2 provides the full description of eddy current-induced phase accumulation $\Delta\phi(n, r)$, just before the next RF pulse, that could be used to simulate the steady-state disruption.

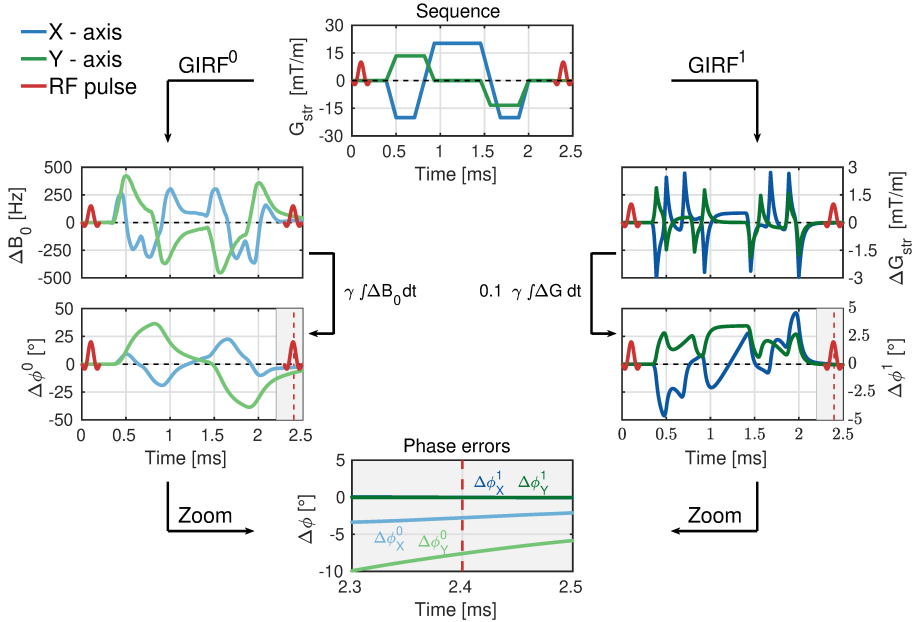


Figure 3.1: Eddy currents and bSSFP signal model: Top image shows the gradient waveforms corresponding to a typical 2D Cartesian bSSFP acquisition. **Left column:** The gradient waveform is processed with the $GIRF^0$, which induces a field modulation ΔB_0 that decays slowly in time. Integrating ΔB_0 over time gives the eddy current-induced phase error $\Delta\phi^0$, which is nonzero at the end of the repetition block (red dashed line). **Right column:** The gradient waveform is processed with the $GIRF^1$, which induces a gradient modulation ΔG_{str} that decays rapidly in time. Integrating the ΔG_{str} at 10 cm off iso-center gives eddy current-induced phase error $\Delta\phi^1$, which is nonzero at the end of the repetition block (red dashed line). **Bottom image:** Shows a zoom image of the last 200 μs of the repetition block, which demonstrates the nonzero phase errors. Note that $\Delta\phi^0 \gg \Delta\phi^1$ for both axes. Note that the blue shades indicate the X-axis and the green shades indicate the Y-axis. Lighter colors indicate the zeroth order effects and darker colors indicate the first order effects.

3.2.2 Reduced bSSFP signal model

In Eq.3.2, the total phase error $\Delta\phi(n, r)$ is dependent on the spatial coordinate r , which complicates a straightforward signal model. We observed from system measurements that in general $\Delta\phi^0 \gg \Delta\phi^1$ holds true for all sequences. Figure 3.2 provides evidence to support this assumption by showing measured field responses for three sequences. These sequences were selected to have minimal dead-time between the spatial encoding gradients and the sequential RF pulse to maximize the impact of first order effects. A physical explanation to justify $\Delta\phi^0 \gg \Delta\phi^1$ could be that short lived eddy currents are more prevalent in the first order effects, compared to longer lived eddy currents in the zeroth order effects. Using this assumption we can simplify Eq.3.2 to Eq.3.3.

$$\Delta\phi(n) = \sum_{a,x \in x,y,z} \gamma \int_0^{TR} [GIRF_{ax}^0 * G_{ax}(n, t)] dt \quad (3.3)$$

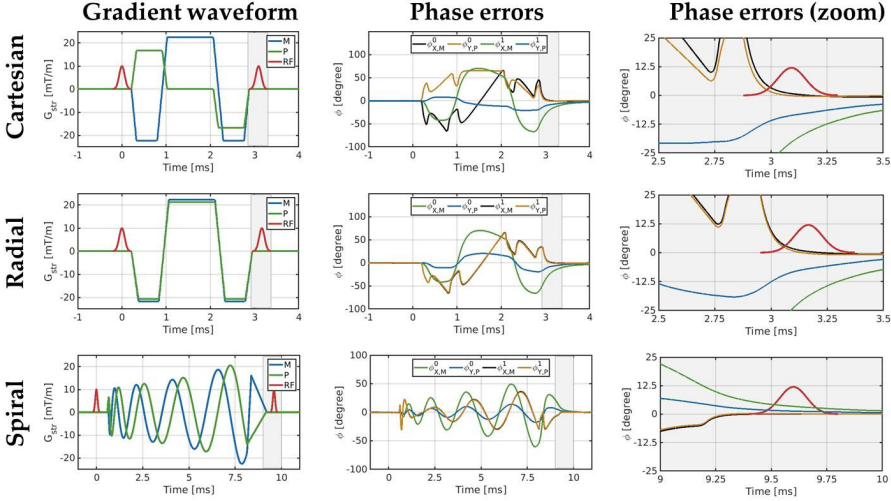


Figure 3.2: Comparison of zeroth order vs first order eddy current-induced phase errors: The three rows represent three different sequences where the RF pulse is positioned as close to the gradient waveform as possible. This setup provides a scenario where the faster decaying first order effects could induce large phase errors. Column 1 indicates the investigated gradient waveform. Column 2 represents the corresponding phase errors. Column 3 represents a zoom of the phase error focused on the sequential RF pulse. The phase error at $t = TR$ (center RF pulse) were for Cartesian: $\Delta\phi_{M,P}^0 = [-20.2^\circ, -7.3^\circ]$ vs $\Delta\phi_{M,P}^1 = [0.9^\circ, 0.0^\circ]$. Radial: $\Delta\phi_{M,P}^0 = [-18.7^\circ, -6.9^\circ]$ vs $\Delta\phi_{M,P}^1 = [0.6^\circ, -0.3^\circ]$. Spiral: $\Delta\phi_{M,P}^0 = [3.5^\circ, 1.4^\circ]$ vs $\Delta\phi_{M,P}^1 = [0.2^\circ, 0.3^\circ]$. Here you can observe that $\Delta\phi^0 \gg \Delta\phi^1$ with an average factor of more than 20. The subscripts in the second column follow the structure of $\Delta\phi_{X,M}^1$, which correspond to the impact of the x gradient coil on the M gradient waveform.

Eq.3.3 is valid when we consider the repetition blocks individually, but becomes incomplete when we take the sequence history into account. The actual phase accumulation $\Delta\phi(n)$ at repetition block n will also be a function of the (unfinished) phase accumulation during repetition block $n-1$ $\Delta\phi(n-1)$. For clearer notation

we write $\Delta\phi(n) = \Delta\phi_n(n) + \Delta\phi_{n-1}(n)$, where the subscript denotes the repetition block from where the phase errors are generated and the brackets denote the repetition block where the phase errors are evaluated. In particular, for balanced gradient waveforms, the unfinished phase accumulation $\Delta\phi_{n-1}(n-1)$ will compensate in the repetition block n to zero. In other words, $\Delta\phi_{n-1}(n-1) = -\Delta\phi_{n-1}(n)$, where we assume that eddy currents are long enough to induce phase errors in the first block, but short enough to decay within the second block. This compensation of the phase accumulation is related to the linear time-invariant behavior of the gradient system, where bipolar gradient waveforms induce opposing and time-delayed phase errors. Therefore, the total phase error in repetition block n becomes Eq.3.4.

$$\Delta\phi_{tot}(n) = \Delta\phi_n(n) - \Delta\phi_{n-1}(n) \quad (3.4)$$

Here $\Delta\phi_{tot}(n)$ is the total eddy current-induced phase error experienced by the magnetization, which is induced by gradient waveforms from the previous repetition block $\Delta\phi_{n-1}(n)$ and the current repetition block $\Delta\phi_n(n)$. Note that this equation directly relates to the concept of using smooth trajectories, which inherently minimize the change of gradient waveforms from TR-to-TR ($\frac{dB}{dT_R}$). Low $\frac{dB}{dT_R}$ ensures that $\Delta\phi_n(n) - \Delta\phi_{n-1}(n) \approx 0$ and therefore little phase accumulation occurs. Throughout this work we calculate $\Delta\phi_{tot}(n)$ for every repetition block and we incorporate the phase error as additional phase accumulation prior to the next RF pulse.

3.2.3 Prospective GIRF-based RF phase cycling

The signal model in Eq.3.3 assumes that $\Delta\phi(n)$ is spatially uniform and can accurately be predicted based on the $GIRF^0$. These spatially uniform effects can be compensated by adjusting the transmit phase of the sequential RF pulse, i.e. setting $\Theta(n)$ equal to $\Delta\phi(n)$ [124]. This adjustment restores the refocusing mechanism of the bSSFP sequences and therefore prevents the disruption of the steady-state. We refer to this method as prospective RF phase cycling (RF-PC) and the mechanism is illustrated in Figure 3.3. The RF-PC scheme then becomes a function of the gradient waveform and can simply be superimposed on conventional phase cycling schemes. Note that RF-PC is only valid under the instantaneous RF pulse assumption, extension to finite-length RF pulses would require a frequency modulated RF pulse design to accommodate the varying $\Delta\phi(n, t)$ errors during the pulse. However, basic Bloch simulations showed that the instantaneous RF pulse assumption provides satisfying results for short pulses ($< 1ms$), which are generally used in bSSFP acquisitions.

3.3 Methods

Gradient impulse response functions were measured to parameterize the signal model. The signal model was then used to simulate single isochromat steady-state disruptions for varying off-resonance conditions (ΔB_0). These simulations

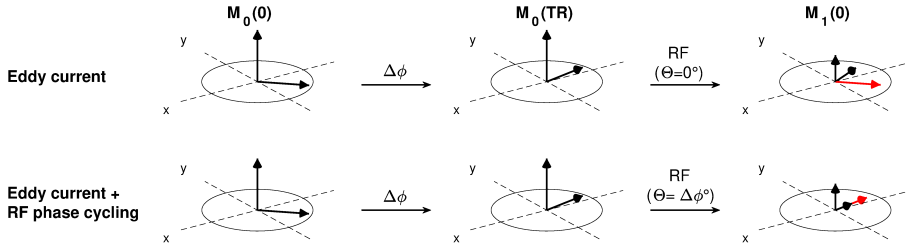


Figure 3.3: Schematic overview of the prospective RF phase cycling (RF-PC) method. **Top row:** Consider the spin ensemble ($M_0(0)$), which experiences ΔB_0 field modulations due to eddy currents. The ΔB_0 induces phase accumulation $\Delta\phi$, which rotates the transverse magnetization 45° along the longitudinal axis (z) ($M_0(TR)$). This rotation is nonzero when the sequential RF pulse is applied, which misaligns the newly excited longitudinal magnetization (red arrow) with the transverse magnetization ($M_1(0)$) (black arrow). This misalignment propagates over multiple repetition blocks and eventually leads to considerable signal disruptions. **Bottom row:** Consider the same spin ensemble with the same eddy current-induced phase accumulation. Now the phase of the RF pulse Θ is modified such that the RF pulse aligns the newly excited longitudinal magnetization with the transverse magnetization, therefore restoring the refocusing mechanism.

provided insight on how to setup the validation experiments. The first validation experiment included phantom acquisitions, where simulated artefact images were compared to measured artefact images. During these experiments linear shim gradients were applied to emphasize the dependence of the steady-state disruption on ΔB_0 . The second validation experiments included brain acquisitions, where prospective RF phase cycling was used to reduce eddy current artefacts.

3.3.1 GIRF measurements

To characterize the gradient system we measured the zeroth and first order field responses on a 1.5T MRI (Ingenia, Philips). Twenty-one triangular gradients with maximum slew rate (180 T/m/s) and varying gradient amplitudes (8.0-22.5 mT/m) were measured using a 15 cm spherical phantom. The zeroth and first order field responses were measured using a variation of the thin slice method [75, 125, 126]. A more detailed description of the measurements are reported in Supporting Information I.

3.3.2 bSSFP signal simulations

To investigate the impact of the eddy current-induced phase errors on the steady-state we computed $\Delta\phi(n)$ for three different spatial encoding schemes: 1) Linear phase encoding (Lin-PE); 2) Random phase encoding (Rnd-PE) and; 3) Golden angle radial (GA-Rad) encoding. Lin-PE was selected because of its widespread usage in clinical protocols and robustness to eddy current effects. Rnd-PE was selected because it resembles the relatively large jumps in k-space that are commonly seen in highly undersampled acquisitions for compressed sensing [66, 127, 128], low-high profile ordering for low latency imaging [129] or k-t sampling patterns [114, 130] for dynamic imaging. GA-Rad was selected to represent non-Cartesian with widespread utility in dynamic imaging [131]. The $\Delta\phi(n)$

depend on the sequence parameters and were based on the acquisitions described in Table-1. The maximum $\Delta\phi(n)$ can be expressed per gradient axes and were $\Delta\phi_x = 6.5^\circ$ for the Cartesian scans and $\Delta\phi_x = -8.8^\circ / \Delta\phi_y = -10.2^\circ$ for the radial scans. These $\Delta\phi(n)$ were included in the Bloch model to simulate a single isochromat's convergence to the steady-state. The isochromat that was simulated had the following properties: $T_1 = 1000$ ms, $T_2 = 80$ ms and $B_1 = 1.0$. Note that the simulations start in the fully relaxed spin state ($M_z = 1$). The simulations were repeated for a range of off-resonances $\Delta B_0 \in [-300\text{Hz}; 300\text{Hz}]$ to create bSSFP signal profiles.

3.3.3 Artefact simulation and experimental validation

To validate the proposed bSSFP signal model we designed two phantom experiments (Cartesian and Radial encoding) that were compared with simulations. In both experiments we acquired artefact-free images using a Lin-PE bSSFP acquisition and we acquired a B_0 -map. These data were acquired with a linear shim gradient (1 mT/m) in one direction to highlight the signal dependence on the ΔB_0 . Both the B_0 -map and the artefact-free image were used with the GIRFs to predict the eddy current-induced image artefacts. The predicted eddy current-induced artefact images were visually compared with measurements with and without RF-PC. All experiments were preceded with 5 seconds of dummy TRs to reduce transient state oscillations and all experiments used a short Gaussian shaped RF pulse with time-bandwidth product = 2.

Random phase encoded 3D Cartesian acquisition 3D k-space data were acquired using a random phase encoded (Rnd-PE) scheme with sequence parameters that facilitate minimal repetition time. Relevant sequence parameters are shown in Table 1. Subsequently the scan was re-acquired with a random paired phase encoded (Rnd-P-PE) scheme, which is known to reduce eddy current-induced image artefacts [115]. The acquisitions were repeated using RF-PC with maximum phase errors of $\Delta\phi_x = -6.5^\circ / \Delta\phi_y = -8.1^\circ$. Note that the phase errors of all the phase encode lines are a linear combination of $\Delta\phi_x$ and $\Delta\phi_y$.

Golden angle 2D Radial acquisition: 2D k-space data were acquired using a golden angle radial (GA-Rad) scheme with sequence parameters that facilitate a minimal repetition time. Relevant sequence parameters are shown in Table 1. Subsequently the scan was re-acquired with a tiny golden angle (tGA-Rad) scheme, which is known to reduce eddy current-induced image artefacts [121]. The acquisitions were repeated using RF-PC with maximum phase errors of $\Delta\phi_x = -8.8^\circ / \Delta\phi_y = -10.2^\circ$. Note that the phase errors corresponding to a specific radial angle is a linear combination of $\Delta\phi_x$ and $\Delta\phi_y$.

3.3.4 *In vivo* experiments:

This study was approved by the local institutional review board. Following written informed consent, two healthy volunteers were scanned. Three-dimensional random encoded Cartesian and 2D golden angle radial scans were acquired in the brain with and without RF-PC. Sequence parameters were equivalent to the

phantom experiments (Table 1), besides the linear shim that was disabled. Scans were acquired with volume shimming and B_0 -maps were acquired to emphasize the dependency of the eddy current artefacts on B_0 . Images were reconstructed on the scanner and visually compared.

3.4 Results

3.4.1 GIRF measurements

The measured GIRFs are shown in Figure 3.4. The spectral resolution for the measurements was 33 Hz. The $GIRF^0$ show distinct profiles for the three different axes. The $GIRF_{X,Y}^0$ show larger magnitudes than the $GIRF_Z^0$ around the low frequency range, which corresponds to larger eddy current-induced ΔB_0 errors. The $GIRF^0$ show distinct peaks around 1780 Hz and 6800 Hz, which could be related to mechanical oscillation frequencies [76]. Note that the SNR of the measurements was too low for adequate response determination outside the 10 kHz range. The $GIRF^1$ show similar behavior for all three axes and have close to zero gradient delay around the low frequencies. The SNR of these measurements was sufficient up to the 20 kHz range.

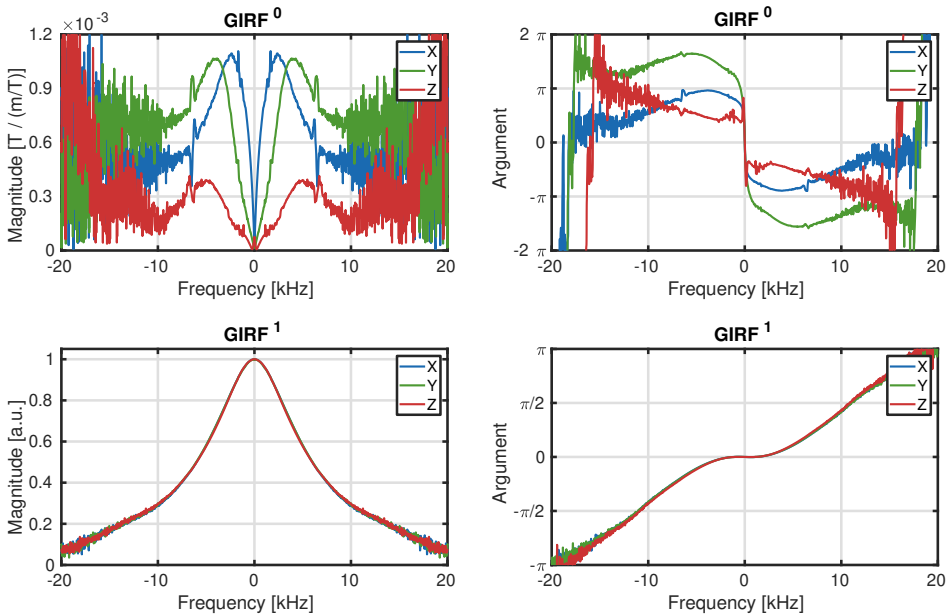


Figure 3.4: Gradient impulse response functions (GIRF): Top row shows $GIRF^0$ with the magnitude on the left and the complex argument on the right. The bottom row shows $GIRF^1$ with magnitude on the left and the complex argument on the right.

3.4.2 bSSFP signal simulations

The impact of the eddy currents corresponding to the three spatial encoding schemes are shown in Figure 3.5. The first ≈ 100 readouts show oscillations due

to the normal transient behavior of the magnetization. The Lin-PE Cartesian acquisition showed minor differences from the nominal (default) signal evolution across the entire off-resonance range. However, the Rnd-PE Cartesian acquisition showed strong deviations across the entire off-resonance range. Note that these deviations are erratic and highly coupled to the "randomness" of the encoding pattern. The bSSFP signal profile shows only small deviations in the average signal in time, but shows large standard deviations. The GA-Rad scheme shows minor magnitude deviations for the on-resonant case, but shows very large deviations slightly off-resonance. The bSSFP signal profile shows an additional pair of banding artefacts that are not seen with the other encoding schemes. The position of the bands depend on both the repetition time and the angular increment of the radial acquisition.

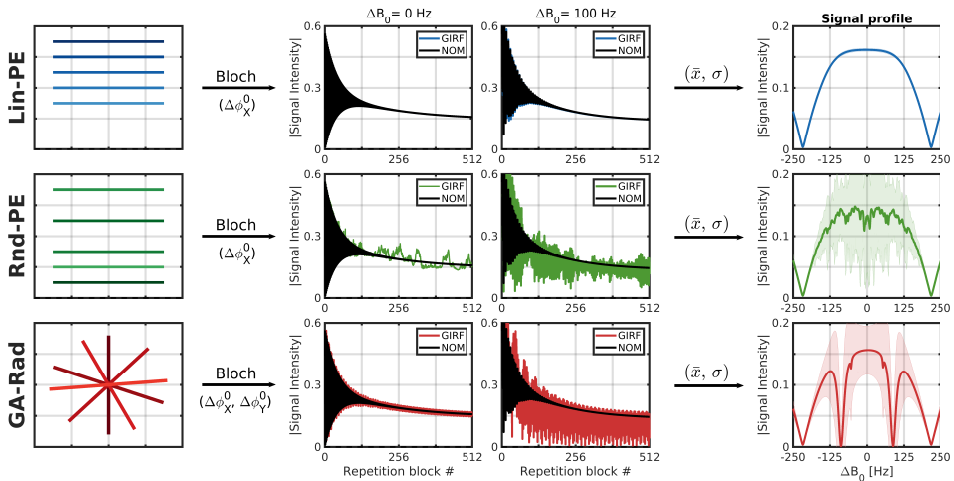


Figure 3.5: BSSFP Bloch simulations in combination with the gradient impulse response functions (GIRF) for three different acquisitions: Top row: Linear phase encoded (Lin-PE) Cartesian acquisition induces smoothly varying phase errors $\Delta\phi_0^x = 6.5^\circ$, which do not disrupt the steady-state across the entire off-resonance range. **Middle row:** Random phase encoded (Rnd-PE) Cartesian acquisition induces erratic phase errors ($\Delta\phi_0^x = 6.5^\circ$), which considerably disrupt the steady-state across the entire off-resonance range. **Bottom row:** Golden angle encoded radial (GA-Rad) acquisition induces sinusoidal varying phase error ($\Delta\phi_0^x = -8.8^\circ$ and $\Delta\phi_0^y = -10.2^\circ$), which disrupt the steady-state across the entire off-resonance range. At specific off-resonance frequencies additional zero signal bands occur. Note that the signal profiles represent the magnitude of the mean and the standard deviation of the complex signal intensities over the last 200 repetition blocks in time. NOM = nominal (without eddy current). GIRF is with eddy current.

3.4.3 Artefact simulation and experimental validation

Random (paired) phase encoded 3D Cartesian acquisitions: The eddy current-induced image artefacts induced by the random phase encoded sampling patterns are shown in Figure 3.6. The simulated Rnd-PE image closely resembles the measured artefact image. Both the images show a hypo-intense streak in the center and show large intensity fluctuations from top to bottom. The Rnd-paired-PE measured image shows reduced intensity fluctuations compared to the Rnd-

PE. The reduction is also reflected in the simulated image, which is similar to the measured image in magnitude of the intensity fluctuations. RF-PC considerably reduced these artefacts for the Rnd-PE as well as Rnd-paired-PE acquisitions. Note that both images have small residual artefacts left compared to the artefact free image, where the Rnd-paired-PE showed the smallest residual artefacts.

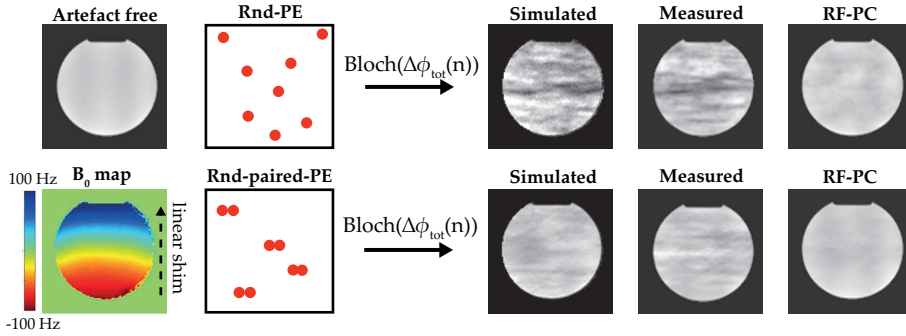


Figure 3.6: Random (paired) phase encoded 3D Cartesian acquisitions - artefact simulation and experimental validation: First column shows the measured artefact-free image and the measured B_0 map. Second column illustrates the 3D Cartesian sampling patterns. Top row of the remaining columns shows the random phase encoded (Rnd-PE) acquisition and the bottom row shows the random paired phase encoded (Rnd-paired-PE) acquisition. Third column shows the simulated artefact images that were based on the artefact-free image, B_0 map and the proposed bSSFP signal model. Fourth column shows the measured artefact image. Fifth column shows the measured RF phase cycled images.

(Tiny) golden angle 2D radial acquisitions: The eddy current-induced image artefacts due to the golden angle radial sampling are shown in Figure 3.7. The simulated GA-Rad artefact image closely resembles the measured artefact image. Both the images show hypointense and hyperintense lines at the same locations. Note that these lines exactly coincide with the shape of the B_0 -map and with the locations of the additional bands in the bSSFP signal profile shown in Figure 3.5. The RF-PC acquisitions considerably reduced the artefacts, but small residual artefacts remain compared to the artefact free image. The simulated tGA-Rad artefact image and the measured artefact image are almost identical, both show no visual artefacts. The RF-PC acquisition does not introduce additional artefacts and maintains the image quality.

3.4.4 In vivo experiments - Brain imaging

Random phase encoded 3D Cartesian acquisitions: Three-dimensional brain scans were acquired in a healthy volunteer that include a B_0 -map, Lin-PE, Rnd-PE with/without RF-PC and Rnd-P-PE with/without RF-PC (Figure 3.8). The B_0 -map shows that large field inhomogeneity that is typically seen around the tissue/air interfaces. The Rnd-PE acquisition shows large image artefacts that completely obscure the image structures in the brain. Repeating the acquisition with RF-PC considerably reduces these artefacts. Note that small residual artefacts are still visible. The Rnd-P-PE acquisition shows less image artefacts than

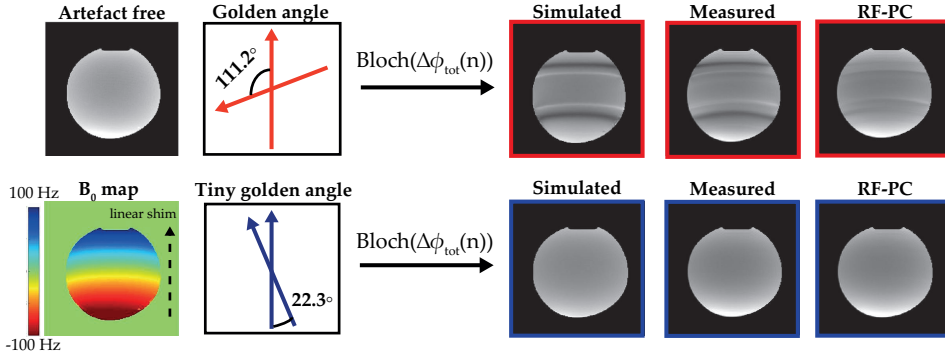


Figure 3.7: (Tiny) golden angle 2D radial acquisitions - artefact simulation and experimental validation: First column shows the measured artefact-free image and the measured B_0 map. Top row of the remaining columns shows the golden angle radial (GA-Rad) acquisition and the bottom row shows the tiny golden angle (tGA-Rad) acquisition. Third column shows the simulated artefact images that were based on the artefact-free image, B_0 map and the proposed GIRF-based bSSFP signal model. Fourth column shows the measured artefact image. Fifth column shows the measured RF phase cycled images.

the Rnd-PE acquisition. Repeating the acquisition with RF-PC further reduces the image artefacts and the image appears similar to the Lin-PE acquisition.

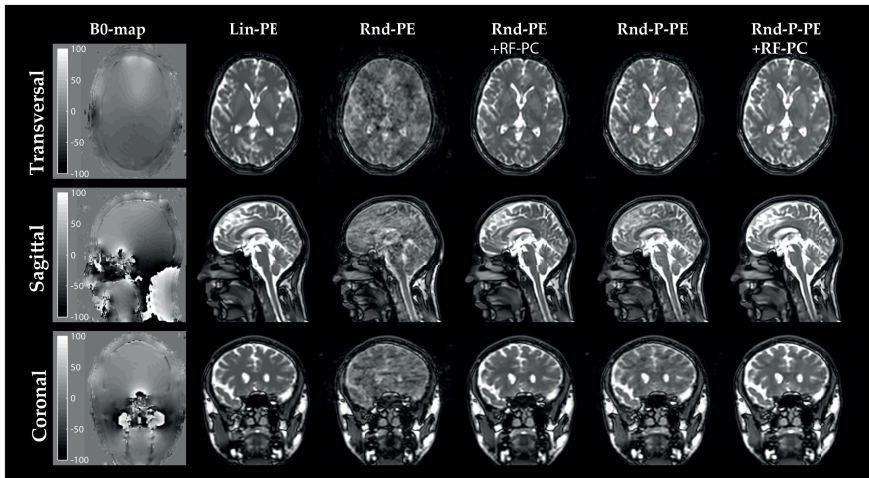


Figure 3.8: *In vivo* random phase encoded 3D Cartesian acquisitions. First column shows the B_0 -map. Second column shows the Cartesian acquisition with linear profile ordering (Lin-PE). Third column shows the Cartesian acquisition with random phase encode ordering (Rnd-PE). Fourth column shows Rnd-PE with RF phase cycling (RF-PC). Fifth column shows the Cartesian acquisition with random paired phase encode ordering (Rnd-P-PE). Last column shows Rnd-P-PE with RF-PC. Sequence parameters are shown in Table.1.

Golden angle 2D radial acquisitions: Two slices were examined using six acquisitions that include a B_0 -map, Lin-PE, GA-RAD, GA-RAD-RFPC, tGA-RAD and tGA-RAD-RFPC (Figure 3.9). The first slice shows large field inhomogeneity around the auditory canals, which leads to eddy current-induced image artefacts

around these areas in the GA-RAD image. These artefacts include hypo-and-hyper-intense regions, which are clearly visible in the zoom image. These artefacts are not present in the tGA and Lin-PE images and are considerably reduced in the GA-RAD-RFPC image. The second slice shows large field in-homogeneity's around the frontal lobe, which leads to eddy current-induced image artefacts in the GA-RAD image. These artefacts include dark and bright tight bands with curvature similar to the B_0 -map. These artefacts are not present in the tGA and Lin-PE images and are considerably reduced in the GA-RAD-RFPC image, but residual artefacts remain. Note that there are subtle differences in image contrast between lin-PE and the GA-Rad/tGA-Rad acquisitions. These differences are presumably related to off-resonance effects or small k-space trajectory errors in the reconstruction.

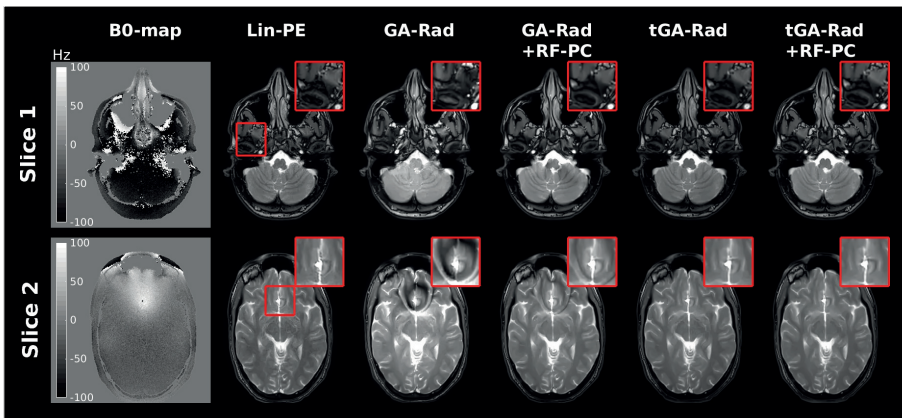


Figure 3.9: *In vivo* 2D golden angle radial acquisitions. Two slices were acquired with a B_0 -map, artefact-free reference (Lin-PE), golden angle radial (GA-RAD), golden angle radial with RF phase cycling (GA-RAD-RFPC), tiny golden angle radial (tGA-RAD) and tiny golden angle radial with RF phase cycling (tGA-RAD-RFPC). In both slices the GA-RAD shows eddy current-induced image artefacts that are considerably reduced after RF phase cycling. Tiny golden angle images show no deviations from the reference image and adding RF phase cycling does not introduce new artefacts.

3.5 Discussion

In this study we used the gradient impulse response function to formulate an explicit bSSFP signal model that predicts the impact of eddy currents on the steady-state. In particular, we showed that the zeroth order impulse response function is the primary factor to describe the impact of eddy currents on the steady-state, while the first order impulse response functions play only a minor role. The proposed signal model was validated using computer simulations and experimental imaging which showed good correspondence. Secondly, we revisited a prospective eddy current compensation method that uses RF phase cycling (RF-PC) schemes to reduce the steady-state disruptions. We showed that RF-PC is viable without additional field monitoring hardware by using the gradient impulse response function. The gradient impulse response functions were used in

combination with the spatial encoding gradients to prescribe RF phase cycling schemes that can easily be computed on-the-fly. The proposed RF-PC method does not require any pre-scans or significant sequence modifications and is in principle applicable to any MRI examination.

The proposed bSSFP signal model provides insight into the effectiveness of several pre-existing methods to mitigate eddy currents effects. First, we consider the phase encode pairing method proposed by Bieri et al., in which the method mitigated eddy currents artefacts in a wide off-resonance range for relatively small phase errors ($\Delta\phi$) [115]. In this work we verified their findings that phase encode pairing reduces the eddy current effects, however for larger phase errors considerable residual artefacts remain (Figure 3.6) [124]. In [115] an explanation was given for the effectiveness of the pairing method, which was that the default $[0 \ 180^\circ]$ bSSFP phase cycling scheme cancels out two sequential near identical phase errors. Our proposed signal model provides an alternative explanation for the effectiveness of the phase encode pairing, which is related to the approximation of the eddy current behavior as a linear time invariant system. The approximation implies that the total phase error in repetition block n is the contribution of the current repetition block (n) minus the contribution of the previous repetition block ($n-1$), i.e. $(\Delta\phi(n) = \Delta\phi_n(n) - \Delta\phi_{n-1}(n))$. From this observation it is apparent that phase encode pairing would make the total phase error zero every other repetition block, therefore considerably reducing the steady-state disruption. The second pre-existing method we consider is the use of tiny golden angles in radial sampling. The effectiveness of the tiny golden angles can be explained using the same observation as for the paired phase encoding. The tiny golden angles induce smoother changes in $\Delta\phi(n)$ than the golden angle and therefore induce a smaller $\Delta\phi_{tot}(n+1)$. The overall underlying observation is that eddy current-induced steady-state disruption are minimized if the phase error varies smoothly between sequential repetition blocks. This view of looking at eddy currents has some consequences for the design of sampling patterns in bSSFP. The primary consequence is that smoothness of the sampling patterns should be prioritized over phase encode pairing, because it minimizes $\Delta\phi_{tot}$ instead of nulling it every other repetition block. Alternatively, sampling patterns could be designed such that these minimize $d\Delta\phi_{tot}/dn$ instead of $\Delta\phi_{tot}$. These sequences would yield large, but constant, phase errors which do not disrupt the steady-state and offer more flexibility in pattern design.

The RF-PC method provides a general prospective compensation strategy to reduce eddy current-induced steady-state disruptions in bSSFP imaging. The compensation method is based on the observation that zeroth order eddy currents (global) effects were the dominant contributor to the steady-state disruption. However, this observation is only valid for the MR systems that were investigated in this study. Other systems could, for example, exhibit stronger mechanical resonances that could enhance the phase errors of the first order eddy currents for specific frequencies. These strong resonances were not observed on our systems and therefore the eddy current effects were considered global. As a consequence of these effects being global, the compensation method only requires minor sequence modification (RF phase adjustments) that does not deteriorate the performance

(e.g. smooth encoding schemes). RF-PC can therefore be used in conjunction with other methods, enabling more robust artefact suppression. The second advantage of our method is that the specific RF phase cycling schemes can be computed on the fly and is easy to generalize for any MRI acquisition.

The proposed bSSFP signal model and RF-PC method have several limitations that require discussion. The primary uncertainty in the signal model is coupled to the assumption that gradient system was modeled as a linear time-invariant system. Previous work showed that the assumption is valid to a certain extent, but may be violated due to for example gradient heating [132, 133]. The second limitation is that we did not perform higher order gradient impulse response measurements, which may induce additional phase errors that we did not account for. However, including the higher order phase errors in the RF-PC compensation strategy is not straightforward because these errors have heterogeneous spatial distributions. The third limitation is that the RF-PC method operates under the instantaneous RF pulse assumption, which approximates the real system only for very short RF pulses. In reality, we have a time-varying phase error $\Delta\phi(t)$ during the RF pulse that requires frequency modulated RF pulses for exact compensation. All these limitations contributed to the small residual artefacts observable in the RF-PC images. In the future, we envision that the second and third limitation could be jointly tackled by designing dedicated frequency modulated RF pulses, supplemented by small correction gradients [124], that generate the exact spatio-temporal transmit distribution to compensate higher order phase errors. However, implementation of such complex pulse sequences requires dedicated multi-transmit hardware and is out of scope for this study.

Overall, we believe this work contributes to the general understanding of the impact that eddy currents can play in bSSFP sequences. The proposed RF-PC method could improve the robustness of bSSFP sequences for clinical usage. In particular, the implementation of non-Cartesian sequences could benefit greatly from this method, since they in general exhibit less smooth encoding schemes. In addition, the proposed GIRF-based signal model can be used for numerical sequence optimization or to predict the impact of eddy currents on other sequences such as spoiled SSFP sequences or spin-echo sequences. In addition, we believe that a rigorous understanding of the impact of eddy current on the signal evolution is crucial for quantitative imaging applications that require precise modeling of the physical MR acquisition [112, 134].

3.6 Conclusion

To conclude, the zeroth order gradient impulse response function is the primary factor to predict eddy current-induced steady-state disruption in bSSFP imaging and the severity of this disruption strongly depends on the local off-resonance frequency. The eddy current-induced steady-state fluctuations can be considerably reduced by prospectively adapting the RF phase cycling based on the gradient impulse response function. We demonstrated a straightforward implementation of the prospective RF phase cycling method, which we believe could improve the

robustness of bSSFP imaging for clinical usage and may have considerable impact on bSSFP based quantitative MRI.

Acknowledgments

This work is part of the research program HTSM with project number 15354, which is (partly) financed by the Netherlands Organization for Scientific Research (NWO) and Philips healthcare.

If I have seen further it is by standing on the shoulders of Giants.

- Isaac Newton

Multiresolution radial MRI in pre-beam imaging (MR-RIDDLE)

Bruijnen, Tom
Stemkens, Bjorn
Legendijk, Jan J.W.
van den Berg, Cornelis A.T.
Tijssen, Rob H.N.

The following chapter is based on:
Multiresolution radial MRI to Reduce IDLE time in pre-beam imaging on an
MR-Linac (MR-RIDDLE), 2019, *Physics in Medicine and Biology*;
27;64(5):055011

Abstract

Online adaptive MR-guided radiation therapy improves treatment quality at the expense of considerable longer treatment time. The treatment lengthening partially originates from the preparatory (pre-beam) MR imaging required to encode all the information needed for contour propagation, contour adaptation and replanning. MRI requires several minutes of scan time before the encoded information is converted to usable images, which results in long idle times before the first clinical tasks are performed. In this study we propose a novel imaging sequence, called MR-RIDDLE, that reduces the idle time and therefore speeds-up the workflow in online MR-guided radiation therapy. MR-RIDDLE enables multiresolution image reconstruction to commence during data acquisition where low resolution images are available within one minute, after which the data collection continuous for subsequent high-resolution image updates. We demonstrate that the low resolution images can be used to accurately propagate contours from the pre-treatment scan. For abdominothoracic tumours MR-RIDDLE inherently captures a motion-blurred representation of the mid-position, which we were able to deblur using a combination of an internal motion surrogate and auto-adaptive soft-gating filters. Our results demonstrate that MR-RIDDLE provides a robust, flexible and time-efficient strategy for pre-beam imaging, even for cases with large respiratory movements or baseline shifts within the acquisition. We anticipate that this novel concept of parallelising the MR imaging and the clinical tasks has the potential to considerably speed-up and streamline the online MR-guided radiation therapy workflow.

Keywords: radiotherapy, MR-guided radiation therapy, MRI guidance, multiresolution, golden angle radial, pre-beam imaging, MR-linac, radiotherapy workflow

4.1 Introduction

Hybrid MRI-radiotherapy systems have emerged as powerful platforms to simultaneously visualize and treat patients with cancer [38, 40, 42, 135, 136]. Online adaptive MR-guided radiation therapy improves treatment quality at the expense of considerable longer treatment time. Long treatment times reduce patient comfort, reduce the effectiveness of the therapy, and decrease total patient treatment capacity per MR system. The treatment lengthening partially originates from the preparatory (pre-beam) MR imaging required to encode all the information needed for online treatment planning. The current online workflow of the Elekta Unity 1.5T MR-Linac (Elekta AB, Stockholm, Sweden) is illustrated in Fig 4.1 [43]. The design of dedicated online MR scans (pre-beam scans) that speed-up and support this clinical workflow is a completely unexplored line of research.

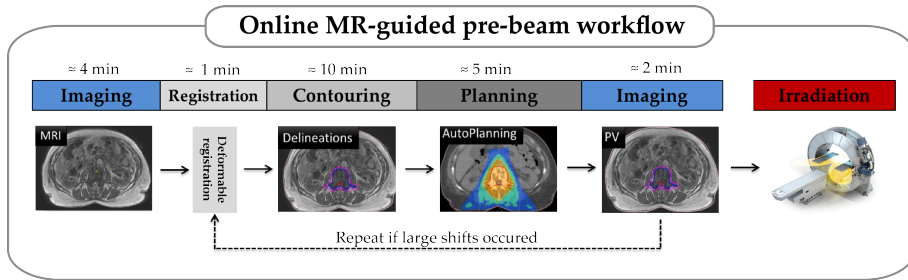


Figure 4.1: Overview of the online MR-guided workflow for a patient with a spine tumor. First the daily MR scan is required ($\approx 4min$). The MR scan is registered to the pre-treatment CT or MR scan ($\approx 1min$). The obtained deformation is used to propagate the contours to the daily MR. The contours are manually adapted to the current anatomy ($\approx 10min$, dependent on anatomy). The updated contours are used to generate a new treatment plan ($\approx 5min$). When the treatment plan is almost finished a second MR scan is acquired for position verification ($\approx 2min$). If no large shifts occurred between the first and the second MR scan the treatment can commence.

Pre-beam imaging in online MR-guided radiation therapy has vastly different design considerations than in the offline setting of diagnostic imaging in radiology. The online workflow strongly relates to that of an interventional setting where the first images have to be available with minimal idle time to initialize the replanning. Furthermore, subsequent images should be available on demand to check the validity of the anatomical state before starting radiation therapy. Further, for abdominothoracic tumors the anatomy needs to be captured in a representative motion state (e.g. mid-position) [59, 60]. Typical (diagnostic) sequences are unable to meet these requirements simultaneously. The ability to encode all the required information in a single MR scan that is also able to reconstruct the desired information at the correct moment in time would be invaluable for MR-guided radiation therapy.

In this work we describe the design and implementation of such a single MR scan that is optimised in conjunction with the clinical workflow to facilitate fast online treatment planning. We named the combination of the MR scan and the corre-

sponding processing MR-RIDDLE: Multiresolution Radial MRI to Reduce IDLE time in pre-beam imaging on an MR-Linac. The scan is based on a continuous 3D gradient echo golden angle stack-of-stars trajectory that enables reconstruction with flexible spatial and temporal resolution [33, 131]. The golden angle stack-of-stars trajectory enables image reconstruction to commence during data acquisition, where the reconstruction resolution is flexible and optimised with respect to the amount of data acquired at each instance in time. As a consequence, low resolution images are available after just a few seconds of scanning, which we hypothesize can be used to propagate the pre-treatment contours and therefore accelerate the clinical workflow [61, 137].

The proposed method extends to anatomies affected by respiratory motion by combining a free-breathing acquisition with a motion-weighted image reconstruction. The stack-of-stars trajectory inherently portrays the time-averaged (blurred) position (mid-position) [138], while simultaneously providing a self-navigated motion surrogate [139]. The combination of these two enables a motion-weighted image reconstruction that is able to reconstruct a deblurred mid-position volume with minimal processing time [140, 141]. The method will be especially attractive for patients that are unable to suspend respiration for a sufficient amount of time. We envision that our proposed method will provide a robust and relatively simple approach for online mid-position-based MR-guided radiation therapy treatment planning.

4.2 Methods

4.2.1 Conceptual overview

Figure 4.2 provides an overview of the MR-RIDDLE pre-beam imaging method, which consist of radial k-space data acquisition, multiresolution image reconstruction and motion-weighted image reconstruction. K-space data are continuously acquired during free-breathing using a golden angle stack-of-stars trajectory. The image reconstruction commences at multiple time-points during the data acquisition and aliasing-free images are obtained by optimizing the reconstruction resolution with respect to the amount of acquired k-space data. Upon reaching the maximum spatial resolution, respiratory motion surrogates are estimated directly from the k-space data to perform motion-weighted image reconstructions that reduce motion-induced blurring. Note that the proposed method is a form of an expanding window image reconstruction and not a (conventional) sliding window reconstruction.

4.2.2 MRI data acquisition

MRI data were acquired using a golden angle stack-of-stars trajectory where all phase encodes along k_z were scanned sequentially. The trajectory has four major advantages for the radiation therapy workflow. First, the radial trajectory repeatedly samples the k-space centre and therefore is inherently robust against motion-induced artefacts [33, 142]. Second, each readout contributes equivalently

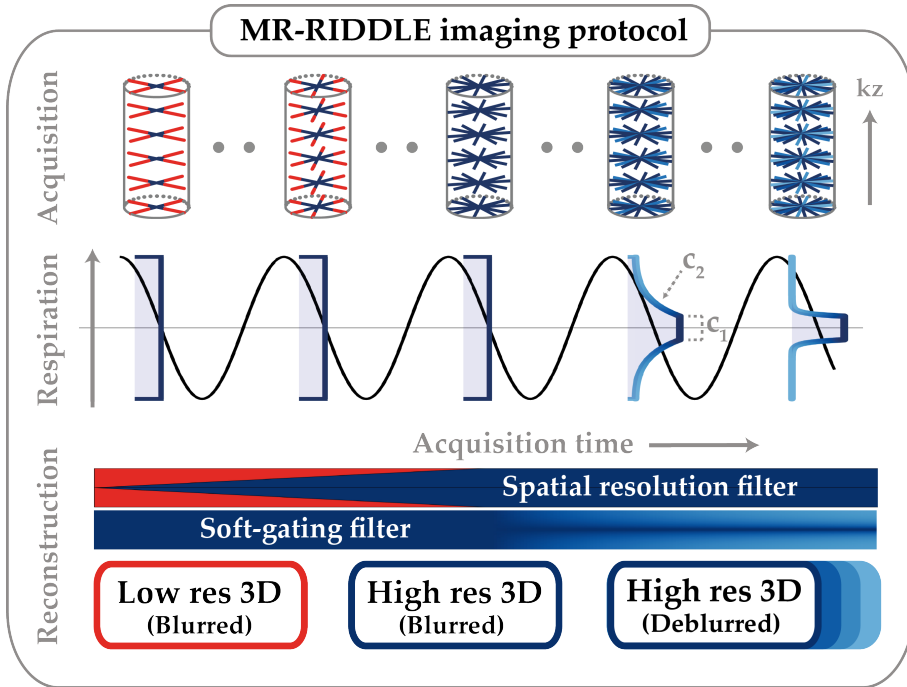


Figure 4.2: Overview of the MR-RIDDLE protocol: K-space data are acquired during free breathing using a golden angle stack-of-stars trajectory. Top row: The acquired k-space data is block-filtered (red) such that the residual k-space (blue) complies with the Nyquist criterion and aliasing-free (multiresolution) images can be reconstructed at any moment in time. Upon reaching the acquisition spatial resolution, the k-space data is motion-weighted using a soft-gating filter to reduce motion-induced blurring (middle row). The soft-gating filter is parametrised with the coefficients c_1 and c_2 . The light-blue in the soft-gating filters indicates the downweighting of the data, which is also shown in the middle row.

in k-space content to the complete image and therefore inherently portrays the time-averaged (blurred) position of the anatomy [138]. Third, the repeated sampling of the k-space centre enables extraction of a motion-state surrogate signal that allows a motion-weighted image reconstruction to effectively deblur the motion-blurred anatomy [140]. Fourth, the golden angular increment ensures near uniform k-space filling at any instance in time, which enables image reconstruction from arbitrary imaging windows [131].

4.2.3 MRI data processing

Radially acquired MR data are prone to geometrical distortions and image artefacts due to gradient systems imperfections [69, 143, 144]. To mitigate the artefacts, the zeroth and first spatial order gradient impulse response functions of the gradient system were characterised and used for k-space trajectory correction and phase corrected image reconstructions [53, 76].

The centre k-space sample along the partition direction (kz) was used as a surro-

gate for the global motion [139]. The surrogate was calculated by concatenating the projections for all the receivers coils into one 2D matrix and applying principal component analysis to detect the main variation in the frequency range (0.0-0.5 Hz) [145]. The motion surrogate was determined for each radial angle in the partition and thus the temporal resolution of the surrogate depends on the number of partitions (kz) times the repetition time.

4.2.4 MR-RIDDLE reconstruction for non-moving organs

The proposed method reconstructs aliasing-free images at multiple time-points during the acquisition by optimizing the reconstruction resolution with respect to the amount of acquired data. The reconstruction resolution is controlled by filtering the in-plane k-space with a block filter with isotropic width (W) that corresponds to reconstruction resolution (N). The relationship between the width of the block filter and the number of acquired projections (N_{proj}) for golden angle radial stack-of-stars is defined by Equation 4.1, assuming no undersampling in the partition direction and isotropic in-plane image size. The final image resolution will equal the acquisition resolution (N_{acq}).

$$W(t) \propto N(t) = \begin{cases} \frac{2N_{proj}(t)}{\pi N_{acq}} & \text{if } \frac{2N_{proj}(t)}{\pi} < N_{acq} \\ \text{otherwise} & \end{cases} \quad (4.1)$$

After in-plane resolution filtering, the k-space data of the individual coils were multiplied by a fixed Ram-Lak filter for density compensation followed by the non-uniform fast Fourier transform (NUFFT) [146]. The coil images were combined using a Roemer coil combination [147] where the coil sensitivity maps were estimated from the low resolution images using ESPIRiT [148].

4.2.5 MR-RIDDLE reconstruction for moving organs

For abdominothoracic anatomies the multiresolution approach extends to the motion dimension in the form of a motion-weighted image reconstruction (soft-gating) [140]. Imaging data that are acquired far away from the target motion position are downweighted in the reconstruction using soft-weights. These soft-weights (sw) are optimised with respect to the acquired k-space data (\mathbf{y}) for a certain set of parameters ($\mathbf{c} = [c_1, c_2, c_3]$) for the exponential weighting function shown in Equation 4.2 [141, 149].

$$sw(\mathbf{y}, \mathbf{c}) = \begin{cases} -c_2(|d(\mathbf{y})| - c_1 - c_3 k_r^2(\mathbf{y})) & \text{if } |d(\mathbf{y})| > c_1 \\ 1 & \text{otherwise} \end{cases} \quad (4.2)$$

$$c_2 = \min_{c_2} \left\| \frac{\pi}{2} N_{acq} - \frac{1}{N_{samp}} \sum sw(\mathbf{y}, \mathbf{c}) \right\|^2 \quad (4.3)$$

The soft-weights are derived from both the set of parameters \mathbf{c} and the normalized distance $d(\mathbf{y})$ between the current motion state and the target motion state. Here $d(\mathbf{y})$ is defined as a normalized proxy ($d(\mathbf{y}) \in [0, 1]$) for the physical distance to the target motion state. The threshold c_1 defines the region that is considered motion-free and parameter c_2 controls the downweighting in the regions where $|d(\mathbf{y})| > c_1$. In addition, the penalty term $c_3 k_r (k_r^2 = k_x^2 + k_y^2)$ differentiates between low and high frequencies within a readout to equalise their contribution to the total artefact power [150]. The parameters c_1 and c_3 were fixed to $c_1 = 0.5$ and $c_3 = 0.1$ based on empirical observations, while c_2 was adapted dynamically over the acquisition. Soft-gating is in essence a sub-sampling operator and therefore c_2 can be optimised to fulfil the Nyquist theorem at any point in time, which for the stack-of-stars case can be defined as in Equation (4.3). Here, N_{samp} is defined as the number of samples acquired per k-space readout. The optimization effectively imposes the maximum amount of soft-gating without sub-Nyquist sampling. The search for the optimal c_2 can be approximately solved very fast using a brute-force search in the parameter space $\in [0 : 0.01 : 20]$. The k-space data were then multiplied with the soft-weights followed by the image reconstruction as explained in the previous paragraph.

4.3 Experiments

4.3.1 Digital phantom (XCAT) simulations on non-moving organs: proof of concept

To establish whether MR-RIDDLE reconstructs aliasing-free images from arbitrary imaging windows, we performed *in-silico* experiments using the 4D extended cardiac-torso (XCAT) digital phantom [151]. In short, the simulations were single receive channel acquisitions on discrete temporal volumetric XCAT data and did not include a magnetization model. The k-space data were obtained by applying the adjoint NUFFT and adding complex Gaussian noise $\aleph(0, 0.5\% |k(0, 0, 0)|)$. A detailed description of the simulation setup can be found in Supplementary information I.

Multiresolution images were reconstructed at 10s intervals, using all the available data, and were qualitatively analysed for residual aliasing artefacts. The multiresolution images were effectively reconstructed with a different aperture and therefore show different point-spread functions.

4.3.2 Digital phantom (XCAT) simulations on moving anatomy: mid-position validation

To assess the capability of MR-RIDDLE to cope with respiratory motion and tumour drift in the thorax, we performed *in silico* experiments similar to the non-moving experiment. The XCAT phantom was parametrised such that the maximum respiratory amplitude of the diaphragm in the feet-head direction was at the higher end of physiological reported motion (± 3 cm) [152, 153]. In addition, we superimposed a gradual baseline shift of up to 2 cm. We inserted a

spherical tumour (1 cm diameter) in the left lung that moved along with the prescribed motion. A detailed description of the simulation setup can be found in supplementary information I.

Images were reconstructed every 10 seconds using all the available imaging data, where the spatial resolution and extent of soft-gating increased in time. These reconstructions were used to assess the ability of MR-RIDDLE to effectively deblur the motion-induced image artefacts while portraying the tumour mid-position. The mid-position was defined as the average position over the whole examined period. The mid-position of the tumour was estimated by registering the reconstructed volumes to the XCAT exhale volume. The registration was done using a masked, cross-correlation, based rigid registration method [154] and the tumour position in feet-head was extracted. The measured tumour position from the reconstructed (multiresolution) volumes was then compared against the analytical tumour positions provided by XCAT (Supplementary information II). Note that the proposed method is a form of an expanding window image reconstruction and not a (conventional) sliding window reconstruction.

4.3.3 MRL imaging: contour propagation to low resolution images

To demonstrate one example of the potential workflow gain of MR-RIDDLE we implemented the sequence on an Elekta Unity 1.5T MR-Linac (Elekta AB, Stockholm, Sweden). The key idea is that a low resolution image already suffices to accurately propagate the organ contours from the pre-treatment scan and therefore speed-up the clinical workflow. We acquired multiple MR-RIDDLE scans in six volunteers in the upper abdomen with different contrasts. The sequence parameters for the scans are specified in supplementary information I. MR-RIDDLE images were reconstructed at 10s intervals, using all the available data, without any image acceleration such as parallel imaging. The final reconstructed image was then selected as the reference and used to delineate the liver, the right kidney and the aorta. Note that the reference is from the same acquisition, i.e. not from a separate scan. All the reconstructed images were then deformable registered to the reference image using an in-house validated optical flow algorithm ($\alpha = 0.3$) [99, 100]. The resulting deformation vector fields were used to propagate the contours to the MR-RIDDLE images. The propagated contours were quantitatively compared on each time-point versus the reference using the Dice coefficient and the mean deformation vector ($|DVF_{xyz}|$) (Equation 4.4). Note that in the case that no significant drift occurred within the 180s scanning the Dice should be close to 1 and the $|DVF_{xyz}|$ close to 0 for all time-points.

$$|DVF_{xyz}| = \frac{1}{N^2} \sqrt{\sum_{n=1}^N DVF_x^2 + DVF_y^2 + DVF_z^2} \quad (4.4)$$

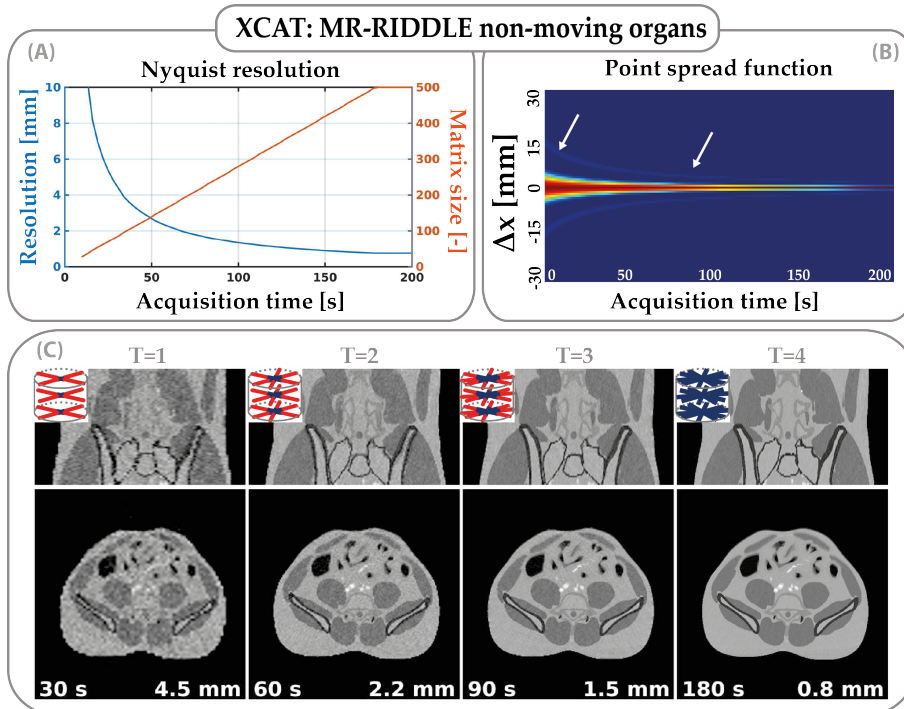


Figure 4.3: MR-RIDDLE simulations on non-moving organs: **A)** Spatial resolution and reconstruction matrix size (reciprocal to spatial resolution) as a function of the acquisition time. **B)** In-plane (kx,ky) point-spread-function as a function of the acquisition time. **C)** Multiresolution images reconstructed at four time-points for the sagittal and transverse planes. The inserts in the top left indicate the width of the block filter to adjust the spatial resolution. Red samples are discarded while the blue samples are accepted.

4.4 Results

4.4.1 Digital phantom (XCAT) simulations on non-moving anatomy: proof of concept

The relationship between the acquisition time and the in-plane (kx,ky) spatial resolution of the reconstructed images is shown in Fig.4.3A. Images with 5 mm resolution were reconstructed within 25 s of scanning time, while 180 s were required to achieve acquisition resolution (0.8 mm). The effect of the multiresolution filter (i.e. block filter width) is shown in Fig.4.3B, which shows reduced Gibbs ringing and a narrower point spread function with increasing scan time. The multiresolution images showed no residual aliasing artefacts at any reconstructed time-points (Fig.4.3C). The signal-to-noise (SNR) increased with acquisition time linearly until reaching the acquisition resolution. The SNR increases linearly because both, the widening of the block filter and the prolonged scanning, include more samples for image reconstruction.

4.4.2 Digital phantom (XCAT) simulations on moving organs: mid-position validation

Multiresolution images were reconstructed and showed no aliasing artefacts (Fig4.4.A). From left to right the spatial resolution increases and the motion-induced blurring reduces by gradually increasing the soft-gating. The reconstructions at time-points < 10 s showed differences in tumour position of more than 5 mm compared to the true mid-position in the feet-head direction (Fig4.4.B). This difference in tumour position is presumably caused by the inability of the reconstruction and registration algorithms to function at very coarse image resolution (12 mm). Note that the proposed method was able to follow the systematic tumour drift inferred by the motion waveform shown in the top of Figure 4.4B. The tumour position was within 1 mm of the true mid-position after 20 s of acquisition time with mean difference of $0.6 \pm 0.3mm$ in the feet-head direction.

4.4.3 MRL imaging: contour propagation to low resolution images

Multiresolution images were reconstructed on a five second interval and typical image quality for spoiled gradient echo and balanced gradient echo are shown in Figure 4.5. The final reconstruction was used to delineate the liver, the right kidney and the aorta. The reconstructions on different time-points show the same improvements in image quality as observed in the simulations. The image acquisition time is shown in the left bottom corner of the axial slices while the additional reconstructions times were approximately 10 seconds for the first volume and 20 seconds for 3 minutes of acquisition.

The multiresolution images were deformable registered to the final reconstructed image using optical flow and the obtained DVFs were used to analyse the propagated contours for the aorta, kidney and the liver. The mean $|DVF_{xyz}|$ were around 0.5 mm after 30 seconds of scanning time and gradually approached zero over all six volunteers. Note that the mean $|DVF_{xyz}|$ should converge to zero, because the final image is the reference. The DVFs were used to warp to propagate the contours and the corresponding Dice coefficients were larger than 0.97 after 30 seconds of scanning and were approximately 1 after 150 seconds.

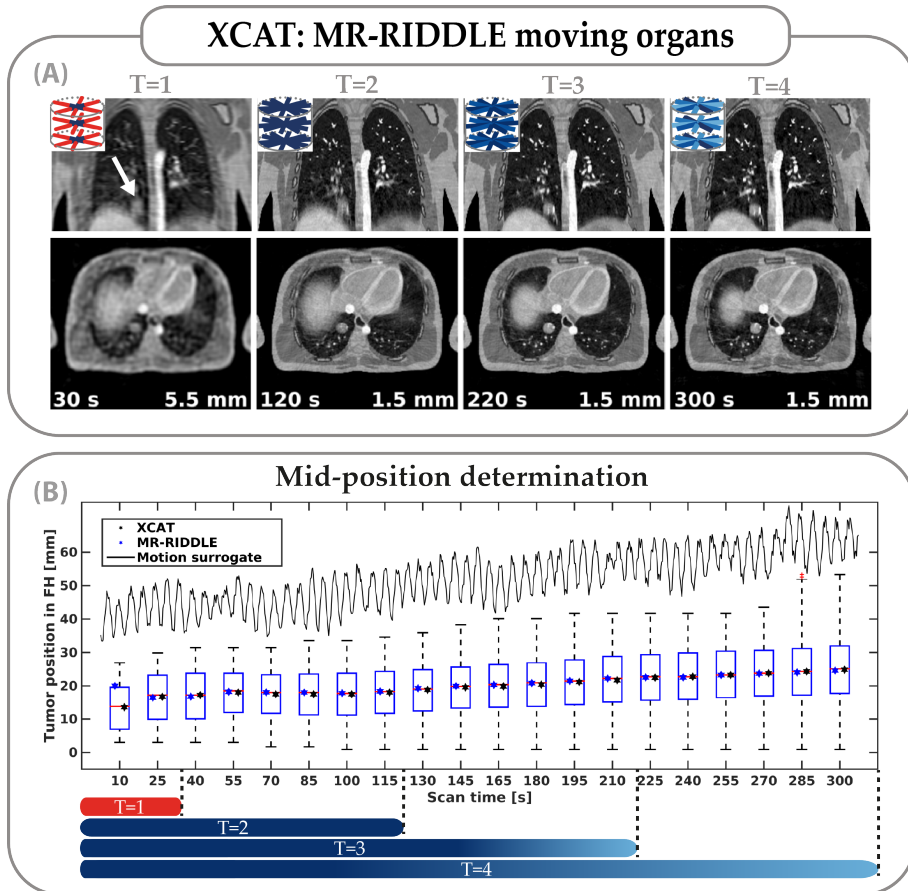


Figure 4.4: MR-RIDDLE simulations on a moving thoracic anatomy. A) Multiresolution images reconstructed at four time-points for the coronal and transverse planes. First and second column indicate different reconstruction resolutions while the third and fourth column have different soft-gating filters. **B)** Drift analysis. XCAT was parametrised such that the diaphragm moved up to 5 cm in feet-head between the maximum and minimum points of the motion surrogate (solid black line). The boxplots cover the range of the tumour positions in the feet-head direction up till the current point in time. The stars indicate the center position of the tumour both in the MR-RIDDLE reconstructions (blue) and the true XCAT mid-positions (green).

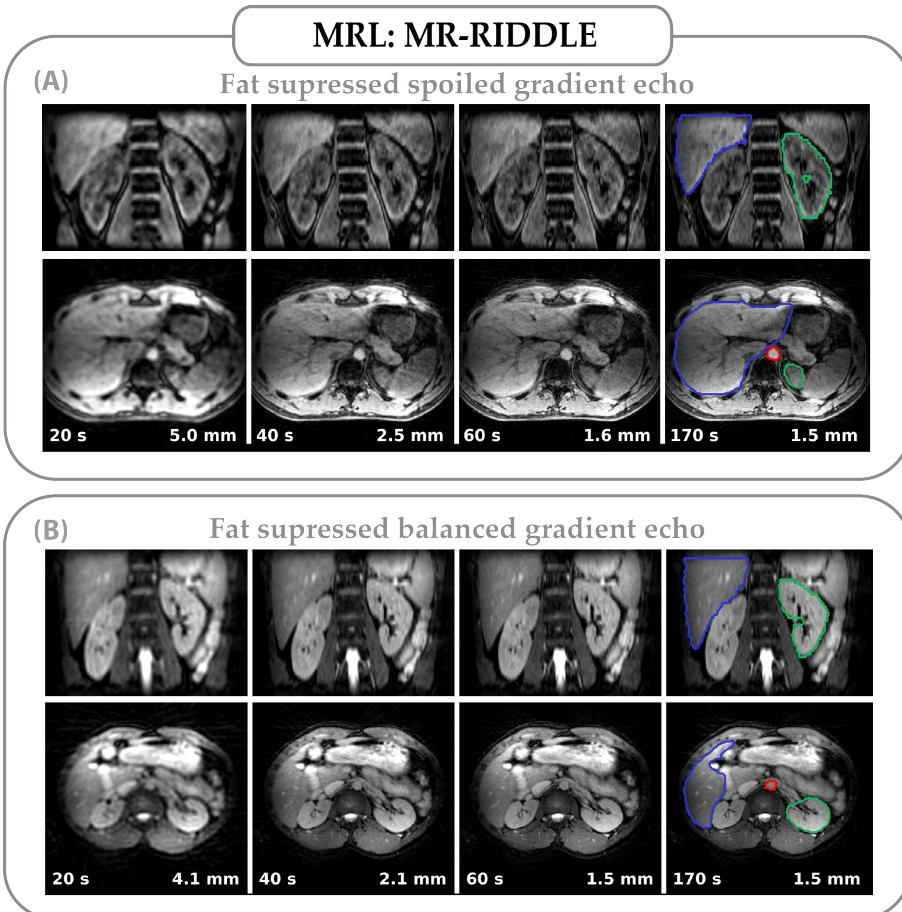


Figure 4.5: *In vivo* MR-RIDDLE reconstructions on a 1.5T MR-Linac. **A)** 3D golden angle stack-of-stars spoiled gradient echo with short inversion time inversion recovery (STIR). Sequence parameters were: flip angle= 12° , TR/TE=4.8/2.0 ms, field-of-view= $330 \times 330 \times 152 \text{ mm}^3$, acquisition resolution= $1.5 \times 1.5 \times 4.0 \text{ mm}^3$. **B)** 3D golden angle stack-of-stars balanced gradient echo with STIR. Sequence parameters were: flip angle= 30° , TR/TE=4.2/2.1 ms, field-of-view= $330 \times 330 \times 152 \text{ mm}^3$, acquisition resolution= $1.5 \times 1.5 \times 4.0 \text{ mm}^3$.

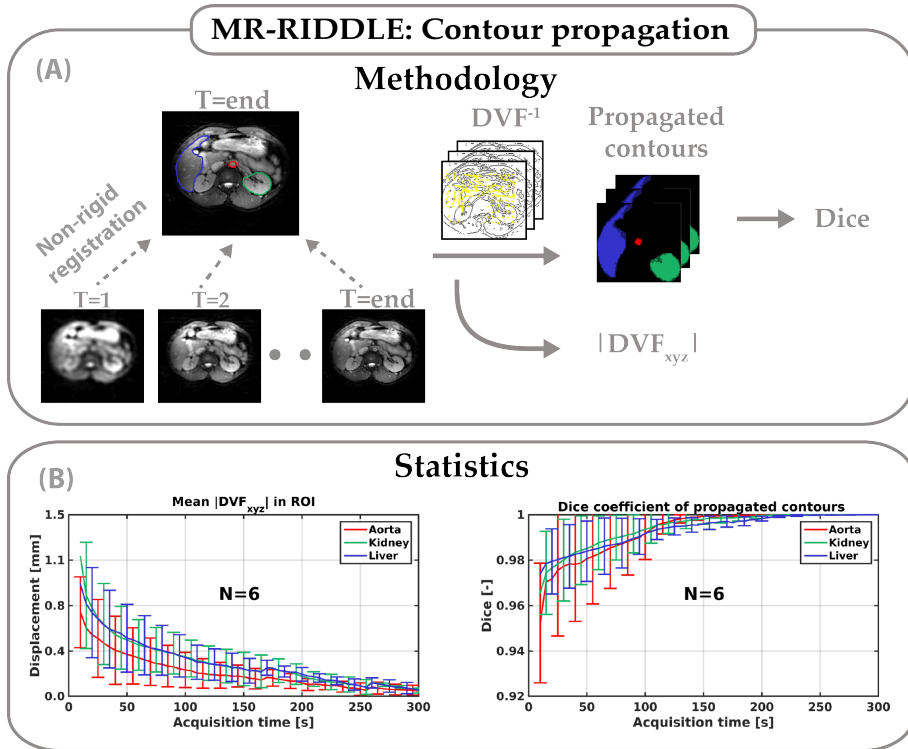


Figure 4.6: Analysis of the propagated contours for the multiresolution MR-RIDDLE reconstructions. **A)** The methodology used to assess the contours. All the reconstructed images were registered to the final reconstruction using optical flow ($\alpha = 0.3$). The obtained DVFs were analysed using the total displacement vector in the aorta, kidney and liver. Additionally, the DVFs were used to deform the organ segmentations to calculate the corresponding Dice coefficients. **B)** The mean displacement vector and mean Dice coefficient across six volunteers are shown as a function of the acquisition time.

4.5 Discussion

Here, we are the first to design and to implement a method that encodes all the information required for treatment planning in a single pre-beam scan to reduce the idle time in the clinical workflow. In particular, we showed in digital simulations that MR-RIDDLE produces usable (low-resolution) images after 30 seconds of imaging, after which higher-resolution image-updates are available on demand. Then we showed with a 4D digital phantom that MR-RIDDLE inherently captures the mid-position of the anatomy, with a precision better than 1 mm, even for cases with large respiratory movements or baseline shifts. Finally, we demonstrated on a 1.5T MR-Linac, in six volunteers and multiple contrasts, that MR-RIDDLE reliably produces high quality mid-position volumes for initialization of contouring in well under a minute without introducing additional registration uncertainties.

The major advantage of MR-RIDDLE is the ability to provide usable low-resolution

images for contouring within one minute. These low-resolution images reduce the time required to start recontouring with 2:34 min for the protocol used in [43], while simultaneously allowing even higher resolution acquisitions (Supplementary information III). In addition, MR-RIDDLE enables images to be reconstructed from arbitrary temporal windows, which could be used for position verification scans that are commonly performed just prior to irradiation. These position verification scans would be instantly available on demand with our proposed method, which further reduces the idle time in the workflow (1:40 min for the example in Fig.4.1). Moreover, MR-RIDDLE does not rely on prospective motion compensation techniques (e.g. gating). Instead, our free-breathing approach captures all the information and as a consequence makes the method applicable even to patients that are not able to suspend their breath. In addition, the soft-gated image reconstruction is able to reconstruct a deblurred mid-position volume with minimal processing time ($< 5s$). The proposed method considerably simplifies the currently used mid-position method, which requires the reconstruction of a 4D volume followed by multiple 3D image registrations [60]. We envision that our proposed method will provide a robust and relative simple approach for online mid-position based MR-guided radiation therapy treatment planning.

Aside from pre-beam imaging, MR-RIDDLE could potentially be used as a real-time method to track the mid-position of slower moving anatomy, such as the prostate. In these type of applications we could increase the temporal resolution (decrease spatial resolution) together with sliding window reconstructions to provide robust and consistent large field-of-view 3D volumes for tracking. The sliding windows used for these reconstructions are completely flexible and can be tailored in terms of temporal and spatial resolution for targeted applications. For these reconstructions we could use a 95% DICE score cut-off (Figure 4.6) and get accurate deformation vector fields with a temporal window of only 22 seconds without acceleration methods.

Besides online MR-guided radiation therapy, MR-RIDDLE could be used in diagnostic scans for patients that are unable to remain sufficiently still. For these patients the longest scanning period without bulk motion could be detected in retrospect and the motion-free images can be recovered using a lower-resolution reconstruction, which would reduce the number of failed scans. The current implementation of MR-RIDDLE supports spoiled gradient echo or balanced gradient echo contrast, but not pure T2 contrast. However, emerging approaches to generate T2 contrast with stack-of-stars sequences are promising [155].

MR-RIDDLE has several limitations that require discussion. First, the method enables high resolution pre-beam acquisitions at a cost of a minor increase in repetition time compared to conventional low-resolution acquisitions. The increase in repetition time is a function of machine hardware parameters and is discussed in supplementary information IV. Second, the quality of the soft-gated image reconstruction to deblur the anatomy in the mid-position depends largely on the motion surrogate. Systematic shifts of this motion surrogate could introduce a position bias, however the inclusion of multiple surrogates could tackle this issue. Note that the MR-RIDDLE reconstructions will always have a small delay

in detecting these systematic shifts due to the intrinsic blurring caused by the temporal window. Third, MR-RIDDLE is not easily translatable to spin-echo type of sequences that are commonly used in radiation therapy.

So far, MR-RIDDLE was only evaluated in volunteers in an offline setting. In future work we aim to embed the image reconstruction in the online workflow to perform treatment simulations. Using the treatment simulations we can begin to determine optimal reconstruction timings, investigate the convergence to sharp reconstructions in abdominal/thoracic regions and to examine the overall practicality of the method in the clinical workflow. Moreover, MR-RIDDLE could be extended to reconstruct respiratory resolved 4D MRI's from the exactly the same dataset [156] [157]. These respiratory-resolved 4D MRI's do not capture systematic baseline shifts and therefore could be supplemented with a low spatial/high temporal resolution sliding window (as discussed in the real-time method) for complete motion estimation. Both these extensions are excellent examples of the potential of the flexibility of the golden angle sampling scheme that allows the user to encode information of multiple temporal and spatial resolutions in a single scan.

The current implementation of MR-RIDDLE did not use acceleration techniques such parallel imaging due to the long processing times required for 3D non-Cartesian sensitivity encoding. The longer processing time would counteract the saved acquisition time and therefore not speed-up the workflow. An alternative method to accelerate the imaging would be to use partial Fourier, Cartesian sensitivity encoding in the partition direction or use variable density or asymmetric field-of-view stack-of-stars sampling schemes. Using these methods we believe to gain a factor of 2-3 acceleration on top of the imaging times reported in this work.

4.6 Conclusion

MR-RIDDLE is capable of producing a mid-position volume for initialization of contouring or contour propagation in well under a minute, after which the image acquisition continues to collect data for high-resolution image updates. Moreover, continuing the data acquisition during the recontouring enables the final image reconstruction to be very high resolution, which is infeasible with conventional sequences. MR-RIDDLE creates a more streamlined and time-efficient workflow where continuous data acquisition and human interaction are performed in parallel.

4.7 Acknowledgments

This work is part of the research program HTSM with project number 15354, which is (partly) financed by the Netherlands Organization for Scientific Research (NWO). Bjorn Stemkens declares to be a majority shareholder of MRCode BV. Rob Tijssen and Cornelis van den Berg declare to be a minority shareholder of MRCode BV.

He who conquers himself is the mightiest warrior.

- Confucius

Free-breathing 3D T2-weighted turbo spin-echo body MRI

Bruijnen, Tom
Schakel, Tim
Akdag, Osman
Brael, Charlotte V.M.
Lagendijk, Jan J.W.
van den Berg, Cornelis A.T.
Tijssen, Rob H.N.

The following chapter is based on:

Free-breathing motion compensated 3D T2-weighted turbo spin-echo MRI for body imaging, 2020, *Submitted to Magnetic Resonance in Medicine*

Abstract

Purpose: To develop and evaluate a free-breathing respiratory motion compensated 4D (3D+respiration) T_2 -weighted turbo spin echo sequence with application to radiology and MR-guided radiotherapy.

Methods: k-space data are continuously acquired using a rewind Cartesian acquisition with spiral profile ordering (rCASPR) to provide matching contrast to the conventional linear phase encode ordering and to sort data into multiple respiratory phases. Low-resolution respiratory-correlated 4D images were reconstructed with compressed sensing and used to estimate non-rigid deformation vector fields, which were subsequently used for a motion compensated image reconstruction.

rCASPR sampling was compared to linear and CASPR sampling in terms of point-spread-function (PSF) and image contrast with *in silico*, phantom and *in vivo* experiments. Reconstruction parameters for low-resolution 4D-MRI (spatial resolution and temporal regularization) were determined using a grid search. The proposed motion compensated rCASPR was evaluated in eight healthy volunteers and compared to free-breathing scans with linear sampling. Image quality was compared based on visual inspection and quantitatively by means of the gradient entropy.

Results: rCASPR provided a superior PSF (similar in k_y and narrower in k_z) and showed no considerable differences in images contrast compared to linear sampling. The optimal 4D-MRI reconstruction parameters were spatial resolution=4.5 mm³ (3x reduction) and $\lambda_t = 1 \cdot 10^{-4}$. The groupwise average gradient entropy was 22.31 ± 0.07 for linear, 22.20 ± 0.09 for rCASPR, 22.14 ± 0.10 for soft-gated rCASPR and 22.02 ± 0.11 for motion compensated rCASPR.

Conclusion: The proposed motion compensated rCASPR enables high quality free-breathing T2-TSE with minimal changes in image contrast and scan time. The proposed method therefore enables direct transfer of clinically used 3D TSE sequences to free-breathing.

Keywords: Motion correction, turbo spin-echo, fast spin-echo, motion compensated image reconstruction, compressed sensing

5.1 Introduction

Respiratory motion during Magnetic Resonance Imaging (**MRI**) has been a long standing problem that leads to considerable reductions in image quality [30]. The solutions traditionally proposed in the radiology workflow are breathhold or respiratory triggered scans, which are effective at reducing motion artefacts at the cost of limited spatial resolution, increased scan time and reduced patient comfort. The solutions traditionally proposed in the MR-guided radiotherapy workflow are respiratory correlated 4D-MRI scans [35], which sort the data into multiple motion states based on a respiratory surrogate signal. These 4D-MRI scans simultaneously reduce motion artefacts and quantify the respiratory motion, but require considerably longer scan times and often show reduced image quality compared to breathhold and gated scans. This reduction in image quality is one of the main reasons why 4D-MRI methods are not widely adopted in clinical exams. Recent advances using motion robust sampling trajectories [33, 131], self-navigation [139, 158], compressed sensing image reconstruction [159, 160] and motion compensated image reconstruction [161, 162] have improved image quality considerably, but are often limited to T_1 -weighted (T_1 -w) gradient echo (**GRE**), while many clinical applications require T_2 -weighted (T_2 -w) turbo spin-echo (**TSE**) scans [163, 164]. T_2 -w TSE has clinical utility in multiple abdominal applications, ranging from the diagnostics of focal hepatic masses [165] and biliary disorders [166] to contouring of pancreatic tumours for radiation therapy [152]. Therefore, there is a clear need for a motion robust 4D (3D+respiration) free-breathing sequence that is able to provide similar image contrast as conventional T_2 -w TSE exams.

T_2 -w TSE scans are typically acquired using 2D multi-slice methods, which offer lower spatial resolution in the slice direction (compared to 3D). The low spatial resolution in the slice direction impedes retrospective reformatting into freely selectable view orientations, which is diagnostically favorable for specific applications [167]. Motion robust 3D T_2 -w TSE scans in free-breathing are currently uncommon in clinical applications and have sparked little interest in research. One of the reasons is the inherent challenges accompanied with high quality 4D (3D+respiration) T_2 -w TSE. The main challenge is the reduced flexibility in selection of k-space trajectory, because non-Cartesian schemes (e.g. radial) repetitively sample the k-space center and therefore impact the T_2 -weighting. These differences in T_2 -weighting lead to an undefined image contrast and, as pointed out by Benkert et al. [168], can only be circumvented by using k-space filtering [169] techniques or model-based reconstructions [170]. Alternatively, Benkert et al. proposed a stack-of-stars trajectory to place the echo train along the Cartesian sampled direction (k_z) [168], which directly couples the echo train length to the number of partitions in the k_z direction. The second challenge is that the acquisition times of 3D T_2 -w TSE are longer than for GRE (2-3 times), which requires aggressive undersampling to reduce scan times to clinically acceptable levels and subsequently requires efficient image reconstruction algorithms to cope with the highly undersampled data [171].

In this work we further develop motion robust free-breathing 4D (3D+respiration)

T_2 -w TSE imaging in order to improve the image quality to make it comparable to respiratory triggered or breathhold examinations. First, we propose a novel k-space trajectory called a rewind spiral acquisition with spiral profile ordering (rCASPR), which is an extension of the regular CASPR trajectory [172]. A kin to CASPR, rCASPR provides self-navigation, golden angle profile ordering and inherent motion robustness due to variable density sampling [173]. In addition, rCASPR increases the maximum viable echo train length to better accommodate T_2 -contrasts for TSE imaging, which allows direct matching of the T_2 contrast to the conventional linear sampled 3D TSE scans. Second, we perform a motion compensated image reconstruction [161] similar to the work of Kolbitsch et al. [174], in which the motion fields are estimated from a high resolution respiratory-correlated 4D-MRI. Instead of using the high resolution 4D-MRI, we propose to estimate the motion fields from a low resolution 4D-MRI, which according to previous works does not significantly reduce the quality of the deformation vector fields [175] [80]. The reduction in spatial resolution is more aggressive than the approaches of previous works that used only a 1.5x reduced spatial resolution [176] or high spatial regularization [177] and considerably speeds-up the computation of the 4D-MRI.

The proposed free-breathing 4D T_2 -w TSE implementation is investigated in eight healthy volunteers. First, we assess the point-spread-function (PSF) and similarity in image contrast between rCASPR and conventional linear sampling. Second, we determine the optimal hyperparameters (spatial resolution and regularization parameter) for 4D-MRI based motion estimation. The quality of the motion fields are evaluated by using them in the motion compensated image reconstruction and subsequently evaluating the reconstructed images using the gradient entropy metric [178]. Third, the general image quality of motion compensated rCASPR is compared against conventional linear sampling, rCASPR without motion correction and rCASPR with soft-gating [140,141] using the gradient entropy metric [178].

5.2 Methods

5.2.1 MRI acquisition and preprocessing

All subjects were scanned on a 1.5T radiotherapy MR system (Philips, Ingenia, Best, the Netherlands) using a 12 channel posterior and 16 channel anterior receive coil. This study was approved by the local institutional review board and informed consent was obtained from all the participants. Eight volunteers were scanned with a TSE sequence with variable refocusing flip angle train to maximize the shot length for the desired T_2 contrast. Relevant sequence parameters for both acquisitions are shown in Table 5.1. All scans were acquired two times, once with the standard linear scheme and once with the proposed golden angle rCASPR scheme (Fig 5.1).

rCASPR samples phase encodes on rotated spiral interleaves, including the $k_{y,z} = (0,0)$ for each interleave, similar to CASPR. However, rCASPR starts at the periphery and samples half of the phase encodes going inwards and samples the

Table 5.1: Scanner and sequence parameters of the volunteer imaging experiments.

Sequence settings	
T_2 -TSE	
Field strength	1.5T
Spatial resolution	1.3 x 1.3 x 2.0 mm ³
Matrix size	308 x 270 x 133
Field-of-view	400 x 350 x 400 mm ³
Repetition time	1000 ms
Effective echo time	230 ms
Echo train length	114
Echo spacing	3.7 ms
Readout bandwidth	855 Hz/pixel
Scan time	248 s

other half of the phase encodes going outwards (Fig 5.1C). In other words, CASPR samples a spiral-out while rCASPR samples a spiral-in-out. The rCASPR phase encodes are selected with a nearest neighbour interpolation from an analytical Archimedean spiral with one revolution per shot. The rCASPR sampling scheme ensures that no duplicate phase encodes are acquired within one spiral interleave. Between the different spiral interleaves, the $k_{y,z} = (0, 0)$ phase encode is repeated in order to enable self-navigation and motion estimation. Contrast control to specific effective echo times can be achieved by shifting the entire spiral interleave. This will shift the acquisition of the $k_{y,z} = (0, 0)$ phase encodes earlier/later in the TSE train. The shifted phase encodes are added to the start or end of the TSE train, depending on the direction of the shift. More details on the sampling scheme are provided on github [179].

Prior to the TSE sequences a reference scan, implemented by the vendor, was acquired to generate the coil sensitivity maps (**CSM**) [180]. K-space data were exported using Reconframe (Gyrotools, Zurich, CH) and were prewhitened and coil compressed to 16 virtual channels. The multi-channel $k_{x,y} = (0, 0)$ projections were used to estimate the respiratory motion surrogate using the coil clustering method [158, 160]. The motion surrogate was subsequently used to soft-gate or to reorder the data across respiratory phases using amplitude binning. Note that both the soft-gating and data reordering operate on complete spiral interleaves and not on partial spiral interleaves. All images were reconstructed offline in Matlab.

5.2.2 Respiratory-correlated 4D-MRI reconstruction

Prior to image reconstruction the k-space data were cropped to lower spatial resolution to reduce the undersampling factor. The extent of reduction in spatial resolution will be addressed in subsection 2.8. The surrogate signal was used to reorder the k-space data across 8 respiratory phases using soft-gating with a Gaussian kernel that partially included data from neighbouring phases [140,

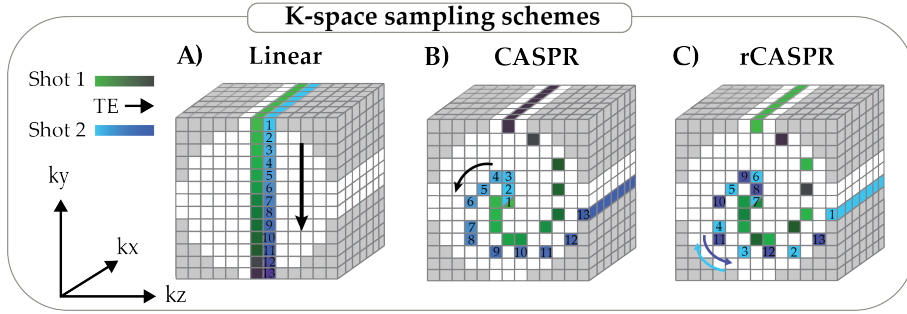


Figure 5.1: K-space sampling schemes for turbo spin-echo imaging. **A)** The linear scheme samples phase encodes along linear lines, which is widely used in clinical TSE sequences. **B)** The CASPR scheme samples phase encodes along spiral interleaves starting in the center and moving to the periphery (spiral-out). The order of phase encodes is indicated with the numbers, starting from 1 and moving to 13. Subsequent spirals are rotated with the golden ratio 137.5° . **C)** The rCASPR scheme samples phase encodes along spiral interleaves, starting on the periphery, moving inwards and moving outwards again, i.e. spiral-in-out (as indicated by the numbers). *CASPR = Cartesian acquisition with spiral profile ordering, rCASPR = rewound Cartesian acquisition with spiral profile ordering, TSE = turbo spin-echo.*

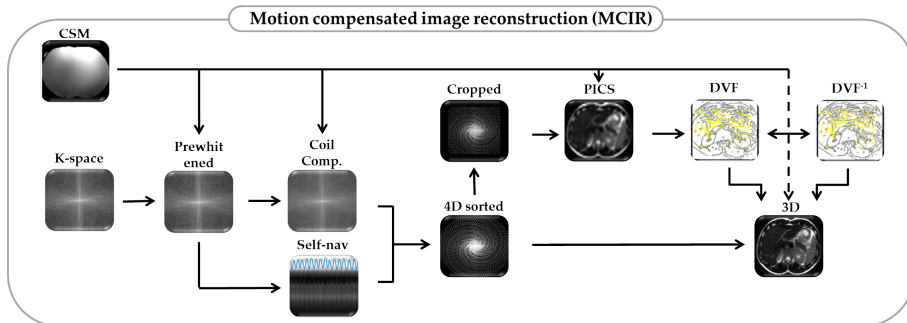


Figure 5.2: Overview of the proposed image reconstruction framework. Input consists of measured k-space data and a pre-scan to estimate the CSM and noise levels. The k-space data is prewhitened and coil compressed using information from the pre-scan. In parallel, the self-navigation profile is estimated from the multi-coil k_z projections. The k-space data is binned in respiratory phases and subsequently cropped to lower spatial resolution. The low resolution k-space is reconstructed using PICS and registered to obtain the DVFs. The DVFs are inverted (DVF_s^{-1}) and interpolated to high resolution. The high resolution DVFs are used together with the high resolution binned k-space data for the motion compensated image reconstruction. *CSM = coil sensitivity maps, PICS = parallel imaging and compressed sensing, DVF = deformation vector field*

141, 181]. The soft-weights (W_t) were constrained to restrict the total number of samples to $\sum_{i=1}^{N_{spirals}} W_{t,i} = 1.5 \cdot \frac{N_{spirals}}{N_{phases}}$, with $N_{spirals}$ as the number of acquired spiral interleaves and N_{phases} as the number of respiratory phases. Respiratory resolved images were reconstructed using parallel imaging and compressed sensing (**PICS**) with locally low-rank constraints [182] using the BART toolbox [183]:

$$x_t = \min_{x_t} \|W_t(FSx_t - y_t)\|_2 + \lambda_t \|x_t\|_* \quad (5.1)$$

With W_t as the soft-weights for the different respiratory phases, F as the Fast Fourier Transform, S as the coil sensitivities, x_t as the respiratory phases images, y_t as the respiratory sorted k-space data, λ_t as the regularization parameter and $\|x_t\|_*$ as the nuclear norm.

5.2.3 Motion estimation

The low-resolution 4D images were interpolated (cubic) to the original high resolution matrix size. The respiratory phase images were registered to the exhale position to obtain the deformation vector fields (**DVF**) using Matlab’s implementation of the diffeomorphic demons algorithm (*imregdemons*) [184, 185]. The demons algorithm uses the mean squared error as an image similarity metric. The algorithm used three resolution levels with regularization parameter (α) set to the voxel equivalent of 5 mm. Note that we also evaluated two other registration methods [100, 186], but found that the demons algorithm was better at handling residual aliasing artefacts in the images (not reported). Subsequently, the registration was repeated in the opposing direction to get an initial guess for the inverse DVFs (DVF^{-1}). The DVF and DVF^{-1} were subsequently post-processed to enforce inverse consistency as reported in [187].

5.2.4 Motion compensated 3D-MRI reconstruction

The final motion compensated image is reconstructed by incorporating the DVFs in the signal model:

$$x = \min_x \|FSU^H x - y\|_2 + \lambda_w \|\Psi x\|_1 \quad (5.2)$$

With U^H as the operator that warps the exhale image to the different respiratory phases and x as the ideal exhale image, y as the k-space data, λ_w as the regularization parameter (0.001) and Ψ as the wavelet transform as a sparse prior. The data consistency problem was solved using a modified version of the non-linear conjugate gradient algorithm provided by Feng et al. [160] with gradient update step as proposed by Polak and Ribiere [188]. More implementation details can be found in the publicly available code [179].

5.2.5 Soft-gated 3D-MRI reconstruction

To compare the proposed motion compensated image reconstruction rCASPR with a retrospectively gated reconstruction, the data were reconstructed using soft-gating. All the k-space data were included to generate soft-weights (W) with an effective acceleration factor of 2, i.e. $\sum_{i=1}^{N_{spirals}} W_i = \frac{N_{spirals}}{2}$. The soft-weights

were generated with the exhale position as a reference with a Gaussian weighting kernel [189]. The weights were included in the PICS reconstruction using the BART toolbox [183]:

$$x = \min_x \|FSx - y\|_2 + \lambda_w \|\Psi x\|_1 \quad (5.3)$$

With W as the soft-weights.

5.2.6 Point spread function analysis: Linear vs. rCASPR

The key concept of rCASPR sampling is to maintain the contrast of the conventional T_2 TSE sequences, which often use linear sampling. However, rCASPR samples high frequencies with a mix of short and long echo times, which inevitably leads to a small difference in image contrast and the corresponding T_2 point spread function. To investigate the difference in T_2 point spread function we setup a small *in silico* experiment. The refocusing flip angle trains along with the subscribed phase encode scheme of the *in vivo* scans were extracted from the MR system. The flip angle patterns were used to simulate a TSE scan for a tissue type with $T_1 = 1000$ ms and $T_2 = 100$ ms using extended phase graphs [190]. The phase encode schemes were used to calculate echo time maps. The signal response and echo time maps were used to sample a single point in image space that exhibits T_2 decay along the echo train. The fully sampled k-space data was subsequently reconstructed using a fast Fourier Transform (with zero-padding) and the resulting 1D and 2D point spread functions (PSF) were compared between rCASPR and linear sampling.

5.2.7 Comparison of image contrast: Linear vs. rCASPR

The rCASPR sampling scheme was introduced to facilitate 4D image reconstruction, while minimizing differences in image contrast. To assess these differences in image contrast two experiments were performed. First, a gel tube phantom with varying T_1 and T_2 values was measured with linear, CASPR and rCASPR scans. The mean value within the tubes was computed and compared using the normalized root mean squared error. Second, one dataset of a volunteer was analyzed to inspect differences in image contrast between linear and rCASPR reconstructions (no motion correction). The root mean square error between the images was calculated and line profiles were extracted from static anatomy and qualitatively compared.

5.2.8 Optimal spatial resolution for 4D-MRI based motion estimation

The rCASPR scheme samples the k-space with variable density and therefore has an increasing undersampling factor with respect to the radial coordinate. This property is exploited in the respiratory-correlated 4D-MRI reconstruction to reduce the undersampling factor by reducing the spatial resolution. The key idea

here is that lowering the spatial resolution reduces residual aliasing artefacts and motion blurring in the PICS reconstruction, while not affecting the final motion estimation [175]. In addition, a reduction in spatial resolution considerably reduces the computational requirements. The reduction in spatial resolution could improve the motion estimation and ultimately lead to higher image quality for the motion compensated rCASPR. However, the quality of the motion estimation is difficult to quantify from the DVFs directly [191]. Therefore we propose to measure the image quality of the motion compensated rCASPR reconstructions as a surrogate for the quality of the 4D-MRI based motion estimation. For the optimization a grid search was performed for one volunteer with spatial resolution $\in [1.5 : 1.5 : 7.5] \text{ mm}^3$ and $\lambda_t \in [5.0, 10.0, 20.0, 50.0, 100.0] \cdot 10^{-4}$. In total 25 4D-MRIs were used for motion compensated image reconstructions. These reconstructions were subsequently analyzed using the global gradient entropy (**GE**) to determine the optimal hyperparameters [178]. These hyperparameters were expected to be representative for the complete group and were therefore used for all volunteer motion compensated image reconstructions.

5.2.9 Comparison of image quality: Linear vs rCASPR

The proposed motion compensated rCASPR was compared to linear, rCASPR and soft-gated rCASPR in eight healthy volunteers for T_2 -w TSE. The image quality was compared by computing the (global) gradient entropy for all the reconstructed images [178]. A reduction of the gradient entropy corresponds to an increase in image quality. Note that all reconstructions were performed with the same spatial regularization parameter (λ_w) such that the gradient entropy is reflective of the removal of motion artefacts.

5.3 Results

5.3.1 Point spread function analysis: Linear vs rCASPR

Figure 5.3 shows the result of the *in silico* point spread function analysis. Figure-5.3A shows the flip angle train and B the corresponding T_2 decay that is used in combination with the echo time maps (Figure-5.3C) for linear and rCASPR sampling. Note that the echo time map of linear sampling shows that the phase encode scheme is optimized for acquisition efficiency and therefore does not sample straight columns. The echo time maps leads to the 1D and 2D point spread functions shown in Figure-5.3D+E. The point spread function is similar in the Y direction and narrower for rCASPR sampling in the Z direction.

5.3.2 Comparison of image contrast: Linear vs. rCASPR

Figure 5.4A shows the phantom scan of the gel tube phantom with varying T_1 and T_2 values. Note that the image contrast of rCASPR is more similar to the linear scan than CASPR, which is also reflected in the normalized root mean squared error values that are 0.018 and 0.08 for rCASPR and CASPR respectively. These findings are also reflected in the mean signal intensities per tube as shown in the

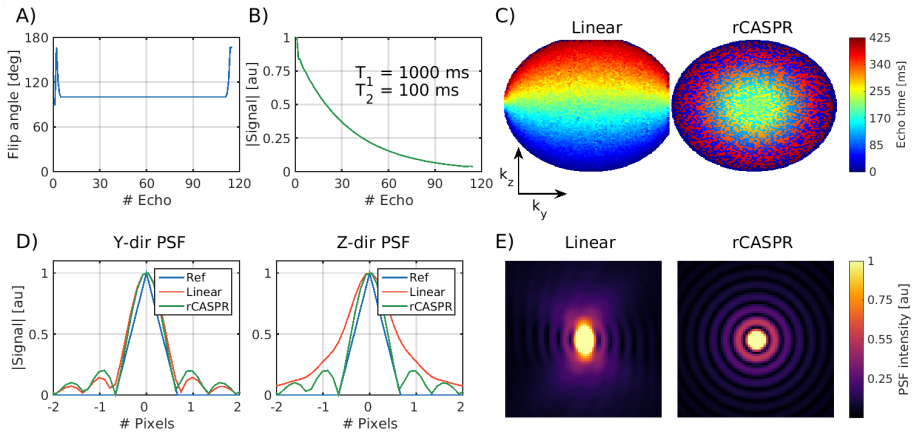


Figure 5.3: Point spread function analysis of linear and rCASPR sampling. **A)** Refocusing angle train used for the experiments. **B)** Extended phase graph signal simulation for a spin with $T_1/T_2 = 1000/100$ ms. **C)** Echo time maps of all the sampled phase encodes. **D)** 1D point spread functions in the Y and Z directions. Note that the PSF of rCASPR is superior in the Z direction and similar in the Y direction compared to linear. **E)** 2D point spread functions for both linear and rCASPR.

barplot in Figure 5.4B. Figure 5.4C shows *in vivo* data of the linear and rCASPR sampling with RMSE = 0.051. The rCASPR reconstructions show reduced motion artefacts (green arrow) compared to linear sampling. The right side of the figure shows line intensity profiles, which are well aligned between the scans.

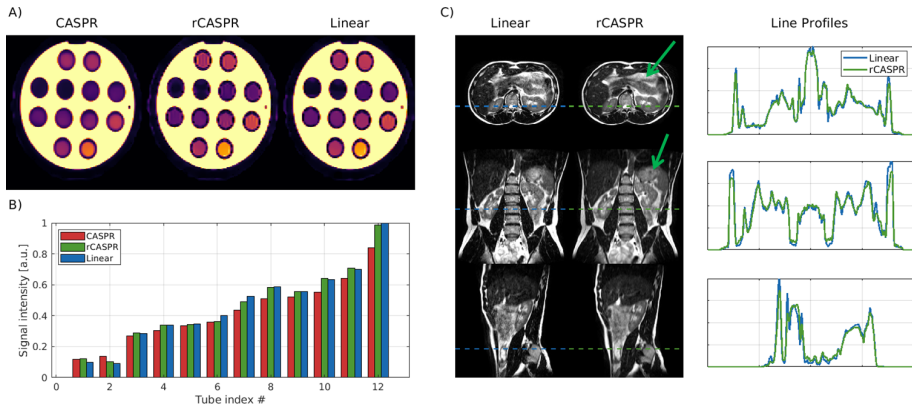


Figure 5.4: Image contrast comparison of linear vs rCASPR sampling schemes in T_2 -TSE. **A)** Gel tube phantom measurements of CASPR, rCASPR and Linear sampling schemes. **B)** Bar plots of the mean image intensities of the gel tubes for CASPR, rCASPR and Linear sampling. Note that rCASPR and Linear provide similar image intensities. **C)** Free-breathing abdominal 3D scans of a volunteer with Linear and rCASPR with identical scan parameters. Note that rCASPR shows reduced motion artefacts and slight blurring compared to the linear sampling scheme (green arrows). **D)** Line intensity profiles through the dashed lines from C). *Acronyms: rCASPR = rewind Cartesian acquisition with spiral profile ordering, TSE = turbo spin echo.*

5.3.3 Optimal spatial resolution for 4D-MRI based motion estimation

Figure 5.5-A shows a coronal slice of the exhale position in the 4D-MRI for the different spatial resolution levels. The low resolution images show reduced aliasing artefacts, which are especially pronounced in the liver. Figure 5.5-B shows the magnitude of the DVFs for the same coronal slice with varying temporal regularization and spatial resolution levels. There are two obvious trends within the data; the $|DVF|$ increases with reducing spatial resolution and that the $|DVF|$ also decreases with increasing regularization parameter λ_t . These trends seem to be stronger on the left side of the image, which corresponds with the anatomical position of the liver. The DVFs were subsequently used in the motion compensated image reconstruction. Figure 5.5-C shows the gradient entropy of the motion compensated image reconstructions for the varying regularization parameters and spatial resolution levels. The minimum within the parameter space is indicated with the red dot and corresponds with spatial resolution = 4.5 mm^3 and $\lambda_t = 1 \cdot 10^{-3}$.

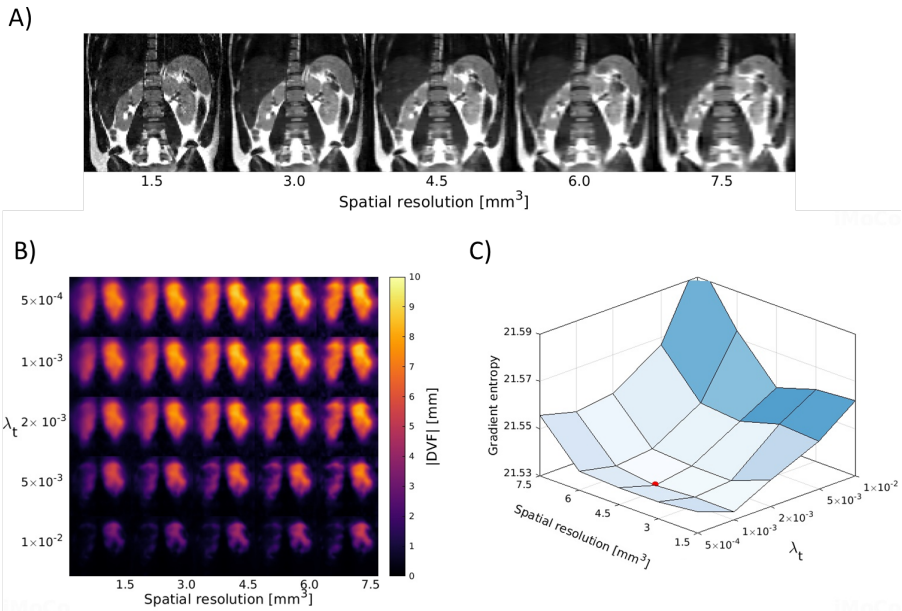


Figure 5.5: Hyperparameter grid search for optimal spatial resolution and temporal regularization (λ_t). **A)** Top row shows a coronal slice reconstructed with five different spatial resolutions ($1.5 - 7.5 \text{ mm}^3$). **B)** The magnitude of the exhale-inhale motion fields derived from the 4D-MRIs with varying spatial resolution and temporal regularization. The investigated hyperparameters were in range: for spatial resolution $\in [1.5 : 1.5 : 7.5] \text{ mm}^3$ and $\lambda_t \in [5.0, 10.0, 20.0, 50.0, 100.0] \cdot 10^{-4}$. **C)** The optimization landscape that describes the gradient entropy for the motion compensated image reconstructions with the DVFs shown in panel B). Note that a lower gradient entropy corresponds with higher image quality and that the minimum of the function is indicated with red sphere. *Acronyms: DVF = deformation vector field.*

Figure 5.6 shows the respiratory-correlated 4D-MRI reconstructions for four of the volunteers with the optimal hyperparameters described in the previous paragraph. The figure also shows the $|DVF|$ that describes the transformation between the exhale and inhale respiratory phase. Most volunteers show maximum displacement at the top of the liver larger than 1 cm, only volunteer 2 shows considerably smaller motion. As expected, almost no motion is visible in the static regions of the image (e.g. spine), indicating that residual aliasing artefacts do not affect the motion estimation.

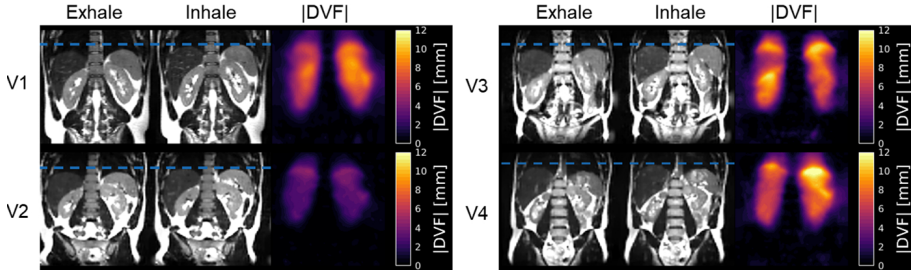


Figure 5.6: Respiratory correlated low-resolution 4D image reconstructions with the corresponding deformation vector fields. The different volunteers are indicated with "V_x", where "x" refers to the volunteer index. The two grayscale images show the image reconstructed at the inhale and exhale position and the color coded images show the $|DVF|$ that describes the motion between these respiratory positions. Note that all volunteers show peak motion ≈ 1 cm with the exception of volunteer 2. The blue dashed line indicates the position of the liver/spleen in the exhale phase and aids in the visualization for the inhale phase. Acronyms: $DVF = \text{deformation vector field}$.

5.3.4 Comparison of image quality: Linear vs rCASPR

The comparison of image quality in two out of the eight volunteers are shown in Figures 5.7-5.8. The results of two other volunteers are shown in Supporting information I. Figure panels A-D show the linear, rCASPR, soft-gated rCASPR and motion compensated rCASPR reconstructions. Note that the soft-gated and motion compensated rCASPR are reconstructed at the exhale position. Zoom images of regions of interest are shown in blue boxes. Blue numbers at the left bottom display the gradient entropy calculated from the entire image. In general, image quality slightly increases when changing the sampling scheme from linear to rCASPR. The addition of soft-gating to rCASPR further increases the image quality. The largest improvement in image quality is observed when transitioning from no correction to the motion compensated image reconstruction.

The groupwise average gradient entropy was 22.31 ± 0.07 for linear, 22.20 ± 0.09 for rCASPR, 22.14 ± 0.10 for soft-gated rCASPR and 22.02 ± 0.11 for motion compensated rCASPR. Supporting Information II shows a video of the motion compensated rCASPR reconstruction warped with the DVFs for all the volunteers.

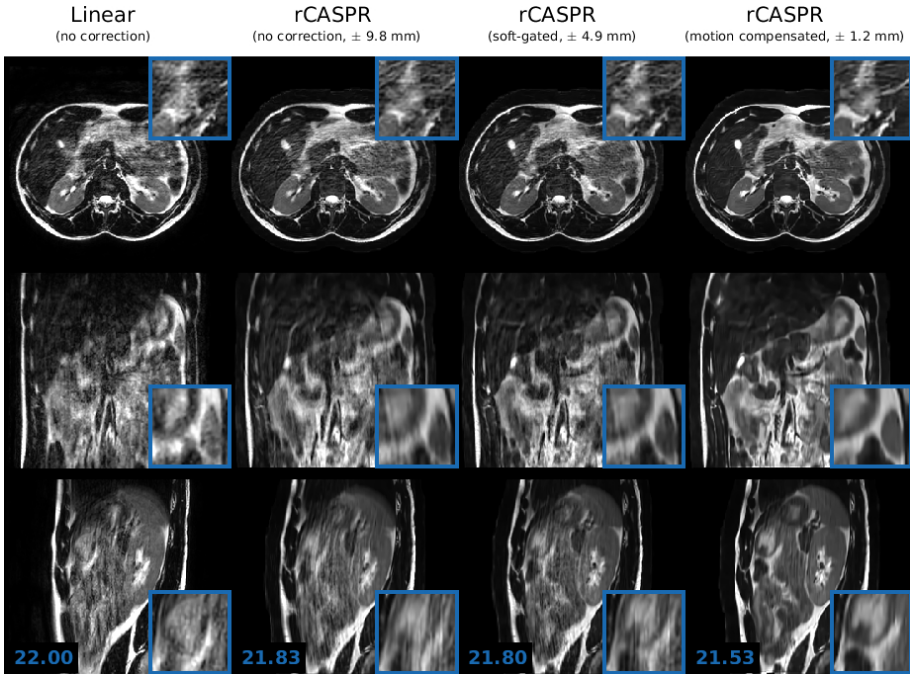


Figure 5.7: Volunteer 1: Comparison of image quality in T_2 -w free-breathing 3D turbo spin echo scans for linear, rCASPR, soft-gated rCASPR and motion compensated rCASPR. For all the reconstructions the residual peak-to-peak motion was estimated using the 4D-MRI. For rCASPR the residual motion was ± 9.8 mm, soft-gating rejected 50% of the data such that the residual motion was ± 4.9 mm and motion compensation had residual intrabrain motion of ± 1.2 mm. The numbers in left bottom corner indicate the global gradient entropy. Blue boxes present zoomed regions. *Acronyms: rCASPR = rewound cartesian acquisition with spiral profile ordering.*

5.4 Discussion

The key idea of this study was to develop a free-breathing 4D (3D+respiration) T_2 -w TSE scan that matches the T_2 contrast of conventional linearly sampled 3D TSE scans while providing high quality motion corrected images. We proposed a sequence based on a novel golden angle rCASPR k-space trajectory that can maintain the desired T_2 contrast, while enabling self-navigation and respiratory correlated 4D-MRI. We proposed to reconstruct the 4D-MRI with reduced spatial resolution to obtain higher quality motion estimates with less computation time. The 4D-MRI reconstruction parameters (spatial resolution and temporal regularization) were optimized with a grid search guided by gradient entropy of the motion compensated image reconstruction. The optimal hyperparameters were spatial resolution = 4.5 mm³ (3x reduction) and $\lambda_t = 1 \cdot 10^{-3}$. The deformation vector fields were subsequently incorporated in the motion compensated rCASPR reconstruction, which was compared to linear, rCASPR and soft-gated rCASPR reconstructions. The image analysis indicated that motion compensated rCASPR provided the highest image quality in terms of the gradient entropy for all cases.

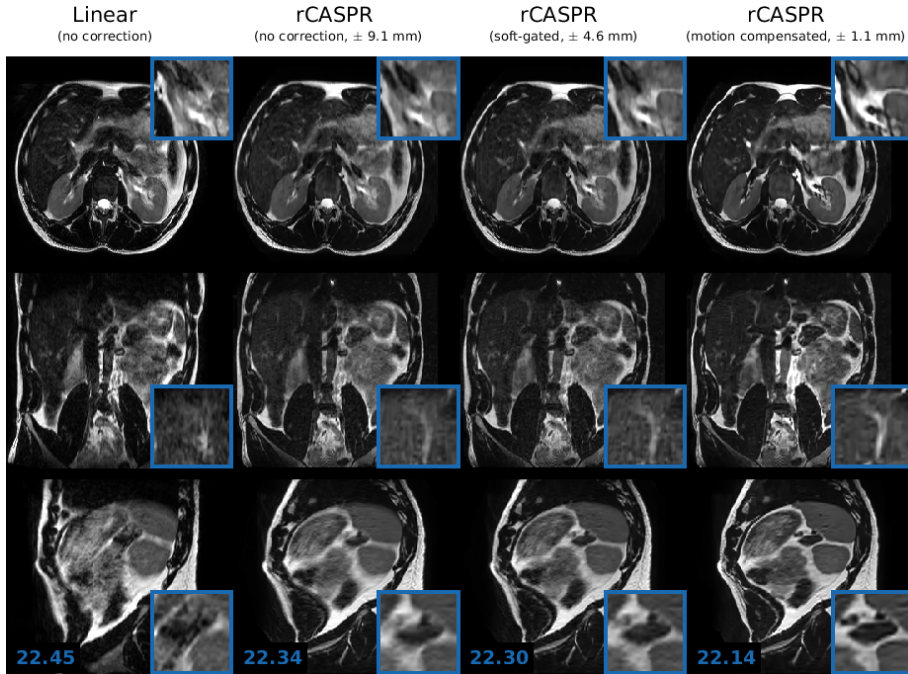


Figure 5.8: Volunteer 2: Comparison of image quality in T_2 -w free-breathing 3D turbo spin echo scans for linear, rCASPR, soft-gated rCASPR and motion compensated rCASPR. For all the reconstructions the residual peak-to-peak motion was estimated using the 4D-MRI. For rCASPR the residual motion was ± 9.1 mm, soft-gating rejected 50% of the data such that the residual motion was ± 4.6 mm and motion compensation had residual intrabrain motion of ± 1.1 mm. The numbers in left bottom corner indicate the global gradient entropy. Blue boxes present zoomed regions. *Acronyms: rCASPR = rewound cartesian acquisition with spiral profile ordering.*

An important aspect of this study that warrants discussion is the reliability and generalizability of the hyperparameters for the low resolution 4D-MRI reconstruction. The reliability is mainly dependent on the performance of the gradient entropy metric used as a surrogate for image quality. The gradient entropy was used in previous works on motion correction [141, 177, 192, 193] and McGee et al. [178] reported that the gradient entropy corresponded best with observer scores out of 24 metrics in the context of motion correction. However, other image quality metrics may yield different optimal hyperparameters, which could potentially improve the image reconstructions. An alternative approach could be to use a metric directly on the motion fields, such as biomechanical quality assurance criteria [191]. Note that the 4.5mm^3 found in this work correspond well with findings by Glitzner et al. [175]. The generalizability of the optimal hyperparameters is primarily dependent on the combination of the following variables: the acceleration factor, the image registration method and the scale of the physiological motion. For example, high acceleration will require reduced spatial resolution or high spatial regularization to mitigate aliasing artefacts or require an image registration algorithm that is resilient to aliasing artefacts [194]. There-

fore, the findings of optimal hyperparameters reported in this work are likely to be method-specific and therefore do not necessarily generalize to other combinations of acquisition and reconstruction methods.

Overall, we believe that this work demonstrates the feasibility of free-breathing respiratory-correlated 4D (3D+respiration) T_2 -w TSE. The combination of the rCASPR sampling scheme and motion estimation from low-resolution 4D-MRI allows high quality image reconstruction from a relatively short scan time (< 5 min). For radiology, the proposed motion compensated rCASPR could potentially replace respiratory triggered 3D T_2 -w TSE scans, which could lead to simpler imaging workflows and improved robustness. Examples of these applications include: magnetic resonance urography, magnetic resonance cholangio-pancreatography and dynamic contrast enhanced imaging of the liver. However, future studies are required to compare the proposed free-breathing motion compensated rCASPR scan to prospectively respiratory triggered scans. For MR-guided radiotherapy, the motion compensated rCASPR provides a practical and efficient solution to quantify motion and ensure that the tumor is always covered by the radiation beam during free-breathing. In addition, the high quality motion compensated rCASPR images allow the definition of a highly accurate target contour, which is crucial for radiotherapy treatment planning. motion compensated rCASPR could also be used on a hybrid MRI-Linac to robustly assess day-to-day variations of the anatomy in free-breathing [38]. For PET/MRI, the motion compensated rCASPR could be used to conveniently maintain clinically used contrasts while concurrently quantifying the motion for the motion compensated PET reconstruction [174, 195].

5.5 Conclusion

The proposed rCASPR sampling scheme, in combination with motion estimation from low-resolution 4D-MRI, enables high quality motion compensated image reconstruction. The proposed implementation enables direct transfer of contrast of 3D T_2 -w TSE sequences to the free-breathing 4D (3D+respiration) T_2 -w TSE counterparts with minimal changes in image contrast and scan time. Future studies are required to compare the image quality of the proposed method to respiratory triggered acquisitions, which are often the clinical standard.

5.6 Acknowledgments

This work is part of the research programme HTSM with project number 15354, which is (partly) financed by the Netherlands Organisation for Scientific Research (NWO) and Philips Healthcare.

If you talk about it, it's a dream, if you envision it, it's possible, but if you schedule it, it's real.

- Anthony Robbins

Non-rigid 3D motion estimation using low-rank MR-MOTUS

Huttinga, Niek R.F.
Bruijnen, Tom
van den Berg, Cornelis A.T.
Sbrizzi, Alessandro

The following chapter is based on:
Non-rigid 3D motion estimation at high temporal resolution from prospectively
undersampled k-space data using low-rank MR-MOTUS, 2020, *Magnetic
Resonance in Medicine*;85(4):2309-2326

Abstract

Purpose: With the recent introduction of the MR-LINAC, an MR-scanner combined with a radiotherapy LINAC, MR-based motion estimation has become of increasing interest to (retrospectively) characterize tumor and organs-at-risk motion during radiotherapy. To this extent, we introduce low-rank MR-MOTUS, a framework to retrospectively reconstruct time-resolved non-rigid 3D+t motion-fields from a single low-resolution reference image and prospectively undersampled k-space data acquired during motion.

Theory: Low-rank MR-MOTUS exploits spatio-temporal correlations in internal body motion with a low-rank motion model, and inverts a signal model that relates motion-fields directly to a reference image and k-space data. The low-rank model reduces the degrees-of-freedom, memory consumption and reconstruction times by assuming a factorization of space-time motion-fields in spatial and temporal components.

Methods: Low-rank MR-MOTUS was employed to estimate motion in 2D/3D abdominothoracic scans and 3D head scans. Data were acquired using golden-ratio radial readouts. Reconstructed 2D and 3D respiratory motion-fields were respectively validated against time-resolved and respiratory-resolved image reconstructions, and the head motion against static image reconstructions from fully-sampled data acquired right before and right after the motion.

Results: Results show that 2D+t respiratory motion can be estimated retrospectively at 40.8 motion-fields per second, 3D+t respiratory motion at 7.6 motion-fields per-second and 3D+t head-neck motion at 9.3 motion-fields per second. The validations show good consistency with image reconstructions.

Conclusion: The proposed framework can estimate time-resolved non-rigid 3D motion-fields, which allows to characterize drifts and intra and inter-cycle patterns in breathing motion during radiotherapy, and could form the basis for real-time MR-guided radiotherapy.

Keywords: Motion estimation, Model-based reconstruction, MR-guided radiotherapy, MR-LINAC

6.1 Introduction

Uncertainty in tumor and organs-at-risk locations due to unknown respiratory-induced organ motion diminishes the efficacy of radiotherapy in the abdomen and thorax in two ways. Firstly, tumors are irradiated with larger treatment margins, which results in increased radiation dose and toxicity to healthy tissue. Secondly, it prevents an accurate (retrospective) estimation of the actual dose accumulated in the targeted tumor and healthy surrounding tissue during the treatment.

Recently, the MR-LINAC was introduced as the combination of an MR-scanner and a linear accelerator (LINAC) in a single device [38, 40, 41, 135], which has the potential to address both points above. Achieving this goal, however, poses the following technical challenge: real-time reconstructions at 5 Hz [196, 197] of internal body motion during the treatments. A fundamental step towards real-time reconstructions is the retrospective estimation of time-resolved motion-fields. Additionally, these retrospectively calculated motion-fields are valuable for the calculation of accumulated dose and can be taken into account for more accurate radiation planning of subsequent treatments. To this extent, we focus on the retrospective reconstruction of time-resolved 3D+t respiratory motion with a temporal resolution of 5 motion-fields-per-second. We envision that this framework could eventually be adapted to prospective real-time reconstructions [80].

In MR-guided radiotherapy, tumor and organs-at-risk motion is typically estimated from cine-MR-images followed by image registration. For time-resolved motion estimation, these cine-MR-images would thus require sufficient temporal resolution and spatial coverage to resolve the targeted motion. This is in general achievable in 2D, and also in 3D for slowly moving targets such as pelvic tumors [198]. However, in 3D it is more challenging for faster moving targets like lung tumors, that require at least 5 motion-fields-per-second [196, 197].

Several strategies have previously been proposed to extract tumor and organ-at-risk motion from MR-images, three of which will be reviewed below. With the first strategy, average respiratory motion is estimated from a respiratory-resolved 3D+t MRI. This approach retrospectively sorts image slices or k-space readouts in 3D acquisitions according to their respective respiratory phases, extracted using a respiratory motion surrogate (e.g. pneumatic belt, self-navigation signal or navigator). Examples include the works in [160, 181, 199–201] (see [35] for a more complete overview). Although the retrospective sorting in these methods allows for efficient use of all acquired data, it makes strong assumptions on the periodicity of respiratory motion and characterizes only average 3D+t breathing motion. Although this is useful to reduce treatment margins, it may not be sufficient for accurate accumulation of the delivered dose.

A different strategy uses multi-slice/orthogonal 2D+t cine-MRI for 3D+t motion estimation [138, 202–208]. The reduction in the spatial dimension allows for higher temporal resolution, and is combined with a model that links the lower-dimensional image data to 3D motion-fields. This strategy assumes, however, that a good fit on lower-dimensional images implies a good fit in the full 3D domain. Although this is reasonable for small volumes, since slices cover a large fraction

of the volume in such a case, it may be less valid for larger volumes which may be required for dose accumulation.

The third strategy does not rely on sorting, but reconstructs images from highly undersampled k-space data. Even with parallel imaging [180, 209], this typically eventually results in lower SNR, lower spatial resolution, and/or undersampling artifacts. Nevertheless, it has been shown that motion-fields can be estimated from these images with sufficient accuracy [61, 210–212]. Additionally, iterative reconstructions based on compressed sensing [66] have been proposed to exploit the spatio-temporal sparsity of images. However, for the intended application the reported temporal resolution was too low [212–214], or the FOV was too small [215, 216].

Following a different approach, we have previously introduced MR-MOTUS [80] (Model-based Reconstruction of MOTion from Undersampled Signal), a new framework that allows to reconstruct whole-body non-rigid 3D motion-fields directly from k-space data. The key ingredient of MR-MOTUS is a signal model that explicitly relates dynamic k-space data to the combination of a static reference image and dynamic motion-fields. Assuming a reference image is available, and data is acquired in steady-state, motion-fields can be reconstructed directly from k-space data by solving the corresponding non-linear inverse problem. Since motion-fields are spatially correlated and therefore compressible, few data are required for the reconstructions.

The possibility to reconstruct motion from few k-space data makes MR-MOTUS a natural candidate for time-resolved 3D+t motion estimation, which is not directly restricted to the achievable temporal resolution in MR-images. Our work presented in [80], however, represents a proof-of-concept, and demonstrates MR-MOTUS in an experimental setting. Four points of improvement should be addressed for the extension of MR-MOTUS to time-resolved 3D+t motion estimation:

1. Only spatial correlation in motion-fields was exploited, and a single static motion-field was reconstructed for each single snapshot of k-space data. Additionally exploiting temporal correlation, and jointly reconstructing the 3D+t motion-field series at once, could improve the reconstruction quality and lower requirements of computing time and memory.
2. Only the body coil was used for data acquisition to obtain homogeneous coil sensitivity. This did not represent a practical setting and multi-coil acquisitions would be favorable in terms of SNR.
3. The required reference image was obtained from a separate MR-scan during breath-hold. Ideally, no breath-holds are required and reconstructions can be performed on data acquired in free-breathing conditions.
4. 3D motion-fields were previously reconstructed from retrospectively undersampled Cartesian k-space data, while the motion estimation application requires prospectively undersampled acquisitions with an efficient non-Cartesian trajectory.

In this work we address the aforementioned points of improvement and extend the framework to experiments in a realistic setting, in which reference image and time-resolved 3D+t motion-fields can be reconstructed from multi-coil, free-breathing, prospectively undersampled non-Cartesian 3D k-space data. The reconstruction of time-resolved motion-fields yields a large number of unknowns in 3D, which are needed to represent 3D motion-fields over a large number of timepoints (> 100). We propose to use a spatio-temporal low-rank motion model, which yields a compressed representation of motion-fields in space and time. Several works have previously proposed low-rank motion models for motion estimation [138, 217–221], and the analyses in [138, 217, 218] suggest that a rank-2 motion model can accurately describe respiratory motion. Consequently, the low-rank motion model can reduce the number of unknowns by two orders of magnitude, thereby introducing a regularization in both space and time and significantly reducing memory consumption and reconstruction times for 3D+t reconstructions. We will refer to the extended framework as low-rank MR-MOTUS.

We demonstrate and validate low-rank MR-MOTUS in a total of 6 *in-vivo* experiments on 2 healthy subjects and several moving anatomies. 2D/3D whole-body respiratory motion is included in view of the MR-guided radiotherapy application, and 3D head-and-neck motion is included for additional validation and as a demonstration to handle different types of motion. The 2D respiratory motion reconstruction is validated against 2D time-resolved compressed sensing, the 3D respiratory motion reconstruction against respiratory-resolved 3D image reconstruction, and the 3D head-and-neck motion against 3D static images acquired right before and right after the motion.

6.2 Theory

6.2.1 Background MR-MOTUS

We assume a general d -dimensional setting, with targeted case $d = 3$, and we follow the convention that bold-faced characters denote vectorizations. We define $\mathbf{x}_0 \mapsto \mathbf{x}_t$ as the mappings from coordinates $x_0 \in \mathbb{R}^d$ in a reference image to new locations $\mathbf{x}_t \in \mathbb{R}^d$ at time t . The mappings are characterized by the motion-fields d_t through $\mathbf{x}_t = \mathbf{x}_0 + d_t(\mathbf{x}_0)$. This will be written in concatenated vector-form as

$$\mathbf{X}_t = \mathbf{X}_0 + \mathbf{D}_t \quad (6.1)$$

where $\mathbf{X}_t, \mathbf{X}_0, \mathbf{D}_t \in \mathbb{R}^{Nd \times 1}$ denote the vertical concatenations over N spatial points in a d -dimensional setup. The MR-MOTUS forward model [80] explicitly relates the motion-fields \mathbf{D}_t and a static reference image $\mathbf{q}_0 \in \mathbb{C}^N$ to dynamic, single-channel (and possibly non-Cartesian) k-space measurements $\mathbf{s}_t \in \mathbb{C}^{N_k}$:

$$\mathbf{s}_t = \mathbf{F}(\mathbf{D}_t | \mathbf{q}_0) + \boldsymbol{\epsilon}_t. \quad (6.2)$$

Here $\boldsymbol{\epsilon}_t \in \mathbb{C}^{N_k}$ is the complex noise vector and $\mathbf{F} : \mathbb{R}^{Nd} \mapsto \mathbb{C}^{N_k}$ is the vectorization of the forward operator defined as

$$F(\mathbf{d}_t)[\mathbf{k}] = \int_{\Omega} q_0(\mathbf{x}_0) e^{-i2\pi\mathbf{k} \cdot [\mathbf{x}_0 + \mathbf{d}_t(\mathbf{x}_0)]} \mathbf{x}_0 \quad (6.3)$$

where $\mathbf{k} \in \mathbb{R}^d$ denotes the k-space coordinate. By fitting the non-linear signal model in Equation 6.3 to acquired k-space data, motion-fields can be reconstructed directly from k-space measurements.

6.2.2 Reconstruction problem formulation for space-time reconstructions

In this work we follow [222] and formulate the reconstruction problem for space-time motion-fields \mathbf{D} as follows:

$$\min_{\mathbf{D}} \sum_{t=1}^M \|\mathbf{F}(\mathbf{D}_t) - \mathbf{s}_t\|_2^2 + \lambda_R \mathcal{R}(\mathbf{D}). \quad (6.4)$$

Here $\mathcal{R}(\mathbf{D}) > 0$ is a regularization functional, with corresponding parameter $\lambda_R > 0$, which models a-priori assumptions in order to exploit correlations in both space and time.

Parameterization with a low-rank space-time motion model

A straightforward parameterization of \mathbf{D} considers one motion-field per dynamic, i.e. $\mathbf{D} = [\mathbf{D}_1, \dots, \mathbf{D}_M] \in \mathbb{R}^{Nd \times M}$. This is, however, impractical from a computational point-of-view, since the number of parameters scales with the number of dynamics: $|\mathbf{D}| = NMd \sim M$. For a typical scenario, $N \sim 10^6$, $M \sim 10^2$ and $d = 3$, in which case

$$|\mathbf{D}| \sim 10^8. \quad (6.5)$$

Hence, this parameterization is inconvenient since it results in high memory consumption and long reconstruction times.

Instead, we propose a parameterization with a low-rank motion model, to simultaneously reduce the number of parameters for the reconstruction and introduce a natural regularization in both space and time. The model enforces the following factorization of the motion-fields that separates the spatial and temporal contributions:

$$\mathbf{D} = \left(\begin{array}{c|ccc} & & & \\ \mathbf{D}_1 & \dots & \mathbf{D}_M & \\ & & & \end{array} \right) = \left(\begin{array}{c|ccc} & & & \\ \Phi^1 & \dots & \Phi^R & \\ & & & \end{array} \right) \left(\begin{array}{ccc} - & \Psi^1 & - \\ & \vdots & \\ - & \Psi^R & - \end{array} \right) = \Phi \Psi^T. \quad (6.6)$$

Here R denotes the number of components of the model; $\Phi \in \mathbb{R}^{Nd \times R}$ denotes the matrix with spatial components, and $\Psi \in \mathbb{R}^{M \times R}$ denotes the matrix with temporal components. The model (6.6) will be referred to as the low-rank model, since $\text{rank}(\mathbf{D}) \leq R$. The upper limit is achieved for R linearly independent components. A similar explicit low-rank factorization was recently proposed in the context of image reconstructions in [213], with the same motivations as mentioned above.

The number of parameters in the low-rank model is $|\mathbf{D}| = |\Phi| + |\Psi| = (Nd + M)R$. Analyses in the works [138, 217, 218] suggest that $R = 2$ is sufficient to accurately model respiratory motion. Hence, for the typical scenario considered above ($N \sim 10^6$, $M \sim 10^2$, $d = 3$), this implies

$$|\mathbf{D}| \sim 10^6, \quad (6.7)$$

which is two orders of magnitude lower than Equation 6.5 and makes the reconstructions more convenient in practice.

We follow a standard approach in non-rigid medical image registration [223] and represent both the spatial components Φ and the temporal components Ψ of the motion-fields in cubic B-spline bases. This results in representation coefficients α, β for respectively Φ and Ψ .

Regularization functional

The motion-field reconstruction problem in Equation 6.4 is typically ill-posed, and requires incorporation of a-priori knowledge of the motion-fields in terms of additional regularization terms. Since organs such as the liver, spleen and kidney consist of liquid filled tissue structures, they can be assumed incompressible and thus volume-preserving under motion [224]. This assumption can be incorporated into the reconstruction problem with the following regularization, based on the determinant of the Jacobian of the transformation corresponding to the motion-fields [225]:

$$\mathcal{R}(\mathbf{D}) := \sum_{t=1}^M \|\mathbf{W}(\mathcal{J}(\mathbf{D}_t) - \mathbf{1})\|_2^2. \quad (6.8)$$

Here $\mathcal{J}(\cdot)$ computes the determinant of the Jacobian, and \mathbf{W} is a diagonal matrix with weights per voxel. The weights are added to exclude regions where the regularization is less realistic, e.g. in the lungs. As weights we have taken the magnitude of the reference image, scaled to unit norm. For the implementation of this regularization term we follow the approach in [225], and compute spatial derivatives analytically using the spline parameterization of the motion-fields.

Final reconstruction problem formulation

Substituting the spline representation, low-rank model (6.6) and regularization (6.8) into the objective function (6.4) results in the following minimization problem to reconstruct space-time motion-fields:

$$\{\alpha^\dagger, \beta^\dagger\} = \underset{\Phi \Psi^T = [\mathbf{D}_1, \dots, \mathbf{D}_M]}{\operatorname{argmin}} \sum_{t=1}^M \|\mathbf{F}(\mathbf{D}_t) - \mathbf{s}_t\|_2^2 + \lambda_R \sum_{t=1}^M \|\mathbf{W}(\mathcal{J}(\mathbf{D}_t) - \mathbf{1})\|_2^2, \quad (6.9)$$

where $\lambda_R \in \mathbb{R}^+$ is the regularization parameter that balances the terms. Note that no temporal regularization is added, since the low-rank model already acts as a strong regularization in both space and time.

6.3 Methods

Experiments overview

The following data were acquired in three different experiments per volunteer for two volunteers:

1. 2D+t abdominothoracic data;
2. 3D+t abdominothoracic data;
3. 3D+t head-and-neck data.

The 2D+t abdominothoracic data allows for a validation against time-resolved image reconstruction at a high temporal resolution. The 3D+t abdominothoracic data is the targeted case for the application in MR-guided radiotherapy. The 3D+t head-and-neck data is included as a demonstration to handle different types of motion, and for additional validation. All reconstructions are analyzed by comparison with image reconstructions on the same data. The Jacobian determinant of the transformation corresponding to the motion-fields is analyzed as an additional sanity check: $\mathbf{x}_0 \mapsto \mathbf{x}_0 + \mathbf{d}_t(\mathbf{x}_0)$. More details regarding the experiments is provided below, organized per subsection.

Data acquisition

All data were acquired on a 1.5T MRI scanner (Ingenia, Philips Healthcare, Best, the Netherlands) using a steady-state spoiled gradient echo sequence (SPGR) with anterior and posterior receive arrays. As readouts we employed golden-angle radial for 2D [131], and golden-mean kooshball radial for 3D [71]. The volunteers provided written informed consent prior to the scans, and all scans were approved by the institutional review board of the University Medical Center Utrecht and carried out in accordance with the relevant guidelines and regulations. See Table 6.1 for other relevant acquisition parameters.

Reconstruction details

We followed the approach outlined in section 6.2.2, and reconstructed motion-fields from multi-coil k-space data acquired during motion by solving the minimization problem (6.9). The low-rank MR-MOTUS workflow is schematically summarized in 6.1. The reconstruction problem (6.9) was solved with L-BFGS [226], using the MATLAB implementation from [227]. The L-BFGS memory parameter was set to 20 and sampling density compensation [228, 229] was applied to improve the conditioning of the reconstruction. The multi-coil data was compressed to a single channel prior to all reconstructions, see Supporting Information Section 1 for more details. The regularization parameter λ_R was chosen according to $\lambda_R \sim 1/M$ and the data \mathbf{s}_t were scaled by the norm of the density-compensated k-space data in order to obtain consistent values between experiments. The reconstruction parameters were determined with a heuristic parameter search (see Supporting Information Section 3). We refer to Table 6.1 for all parameter settings and to Supporting Information Section 4 and the Supporting Information in [80] for more implementation details.

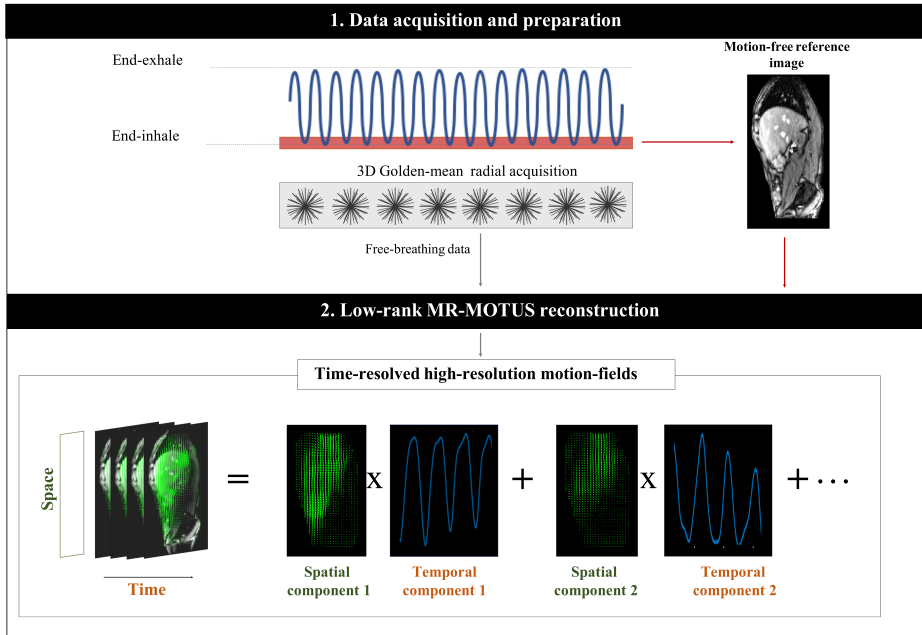


Figure 6.1: Overview of the low-rank MR-MOTUS framework. First, data is acquired during free-breathing with a golden-ratio radial trajectory (2D: golden-angle radial [131], 3D: golden-mean radial kooshball [71]). Then, DC-based phase-binning is performed on end-inhale to reconstruct a motion-free reference image. Finally, the reference image and free-breathing data are fed into the low-rank MR-MOTUS reconstructions, resulting in time-resolved 3D motion-fields. The motion-fields are reconstructed with an explicit constraint on the maximum rank. That is, as a sum of component motion-fields with each a different temporal behavior. The number of such components is pre-determined.

6.3.1 Experiment 1: 2D+t *in-vivo* respiratory motion reconstructions from abdominothoracic data

In the first experiment, a reference image and motion-fields were reconstructed from the same 2D+t data acquired during 20 seconds of free-breathing. The reference image was reconstructed from the end-inhale bin after phase-binning based on the self-navigation signal of $\mathbf{k} = 0$ values per readout (denoted as k_0 -values), see Supporting Information Section 2 for more details. The motion-fields were reconstructed at 40.8 Hz, i.e. 24.5 ms/frame, by assigning every 5 consecutive non-overlapping spokes to one dynamic. The low-rank model (6.6) was employed with $R = 3$, yielding motion-fields with rank ≤ 3 . Additional relevant reconstruction and acquisition parameters can be found in Table 6.1.

The motion-fields were analyzed by comparison with a time-resolved compressed sensing 2D+t reconstruction (CS2Dt) on the same free-breathing data, and by means of the Jacobian determinant. For the comparison with CS2Dt, the MR-MOTUS reference image was warped with the reconstructed motion-fields to obtain a dynamic image sequence as follows. First, the motion-fields are interpolated to the same spatial resolution as the image reconstruction using cubic interpola-

Acquisition details

Parameter	2D resp. motion	3D resp. motion	3D head-and-neck motion
FOV [m]	$0.50 \times 0.50 \times 0.01$	$0.44 \times 0.44 \times 0.44$	$0.38 \times 0.38 \times 0.38$
Acquisition matrix size	$164 \times 164 \times 1$	$146 \times 146 \times 146$	$126 \times 126 \times 126$
Spatial acq. resolution [mm]	$3.00 \times 3.00 \times 10.00$	$3.00 \times 3.00 \times 3.00$	$3.00 \times 3.00 \times 3.00$
Repetition time [ms]	4.90	4.40	5.40
Echo time [ms]	2.30	1.80	2.30
Flip angle [°]	20	20	20
Bandwidth [Hz]	298.72	541.48	284.73
Trajectory	2D golden-angle radial	3D golden-mean radial kooshball	3D golden-mean radial kooshball
Pulse sequence	2D SPGR	3D SPGR	3D SPGR
Coils (#Channels)	Anterior + Posterior (24)	Anterior + Posterior (24)	Anterior + Posterior (24)
Scanner	Philips Ingenia 1.5T	Philips Ingenia 1.5T	Philips Ingenia 1.5T

Reconstruction details

Parameter	2D resp. motion	3D resp. motion	3D head-and-neck motion
Motion model components	$R = 3$	$R = 3$	$R = 6$
Reference image resolution [mm]	$6.70 \times 6.70 \times 10.00$	$6.70 \times 6.70 \times 6.70$	$9.05 \times 9.05 \times 9.05$
Regularization parameter	$\lambda_R = 1.5 \cdot 10^1$	$\lambda_R = 1.5 \cdot 10^1$	$\lambda_R = 1.4 \cdot 10^3$
Number of iterations	50	50	300
Splines per spatial dimension	18	16	3
Splines in time	1.28 / second	8.25 / second	5 / second
Temporal motion resolution	40.8 Hz: 5 spokes / dynamic	7.6 Hz: 30 spokes / dynamic	9.3 Hz: 20 spokes / dynamic
Reconstructed motion duration [s]	20	33	40
Reconstruction time	4 minutes	50 minutes	2 hours

Table 6.1: Details of the *in-vivo* experiments as described in section 6.3.1-section 6.3.3: the top half lists acquisition details, and the bottom half lists reconstruction details for the time-resolved experiments. For the respiratory-resolved reconstruction in section 6.3.2 the same parameters were used as listed in the ‘3D resp. motion’ column, but effectively resulted in a temporal motion resolution of about 5Hz, with 18062 spokes per dynamic, due to the sorting.

tion. Second, the forward model (6.2) was evaluated on a Cartesian k-space grid using the reconstructed motion-fields \mathbf{D}_t . Finally, an inverse Fourier transform was performed to obtain one image per dynamic. The CS2Dt was reconstructed at a temporal resolution of 122.5 ms/frame by assigning every 25 consecutive non-overlapping spokes to one dynamic, and was performed with the BART toolbox [183] using spatial L_1 -wavelet and temporal total variation regularization. The temporal resolution of the CS2Dt was chosen as an integer multiple of the MR-MOTUS resolution to allow comparison at the coarser CS2Dt temporal resolution. The comparison was performed by means of the relative error norm (REN). The REN between vectors \mathbf{a}, \mathbf{b} was defined as $\text{REN}(\mathbf{a}, \mathbf{b}) = \frac{\|\mathbf{a} - \mathbf{b}\|}{\|\mathbf{b}\|}$.

6.3.2 Experiment 2: 3D+t *in-vivo* respiratory motion reconstructions from abdominothoracic data

In the second experiment we considered the targeted case for MR-guided radiotherapy: a reference image and motion-fields were reconstructed from 3D+t data acquired during 33 seconds of free-breathing. The targeted high temporal resolution does not allow for a straightforward validation by comparison with dynamic 3D image reconstruction. For validation purposes, we therefore compared MR-MOTUS with respiratory-resolved image reconstruction by performing both reconstructions on respiratory-sorted data.

Finally, we performed 3D+t time-resolved motion reconstruction to demonstrate the ability to reconstruct motion at high temporal resolution from time-resolved k-space data. The reference image for both reconstructions was reconstructed from

the end-inhale bin after phase-binning based on the k_0 -value per readout (see Supporting Information Section 2), and the low-rank model (6.6) was employed with $R = 3$. See Table 6.1 for all reconstruction and acquisition parameters.

For the respiratory-resolved reconstructions phase-binning was performed in 20 equal-sized bins based on the k_0 -value per readout. The images were independently reconstructed for each bin using 28 iterations of CG-SENSE [229]. The motion-fields were reconstructed over all bins simultaneously with low-rank MR-MOTUS by solving Equation 6.9 with 20 dynamics. The quality of the MR-MOTUS reconstruction was assessed by means of the Jacobian determinant and by comparison with the respiratory-resolved image reconstruction. For the latter, a reference image was warped with the reconstructed motion-fields to obtain a dynamic image sequence, as described in subsection 6.3.1, and the two image sequences were compared in terms of REN. The reference image that was warped using the MR-MOTUS motion-fields was selected as the end-inhale phase of the respiratory-resolved image reconstruction (motion state #10) in order to reduce effects of image intensity, image quality, or contrast differences on the comparison of the two image sequences.

For the time-resolved 3D+t reconstructions, motion-fields were reconstructed at 7.6 Hz, i.e. 132 ms/frame, by assigning every 30 consecutive non-overlapping spokes to one dynamic. The reconstructions were analyzed by means of the Jacobian determinant and the average motion of the kidney was compared between the time-resolved and respiratory-resolved MR-MOTUS reconstructions. This motion was computed as the mean of the displacements over a manually segmented mask of the right kidney. For comparison between respiratory-resolved and time-resolved, the motion magnitudes of each respiratory bin in the respiratory-resolved reconstruction were assigned to the original, time-resolved, spoke indices that were sorted into that particular bin.

6.3.3 Experiment 3: 3D+t *in-vivo* head-and-neck motion reconstructions

With the third experiment, 3D+t motion-fields were reconstructed from data acquired during head-and-neck motion. The subject was instructed to hold still in position 1 during the first 70 seconds of the acquisition, then move to position 2 and hold still for 70 seconds, then move freely for 40 seconds, and finally hold still afterwards in position 3 for 70 seconds. Data acquired in position 1 was used to reconstruct a reference image, data acquired during movement from position 2 to position 3 was used to reconstruct motion-fields, and position 2 and 3 were used as fully-sampled "checkpoints" to serve as validation; the beginning and end of the dynamic motion reconstruction should respectively coincide with positions 2 and 3. To verify this, the reference was warped with the reconstructed motion-fields as described in section 6.3.1, and the first and last dynamic of the resulting image sequence were visually compared with the fully-sampled checkpoints. As a second analysis, the mean and standard deviation of the determinant of the Jacobian were computed for all dynamics, over all voxels within the body. The latter were determined by a threshold on the magnitude of the signal per voxel.

The low-rank motion model was employed with $R = 6$ to accommodate the head-and-neck motion which includes rotations in multiple planes. The motion-fields were reconstructed at a temporal resolution of 9.3 Hz, i.e. 108 ms/frame, by assigning every 20 consecutive non-overlapping spokes to one dynamic. Additional reconstruction and acquisition parameters can be found in Table 6.1.

6.4 Results

6.4.1 Experiment 1: 2D *in-vivo* respiratory motion reconstructions from abdominothoracic data

The time-resolved 2D respiratory motion was reconstructed with 40.8 motion-fields-per second. The Jacobian determinant and the comparison with CS2Dt is shown in Figure 6.2. The visual comparison with 2D+t compressed sensing image reconstruction corresponding to 6.2B is shown in 6.9. It can be observed that good agreement is obtained for most phases of the respiratory cycle, with a small mismatch in end-exhale in the upper back near the spine-liver interface. The Jacobian determinants show small deviations from unity within the organs (green), and compression in the lungs (blue) except for the arteries. The qualitative results are supported by the quantitative results in 6.2B, which show that the warped MR-MOTUS images considerably reduce the REN.

The warped reference images corresponding to the reconstructed motion-field, overlaid with the motion-field are shown in 6.10 and 6.11. Moreover, these show the decomposition in the reconstructed low-rank components. For volunteer 1, the first two components show pseudo-periodic temporal behaviours, and the first is most prominent in magnitude. Both components show realistic movement of organs such as the liver and kidney, but also small unrealistic motion in the spine near the liver in end-exhale. Interestingly, the third component shows a temporal behavior with a slight drift upwards, and the corresponding spatial motion-field indicates a global rotation. Similar movement can also be observed in the ground-truth CS2Dt reconstruction in 6.9. This movement could be caused by relaxation of the gluteus maximus muscle in the upper leg and buttocks. Similar motion patterns can be observed in 6.11 for volunteer 2, but the global rotation is less pronounced in the ground-truth CS2Dt reconstruction.

6.4.2 Experiment 2: 3D *in-vivo* respiratory motion reconstructions from abdomen/thorax data

The comparison between MR-MOTUS and respiratory-resolved image reconstruction is shown in 6.3, 6.4, 6.15 and 6.12. It can be observed that good visual agreement is obtained between the two reconstructions for both volunteers. This is especially visible from the position of the top of the liver dome. The Jacobian determinants of the reconstructed motion-fields are shown in 6.4A. The lungs show compression (blue), except for the arteries, and small deviations from unity can be observed in the rest of the body. Deviation from unity can be observed at the spine-liver interface, where a large volumetric compression is reconstructed. We

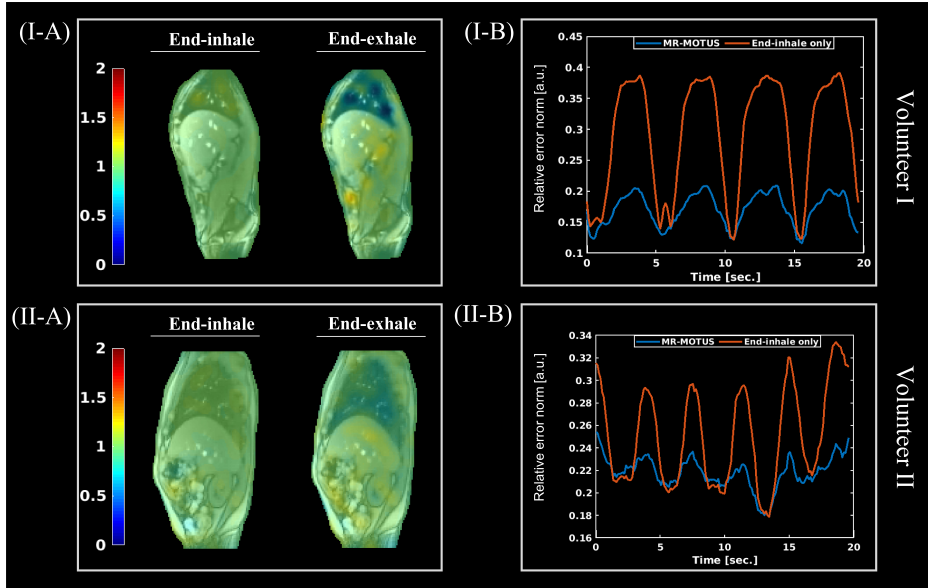


Figure 6.2: A) Jacobian determinants of the reconstructed motion-fields in end-inhale (left) and end-exhale (right). The first end-exhale and second end-inhale positions were selected from all dynamics for this visualization. B) Relative error norm (REN) between MR-MOTUS warped reference images and CS2Dt reconstruction over all dynamics (blue), and a baseline REN between the fixed MR-MOTUS end-exhale warped reference image and CS2Dt. The top row (I) shows the results for volunteer 1, whereas the bottom row (II) shows the results for volunteer 2. The comparison is also visualized in 6.9, and the reconstructed motion-fields decomposed in the low-rank model components are visualized in 6.10 and 6.11.

expect this is related to the attachment of liver tissue to the spine during exhalation. The quantitative comparison in 6.4B shows best agreement at motion state 10 (inhale) and worst agreement in motion state 19 (exhale). The sharp peak at motion state 10 can be explained by the fact that we took motion state 10 as the reference image to compute the warped reference images for MR-MOTUS. The warped reference images reconstructed from the respiratory-sorted data, overlaid with the motion-field, are visualized for both volunteers in 6.13 and 6.14. Moreover, these show the decomposition in the reconstructed low-rank components. For both volunteers the first component shows a pseudo-periodic behavior in time and is most prominent in magnitude; the other components make only minor contributions. These large contributions of pseudo-periodic components could be due to the periodicity assumption underlying the respiratory-sorting. Small unrealistic motion can be observed for volunteer 1 at the spine-liver interface and at the back of the spine, similar to the 2D reconstructions. Additionally, a small rotating motion can be observed in the motion-field for volunteer 1 at the interface with the rib cage in the coronal slice on the bottom right. We expect the latter is caused by a combination of the volume-preserving regularization and the inability of the motion model to resolve the sliding motion that is present in this area.

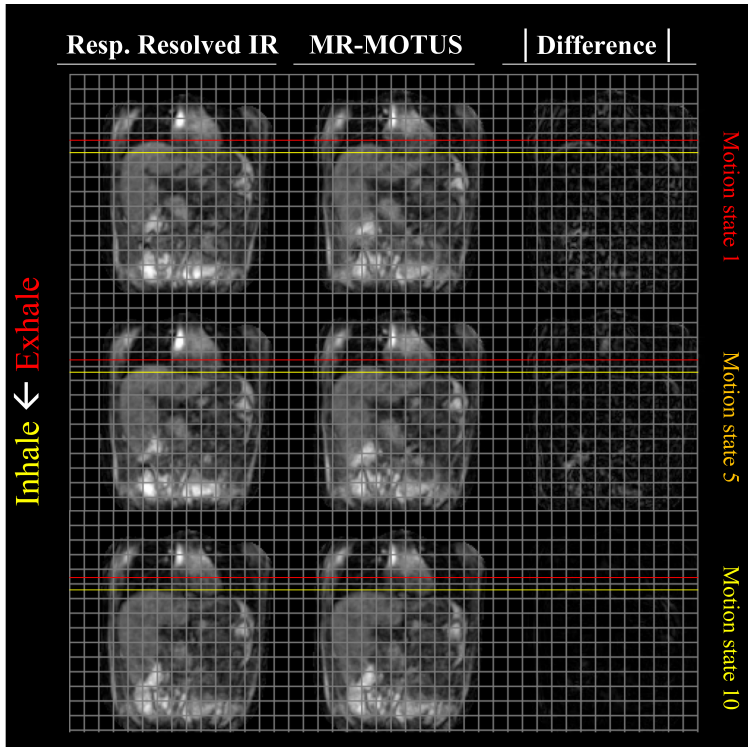


Figure 6.3: Respiratory-resolved image reconstruction (Resp. Resolved IR, left), MR-MOTUS warped reference image (middle), and pixel-wise absolute difference between the two reconstructions (right), as mentioned in section 6.3.2 and section 6.4.2. The red and yellow horizontal lines indicated respectively end-exhale and end-inhale positions. A video corresponding to this figure of volunteer 1 is provided in 6.15. A similar video for volunteer 2 is provided in 6.12.

The time-resolved 3D respiratory motion was reconstructed with 7.6 motion-fields-per-second. The warped reference images reconstructed from the time-resolved data, overlaid with the motion-field, are visualized for both volunteers in 6.16 and 6.17. Similar motion is obtained as with the respiratory-sorted data, but the reconstructed motion components are now similar in magnitude. All components show pseudo-periodic temporal behavior, and the first component of volunteer 1 indicates a small drift. Similar to the respiratory-resolved reconstructions, small unrealistic motion at the spine-liver interface and anterior side of the spine can be observed for volunteer 1. Additionally, the same small rotation can be observed near the rib cage in the bottom right of the coronal slice. The Jacobian determinants of the reconstructed motion-fields are shown in 6.5. Similar patterns can be observed in end-exhale as for the respiratory-resolved motion reconstructions. Interestingly, the end-inhale image for volunteer 1 shows a small expansion in the lungs, possibly indicating that a deeper inhale than the reference image was reconstructed while the reference image was obtained using respiratory-sorting on end-inhale. Finally, the comparison between the average kidney motion in the time-resolved and respiratory-resolved MR-MOTUS recon-

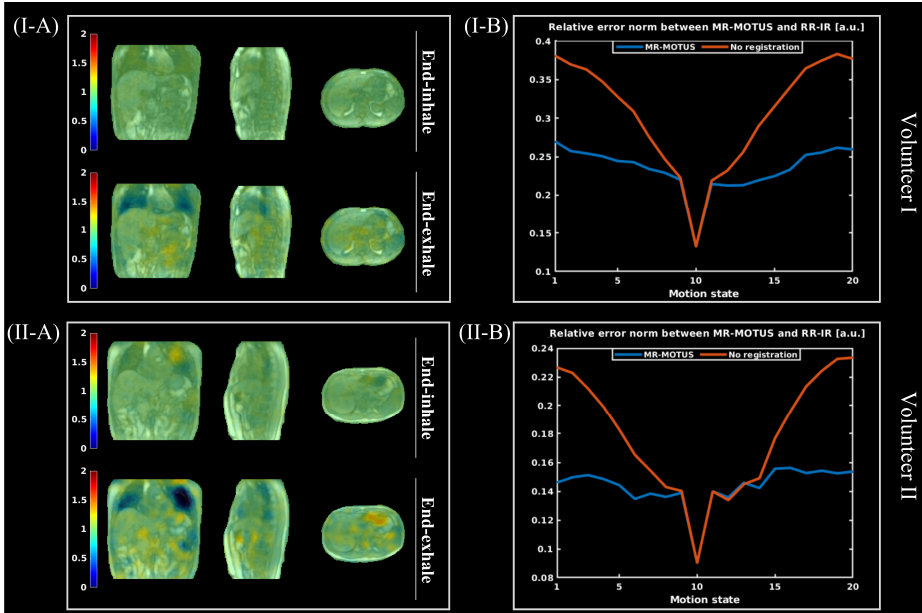


Figure 6.4: A) Jacobian determinants of the reconstructed respiratory-resolved motion-fields in end-inhale (top) and end-exhale (bottom). The first end-exhale and second end-inhale positions were selected from all dynamics for this visualization. B) Relative error norm (REN) with respiratory-resolved image reconstruction (RR-IR) for every motion state. The blue graph indicates the REN between MR-MOTUS and respiratory-resolved image reconstruction. The orange graph indicates a baseline comparison between the (fixed) end-inhale image of the MR-MOTUS reconstruction and the (dynamic) respiratory-resolved image reconstruction. The sharp peak is caused by taking the 10th dynamic as the reference image for this comparison. The top row shows the results for volunteer 1, and the bottom row shows the results for volunteer 2. Videos corresponding to the comparisons in (B) are provided in 6.15 and 6.12.

structions is visualized in 6.6. The phase of the reconstructions are most similar in feet-head (FH) and anterior-posterior (AP), while in left-right (LR) different patterns can be observed. However, it should be noted that the motion in FH and AP is two orders of magnitude higher than in LR. The motion magnitude is similar for both reconstructions, but the respiratory-resolved reconstruction shows a constant amplitude over time since it only reconstructs an average breathing cycle. The time-resolved reconstruction shows changing motion amplitudes over time. The phase difference between the two reconstructions may be explained by imperfect respiratory-sorting.

6.4.3 Experiment 3: 3D *in-vivo* head-and-neck motion reconstructions

The time-resolved 3D head-and-neck motion was reconstructed with 9.3 motion-fields-per-second. The MR-MOTUS warped reference images from 3D data acquired during head-and-neck motion are visualized for both volunteers in 6.18 and 6.19. Clearly, rigid motion-fields are reconstructed within the skull, and

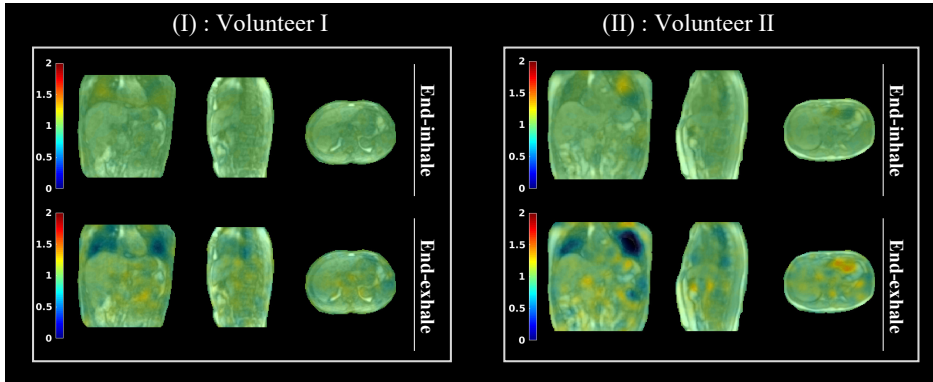


Figure 6.5: Jacobian determinants of the reconstructed time-resolved motion-fields in end-inhale (top) and end-exhale (bottom). The left figure shows the results for volunteer 1 and the right figure the results for volunteer 2. Videos corresponding to the reconstructions in this figure are provided in 6.16 and 6.17.

non-rigid motion-fields at the neck. 6.7 shows the Jacobian determinants of the reconstructed motion-field over time (A), and the reconstructed temporal components (B) for both volunteers. The Jacobian determinant is close to 1 over the whole reconstructed time, with slightly more deviations for volunteer 1. These can be attributed to larger and more irregular motion than volunteer 2. The temporal components are relatively flat at the start and the end, corresponding to the static begin and end positions. The more extreme motion of volunteer 1 can also be observed from the larger magnitudes of the temporal components and from 6.18. 6.8 shows the checkpoint validation for volunteer 2. It can be observed that good agreement is obtained between the fully-sampled checkpoint images and the MR-MOTUS reconstructions.

6.5 Discussion

We have previously introduced MR-MOTUS [80], a framework to estimate motion directly from minimal k-space data and a reference image by exploiting spatial correlation in internal body motion. In this work, we introduce low-rank MR-MOTUS: an extension of MR-MOTUS from 3D to 3D+t reconstructions in a realistic experimental setting, where both reference image and motion-fields are reconstructed from data acquired during free-breathing. Low-rank MR-MOTUS employs a low-rank motion model that constrains the degrees of freedom in space and time, thereby reducing memory consumption and functioning as a regularization in both space and time. It was demonstrated that the proposed method can reconstruct high quality whole-body 3D motion-fields with a temporal resolution of more than 7.6 motion-fields-per-second, while showing consistency with static, respiratory-resolved and time-resolved image reconstructions. Prospectively undersampled data were acquired with a non-Cartesian trajectory and multi-channel receivers, thereby bridging the gap towards clinical application.

The ability of the proposed framework to estimate time-resolved rather than

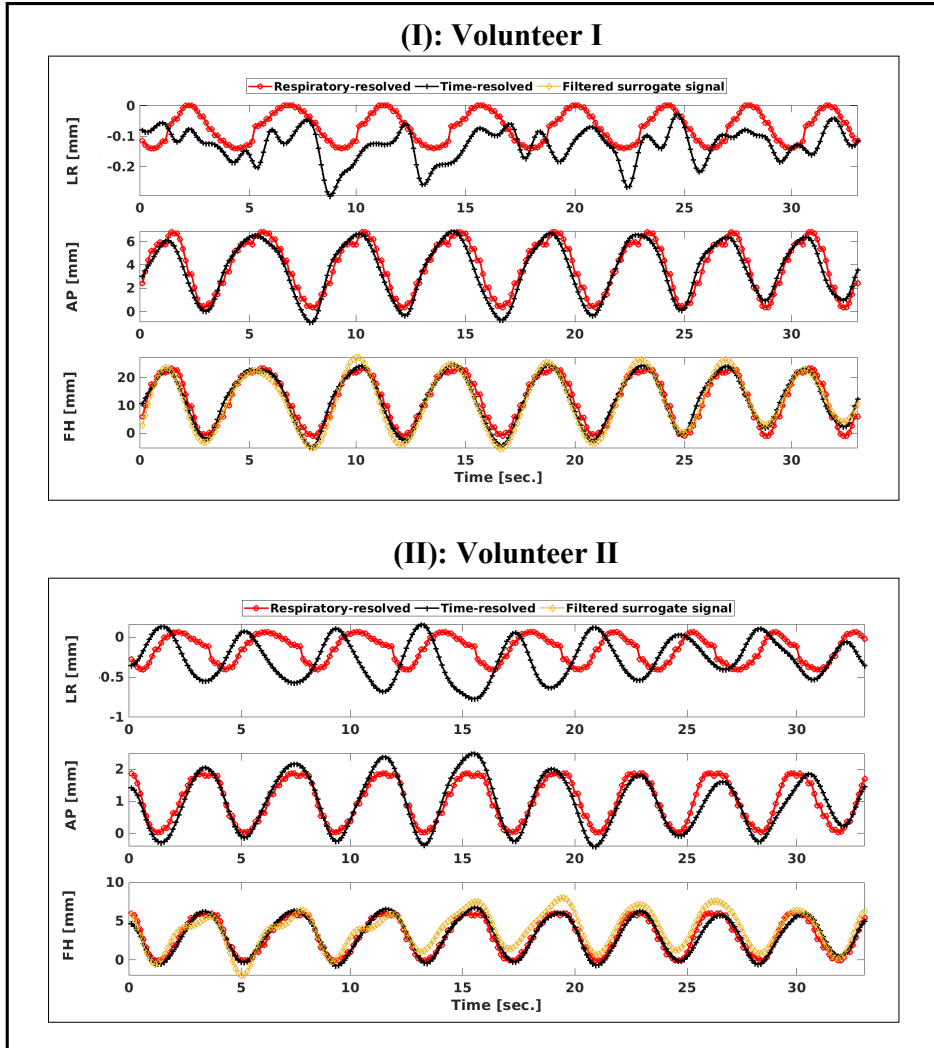


Figure 6.6: This figure shows the average motion of the right kidney over time, for both the respiratory-resolved and the time-resolved MR-MOTUS reconstructions mentioned in section 6.3.2 and section 6.4.2. The respiratory-resolved MR-MOTUS reconstruction was projected back on the time axis, as described in section 6.3.2 and section 6.4.2. The average motion magnitudes were computed over a manually segmented mask of the right kidney. Videos of reconstructions corresponding to these figures are provided in 6.16 and 6.17.

respiratory-resolved motion is promising as it allows to characterize drifts and intra and inter-cycle breathing patterns. This is in contrast with respiratory-resolved methods that require sorting to obtain suitable images [138, 160, 171, 181, 199–201, 230, 231]. The sorting effectively results in (a motion model for) average breathing motion, which may have trouble capturing drifts and inter-cycle variations. Some works have been proposed to reconstruct time-resolved MR-images without the need of retrospective sorting. However, the reported

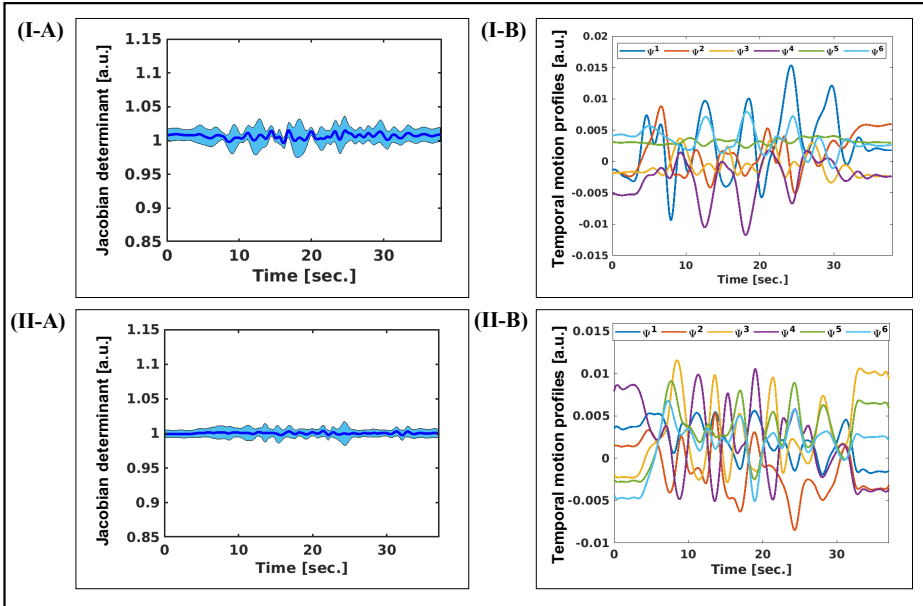


Figure 6.7: This figure corresponds to the head-and-neck reconstructions in section 6.3.3 and section 6.4.3. A) The mean (solid line) and standard deviation (shaded area) of the Jacobian determinants of the reconstructed motion-fields over time. B) The reconstructed temporal profiles Ψ^i , scaled by the norm of the corresponding Φ^i to be able to compare their magnitudes. The top row and bottom rows respectively show the results for volunteer 1 and 2. Videos corresponding to the reconstructions in these figures are provided in 6.18 and 6.19.

temporal resolution was too low [212–214], or the FOV was too small [215, 216]. The time-resolved motion estimation of low-rank MR-MOTUS in combination with an MR-LINAC can be particularly beneficial for MR-guided radiotherapy; the (retrospective) reconstruction of 3D+t time-resolved tumor and organs-at-risk motion during treatment can be used for accurate dose accumulation [220], allowing for an accurate assessment of the treatments.

The resulting motion model explicitly separates a high-dimensional static spatial component from a low-dimensional dynamic temporal component. The low-dimensional compression of the dynamic behavior could be exploited to reduce the number of parameters and reconstruction times of future real-time reconstructions, analogously to recently proposed approaches in [138, 208, 232, 233]. Our method could thereby form the basis for future work on real-time MR-based motion estimation, where reconstructions are performed on-the-fly to track tumor and organs-at-risk motion.

Low-rank models in the context of motion estimation have been investigated before in several works, most of which retrospectively perform compression to a low-rank model using principal component analysis [138, 217, 219, 220]. Others decouple the motion-fields into spatial components and temporal components based on surrogate signals [207, 208, 221]. The approach in this work is different in the sense that it explicitly and a-priori enforces a structure that yields low-

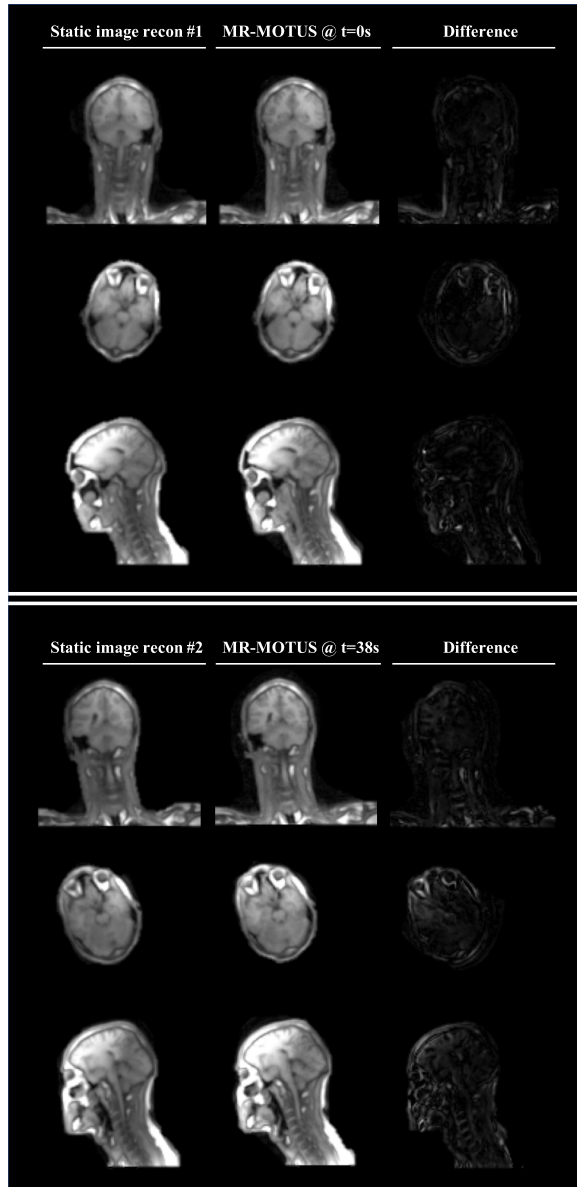


Figure 6.8: This figure shows the checkpoint validation for the head-and-neck reconstructions of volunteer 2, as mentioned in section 6.3.3 and section 6.4.3. The left columns shows the fully-sampled checkpoint image, the middle column shows the MR-MOTUS warped reference images and the right column shows the absolute pixel-wise difference. The top part corresponds to the comparison with the checkpoint acquired right before the start of the motion, and the bottom part corresponds to the checkpoint acquired right after the start of the motion. A video corresponding to this figure is provided in 6.19. A similar video for volunteer 1 is provided in 6.18.

rank motion-fields, and does not assume dependence on surrogate signals for the motion model. Similar approaches have been studied in the context of image reconstruction [213, 215, 234–238].

This work includes some limitations and assumptions that should be addressed. Both the respiratory-resolved and time-resolved 3D respiratory motion reconstructions in section 6.3.2 and section 6.4.2 look realistic in general. Yet, small unrealistic motion is reconstructed near discontinuities in the true motion-fields that are present near sliding or attaching/detaching organ surfaces. This can be observed in for example 6.10, at the spine/liver interface in end-exhale; the increase in compression due to the attaching tissue is compensated by unrealistic movement in the spine. This could possibly be resolved with region-specific [239] or non-parametric motion models [240], but is beyond the scope of this work.

Another point of improvement is the compression of multi-channel data to a single channel (Supporting Information Section 1). Contrary to standard coil compression techniques, the aim of the compression in this work is homogeneous coil sensitivity. Consequently, this compression is suboptimal in terms of SNR [147, 241]. 6.20 analyzes the loss between between a Roemer coil combination [147] and the proposed coil compression on the 2D data. This shows an SNR loss factor between 1.5 and 2.5 in most of the body, which increases towards the boundary of the body. Good results were obtained with the coil compression introduced in this work, but more advanced techniques could possibly be used to improve the SNR after the compression.

The last point of improvement is the validation of time-resolved 3D motion-fields. In general this is not straightforward, and we considered three viable options for this: (1) *in-silico* with a digital phantom, (2) with an MR-compatible motion phantom, and (3) *in-vivo* with respiratory-resolved image reconstruction. We have opted for the third option, since this was considered the closest to a practical use-case. The *in-silico* validation does not consider real acquisition-related data corruption (e.g. eddy currents, flow effects), and can, in case of e.g. the XCAT phantom [151], yield unstable motion-fields [242]. MR-compatible motion phantoms, although useful for proof-of-principle validations, have limitations regarding the representation of realistic *in-vivo* anatomies.

The intended application of MR-MOTUS is MR-guided radiotherapy, possibly in real-time. However, the current reconstruction times in MATLAB on a desktop workstation are around 4 minutes for 2D+t with 40 motion-fields/second, around 6 minutes for the respiratory-resolved 3D reconstruction, and around 50 minutes for 3D+t time-resolved respiratory motion with 7.6 motion-fields/second. Hence, the current implementation of the method is not directly applicable for real-time processing, but reconstruction times may be reduced with a different programming language, improved hardware, GPU-accelerations or deep learning.

6.6 Conclusion

We have introduced low-rank MR-MOTUS, an extension of MR-MOTUS, that allows to retrospectively reconstruct whole-body time-resolved 3D+t motion-fields

from prospectively undersampled k-space data and one reference image. Reconstructions were performed for 2D/3D respiratory motion and 3D head-and-neck motion. A temporal resolution of more than 7.8 motion-fields-per-second was obtained, and the motion-fields were consistent with image reconstructions. For MR-guided radiotherapy, the time-resolved 3D motion-fields could be used to reconstruct the respiratory-motion-compensated accumulated dose during the treatment. Furthermore, the explicit decomposition of motion-fields in static and dynamic components could form the basis for future work towards real-time MR-guided radiotherapy.

Acknowledgments

This work was supported in part by the Dutch Research Council (NWO) under Grant 15115.

It is not knowledge, but the act of learning, not possession but the act of getting there, which grants the greatest enjoyment.

- Carl Friedrich Gauss

Magnetic Resonance Fingerprinting on a 1.5T MRI-Linac

Bruijnen, Tom
van der Heide, Oscar
Intven, Martijn P.W.
Mook, Stella
Legendijk, Jan J.W.
van den Berg, Cornelis A.T.
Tijssen, Rob H.N.

The following chapter is based on:

Technical feasibility of Magnetic Resonance Fingerprinting on a 1.5T MRI-Linac, 2020, *Physics in Medicine and Biology*65(22)

Abstract

Hybrid MRI-linac (**MRL**) systems enable daily multiparametric quantitative MRI to assess tumor response to radiotherapy. Magnetic Resonance Fingerprinting (**MRF**) may provide time efficient means of rapid multiparametric quantitative MRI. The accuracy of MRF, however, relies on adequate control over system imperfections, such as eddy currents and B_1^+ , which are different and not as well established on MRL systems compared to diagnostic systems. In this study we investigate the technical feasibility of gradient spoiled 2D MRF on a 1.5T MRL. We show with phantom experiments that the MRL generates reliable MRF signals that are temporally stable during the day and have good agreement with spin-echo reference measurements. Subsequent *in-vivo* MRF scans in healthy volunteers and a patient with a colorectal liver metastasis showed good image quality, where the quantitative values of selected organs corresponded with the values reported in literature. Therefore we conclude that gradient spoiled 2D MRF is feasible on a 1.5T MRL with similar performance as on a diagnostic system. The precision and accuracy of the parametric maps are sufficient for further investigation of the clinical utility of MRF for online quantitatively MRI-guided radiotherapy.

Keywords: Radiotherapy, Magnetic Resonance Fingerprinting, MRI-Linac, Tumor response monitoring

7.1 Introduction

One of the promises of magnetic resonance guided radiation therapy on hybrid MRI-linac (MRL) systems [38, 40, 135, 136] is the ability to assess tumor response on a daily basis. The daily response is currently assessed using anatomical imaging, but could be replaced with precise quantitative imaging techniques [55, 243, 244]. Traditional quantitative imaging techniques based on steady-state methods, such as variable flip angle (T_1 -mapping) [245] or multi-echo spin echo (T_2 -mapping) [246], however, require long acquisition times. The long scan time poses a considerable practical challenge as the on table time is almost entirely filled with anatomical imaging (i.e., high-resolution 3D anatomical imaging for daily plan adaptation and fast real-time imaging for tumor tracking). Typical MRL treatment fractions have at most a couple of minutes of free imaging time available such that it does not interfere with the clinical workflow [43](Fig.1-A). Therefore, the dual requirement of both fast and precise measurements mandates a sequence with a high precision per unit of time, i.e. quantification efficiency, for a practical implementation of online quantitative MRI-guided radiotherapy. Recently, transient-state-based quantitative imaging methods have been proposed to considerably improve this quantification efficiency. Magnetic resonance fingerprinting (MRF) [112, 231, 247] is such a transient-state method that enables rapid multiparametric imaging and therefore could be the ideal tool for therapy monitoring on the MRL.

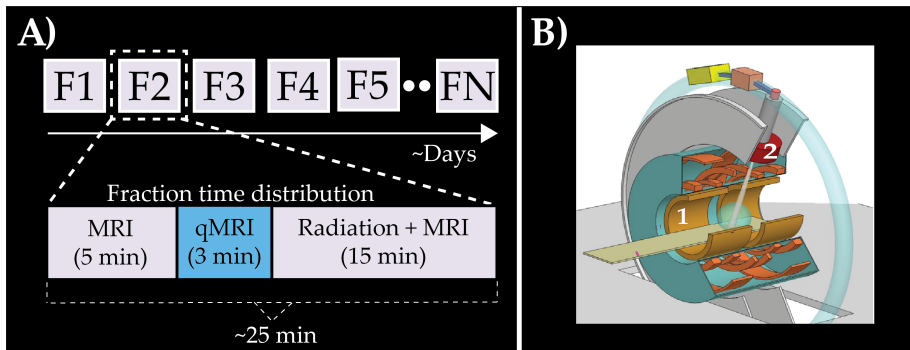


Figure 7.1: Schematic of a MRL radiotherapy treatment schedule. **A)** Example of a fractionation scheme where a patient is treated over multiple radiation fractions (F) distributed across multiple days. During each fraction, MR images are required for multiple purposes. During the first ≈ 5 minutes anatomical images are acquired for radiotherapy treatment planning. The treatment planning takes around 5 min (depending on plan complexity), which can be used for quantitative imaging. Finally the irradiation is started and requires continuous anatomical imaging for motion management. **B)** Impression of the MRL (Unity, Elekta) with the split gradient coil shown in yellow and the linear accelerator gun shown in red, as indicated with number 1 and 2 respectively.

Unlike steady-state methods, which aim to produce a constant MR signal over time, MRF deliberately creates a fluctuating signal (fingerprint) over the course of the acquisition, which is matched on a per voxel basis to a precomputed dictio-

nary of signal responses during image reconstruction. The dictionary is populated with simulated responses for all possible tissue types, in terms of T_1 , T_2 and proton density, to the imposed transient-state MR sequence. Realistic simulations of these MR sequences are essential to accurately quantify the tissue properties [248, 249]. Therefore, the simulation of the MR sequences requires adequate control over system imperfections such as eddy currents and heterogeneous magnetic fields (B_0 and B_1^+). These system imperfections are well characterised and controlled for diagnostic MR systems and MRF has been applied in multiple clinical studies [250–257]. However, these system imperfections are not yet accurately mapped in MRL systems. The 1.5T MRL system used in our institution (Unity, Elekta, Crawley, UK) differs from diagnostic systems in the split gradient and split magnet coil design, the radiolucent 2x4 channel receive coil and a paramagnetic rotating gantry that holds all the beam generating components (Fig.1-B). These hardware modifications have an impact on the system imperfections, such as reduced signal-to-noise ratio [56, 57], reduced uniformity of the static magnetic fields (B_1^+ and B_0) [49, 51], reduced spatial region of gradient linearity [50] and different behavior of the eddy currents [53]. The impact of these system imperfections on the accuracy and precision of MRF parameter quantification is unknown. Therefore, an experimental study on the precision and accuracy of MRF is crucial for the potential application of daily quantitative tumor response monitoring on a 1.5T MRL.

In this work we investigate the technical feasibility of 2D MRF in phantoms and *in-vivo* on a 1.5T MRL. We assess the accuracy, precision and temporal stability of the parameter quantification in a phantom. In addition, we showcase typical image quality of the parameter maps in comparison with clinically used qualitative scans in volunteers and patients.

7.2 Methods

7.2.1 MRF pulse sequence and reconstruction method

A 2D gradient spoiled MRF pulse sequence was implemented on a 1.5T Unity MR-linac equipped with a 2x4 channel radiation translucent receive array. The anterior coil was positioned 5 cm above the subject and the posterior coil was positioned 7 cm beneath the subject. More details on the radiation translucent coils are described by Hoogcarpsel et al. [56]. Imaging data were acquired using the MRF sequence described by Jiang et al. [247], which consists of an adiabatic inversion pulse and a sinusoidal flip angle train. The repetition time was constant along the flip angle train. One radial line was acquired per time-point [258] and subsequent readouts were azimuthally incremented using the tiny golden angle to minimize eddy current effects [121, 259] (Fig.2). The gantry angle of the linear accelerator was kept fixed across and during all the experiments (0 degrees). For each 2D slice active shimming was applied to correct for the first order spherical harmonics. K-space data and k-space trajectory were corrected using the zeroth and first

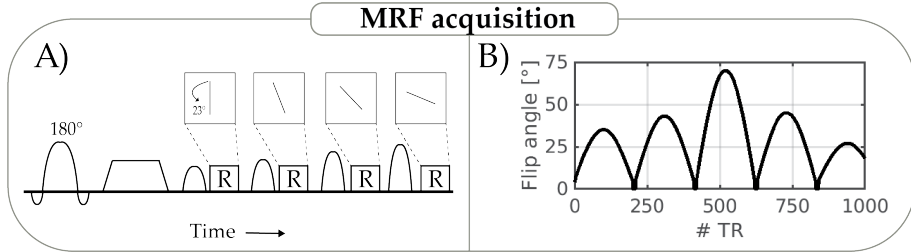


Figure 7.2: MRF acquisition overview. **A)** The MRF scan consists of an adiabatic inversion pulse followed 1000 radial readouts. The radial readouts are rotated with the tiny golden angle for each repetition time. **B)** The flip angle train used for all experiments. Note that the four flip angles shown in panel A) reflect the first four flip angles in the train.

order gradient impulse response functions [53, 76]. The impact of the gradient impulse response function correction on the MRF parameter maps is shown in Supporting Information I. Tissue fingerprints were simulated with extended phase graphs [190] with $T_1 \in [100 : 20 : 3000]$, $T_2 \in [20 : 10 : 1000]$ and inclusion of the slice profile [248]. All data were used to estimate the coil sensitivities using ESPiRiT [148]. MRF k-space data were reconstructed into singular value images with low rank inversion [260] using the BART toolbox [183]. The singular value images were subsequently matched with the dictionary to reconstruct the parametric maps. The code to perform the image reconstruction code and one MRF dataset are available on <https://github.com/tombrijnen/mrf-mrl>.

7.2.2 Phantom studies

MRF data were acquired in a 2D transverse slice of 14 gadolinium-doped gel tubes (TO5, Eurospin II test system, Scotland). Relevant sequence parameters for all scans are shown in Table.1. One fully sampled dataset was acquired, which consists of 276 repeated measurements of the MRF flip angle train, where for each measurement the azimuthal angle of the first spoke was rotated with the golden angle (111.2°). The measurements had a 10 second interval between repetitions to allow for full spin relaxation. Three and sixteen hours later MRF measurements were repeated with two minutes intervals for 30 minutes. Note that the fully sampled MRF scans were reconstructed with the maximum correlation method [112]. In total these scans provide 306 MRF measurements, which are used to estimate the precision, temporal stability and accuracy of the parameter quantification. The precision was quantified by calculating the standard deviation of parameter values within a tube. The temporal stability was quantified by calculating the standard deviation of the mean value within the tube over the repeated measurements. The accuracy was quantified by calculating the mean value within a tube and comparing it to reference measurements. The reference measurements were acquired using two separate inversion recovery (T_1) and spin-echo (T_2) scans. The reference data were acquired with single echo spin-echo measurements with: voxel size = $3 \times 3 \times 10 \text{ mm}^3$ scan time = 60 min, repetition time = 10 s and 10 inversion times $\in [100:3000]$ ms or 10 echo times $\in [20:500]$

ms.

7.2.3 *In-vivo* studies

This study was approved by the institutional review board of the UMC Utrecht (Medisch Ethische Toetsingscommissie Utrecht (METC), ID:17-010, "MRI protocol development for MR-linac") and informed consent was obtained from all the participants. MRF data were acquired in the brain and upper abdomen of a healthy volunteer. One patient with a recurrent colorectal liver metastasis, after hepatic surgery, was scanned using the described MRF sequence with the addition of an custom developed abdominal compression corset to reduce motion artefacts [152]. The complete MRI protocol consisted of multiple 2D MRF scans and qualitative T_1 and T_2 - w scans derived from the clinical protocol. The MRF scans in the upper abdomen were scanned in breathhold for the volunteer and in free-breathing for the patient. Regions of interest were manually selected on specific organs to compute the mean values, which were compared to literature values [261,262]. Relevant sequence parameters for all scans are shown in Table.1.

Table 7.1: Scanner and sequence parameters of the phantom and *in vivo* experiments.

MRF Sequence settings	MRF Sequence settings		
	Phantom	Brain	Abdomen
Field strength	1.5T	1.5T	1.5T
Spatial resolution	2.0 x 2.0 mm ²	1.5 x 1.5 mm ²	2.0 x 2.0 mm ²
Matrix size	125 x 125	186 x 186	175 x 175
Field-of-view	250 x 250 mm ²	280 x 280 mm ²	350 x 350 mm ²
Slick thickness	10 mm	5 mm	10 mm
Repetition time	5.2 ms	7.7 ms	5.3 ms
Echo time	2.5 ms	3.3 ms	2.5 ms
Readout bandwidth	386 Hz/pixel	285 Hz/pixel	379 Hz/pixel
N Flip angles	1000	1000	1000
Scan time	5.2 s	7.7 s	5.3 s

7.3 Results

7.3.1 Phantom studies

An exemplary time-point image of the fully sampled MRF scan along with the MRF proton density, T_1 and T_2 parameter maps are shown in Fig.3. The bottom row shows the raw time domain signal (fingerprint) of voxels in tube 1 and 11 along with the match to the dictionary. For both these voxels the time domain signal shows close agreement with the dictionary match. The agreement holds for all the pixels within the tubes with a mean normalized root mean square error (NRMSE) = 0.06. Small differences between the MRF signal and the dictionary

match are primarily observed during the first 50 snapshots directly after the inversion pulse and during the higher flip angles in time-points 500-600. The MRF reconstructions time was approximately 10 seconds per slice, which does not consider the pre-computation of the dictionaries.

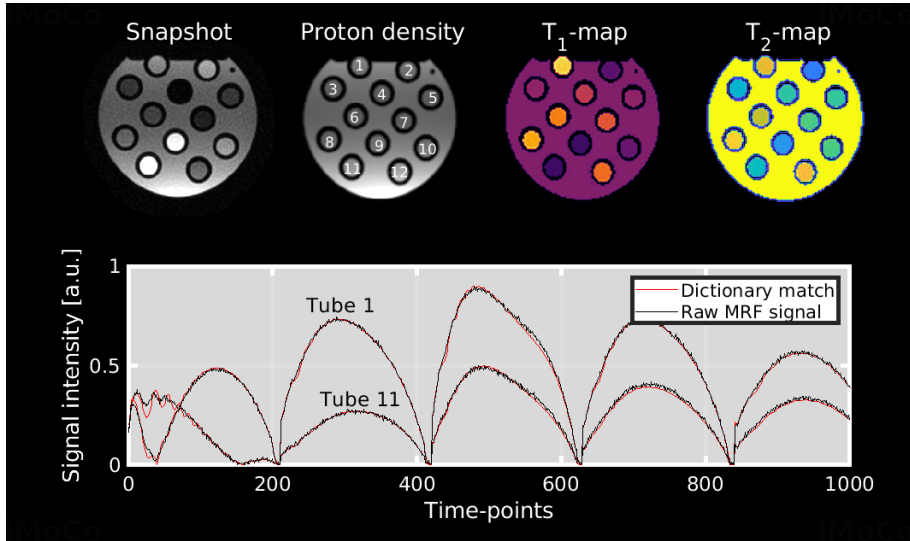


Figure 7.3: Analysis of the raw MRF time domain signal. Top row shows the images reconstructed from the fully sampled MRF measurements. From left-to-right a single time-point image(snapshot) and the reconstructed parameters maps. The bottom row shows the time domain signal of a voxel in tube 1 and a voxel in tube 11. Note that the time signals are in close agreement with the match to the dictionary. See the following link for an animated version: <https://surfdribe.surf.nl/files/index.php/s/KavixXHVaQ4c9Ue>

The parameter quantification of the fully sampled ($R=1$) and undersampled ($R=276$) MRF reconstructions are compared against the spin-echo reconstructions in Fig.4. Both the $R=1$ and $R=276$ MRF reconstructions showed good correlation in average values compared to the spin-echo measurements. The undersampled MRF has coefficients of determination $R_{T_1}^2 = 0.999$ and $R_{T_2}^2 = 0.975$ for T_1 and T_2 , respectively. Note that the accuracy of the T_1 -maps was slightly higher than the T_2 -maps. The precision over all the tubes for the undersampled MRF was $\sigma_{T_1} = 8.6$ ms and $\sigma_{T_2} = 3.0$ ms.

The temporal stability of the parameter quantification (reproducibility) of the repeated measurements is shown in Fig.5. The T_1 values were very stable, while the higher T_2 values show slightly higher deviation over time. The mean values within the tubes had an average standard deviation over time of $\sigma_{T_1} = 6.4$ ms and $\sigma_{T_2} = 2.3$ ms. A more detailed overview of these data is shown in Supporting Information II.

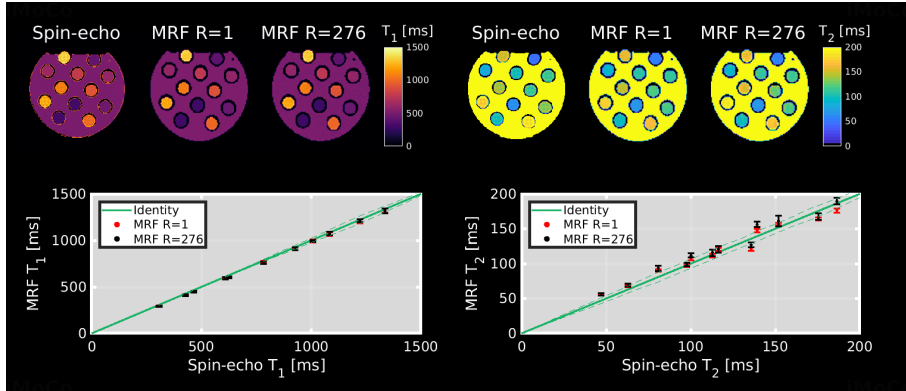


Figure 7.4: Accuracy and precision analysis of MRF parameter quantification in a phantom. Top row shows the spin-echo, fully sampled MRF and undersampled MRF parameter maps. The bottom row shows the correlation of the accuracy estimations for MRF versus the spin-echo. Data show the mean and standard deviation of MRF over a 25 pixel region in the center of the phantom. The dashed green line is the standard deviation of the spin-echo measurements in the same region.

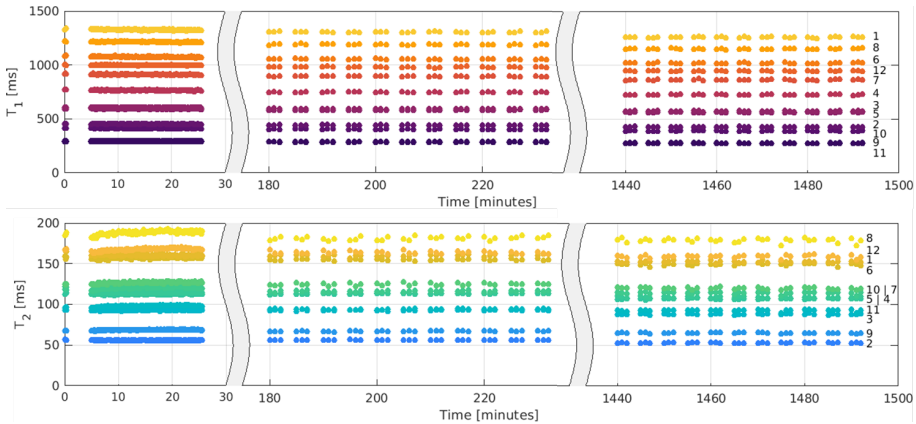


Figure 7.5: Repeated MRF measurement to assess the temporal stability of the parameter quantification. Top row shows the evolution of the mean T_1 values within the tubes and the bottom row shows the evolution of the T_2 values. Note that the tube numbers are added at the right side of the graph and they correspond with the numbers in Fig.3. See the following link for video that shows the parameter maps over time: <https://surfdrive.surf.nl/files/index.php/s/aOB3B2Y1AxeT4mo>

7.3.2 *In-vivo* studies

Brain volunteer data

Two slices of the brain MRF scans in the volunteer are shown in Fig.6. The T_1 and T_2 maps show clear boundaries between white and gray matter. The mean parameter values for gray and white matter are within the range of report literature values (Table.2). Note that the T_2 values are on the low side, which is also reported in other MRF publications [247]. The regions of interest that were

used to compute the mean values are projected on the proton density image. The MRF reconstructions time was approximately 15 seconds per slice, which does not consider the pre-computation of the dictionaries.

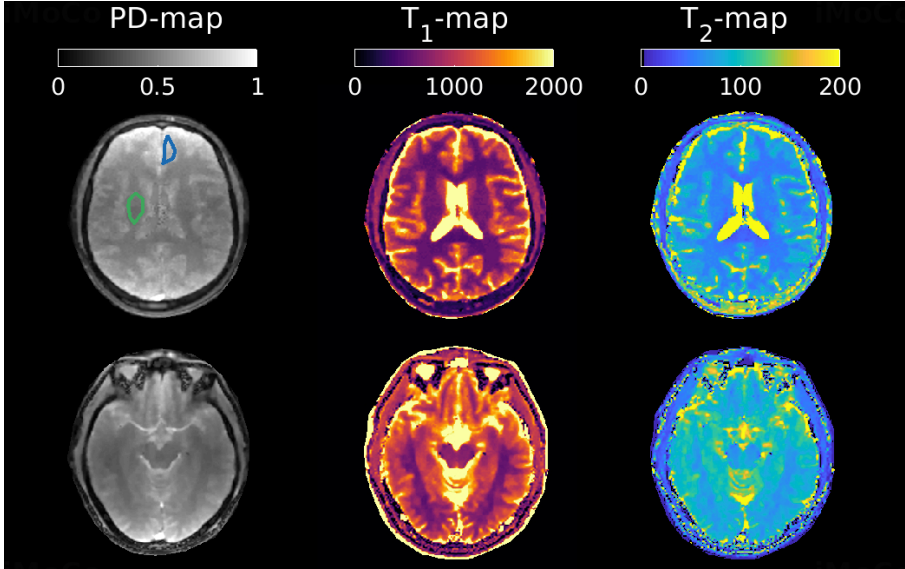


Figure 7.6: 2D brain MRF measurement in a healthy volunteer. Top row shows slice 1 of the MRF parameter maps and bottom row shows slice 2. Averaged $T_{1,2}$ values for white matter (green) and gray matter (blue) are shown in Table.2.

Table 7.2: Comparison of MRF T_1 and T_2 quantification to literature reported values.

MRF parameter	quantification			
	Reference T_1	MRF T_1	Reference T_2	MRF T_2
White matter	608 - 756 ms	626 ± 34 ms	54 - 81 ms	56 ± 4 ms
Gray matter	998 - 1304 ms	1113 ± 91 ms	78 - 98 ms	76 ± 7 ms
Liver	547 - 625 ms	612 ± 42 ms	40 - 52 ms	46 ± 5 ms
Kidney (medulla)	1354 - 1470 ms	1510 ± 144 ms	74 - 96 ms	51 ± 6 ms
Kidney (cortex)	908 - 1024 ms	954 ± 85 ms	83 - 91 ms	54 ± 5 ms
Pancreas	570 - 598 ms	540 ± 59 ms	40 - 52 ms	47 ± 8 ms

Volunteer abdomen data

Two slices of the abdomen MRF scans in the volunteer are shown in Fig.7-8. The boundaries between the medulla and cortex of the kidney are well defined on both the T_1 -map and the T_1 -w image, while the boundary is not visible on the T_2 -w image and T_2 -map. On the left side of the liver a small benign lesion is clearly visible on both the T_1 and T_2 map, which is characterised with a high T_1 and high T_2 . The T_2 values differ between the right and left kidney, which are 35 and 51 ms

respectively. Region of interest analysis for multiple organs are shown in Table.2. The kidney T_2 values also differ slightly between the two scans. However, the T_1 values were constant between the left and right kidney and between slice 1 and 2. The regions of interest that were used to compute the mean values are shown on the proton density image. The MRF reconstructions time was approximately 14 seconds per slice, which does not consider the pre-computation of the dictionaries.

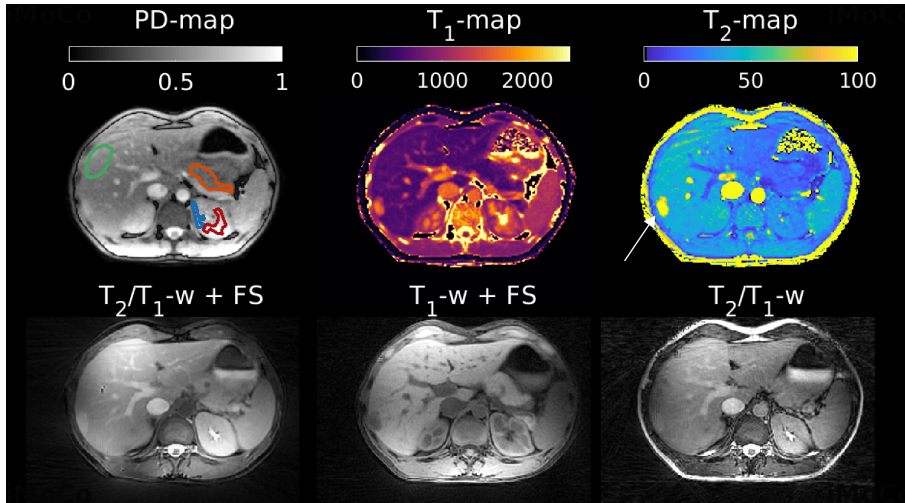


Figure 7.7: Breathhold 2D MRF measurement in a healthy volunteer. Top row shows the MRF parameter maps. Bottom row shows the qualitative images from the clinical protocol. The T_1 -w scan is a spoiled gradient echo sequence, the T_2/T_1 -w is a balanced gradient echo scan and FS = fat suppression. Note that the lesion that is visible in the liver is a benign cyst indicated by the white arrow. Mean T_1 and T_2 values were analyzed in regions of interest for liver (green), pancreas (orange), medulla (red) and cortex (blue) of the kidney.

Patient abdomen data

One slice of the abdomen MRF scan in the patient with a recurrent colorectal liver metastasis after hepatic resection is shown in Fig.9. The metastasis is positioned in the anterior side of the liver and is clearly visible on the T_1 -map, T_1 -w image and on the diffusion-w image, while the lesion is less well defined on the T_2 -map and T_2 -w image. The T_2 -map shows lower values in the liver and spleen compared to the volunteer scans, which could be due to patient motion.

7.4 Discussion

In this study we demonstrated technical feasibility of 2D MRF on a 1.5T MRL system. The phantom study indicated good agreement of parameter quantification ($R_{T_1}^2 = 0.999$ and $R_{T_2}^2 = 0.975$) with reference measurements, high precision ($\sigma_{T_1} = 8.6ms$ and $\sigma_{T_2} = 3.0ms$) and temporally stable measurements during the day ($\sigma_{T_1} = 6.4ms$ and $\sigma_{T_2} = 2.3ms$). The *in vivo* study showed high image quality of the fast MRF scans, where image features in the quantitative maps nicely corresponded with the qualitative scans. We believe these observations provide

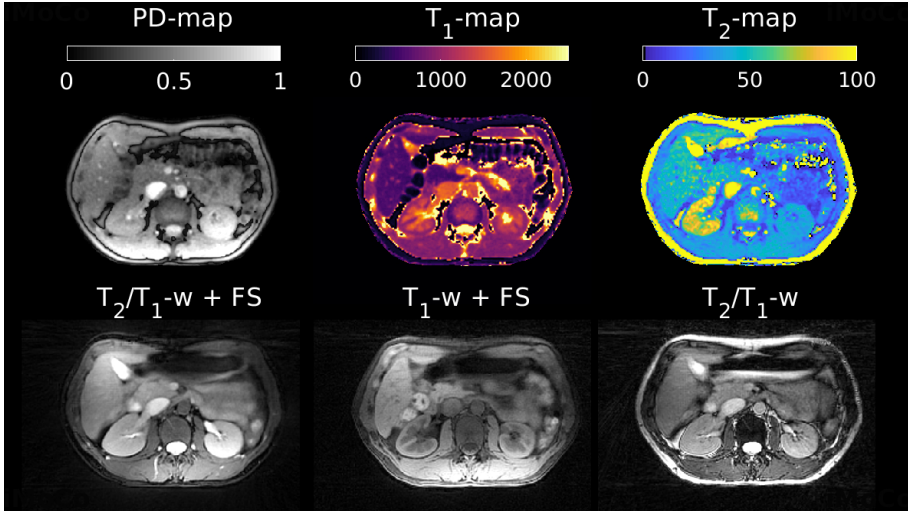


Figure 7.8: Breathhold 2D MRF measurement in a healthy volunteer. Top row shows the MRF parameter maps. Bottom row shows the qualitative images from the clinical protocol. The T_1 - w scan is a spoiled gradient echo sequence, the T_2/T_1 - w is a balanced gradient echo scan and FS = fat suppression.

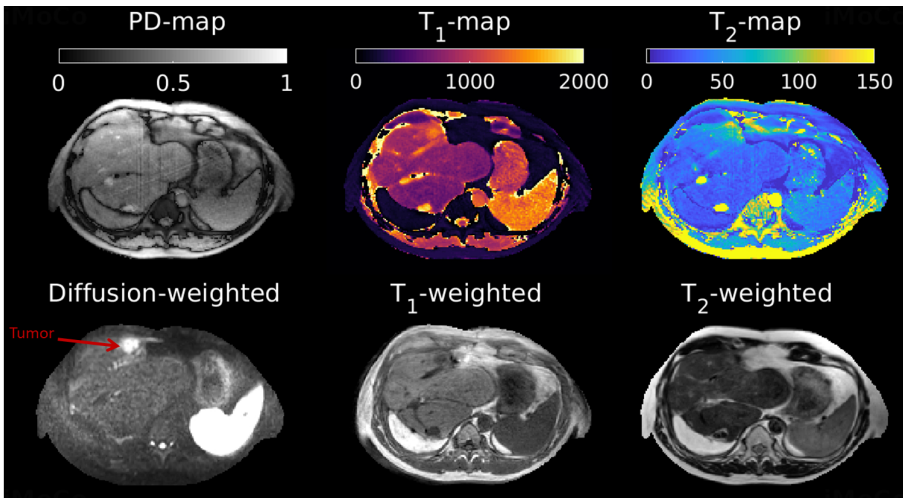


Figure 7.9: Free-breathing 2D MRF measurement in a patient with a colorectal liver metastasis. Top row shows the MRF parameter maps. Bottom row shows the qualitative images from the clinically used protocol. The T_1 - w scan is a spoiled gradient echo sequence, the T_2 - w is a turbo spin echo sequence and the diffusion- w is a spin-echo sequence with EPI readout. The lesion is indicated with the red arrow on the diffusion-weighted image and is also clearly visible on the T_1 scans.

sufficient evidence that MRF is technically feasible on MRL systems and therefore could be further explored for online MR-guided radiotherapy applications on a 1.5T MRL. Besides MRF, these findings also apply for other transient-state

parameter quantification methods [134].

It is important to emphasize that the methodology presented in this work does not necessarily reflect the optimal approach for MRF on a MRL. The use of radial readouts, SSFP and the basic flip angle train reported by Jiang et al. [247] provides a well established basis that we used to determine the general technical feasibility of MRF on a MRL. Future work will focus on the use of spiral readouts or potentially 3D based MRF sequences that would be more optimal for radiation therapy [263]. However, 3D MRF sequences are generally challenging in body imaging due to physiological motion, requiring substantial technical innovation to apply motion correction [264].

The *in-vivo* results presented in this work show some anomalies in the T_2 parameter maps that require some further discussion. The brain images show slightly higher T_2 values in the more inferior positioned slices and the T_2 abdomen images show relatively larger differences between the right and left kidney, while the T_1 values are unaffected for both sites. One possible explanation for these anomalies is uncontrolled B_0 in-homogeneity, however previous research has shown that the B_0 is well controlled for on MRL systems [50, 51]. Another explanation could be that these anomalies are caused by B_1^+ inhomogeneity's, which were not corrected for in these experiments. Other work's have reported on the relevance of B_1^+ effects on liver MRF [255], which primarily affects accuracy of the T_2 quantification (T_1 is relatively unaffected due to the adiabatic inversion pulse). Future work should therefore focus on MRL specific B_1^+ inhomogeneity's and investigate how these compare to inhomogeneity's on diagnostic systems.

A possible use case for the quantitative maps could be patient-specific contrast optimization of the anatomical turbo spin-echo sequences, i.e. the reference MRI on which the treatment is planned. For example, liver metastasis are a heterogeneous group of lesions that show variable signal characteristics on both T_1w and T_2w imaging depending on the primary origin [265, 266]. In this context, MRF could function as a contrast scout scan followed by an on-the-fly flip angle train optimization to maximize the contrast-to-noise ratio between the lesion and the liver. Contrast optimization techniques are well described in literature [267], but have never been applied in an on-the-fly setting for online contrast optimization on either diagnostic MR systems or MRL systems. Future work will focus on the implementation of these patient-specific contrast optimization techniques to investigate the potential improvement in image quality.

The rapid acquisition scheme of MRF (≈ 5 s per slice) could facilitate the integration of quantitative imaging to the clinical MRI-guided radiotherapy workflow without significantly lengthening of the treatment. The primary application of MRF would be for tumor response monitoring over multiple fractions during the treatment. The optimal timing to image changes in quantitative parameters post radiotherapy is an active topic of research [65, 268, 269] and could be pushed

forward with daily MRF on the MRL. The ability to pick up subtle changes in T_1 and T_2 values could be used to distinguish responders from non-responders. Ultimately, these potential changes in T_1 and T_2 could be used to intensify or reduce the (local) radiation during the radiotherapy treatment period based on the measured response.

7.5 Conclusion

Gradient spoiled 2D magnetic resonance fingerprinting is feasible on a 1.5T MRI-Linac with similar performance as on a diagnostic system. The precision and accuracy of the parametric maps are sufficient for further investigation of the clinical utility of magnetic resonance fingerprinting for online quantitatively MRI-guided radiotherapy.

7.6 Acknowledgments

This work is part of the research programme HTSM with project number 15354, which is (partly) financed by the Netherlands Organisation for Scientific Research (NWO) and Philips Healthcare.

Summary and Discussion

MRI will disrupt the field of radiotherapy in the next decade through optimal target visualization (pre-treatment/pre-beam), real-time image guidance (beam-on) and frequent tumor response monitoring (beam-off) to optimize the treatment for the patient. The most important aspect of imaging in all these stages in the radiotherapy workflow is the image quality. High image quality during pre-treatment/pre-beam imaging leads to more precise GTV delineations and eventually enables the concept of dose modulation within the tumor, often referred to as dose painting [270, 271]; high image quality during beam-on imaging improves the motion estimation, which subsequently reduces the PTV margin; high image quality during beam-off imaging leads to a sensitive assessment of early radiation induced tissue changes, which enables the differentiation between responders and non-responders. In addition to the requirement of high image quality, the imaging process on the MR-linac needs to be fast and with low latency to minimize the duration of the online/real-time workflow. Therefore, MR imaging requirements in radiotherapy are considerably different compared to the MR imaging requirements in radiology. Besides the different imaging requirements, the imaging is often performed on MR-linac systems, which differ considerably from conventional diagnostic MR systems. Therefore, the development of dedicated MR imaging techniques that are specifically tailored for adaptive radiotherapy are going to be crucial for optimal clinical implementation of MR-guided ART. This thesis focused on the conceptualization and development of such MR imaging techniques.

8.1 A progressive knowledge reflection

8.1.1 Baseline for fast 2D MRI

Chapter 2 focused on the relatively simple problem of quantifying the 2D motion of tumors in patients with head-and-neck cancer with the primary objective to determine PTV margins for MR simulation. While adequate PTV margins are

relevant in the clinic, another important motivation for this project was to obtain a fundamental understanding of the possibilities and limitations of fast MR imaging techniques, that are readily available on commercial MRI systems, and their interaction with non-rigid image registration techniques. The interaction can be interpreted as the ability of the non-rigid registration algorithm to filter out residual aliasing artefacts and therefore facilitate further acceleration of the imaging. This interaction between imaging and registration is what ultimately dictates the quality of the motion estimates and is therefore the crucial endpoint. The available MR techniques for fast imaging included spoiled gradient echo sequences with Cartesian k-space sampling, which were accelerated with parallel imaging and partial Fourier. The resulting images were subsequently non-rigidly registered using optical-flow [99,100] to obtain the motion estimates. The combination of accelerated imaging and optical-flow provided an optimization landscape with two tuneable parameters, namely the imaging acceleration factor and the spatial regularization factor for the registration. A volunteer study determined that the optimal parameters were an image acceleration of $R = 3$ ($\approx 6Hz$) with a spatial regularization of the optical flow of $\alpha = 0.2$. Further acceleration of the imaging generated coherent aliasing artefacts that the optical-flow algorithm was unable to resolve, which lead to artefacts in the motion estimates (Figure 8.1A-B).

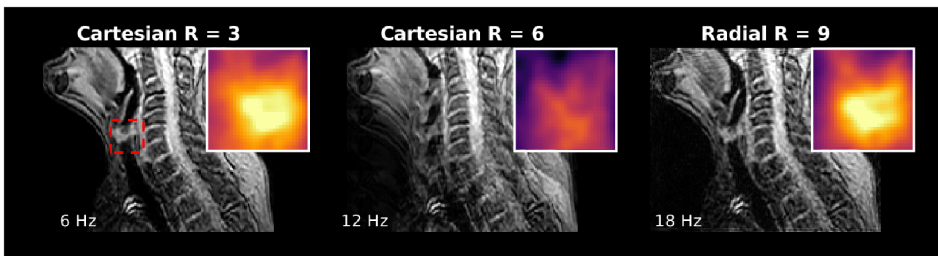


Figure 8.1: Motion estimation of retrospectively undersampled 2D MR scans. All images are reconstructed with parallel imaging. The three zoom images in the right-top show the motion field, within in the dashed red box, obtained with optical flow image registration. **A)** Cartesian scan with $R=3$ shows high image quality and high quality motion estimates. **B)** Cartesian scan with $R=6$ shows residual aliasing artefacts in the image, which translates into a loss of information in the motion fields with respect to A). **C)** Radial scan with $R=9$ shows high image quality with minor streaking artefacts, which provide high quality motion estimates.

8.1.2 Theoretically optimal approach for fast 2D MRI

Parallel to the acquisition of the 2D MRI patient data with readily available MR imaging techniques, we investigated novel imaging techniques that could accelerate the motion estimation [272]. These techniques included balanced SSFP sequences with a golden angle radial k-space trajectory in combination with temporal regularization. In theory, bSSFP sequences are superior to spoiled sequences in terms of signal-to-noise and the golden angle radial trajectory provides incoherent sampling for highly accelerated compressed sensing in the time domain [273,274]. In addition, residual aliasing artefacts arising from radial undersampling manifest as high frequency streaking artefacts, opposed to coherent artefacts with

regular Cartesian undersampling, which the optical-flow algorithms is more resilient towards [194, 210] (Figure 8.1C). However, in practice the golden angle radial bSSFP images were accompanied with a complex arsenal of image artefacts. These artefacts included excessive streaking, introduction of bias fields, occurrences of signal voids that were tightly coupled to the off-resonances (Fig chapter 3). These artefacts completely impede a straightforward use of golden angle radial bSSFP for 2D cine imaging. Many of these artefacts were already described in previous works and were attributed to system imperfections that result into gradient delays [69, 275], phase errors [143, 276], k-space trajectory errors [75, 277] and steady-state disruptions [110, 115, 121]. These individual artefacts all arise from the overarching problem of gradient system imperfections, which are caused by thermal variations in the hardware, bandwidth limitations of the amplifiers, mechanical vibration caused by gradient switching and eddy currents in the gradient coil and other conducting structures [76]. All these individual components have complex behavior and are difficult to accurately model to obtain useful information for the image reconstruction. Therefore, the most practical approach is to lump all these effects together and quantify the linear time-invariant behavior of the entire system in the so called gradient impulse response function [76, 278, 279], as described in Section 1.4.2.

8.1.3 Gradient system characterization

The gradient impulse response functions (GIRFs) were measured on the diagnostic MR systems [53] and were used to analyze the artefacts observed in the 2D radial bSSFP images. The GIRFs were used in combination with existing theory [278] to assess the impact of gradient delays, k-space trajectory errors and global phase errors. The outcome of the assessment was that the impact of the first order eddy current effects, i.e. gradient delays and k-space trajectory errors, were small for radial sampling and corrections did not lead to an improvement in image quality. However, the impact of the zeroth order eddy current effects, i.e. global phase errors, were large and corrections lead to a considerable improvement in image quality. The finding that the zeroth order eddy current effects are more relevant is contradictory to most of the scientific literature on eddy current in radial MRI. Most of the (recent) literature focuses on the gradient delays and trajectory errors [69, 280, 281] and not on the impact of the global phase errors [143]. This discrepancy could in part be explained by differences in the gradient coil hardware between the MRI vendors. Where one vendor provides accurate control over the zeroth order effects with compromised control over the first order effects, while the other vendor's implementation functions vice versa. Nevertheless, measuring the GIRF and applying both the zeroth and first order eddy current correction should provide the best image quality. Note that the observations on the relevance of the zeroth and first order eddy current effects are only valid for projection imaging and do not necessarily hold for center-out radial or spiral acquisitions. The center-out acquisitions typically sample the data on the ramps of gradient waveforms and as a result experience larger deviations of the k-space trajectory.

While the retrospective eddy current corrections improved image quality of the 2D bSSFP golden angle radial scans, considerable image artefacts remained. These artefacts varied over the dynamics (time), followed the shape of the underlying B_0 field and could not be explained using the GIRFs with a conventional eddy current model [278]. The conventional eddy current models only consider the current repetition block and do not consider the long-term history of the eddy currents and their impact on the spin dynamics/steady-state. This relation between the spin dynamics and eddy currents in bSSFP imaging was described before in literature [115] but was not yet completely understood and was therefore the focus of **Chapter 3**. Chapter 3 described a new bSSFP signal model that included the GIRFs and describes this relationship between the eddy currents and the disruption of the steady-state. Digital simulations showed that these disruptions were strongly dependent on the local B_0 field and also on the smoothness of the spatial encoding schemes. The simulations explained the effectiveness of pre-existing methods that showed strong resilience towards steady-state disruptions, such as tiny golden angle increments for radial or phase encode pairing for Cartesian acquisitions. In addition, using the new signal model we could accurately explain the residual image artefacts in the 2D bSSFP golden angle radial scans, but the model did not yet provide means to correct the artefacts. Subsequently we revisited a previously described prospective eddy current compensation method [124] that adjusts the phase of the RF excitation pulse. The method previously required labour-intensive sequence-specific calibration measurements, which made the method impractical for clinical implementation. Using the new signal model we could accurately drive this RF eddy current compensation method without any prior calibration. The signal model was embedded in the MR system and used to compensate the residual eddy current induced phase errors by prospectively modifying the phase cycling scheme of the RF pulse based on the GIRFs. The prospective eddy current correction further improved the image quality of the 2D bSSFP golden angle radial scans and could provide a solid basis for the use of (bSSFP) non-Cartesian scans for MRI in radiotherapy.

8.1.4 MR-RIDDLE for pre-beam imaging

The know-how of using the GIRFs to correct 2D golden angle radial imaging stimulated further investigation of golden angle radial for pre-beam imaging. The golden angle stack-of-stars scans provide advantages over conventional Cartesian scans, which include robustness to motion artefacts, inherent depiction of the time-averaged position, self-navigation of the respiratory cycle and flexibility in the spatiotemporal resolution during image reconstruction. These advantages make the golden angle stack-of-stars scan a possible one-stop-shop solution that obtains all the information required for online radiotherapy treatment planning. **Chapter 4** describes the implementation of such a golden angle stack-of-stars scan, which we named MR-RIDDLE: Multiresolution radial MRI to reduce IDLE time in pre-beam imaging on an MR-linac. MR-RIDDLE capitalizes on the advantages of golden angle stack-of-stars, with the ultimately goal to speed-up and reduce the idle time in the online workflow. The anticipated speed-up primarily comes from the flexibility in the spatiotemporal resolution for image reconstruc-

tion during the MR acquisition. For example, after one minute MR-RIDDLE can reconstruct low-resolution images, after which the data acquisition continues for subsequent higher-resolution updates (e.g. one update every 10 seconds). Finally, the acquired data can also be used to reconstruct a respiratory-resolved 4D-MRI scan [160]. Such a flexible image reconstruction could improve the online clinical workflow in multiple ways, with some concrete examples are listed below: 1) the multi-resolution image reconstruction could be coupled to multi-resolution image registration for faster access to the propagated contours on the daily anatomy; 2) the daily anatomy could be acquired with higher resolution, because lower resolution images are readily available to start the workflow; 3) Golden angle stack-of-stars inherently reconstructs the time-averaged position (e.g. mid-ventilation) position for moving tumors, which reduces the position uncertainty; 4) Access to the 4D-MRI just prior to radiation without additional scans [282, 283]; 5) A low-resolution sliding window reconstruction could be run in parallel to detect possible bulk motion of the patient. 6) The position verification scan prior to irradiation could be performed instantly with the sliding window reconstruction.

The concepts of MR-RIDDLE have the potential to considerably improve the pre-beam MR-linac workflow in theory. In practice, we encountered multiple obstacles that need to be addressed for a successful clinical implementation: 1) Parallel imaging reconstructions of non-Cartesian trajectories take approximately 10 times longer than for Cartesian trajectories, which introduces reconstruction latency's of over a minute for high resolution images. The reconstruction time could be reduced with high performance software implementations with dedicated computation hardware, but would require a significant implementation effort; 2) the golden angle stack-of-stars scan did not provide robust image quality on the MR-linac system since we observed a large inter-subject variability. The variability of the image quality was hypothesized to be caused by the sensitivity of radial scans to off-resonance/chemical shift and residual effects of gradient system imperfections. The residual gradient system imperfections were primarily attributed to higher spatial order eddy currents, which are more prominent further away from the iso-center. The higher order gradient system imperfections were not further investigated, as these would have required additional gradient impulse response measurements [126]; 3) the golden angle stack-of-stars trajectory is mostly restricted to T_1 -w GRE sequences, because the repetitive sampling of the k-space center leads to an undefined T_2 -w contrast for TSE sequences. The restriction to mostly T_1 -w sequences presents a contradiction with the clinical reality, where many tumors are contoured on T_2 -w TSE sequences. This restriction of pre-beam image contrast to T_1 -w reduces the applicability of MR-RIDDLE in a generic clinical setting. The image contrast of the pre-beam imaging should, in my opinion, not be determined by technical aspect of the sequence, but should solely be determined by the optimal contrast to delineate the target. Therefore, the use of golden angle stack-of-stars as a generic solution for pre-beam imaging on an MR-linac is probably not optimal.

8.1.5 rCASPR for pre-beam/pre-treatment imaging

The shortcomings of MR-RIDDLE were tackled in **Chapter 5** with the goal of developing a pre-treatment/pre-beam scan with an improved perspective for clinical implementation. Chapter 5 was inspired by the golden angle Cartesian Acquisition with SPiRal profile ordering (CASPR) work by Prieto et al. [172,284], which effectively proposed a Cartesian sampling scheme that provides many of the favorable properties of the golden angle stack-of-stars trajectory, while not being susceptible to the disadvantages. The CASPR work was initially developed for respiratory motion compensated cardiac MRI using bSSFP sequences and shown by Greer et al. [173] to work for 3D T_1 -w TSE for motion robust arterial spin labeling. Chapter 5 proposed to modify CASPR scheme to a rewinded (in-out) CASPR scheme (rCASPR), which facilitates scanning of T_2 -w TSE sequences with clinically relevant echo times. The key feature of rCASPR is that it allows the 3D TSE used in the clinical workflow (on the Unity system) to be transformed to free-breathing 4D TSE scans, without changing the image contrast.

In practice rCASPR proved to be less resilient to motion artefacts and required more imaging data to obtain a high quality 4D in comparison to the stack-of-stars trajectory. To compensate for the data insufficiency a low-resolution 4D-MRI was reconstructed, which significantly reduces the data requirement. The low-resolution 4D-MRI was used to estimate respiratory motion fields at the original resolution of the imaging. The motion fields were subsequently used in a final high resolution motion compensated image reconstruction [161,177]. The key assumption in this reconstruction framework is that low-resolution images are sufficient for deformable image registration to estimate the motion at sub-voxel resolution [58,80]. The question that then naturally arises is: what is the optimal (low) resolution of the 4D-MRI to estimate high quality motion fields? The answer depends on the complex interplay between the registration technique, the magnitude of the motion and the quality of the images. The quality of the images in turns, depends on the temporal regularization and spatial resolution of the image reconstruction, where a high resolution/low temporal regularization leads to more residual aliasing than low resolution/high temporal regularization. Therefore, the optimal resolution for the 4D-MRI reconstruction is likely to be application-specific and requires a grid-search over the entire tuneable parameters range. The grid search was performed by varying the spatial resolution and the temporal regularization of the 4D-MRI reconstruction and subsequently assessing the image quality of the motion compensated image reconstruction using the gradient entropy metric [178]. The grid search resulted into a $\lambda = 1 \times 10^{-4}$ temporal regularization with 4.5 mm^3 spatial resolution. The reduction in spatial resolution to 4.5 mm^3 was also reported in the study by Glitznier et al. [61], which investigated retrospective spatial downsampling of 3D MRI in combination with image registration. The resulting rCASPR motion compensated image reconstructions showed consistent and high quality, which was a considerable improvement in comparison with the golden angle stack-of-stars scan.

The motion compensated rCASPR technique is currently being evaluated for other types of sequences, e.g. T_1 -w GRE, T_1 -w TSE and magnetic resonance

cholangiopancreatography (MRCP) and so far has displayed consistent and high image quality. The case for the MRCP imaging will be further discussed in Section 8.2.3. In the future rCASPR will be evaluated versus respiratory triggered 2D multi-slice scans, which would be the highest quality reference for many sequences. In addition, future work will include the evaluation of rCASPR for non-respiratory related motion correction, for example for 3D imaging in the pelvis. The only remaining drawback of rCASPR is the relatively long reconstruction times, that are accompanied with the motion compensated image reconstruction ($>30\text{min}$), which currently impedes directly application of rCASPR for pre-beam imaging.

8.1.6 MR-MOTUS for real-time 3D beam-on imaging

Chapter 2 focused on fast 2D time resolved motion estimation for head-and-neck imaging and chapter 5 focused on 3D respiratory resolved motion estimation for abdominotoracic imaging. The scans proposed in these works use most of the available image acceleration techniques such as non-Cartesian trajectories, parallel imaging and compressed sensing. However, the extension of these methods to time-resolved 3D motion estimation still requires an additional order of magnitude acceleration to obtain the required temporal resolution of approximately 5 Hz for real-time imaging [196]. The fundamental bottleneck of this conventional process of motion estimation is the large amount of data that needs to be re-acquired to reconstruct 3D images with sufficient quality, even though the data is strongly correlated between subsequent images in both space and time. Recent works in literature focus on the optimal compression of these spatiotemporal correlations, which included low-rank image models [213, 285] and neural networks [286, 287], but these compressed representations do not offer sufficient acceleration for real-time time resolved 3D MRI. Instead, one would argue that the spatiotemporal correlations are best described directly by compressed motion fields. Consider the toy example shown in Figure 8.2, where the digital phantom moves along a straight line. A low-rank decomposition applied directly on the images yields many basis images. Consider the equivalent low-rank decomposition of corresponding motion fields with respect to the reference image, which yields just one single motion field. Every time-point is then a scalar multiplication of the motion field applied to the reference image. The toy example can be extrapolated to multiple positions, which would further exacerbate the difference in compression ratio's of low-rank models on images opposed to motion fields. The observation that the spatiotemporal correlations are better captured in a low-rank representation of the motion fields is the primary motivation for MR-MOTUS and forms the basis of **Chapter 6**.

Low-rank MR-MOTUS relates the measured k-space data to a low-rank motion model using a low-resolution image as reference. MR-MOTUS requires a k-space trajectory that provides efficient spatiotemporal encoding, such as golden mean cones and kooshball readouts [71, 72]. A robust implementation of these readouts was enabled by the measured GIRFs from Chapter 4. The translation of the application of MR-MOTUS from simulated and retrospectively undersampled data [80] to prospectively undersampled data presented a major implementation effort. As

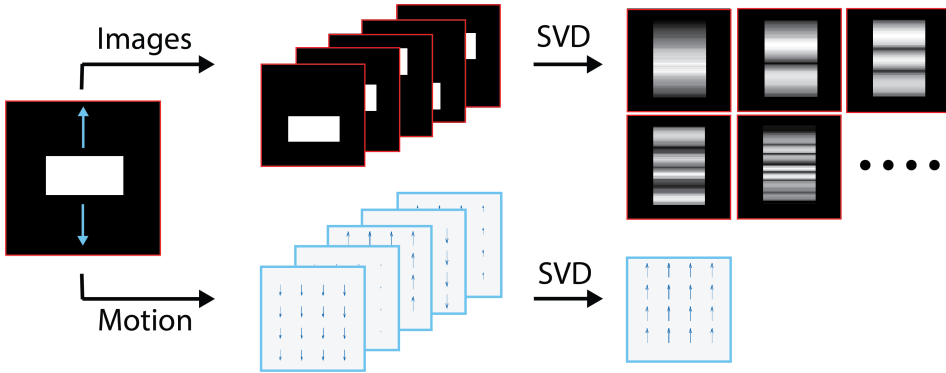


Figure 8.2: Conceptual illustration for the motivation to use low-rank MR-MOTUS over image based motion estimation techniques. Consider a simple rectangle moving rigidly to the top and bottom over a dynamic MR scan. Top row: Singular value decomposition of the dynamic images yield multiple basis images with large singular values. Bottom row: Singular value decomposition of the dynamic vector fields only yields one set of basis vectors, which can exactly describe all the possible motion states. This toy example provides motivation for the use of low-rank compression directly on the motion fields instead of the images, to better describe the spatiotemporal correlations and therefore enable higher imaging acceleration.

MR-MOTUS reconstructs the motion fields directly based on the k-space data, any imperfect measurement condition, such as off-resonances, eddy currents, flow encoding, low signal-to-noise and inhomogeneity of the receive coils, has the potential to affect the motion estimates. For image-based motion estimates techniques these measurement imperfections reside in the phase information, which is generally discarded during image registration. For MR-MOTUS, however, these imperfections need to be addressed or at least suppressed in the motion field reconstructions. The inhomogeneity of the receive coils was solved with a novel k-space coil compression algorithm, while the other imperfections were passively tackled in the sequence design with volume shimming and flow compensation. The remaining measurement imperfections were filtered out in the reconstruction with the low-rank approximation. The current implementation of low-rank MR-MOTUS provides high quality motion estimates with good reproducibility across volunteers in the upper abdomen and thorax for respiratory motion.

8.1.7 MR Fingerprinting for beam-off imaging

Chapter 7 focused on the only remaining imaging phase of the MR workflow which was not yet described in this thesis, the beam-off imaging. The beam-off imaging was defined as the online imaging performed on an MR-linac that is not directly used to adapt the therapy. Instead the beam-off imaging is used to monitor the longitudinal response of the tumor to the therapy. The inclusion of beam-off scans in the online workflow is not straightforward, because the scans require additional imaging time which increases the duration of the fraction. The total duration of the fraction will be one of the key factors for widespread integration/adoption of MR-linac in oncology, as the fraction times are currently significantly longer than conventional linac fractions [43]. Therefore, the development of fast quantitative MRI techniques for MR-linac is crucial for tumor response

monitoring. MR Fingerprinting is such a rapid multiparametric scan that could be the ideal candidate. High quality MR fingerprinting reconstructions require reliable fingerprinting signals, which depend upon a stable MR system. As the MR-linac system includes modified hardware components, such as the gradient coil, the main magnet and the receive coils, we did not know whether MRF would be technically feasible. Therefore we implemented a radial MRF sequence on the MR-linac and acquired experimental phantom and *in vivo* data. The experimental results were promising and warrant further investigation into the clinical utility for MRF on the MR-linac. Future work is required to slightly improve the image quality of the body MRF, which include improved flip angle pattern designs [288, 289] and the use of spiral readouts for more efficient encoding [247].

8.2 Future perspectives

The design and the development of dedicated MR methods for adaptive radiotherapy, described in this thesis, could ultimately lead to an improved treatment for the patient. However, these methods need to be further developed before they can be made accessible for integration into patient care. Further development is likely to pursue one of the following trajectories: 1) An industrial partner (e.g. Philips) includes the technology into the product portfolio, which makes the technology widely available. However, industrial partners necessitate a strong business-case with low risk involvement, which requires strong evidence on the clinical and economic added value of the technology. The evidence has to be provided by the researchers in a clinical setting, which in turn requires a (local) clinical implementation of the technology; 2) An in-house built clinical implementation where we have to overcome a number of challenges. These challenges include the use of own reconstructed images in the clinical workflow, which will require thorough quality assurance. A part of the quality assurance is writing the software according to the in-house quality management system regulations (QMS). Other research sites have already demonstrated the feasibility of such a setup [283]. Another challenge is to program high quality image reconstruction code such that the reconstructed images provide similar quality as the vendor's reconstruction framework. The vendor's reconstruction framework often includes many signal processing methods, which are difficult and time-consuming to implement. Relevant examples of these processing methods include robust coil sensitivity map estimation [180], fold-over suppression using SENSE [290] or image uniformity correction [291]. Therefore, the optimal approach would be to either program the MR methods directly into the vendor's reconstruction framework or to build a software platform that allows real-time interfacing within the vendor's framework [292]. The realization of such a robust interface is crucial for the clinical implementation of dedicated MR methods for adaptive radiotherapy and enables us to speculate on the optimal MR-linac imaging workflow for the future.

8.2.1 MR-linac imaging workflow in 2025

The current clinical MR-linac online workflow has multiple shortcomings, as discussed in Chapter 4, which reduce the time efficiency and treatment quality of

the adaptive radiotherapy. These shortcomings include for the pre-beam phase: static MR scans without motion correction; no simultaneous motion monitoring for bulk movements or respiration; no motion quantification for mid-position reconstructions or internal target volume margin determination. For the beam-on phase: no real-time 3D motion estimation for MLC tracking or dose accumulation. For the beam-off phase: no rapid multiparametric quantitative imaging for tumor response monitoring. These shortcomings will be addressed in the future and are likely to change the MR-linac imaging workflow completely by 2025. Most of the shortcomings are individually addressed by the chapters included in this thesis, but the proposed solutions do not necessarily function effectively in union. Therefore, the remainder of this section describes the merger of the proposed solutions in this thesis for a unified, comprehensive and time-efficient MR-linac imaging workflow.

The way I envision the MR-linac imaging workflow in 2025 is conceptually illustrated in Figure 8.3. One single MR scan is acquired for the whole length of the treatment session, which consists of a combined T_1 -w and T_2 -w MR scan [293] with a rCASPR readout. The rCASPR data is subsequently streamed to three separate data processing pathways. **Pathway 1** is the "Daily MRI" stream that generates highly quality images for contouring using a motion compensated mid-position image reconstruction. These images will be continuously reconstructed with increased spatial resolution, depending on the amount of imaging data that is available, similar to MR-RIDDLE. The Daily MRI stream also reconstructs a respiratory correlated 4D-MRI that could be used for internal target volume determination. **Pathway 2** is the "Bulk motion detection" stream that generates low-resolution images with a high frame rate for bulk motion detection using sliding window image reconstruction. The key idea here is to tune the sliding window width to approximately 3 breathing periods, which makes the scan relatively insensitive to variations in respiration and therefore allows easy detection of bulk motion and tumor drifts [259]. The quantified bulk motion/drifts could be used to correct the image reconstruction of the Daily MRI or to adapt the treatment plan. **Pathway 3** is the "Real-time motion estimation" stream that uses offline MR-MOTUS to learn the spatial basis of the motion fields during the pre-beam imaging phase. The learned spatial basis can subsequently be used in online MR-MOTUS to estimate motion fields with very high temporal resolution (> 10 Hz) [233]. The real-time motion estimates are subsequently used for real-time motion management systems such as MLC tracking or dose accumulation. These three data pathways present a unified, comprehensive and time-efficient MR-linac imaging workflow for adaptive delivery of the radiotherapy.

The proposed MR-linac imaging workflow does not provide room for quantitative MRI prior to or during the radiation delivery. Therefore, the MRF scan has to be positioned at the end of the fraction, which lengthens the treatment (Figure 8.4). However, positioning the MRF scan at the end of the treatment session has some considerable advantages. Advantage 1: The MRF could be seen as a continuation of the single CASPR scan, where only the flip angles are dynamically adjusted while the other sequence parameters remain the same. This continuation enables the MRF reconstruction to include the data acquired prior to the MRF scan

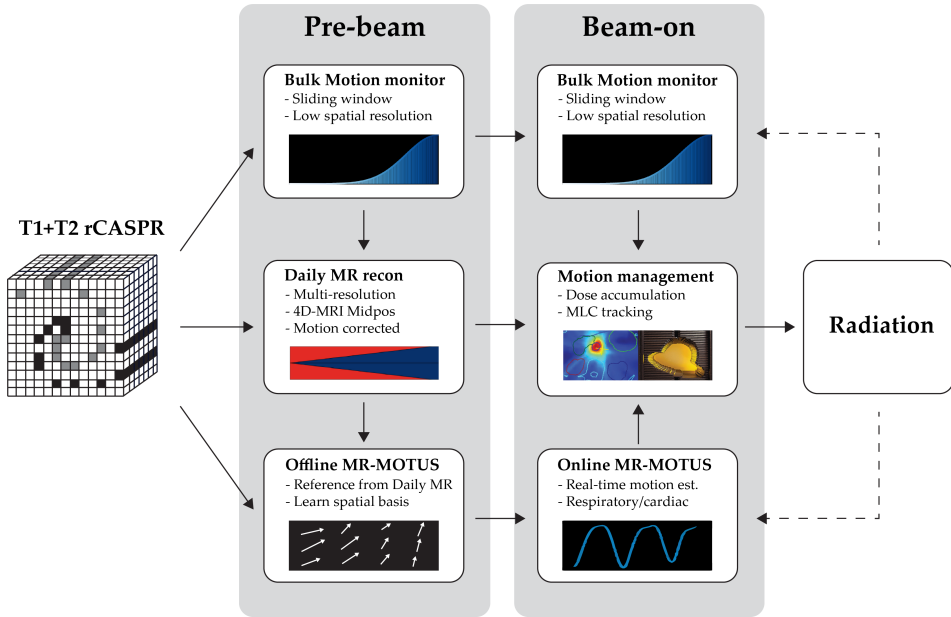


Figure 8.3: Proposed MR-linac imaging workflow for 2025. The imaging consists of a single rCASPR scan with simultaneous acquisition of both T1 and T2 contrast. The k-space data is processed in three different pathways. Pathway 1 reconstructs the Daily MR and includes a multi-resolution motion compensated image reconstruction. Pathway 2 reconstructs low resolution images with a soft-weighted sliding window (soft-weights indicated with the blue curve) to monitor bulk motion. Pathway 3 calibrates MR-MOTUS during the pre-beam phase and estimates real-time 3D motion during the beam-on phase. These three pathways are also interconnected, for example the bulk motion monitor could correct the MR imaging data for the Daily MR recon and the Daily MR recon could provide a high quality reference image required for MR-MOTUS.

as additional measurements, which provides a lot of extra information for the parameter quantification. Advantage 2: The spatial basis for the motion fields reconstructed by MR-MOTUS could be correlated to a motion surrogate that is not dependent on the flip angle [294, 295], which could enable highly efficient motion compensated 3D MRF reconstructions [264].

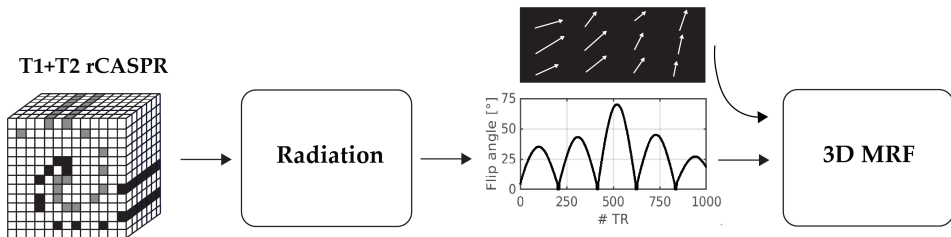


Figure 8.4: Proposed MR-linac beam-off imaging for 2025. The beam-off imaging has to be positioned at the end of the treatment fraction. The beam-off scan can be seen as a continuation of the rCASPR scan, where only the flip angles are dynamically varied. This continuation ensures that all prior data can be included in the MRF reconstruction and the real-time motion information, derived from MR-MOTUS, can be used for motion correction.

8.2.2 MR-linac system: ready for 2025?

The MR-linac imaging workflow for 2025, as described in the previous section, requires a high performing MR system for highly accelerated imaging. The current MR-linac system differs from a diagnostic system in the split gradient and split magnet coil design, the radiolucent 2x4 channel receive coil and a paramagnetic rotating gantry, as outlined in Chapter 7. Some of these differences have, in my opinion, a relatively small impact on the imaging workflow, e.g. the modified magnet coil design and the rotating paramagnetic gantry, while the impact of the split gradient coil and modified receive coil are more relevant. The split gradient coil currently restricts the maximum achievable slew rate to 65 T/m/s (opposed to 200 T/m/s) and the maximum gradient strength to 15 mT/m (opposed to 40 mT/m), which increases the repetition time by up to $\approx 40\%$ for spoiled gradient echo sequences. These gradient restrictions are imposed by software to reduce eddy current artefacts and to limit heating of the gradient coil and surrounding structures [296].

Future work could focus on hardware upgrades of the gradient coil to improve the cooling or software upgrades to improve active eddy current compensation (while maintaining gradient linearity). However, I anticipate that future work will head in the opposite direction (hardware downgrades), namely a reduced region of linearity with an increased slew rate / maximum gradient strength. I believe that the non-linearity and eddy current problems will be largely be resolved using signal processing methods. These signal processing methods include higher order gradient impulse response measurements coupled with a non-Fourier based higher order image reconstruction, which is already in use for over a decade for distortion correction in diffusion weight imaging [79]. An especially interesting topic is the development of the image reconstruction techniques in the Patloc project, which reconstruct images encoded with highly nonlinear gradient coils for accelerated imaging [297, 298]. An intuitive explanation of how these methods can recover signal pile-up due to gradient non-linearity's is that the varying spatial sensitivities of the receive coils can unfold these signals similar to a conventional SENSE reconstruction. Note that these higher order image reconstruction methods could provide a accurate solution for gradient non-linearity correction for MRI in radiotherapy, which recently some groups have picked up [299]. The only downsides of higher order image reconstruction techniques are the necessity of accurate gradient impulse response measurement (one time measurement), a considerable increase in computational load for image reconstruction (less suitable for real-time) and the requirement of a dense receive coil array. Note that a reduction of the linear region could increase the maximum gradient strength and therefore also benefit diffusion weighted imaging.

The current radiolucent 2x4 channel receive coil is, in my opinion, the largest limitation of the Unity MR-linac system. The low amount of receive coils considerably reduces the ability to accelerate the imaging and also restricts the acceleration direction to the axial plane (no sensitivity variation in Z). In addition, the low amount of receive coils impedes the use of an effective higher order image reconstruction, as discussed in the previous paragraph. Therefore the development of

radiolucent dense receive arrays, as pioneered by Zijlema et al. [300,301], will be relevant for the MR-linac imaging workflow.

Another important aspect of the MR-linac, which can be considered as the system hardware, is the high performance computing infrastructure. The current MRI reconstruction computer has 32 Gb of RAM, 12 CPUs and does not contain any GPUs. The lack of GPUs and limited RAM will impede direct integration of the technology described in this thesis and will also impede fast application of deep learning for example for synthetic CT generation [302,303]. New computing hardware could either replace the MRI reconstruction computer or could be integrated inline with the reconstruction computer. The inline integration was already investigated by Borman et al. [292] via a 1 GBit full-duplex Ethernet link, which could stream raw data with ≈ 4 ms latency. Therefore, the inline integration is a viable approach to increase the computing infrastructure of the MR-linac.

To summarize, the current gradient performance restrictions limit the image acceleration, but should be tractable with advanced image reconstruction methods and therefore does not require redesign of the hardware. However, the current radiolucent receive coil and computing infrastructure do not provide sufficient performance to accommodate advanced MR methods to prepare the MR-linac system for 2025.

8.2.3 Dissemination of technology to diagnostic applications

Some of the methods developed in this thesis may also provide value for applications in MR diagnostics. For example, the CASPR work in Chapter 5 describes techniques for high quality free-breathing 3D T₂-w imaging, which are crucial sequences to visualize the biliary and pancreatic ducts in magnetic resonance cholangio-pancreatography (MRCP) [304,305]. Another example is the MR-MOTUS work in Chapter 6, which describes techniques for high spatiotemporal resolution imaging of motion fields, which could also be effective for motion correction in integrated PET-MRI systems. Both these examples will be discussed in more detail in the following two subsections.

Free-breathing motion corrected MRCP using rCASPR

MRCP scans consists of heavy T₂-w 3D turbo spin-echo sequences that are crucial for the diagnosis of biliary and pancreatic duct disease. These MRCP scans are typically acquired with long acquisitions, which are prospectively triggering using a respiratory bellows, but are often still hampered by motion artefacts that reduce diagnostic accuracy [306,307]. The likelihood of these artefacts is reduced at the radiology department in the UMC Utrecht by building in redundancy, in the form of two MRCP scans within a single protocol. However, these MRCP scans take a long time (≈ 7 min each) and therefore take up to 50% of the total examination time. Therefore, the implementation of one single robust MRCP scan has considerable clinical value. One strategy to reduce the motion artefacts is to acquire the data in one single breathhold with high compressed sense ac-

celeration, however these acquisitions do not yet provide similar image quality as successful respiratory triggered scans [308]. An alternative strategy is to use the free-breathing motion compensated rCASPR pipeline, as described in Chapter 5, which could potentially reduce motion artefacts while due to the motion correction and simultaneously reduce scan time due to the continuous acquisition.

In collaboration with the radiology department we have setup a small clinical study in which we acquired the respiratory triggered MRCP as well as the rCASPR MRCP scans in patients with biliary or pancreatic disease. One example of such a dataset is shown in Figure 8.5, where the triggered reference scan is on the left and the continuously acquired rCASPR scan on the right. The rCASPR scan shows a large reduction in motion and flow related image artefacts (green arrows), while showing slightly residual motion blurring (red arrows). Note that the scan time was reduced with approximately 40 %. Future work will include validation in multiple patients and the corresponding clinical evaluation with a radiologists. The initial results nicely demonstrate the versatility of the proposed motion corrected 4D-MRI rCASPR for MR scans with different image contrasts.

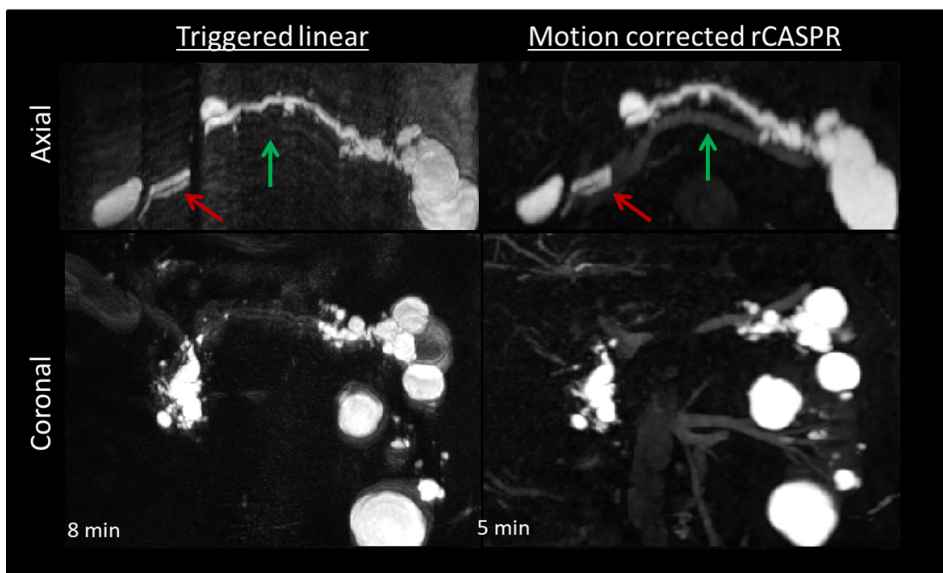


Figure 8.5: Magnetic Resonance Cholangio-Pancreatography (MRCP) scans in a patient with biliary disease. The top and bottom rows shows the axial and coronal maximum intensity projection across 10 slices. The left column shows the images obtained with the conventionally clinically used respiratory triggered scan with linear phase encoding. The right columns shows the images obtained with the proposed motion corrected rCASPR scan. Red arrows indicate regions where the rCASPR scan shows residual motion blurring in comparison with the linear scan. Green arrows indicate regions where the rCASPR scan shows reduced image artefacts in comparison with the linear scan. The scan time for the linear scan was 8 minutes and the scan time for rCASPR scan was 5 minutes. Sequence parameters such as the field-of-view and image resolution were identical for both scans.

Motion corrected PET-MRI for treatment of oligometastatic disease

Integrated PET-MRI systems have been clinically used in radiology as of 2010 [309]. Approximately 80% of the clinical applications, so far, have been focused on oncology and were primarily directed at prostate, brain and head-and-neck cancer [310]. Another emerging application is the detection of small lesions or metastasized lymph nodes in the body [311, 312]. In particular, small tumors/lymph nodes that are affected by respiratory motion will benefit the most from the integrated PET-MRI systems [313]. The ability to detect oligometastatic disease with high precision, coupled with recent clinical insights into the advantages for local treatment for oligometastasis [314, 315], could provide a new treatment regimen for MR-linac systems. The inclusion of such a hybrid PET-MRI system into the MR-linac stereotactic radiotherapy workflow could provide the precision required to irradiate multiple oligometastasis within a single fraction [316]. Such novel treatment modality would be a radical departure from the traditional oncology and could redefine the treatment for patients with metastatic disease. The philosophy of using the PET signal directly for targeting of oligometastatic disease has recently attracted a 100M USD dollar investment for the development of the RefleXion X1 system, developed by Medical (Hayward, CA) [317]. The RefleXion systems is a PET-CT based linear accelerator and therefore does not provide the same possibilities for motion correction of the PET signal compared to the PET-MRI MR-linac pipeline. RefleXion termed the treatment of oligometastatic disease by targeting via the PET signal Biology-guided radiotherapy.

One crucial component for the success of biology-guided radiotherapy is the high target precision of the oligometastasis, which is absolutely required to prevent a too high integral dose. To provide the best possible PET image quality high spatiotemporal motion fields, throughout the entire PET examinations, are required for motion correction. These requirements are very similar to the the online real-time imaging workflow for MR-linac and therefore would equally benefit from the technology described in 8.2.1. The radiotherapy department of the UMC Utrecht is currently developing such an integrated PET-MRI systems with very similar imaging hardware to the Unity MR-linac. In the future I hope to continue to work on the clinical implementation of the MR-linac imaging workflow for 2025 to ultimately contribute to a successful implementation of biology-guided radiotherapy.

8.3 Concluding remarks

The technical developments of this thesis contribute to the usage of MRI in radiotherapy with the ultimate goal to improve the clinical outcomes for patients with cancer. These improvements are partially effectuated through the use of MRI in treatment simulation, but the pinnacle of these improvements resides in the use of the MR-linac system. The MR-linac enables us to continuously monitor the patient's internal anatomy prior to, during and after treatment fractions. The high imaging rate provides us with the unique possibility to not only work towards a 0 mm positioning related margin through real-time replanning, but to

also provide comprehensive soft-tissue characterization to inform us on the local response of the tumor and organs at risk to the therapy. The implementation of such an advanced treatment modality will allow us to accurately determine normal tissue complication probability models and to revisit traditional radiotherapy concepts such as fractionation schemes. However, the current software embedding of the MR-linac does not yet provide sufficient functionality to become the platform to achieve these goals. Some of these software functionalities are related the MR imaging, as discussed in this thesis, while others involve auto-segmentation, real-time image registration and fast plan adaptation. The further development and integration of these new software modules will be absolute essential for the long term clinical impact of the MR-linac.

Samenvatting

Radiotherapie is een therapeutische modaliteit die tumoren door het gehele lichaam niet-invasief kan behandelen. De werkzaamheid van radiotherapie wordt grotendeels bepaald door de hoeveelheid straling (de dosis) die aan de tumor kan worden afgegeven. De maximale tumor dosis wordt in de praktijk vaak beperkt aangezien dit leidt tot een te hoge dosis aan de omliggende gezonde organen. Veel innovatie binnen de radiotherapie is daarom ook gericht op het nauwkeuriger bestralen van tumoren met behulp van medische beeldvorming. MRI is zo'n beeldvormende modaliteit met uitstekende en veelzijdige zacht-weefsel contrast waardoor die zeer geschikt is voor het visualiseren van de tumoren en de omliggende organen. Tevens biedt MRI de flexibiliteit en de snelheid om de fysiologische beweging van de anatomie te visualiseren, in willekeurige oriëntaties, zonder het gebruik van ioniserende straling. Deze voordelen maken MRI de ultieme modaliteit voor de beeldgestuurde radiotherapie.

De radiotherapie afdeling in het UMC Utrecht is volledig ingericht op de hierboven beschreven visie en is al vanaf 2002 bezig met de technische ontwikkeling en vanaf 2017 met de klinische implementatie van de MR-linac. De MR-linac is een combinatie van een radiotherapie versneller met een diagnostische MRI. De MR-linac kan zowel vooraf als tijdens de bestraling beelden opnemen die gebruikt kunnen worden om de behandeling in real-time aan te passen. Echter, zijn de huidige MRI sequenties, afkomstig uit de diagnostiek, niet toereikend om de MR-linac optimaal in te kunnen zetten. Dit proefschrift draagt bij aan de ontwikkeling van nieuwe MRI technieken die specifiek op maat zijn gemaakt voor de beeldgestuurde radiotherapie. Deze MRI technieken worden ingezet tijdens de simulatie van de behandeling (pre-treatment, hoofdstuk 2-3), vlak voor bestraling (pre-beam, hoofdstuk 4-5), gedurende de bestraling (beam-on, hoofdstuk 6) en na afloop van de bestraling (beam-off, hoofdstuk 7).

In **hoofdstuk 2** wordt de beweeglijkheid van de tumoren in patiënten met hoofd-hals kanker bepaald om onzekerheidsmarges (PTV) uit te rekenen voor de be-

handeling. Hiervoor zijn standaard beschikbare spoiled gradient echo MRI scans opgenomen van 100 patiënten en werd de beweging gequantificeerd met niet-rigide beeldregistratie. De beweging werd vervolgens gebruikt om PTV marges op populatie niveau te bepalen. Deze marges waren significant kleiner dan de huidige klinische marges en hebben daarom geleid tot een adaptatie van de marges in de kliniek. Daarnaast gaf dit onderzoek ons inzicht in de limitaties van de standaard beschikbare MRI scans voor het quantificeren van de beweging.

Balanced steady-state free precession (bSSFP) scans zijn, vanuit theoretisch oogpunt, geschikter voor snelle imaging (in vergelijking met de spoiled scans van hoofdstuk 2). bSSFP scans zijn echter gevoeliger voor beeld artefacten die ontstaan door imperfecties in het gradient systeem. Deze imperfecties worden gequantificeerd in **hoofdstuk 3** door het meten van de zogenaamde gradientspoel impulse response functie. We laten zien dat de impulse response alle informatie bevat om deze artefacten te kunnen voorspellen. Ook beschrijven we een nieuwe methode om deze artefacten te corrigeren. De impulse response wordt vervolgens gebruikt in de latere hoofdstukken om robuuste niet-Cartesische scans te faciliteren.

Hoofdstuk 4 richt zich op het ontwerp van een nieuwe pre-beam MR-linac scan (genaamd MR-RIDDLE) die optimaal integreert met de online radiotherapie workflow. MR-RIDDLE gebruikt niet-Cartesische golden angle radieele opnames om beelden te reconstrueren met verschillende resoluties gedurende de MR scan. Hierbij zijn lage resolutie beelden na een hele korte scan tijd beschikbaar, waarna de data opname doorgaat en er continue hogere resolutie updates komen. Wij anticiperen dat dit nieuwe concept, betreffende de parallelisatie van de beeldvorming en de klinische taken, potentie heeft om de online workflow significant te stroomlijnen en te versnellen.

Hoofdstuk 5 richt zich op het ontwerp van een generieke doorgeademde imaging techniek die simultaan de ademhalings beweging quantificeert en corrigeert. Wij stellen een nieuwe acquisitie voor, genaamd rCASPR. rCASPR zorgt voor een vergelijkbaar beeld contrast t.o.v. reguliere klinische scans, terwijl rCASPR het mogelijk maakt om de data te gebruiken voor een 4D-MRI reconstructie. De 4D-MRI wordt vervolgens gebruikt om de ademhalings beweging te quantificeren, hetgeen benodigd is voor de bewegings gecorrigeerde beeld reconstructie. De kerngedachte is dat klinische ademhalings getriggerde scans hiermee eenvoudig vervangen zouden kunnen worden voor doorgeademde rCASPR scans zonder verlies van beeld contrast of toename van de scan tijd. Hiermee zou rCASPR een robuuste en generieke oplossing kunnen bieden voor de pre-treatment of pre-beam imaging om de tumoren in te tekenen.

Hoofdstuk 6 focust op de implementatie van een nieuwe beam-on imaging methode om retrospectief tijdsopgeloste niet-rigide bewegingsvelden te reconstrueren met zeer hoge tijdruimtelijk resolutie (> 10 Hz voor 3D). Hier bouwen wij verder op een, voorafgaand beschreven, bewegings quantificatie framework genaamd MR-MOTUS, wat wordt uitgebreid met een low-rank signaal model en een prospectieve implementatie op de MR-linac. Low-rank MR-MOTUS maakt gebruik van tijdruimtelijke correlaties in de beweging en invertteert een signaal model

dat rechtsstreeks de bewegingsvelden correleert met de k-space data. Deze tijd-sopgeloste bewegingsvelden zijn benodigd voor dosis accumulatie en zouden het fundament kunnen vormen voor real-time bewegings quantificatie for "gaten" en "tracken". Mijn aandeel in dit project bestaat hoofdzakelijk uit de ontwikkeling van de k-space trajectory, de prospectieve implementatie op de MR-linac en het voorbewerken van het ruwe MRI signaal voorafgaande aan MR-MOTUS.

Hoofdstuk 7 onderzoekt de technische haalbaarheid van magnetic resonance fingerprinting (MRF) voor het dagelijks monitoren van de tumorresponse op de MR-linac. MRF is een snelle multi-parametrische kwantitatieve MRI techniek die afhankelijk is van afdoende controle over de systeem imperfecties. Onder deze imperfecties vallen ongewilde wervelstromen en ΔB_1^+ , welke significant verschillen op een MR-linac t.o.v. een diagnostisch systeem. In dit onderzoek concluderen wij dat MRF haalbaar is op een MR-linac systeem waarbij de precisie en de nauwkeurigheid ruim voldoende zijn voor verder onderzoek naar de toepassing van MRF voor online kwantitatieve MRI-gestuurde radiotherapie.

De technische ontwikkelingen beschreven in dit proefschrift dragen bij aan het gebruik van MRI in radiotherapie met het uiteindelijke doel om de klinische resultaten van patiënten met kanker te verbeteren. Deze verbeteringen worden deels bewerkstelligd door het gebruik van MRI in de simulatie fase, maar het hoogtepunt van deze verbeteringen zit in het gebruik van het MR-linac systeem. De MR-linac stelt ons in staat om de interne anatomie van de patiënt continue te monitoren, zowel voorafgaande, gedurende en na de individuele fracties. Deze hoge frequentie van beeldvorming voorziet ons van de unieke mogelijkheid om niet alleen naar een 0 mm positie gerelateerde onzekerheidsmargin te werken, maar ook om naar een alomvattende zacht-weefsel karakterisatie toe te werken. Hierdoor worden wij beter geïnformeerd over de lokale response van de tumor. De klinische implementatie van zo'n geavanceerde therapeutische modaliteit zal ons in staat stellen om nauwkeurig vast te stellen wanneer in gezonde weefsel complicaties optreden en om traditionele radiotherapie concepten zoals de fractionatie schemas opnieuw onder de loep te nemen. Echter, biedt de huidige software embedding van de MR-linac niet voldoende functionaliteit om het platform te worden om deze doelen te bereiken. Een aantal van deze software functionaliteiten zijn gerelateerd aan de MR beeldvorming, zoals beschreven in dit proefschrift, terwijl andere betrekking hebben op auto-segmentatie, beeld registratie en snelle plan adaptatie. De verdere ontwikkeling en integratie van deze nieuwe softwaremodules zal absoluut essentieel zijn voor de lange termijn klinische impact van de MR-linac.

Bibliography

- [1] Tyldesley S, Delaney G, Foroudi F, Barbera L, Kerba M, Mackillop W. Estimating the need for radiotherapy for patients with prostate, breast, and lung cancers: verification of model estimates of need with radiotherapy utilization data from British Columbia. *International journal of radiation oncology, biology, physics* 2011; 79:1507–1515.
- [2] Barton MB, Jacob S, Shafiq J, Wong K, Thompson SR, Hanna TP, Delaney GP. Estimating the demand for radiotherapy from the evidence: a review of changes from 2003 to 2012. *Radiotherapy and oncology : journal of the European Society for Therapeutic Radiology and Oncology* 2014; 112:140–144.
- [3] Ward JF. DNA Damage Produced by Ionizing Radiation in Mammalian Cells: Identities, Mechanisms of Formation, and Reparability. *Progress in Nucleic Acid Research and Molecular Biology* 1988; 35:95–125.
- [4] Jackson SP, Bartek J. The DNA-damage response in human biology and disease. *Nature* 2009; 461:1071–1078.
- [5] Schultheiss TE, Orton CG, Peck RA. Models in radiotherapy: volume effects. *Medical physics* 1983; 10:410–415.
- [6] Palma G, Monti S, Conson M, Pacelli R, Cella L. Normal tissue complication probability (NTCP) models for modern radiation therapy. *Seminars in Oncology* 2019; 46:210–218.
- [7] Connell PP, Hellman S. Advances in radiotherapy and implications for the next century: A historical perspective. *Cancer Research* 2009; 69:383–392.
- [8] Nederlandse Commissie Voor Stralingsdosimetrie, Code of Practice for the Quality Assurance and Control for Intensity Modulated Radiotherapy Disclaimer regarding NCS reports, Technical Report June, Nederlandse Commissie Voor Stralingsdosimetrie, 2013.
- [9] Brahme A, Roos JE, Lax I. Solution of an integral equation encountered in rotation therapy. *Physics in medicine and biology* 1982; 27:1221–1229.
- [10] Brahme A. Optimization of stationary and moving beam radiation therapy techniques. *Radiotherapy and oncology : journal of the European Society for Therapeutic Radiology and Oncology* 1988; 12:129–140.
- [11] Webb S. Optimisation of conformal radiotherapy dose distribution by simulated annealing. *Physics in Medicine and Biology* 1989; 34:1349–1370.
- [12] Bortfeld T, Bürkelbach J, Boesecke R, Schlegel W. Methods of image reconstruction from projections applied to conformation radiotherapy. *Physics in medicine and biology* 1990; 35:1423–1434.
- [13] Brahme A. Multi leaf collimator, 1987.
- [14] Carol M, Grant WHr, Pavord D, Eddy P, Targovnik HS, Butler B, Woo S, Figura J, Onufrey V, Grossman R, Selkar R. Initial clinical experience with the Peacock intensity modulation of a 3-D conformal radiation therapy system. *Stereotactic and functional neurosurgery* 1996; 66:30–34.
- [15] Ling CC, Burman C, Chui CS, Kutcher GJ, Leibel SA, LoSasso T, Mohan R, Bortfeld T, Reinstein L, Spirou S, Wang XH, Wu Q, Zelefsky M, Fuks Z. Conformal radiation treatment of prostate cancer using inversely-planned intensity-modulated photon beams produced with dynamic multileaf collimation. *International journal of radiation oncology, biology, physics* 1996; 35:721–730.
- [16] Otto K. Volumetric modulated arc therapy: IMRT in a single gantry arc. *Medical physics* 2008; 35:310–317.
- [17] Dawson LA, Ménard C. Imaging in Radiation Oncology: A Perspective. *The Oncologist* 2010; 15:338–349.
- [18] Battista JJ, Rider WD, Van Dyk J. Computed tomography for radiotherapy planning. *International journal of radiation oncology, biology, physics* 1980; 6:99–107.
- [19] International Commission on Radiation Units and Measurements (ICRU), ICRU report 50: Prescribing, Recording and Reporting Photon Beam therapy, Technical report, International Commission on Radiation Units and Measurements (ICRU), 1993.

- [20] Van Herk M. Errors and Margins in Radiotherapy. *Seminars in Radiation Oncology* 2004; 14:52–64.
- [21] Van Herk M, Remeijer P, Rasch C, Lebesque JV. The probability of correct target dosage: Dose-population histograms for deriving treatment margins in radiotherapy. *International Journal of Radiation Oncology Biology Physics* 2000; 47:1121–1135.
- [22] Goitein M. Causes and consequences of inhomogeneous dose distributions in radiation therapy. *International journal of radiation oncology, biology, physics* 1986; 12:701–704.
- [23] Verellen D, De Ridder M, Linthout N, Tournel K, Soete G, Storme G. Innovations in image-guided radiotherapy. *Nature reviews. Cancer* 2007; 7:949–960.
- [24] Archambault Y, Boylan C, Bullock D, Morgas T, Peltola J, Ruokokoski E, Genghi A, Haas B, Suhonen P, Thompson S. Making on-Line Adaptive Radiotherapy Possible Using Artificial Intelligence and Machine Learning for Efficient Daily Re-Planning. *MEDICAL PHYSICS INTERNATIONAL JOURNAL* 2020; 8:77–86.
- [25] Wieser HP, Cisternas E, Wahl N, Ulrich S, Stadler A, Mescher H, Müller LR, Klinge T, Gabrys H, Burigo L, Mairani A, Ecker S, Ackermann B, Ellerbrock M, Parodi K, Jäkel O, Bangert M. Development of the open-source dose calculation and optimization toolkit matRad. *Medical physics* 2017; 44:2556–2568.
- [26] Ménard C, van der Heide UA. Introduction: Magnetic resonance imaging comes of age in radiation oncology., jul 2014.
- [27] Chandarana H, Wang H, Tijssen RH, Das IJ. Emerging role of MRI in radiation therapy. *Journal of Magnetic Resonance Imaging* 2018; 48:1468–1478.
- [28] Schmidt MA, Payne GS. Radiotherapy planning using MRI, 2015.
- [29] Lagendijk JJ, Raaymakers BW, Van Den Berg CA, Moerland MA, Philippens ME, Van Vulpen M. MR guidance in radiotherapy, 2014.
- [30] Zaitsev M, Maclaren J, Herbst M. Motion artifacts in MRI: A complex problem with many partial solutions, oct 2015.
- [31] Wood ML, Henkelman RM. Suppression of respiratory motion artifacts in magnetic resonance imaging. *Medical physics* 1986; 13:794–805.
- [32] Ehman RL, McNamara MT, Pallack M, Hricak H, Higgins CB. Magnetic resonance imaging with respiratory gating: techniques and advantages. *AJR. American journal of roentgenology* 1984; 143:1175–1182.
- [33] Block KT, Chandarana H, Milla S, Bruno M, Mulholland T, Fatterpekar G, Hagiwara M, Grimm R, Geppert C, Kiefer B, Sodickson DK. Towards Routine Clinical Use of Radial Stack-of-Stars 3D Gradient-Echo Sequences for Reducing Motion Sensitivity. *Journal of the Korean Society of Magnetic Resonance in Medicine* 2014; 18:87–106.
- [34] Rohlfing T, Maurer CR, O'Dell WG, Zhong J. Modeling liver motion and deformation during the respiratory cycle using intensity-based nonrigid registration of gated MR images. *Medical Physics* 2004; 31:427–432.
- [35] Stemkens B, Paulson ES, Tijssen RH. Nuts and bolts of 4D-MRI for radiotherapy. *Physics in Medicine and Biology* 2018; 63:21TR01.
- [36] Cruz G, Atkinson D, Buerger C, Schaeffter T, Prieto C. Accelerated motion corrected three-dimensional abdominal MRI using total variation regularized SENSE reconstruction. *Magnetic Resonance in Medicine* 2016; 75:1484–1498.
- [37] Lagendijk JJW, Bakker CJ. MRI-guided radiotherapy: a MRI based linear accelerator. In: *ESTRO Istanbul 19th annual meeting*, 2000.
- [38] Lagendijk JJW, Raaymakers BW, Raaijmakers AJE, Overweg J, Brown KJ, Kerkhof EM, van der Put RW, Hårdemark B, van Vulpen M, van der Heide UA. MRI/linac integration. *Radiotherapy and Oncology* 2008; 86:25–29.
- [39] Dempsey J, Benoit D, Fitzsimmons J, Haghghat A, Li J, Low D, Mutic S, Palta J, Romeijn H, Sjoden G. A Device for Realtime 3D Image-Guided IMRT. *International Journal of Radiation Oncology*Biophysics* 2005; 63:S202.
- [40] Mutic S, Dempsey JF. The ViewRay System: Magnetic Resonance-Guided and Controlled Radiotherapy. *Seminars in Radiation Oncology* 2014; 24:196–199.
- [41] Raaymakers BW, Lagendijk JJ, Overweg J, Kok JG, Raaijmakers AJ, Kerkhof EM, Van Der Put RW, Meijnsing I, Crijns SP, Benedosso F, Van Vulpen M, De Graaff CH, Allen J, Brown KJ. Integrating a 1.5 T MRI scanner with a 6 MV accelerator: Proof of concept. *Physics in Medicine and Biology* 2009; 54.
- [42] Lagendijk JJ, Raaymakers BW, van Vulpen M. The Magnetic Resonance Imaging-Linac System, 2014.

- [43] Raaymakers BW, JürgenliemkSchulz IM, Bol GH, Glitzner M, Kotte AN, Van Asselen B, De Boer JC, Bluemink JJ, Hackett SL, Moerland MA, Woodings SJ, Wolthaus JW, Van Zijp HM, Philippens ME, Tijssen R, Kok JG, De Groot-Van Breugel EN, Kiekebosch I, Meijers LT, Nomden CN, Sikkes GG, Doornaert PA, Eppinga WS, Kasperts N, Kerkmeijer LG, Tersteeg JH, Brown KJ, Pais B, Woodhead P, Lagendijk JJ. First patients treated with a 1.5 T MRI-Linac: Clinical proof of concept of a high-precision, high-field MRI guided radiotherapy treatment. *Physics in Medicine and Biology* 2017; 62:L41–L50.
- [44] Kontaxis C, Bol GH, Stemkens B, Glitzner M, Prins FM, Kerkmeijer LG, Lagendijk JJ, Raaymakers BW. Towards fast online intrafraction replanning for free-breathing stereotactic body radiation therapy with the MR-linac. *Physics in Medicine and Biology* 2017; 62:7233–7248.
- [45] Keall P, Vedam S, George R, Bartee C, Siebers J, Lerma F, Weiss E, Chung T. The clinical implementation of respiratory-gated intensity-modulated radiotherapy. *Medical Dosimetry* 2006; 31:152–162.
- [46] Sonke JJ, Aznar M, Rasch C. Adaptive Radiotherapy for Anatomical Changes. *Seminars in Radiation Oncology* 2019; 29:245–257.
- [47] Overweg J, Raaymakers BW, Lagendijk JJW, Brown KJ. System for MRI guided Radiotherapy. In: *International Society for Magnetic Resonance in Medicine (ISMRM)*, 2009.
- [48] Overweg J, Uhlemann F, Jonas P, Amthor T, Forthmann P, Vesanen P, Virta T, Busch C, Brown K. Clinical MR-Linac System. In: *Proc. Intl. Soc. Mag. Reson. Med.* 23, 2015. p. 3070.
- [49] Crijs S, Raaymakers B. From static to dynamic 1.5T MRI-linac prototype: impact of gantry position related magnetic field variation on image fidelity. *Physics in medicine and biology* 2014; 59:3241–3247.
- [50] Tijssen RH, Philippens ME, Paulson ES, Glitzner M, Chugh B, Wetscherek A, Dubec M, Wang J, van der Heide UA. MRI commissioning of 1.5T MR-linac systems – a multi-institutional study. *Radiotherapy and Oncology* 2019; 132:114–120.
- [51] Jackson S, Glitzner M, Tijssen RH, Raaymakers BW. MRI B 0 homogeneity and geometric distortion with continuous linac gantry rotation on an Elekta Unity MR-linac. *Physics in Medicine and Biology* 2019; 64.
- [52] Kooreman ES, van Houdt PJ, Keesman R, Pos FJ, van Pelt VW, Nowee ME, Wetscherek A, Tijssen RH, Philippens ME, Thorwarth D, Wang J, ShuklaDave A, Hall WA, Paulson ES, van der Heide UA. ADC measurements on the unity MR-linac – a recommendation on behalf of the elekta unity MR-linac consortium. *Radiotherapy and Oncology* 2020; .
- [53] Bruijnen T, Stemkens B, Lagendijk JJW, van den Berg CAT, Tijssen RHN. Gradient system characterization of a 1.5T MRI-linac with application to UTE imaging. *International Society for Magnetic Resonance in Medicine (ISMRM)* 2018; p. 235.
- [54] Schakel T, Tijssen RH, Hoogduin HM, Philippens ME. Robust quantitative diffusion weighted MR on an MR-Linac system. In: *Proc. Intl. Soc. Mag. Reson. Med.* 26, 2018. p. 4168.
- [55] Kooreman ES, van Houdt PJ, Nowee ME, van Pelt VW, Tijssen RH, Paulson ES, GurneyChampion OJ, Wang J, Koetsveld F, van Buuren LD, ter Beek LC, van der Heide UA. Feasibility and accuracy of quantitative imaging on a 1.5 T MR-linear accelerator. *Radiotherapy and Oncology* 2019; 133:156–162.
- [56] Hoogcarspel SJ, Zijlema SE, Tijssen RH, Kerkmeijer LG, JürgenliemkSchulz IM, Lagendijk JJ, Raaymakers BW. Characterization of the first RF coil dedicated to 1.5 T MR guided radiotherapy. *Physics in Medicine and Biology* 2018; 63:0–10.
- [57] Zijlema SE, Tijssen RH, Malkov VN, Van Dijk L, Hackett SL, Kok JG, Lagendijk JJ, Van Den Berg CA. Design and feasibility of a flexible, on-body, high impedance coil receive array for a 1.5 T MR-linac. *Physics in Medicine and Biology* 2019; 64.
- [58] Glitzner M, “Motion compensation for MRI-guided radiotherapy”. *Utrecht University*, 2017.
- [59] Wolthaus JW, Schneider C, Sonke JJ, van Herk M, Belderbos JS, Rossi MM, Lebesque JV, Damen EM. Mid-ventilation CT scan construction from four-dimensional respiration-correlated CT scans for radiotherapy planning of lung cancer patients. *International Journal of Radiation Oncology Biology Physics* 2006; 65:1560–1571.
- [60] Wolthaus JWH, Sonke JJ, van Herk M, Damen EMF. Reconstruction of a time-averaged midposition CT scan for radiotherapy planning of lung cancer patients using deformable registration. *Med Phys* 2008; 35:3998–4011.
- [61] Glitzner M, de Senneville BD, Lagendijk JJW, Raaymakers BW, Crijs SPM. On-line 3 D motion estimation using low resolution MRI. *Physics in Medicine and Biology* 2015; 60:N301–N310.
- [62] GurneyChampion OJ, Mahmood F, van Schie M, Julian R, George B, Philippens ME, van der Heide UA, Thorwarth D, Redalen KR. Quantitative imaging for radiotherapy purposes. *Radiotherapy and Oncology* 2020; 146:66–75.

- [63] Mahmood F, Johannesen HH, Geertsen P, Hansen RH. Repeated diffusion MRI reveals earliest time point for stratification of radiotherapy response in brain metastases. *Physics in Medicine and Biology* 2017; 62:2990–3002.
- [64] Wong KH, Panek R, Dunlop A, Mcquaid D, Riddell A, Welsh LC, Murray I, Koh DM, Leach MO, Bhide SA, Nutting CM, Oyen WJ, Harrington KJ, Newbold KL. Changes in multimodality functional imaging parameters early during chemoradiation predict treatment response in patients with locally advanced head and neck cancer. *European Journal of Nuclear Medicine and Molecular Imaging* 2018; 45:759–767.
- [65] Borggreve AS, Heethuis SE, Boekhoff MR, Goense L, van Rossum PS, Brosens LA, van Lier AL, van Hillegersberg R, Lagendijk JJ, Mook S, Ruurda JP, Meijer GJ. Optimal timing for prediction of pathologic complete response to neoadjuvant chemoradiotherapy with diffusion-weighted MRI in patients with esophageal cancer. *European Radiology* 2020; 30:1896–1907.
- [66] Lustig M, Donoho D, Pauly JM. Sparse MRI: The application of compressed sensing for rapid MR imaging. *Magnetic Resonance in Medicine* 2007; 58:1182–1195.
- [67] Zijlstra F, Viergever MA, Seevinck PR. Evaluation of variable density and data-driven K-space undersampling for compressed sensing magnetic resonance imaging. *Investigative Radiology* 2016; 51:410–419.
- [68] Levine E, Daniel B, Vasanawala S, Hargreaves B, Saranathan M. 3D Cartesian MRI with compressed sensing and variable view sharing using complementary poisson-disc sampling. *Magnetic Resonance in Medicine* 2017; 77:1774–1785.
- [69] Block KT, Uecker M. Simple Method for Adaptive Gradient-Delay Compensation in Radial MRI. *International Society for Magnetic Resonance in Medicine (ISMRM)* 2011; p. 2816.
- [70] Lee JH, Hargreaves BA, Hu BS, Nishimura DG. Fast 3D Imaging Using Variable-Density Spiral Trajectories with Applications to Limb Perfusion. *Magnetic Resonance in Medicine* 2003; 50:1276–1285.
- [71] Chan RW, Ramsay EA, Cunningham CH, Plewes DB. Temporal stability of adaptive 3D radial MRI using multidimensional golden means. *Magnetic Resonance in Medicine* 2009; .
- [72] Johnson KM. Hybrid radial-cones trajectory for accelerated MRI. *Magnetic resonance in medicine* 2017; 77:1068–1081.
- [73] Block KT, Frahm J. Spiral imaging: A critical appraisal. *Journal of Magnetic Resonance Imaging* 2005; 21:657–668.
- [74] King KF, Ganin A, Zhou XJ, Bernstein MA. Concomitant gradient field effects in spiral scans. *Magnetic Resonance in Medicine* 1999; 41:103–112.
- [75] Duyn JH, Yang Y, Frank JA, Van Der Veen JW. Simple Correction Method for k-Space Trajectory Deviations in MRI. *Journal of Magnetic Resonance* 1998; 132:150–153.
- [76] Vannesjo SJ, Haerberlin M, Kasper L, Pavan M, Wilm BJ, Barmet C, Pruessmann KP. Gradient system characterization by impulse response measurements with a dynamic field camera. *Magnetic Resonance in Medicine* 2013; 69:583–593.
- [77] Haacke EM, Brown RW, Thompson MR, Venkatesan R, “Magnetic Resonance Imaging: Physical Principles and Sequence Design”. Wiley, 1999.
- [78] Bernstein MA, King KF, Zhou XJ, “Handbook of MRI Pulse Sequences”. Elsevier Science, 2004.
- [79] Wilm BJ, Barmet C, Pavan M, Pruessmann KP. Higher order reconstruction for MRI in the presence of spatiotemporal field perturbations. *Magnetic Resonance in Medicine* 2011; 65:1690–1701.
- [80] Huttinga NR, Van Den Berg CA, Luijten PR, Sbrizzi A. MR-MOTUS: model-based non-rigid motion estimation for MR-guided radiotherapy using a reference image and minimal k-space data. *Physics in Medicine and Biology* 2020; 65.
- [81] Ratko T, Douglas GW, Souza JD, Belinson SE, Aronson N. Radiotherapy Treatments for Head and Neck Cancer Update. *Effective Health Care Program: Comparative Effectiveness Review* 2014; 144.
- [82] Houweling AC, van der Meer S, van der Wal E, Terhaard CH, Raaijmakers CP. Improved immobilization using an individual head support in head and neck cancer patients. *Radiotherapy and Oncology* 2010; 96:100–103.
- [83] Nakata A, Tateoka K, Fujimoto K, Saito Y, Nakazawa T, Abe T, Yano M, Sakata K. The Reproducibility of Patient Setup for Head and Neck Cancers Treated with Image-Guided and Intensity-Modulated Radiation Therapies Using Thermoplastic Immobilization Device. *International Journal of Medical Physics, Clinical Engineering and Radiation Oncology* 2013; 02:117–124.

- [84] Astreimidou E, Bel A, Raaijmakers CPJ, Terhaard CHJ, Lagendijk JJW. Adequate margins for random setup uncertainties in head-and-neck IMRT. *International Journal of Radiation Oncology Biology Physics* 2005; 61:938–944.
- [85] Schubert LK, Westerly DC, Tomé WA, Mehta MP, Soisson ET, Mackie TR, Ritter MA, Khuntia D, Harari PM, Paliwal BR. A Comprehensive Assessment by Tumor Site of Patient Setup Using Daily MVCT Imaging From More Than 3,800 Helical Tomotherapy Treatments. *International Journal of Radiation Oncology Biology Physics* 2009; 73:1260–1269.
- [86] Kwa SL, AlMangani A, Osman SO, Gangsaas A, Levendag PC, Heijmen BJ. Inter- and intrafraction target motion in highly focused single vocal cord irradiation of t1a larynx cancer patients. *International Journal of Radiation Oncology Biology Physics* 2015; 93:190–195.
- [87] Castadot P, Geets X, Lee JA, Christian N, Grégoire V. Assessment by a deformable registration method of the volumetric and positional changes of target volumes and organs at risk in pharyngo-laryngeal tumors treated with concomitant chemo-radiation. *Radiotherapy and Oncology* 2010; 95:209–217.
- [88] International Commission on Radiation Units and Measurements (ICRU). Prescribing, Recording, and Reporting Photon-Beam Intensity-Modulated Radiation Therapy (IMRT) - Report 83. *Journal of the ICRU* 2010; 10:1–58.
- [89] Vugts CAJM, Terhaard CHJ, Philippens MEP, Pameijer FA, Kasperts N, Raaijmakers CPJ. Consequences of tumor planning target volume reduction in treatment of T2-T4 laryngeal cancer. *Radiation oncology (London, England)* 2014; 9:195.
- [90] Leonard RJ, Kendall KA, McKenzie S, Gonçalves MI, Walker A. Structural displacements in normal swallowing: A videofluoroscopic study. *Dysphagia* 2000; 15:146–152.
- [91] Van Asselen B, Raaijmakers CP, Lagendijk JJ, Terhaard CH. Intrafraction motions of the larynx during radiotherapy. *International Journal of Radiation Oncology Biology Physics* 2003; 56:384–390.
- [92] Prévost JB, de Boer H, Pöll J, Voet P, Levendag P. Analysis of the motion of oropharyngeal tumors and consequences in planning target volume determination. *Radiotherapy and Oncology* 2008; 87:268–273.
- [93] Dantas RO, Kern MK, Massey BT, Dodds WJ, Kahrilas PJ, Brasseur JG, Cook IJ, Lang IM. Effect of swallowed bolus variables on oral and pharyngeal phases of swallowing. *American Journal of Physiology - Gastrointestinal and Liver Physiology* 1990; 258.
- [94] Jacob P, Kahrilas PJ, Logemann JA, Shah V, Ha T. Upper esophageal sphincter opening and modulation during swallowing. *Gastroenterology* 1989; 97:1469–1478.
- [95] Bradley JA, Paulson ES, Ahunbay E, Schultz C, Li XA, Wang D. Dynamic MRI analysis of tumor and organ motion during rest and deglutition and margin assessment for radiotherapy of head-and-neck cancer. *International Journal of Radiation Oncology Biology Physics* 2011; 81.
- [96] Hamlet S, Ezzell G, Aref A. Larynx motion associated with swallowing during radiation therapy. *International Journal of Radiation Oncology, Biology, Physics* 1994; 28:467–470.
- [97] GurneyChampion OJ, McQuaid D, Dunlop A, Wong KH, Welsh LC, Riddell AM, Koh DM, Oelfke U, Leach MO, Nutting CM, Bhide SA, Harrington KJ, Panek R, Newbold KL. MRI-based Assessment of 3D Intrafractional Motion of Head and Neck Cancer for Radiation Therapy. *International Journal of Radiation Oncology Biology Physics* 2018; 100:306–316.
- [98] Bol GH, Kotte ANTJ, van der Heide UA, Lagendijk JJW. Simultaneous multi-modality ROI delineation in clinical practice. *Computer Methods and Programs in Biomedicine* 2009; 96:133–140.
- [99] Zachiu C, Denis De Senneville B, Moonen C, Ries M. A framework for the correction of slow physiological drifts during MR-guided HIFU therapies: Proof of concept. *Medical Physics* 2015; 42:4137–4148.
- [100] Zachiu C, Papadakis N, Ries M, Moonen C, Denis De Senneville B. An improved optical flow tracking technique for real-time MR-guided beam therapies in moving organs. *Physics in Medicine and Biology* 2015; 60:9003–9029.
- [101] Matsuo K, Palmer JB. Anatomy and physiology of feeding and swallowing: normal and abnormal. *Physical medicine and rehabilitation clinics of North America* 2008; 19:691–707, vii.
- [102] Wolthaus JW, Sonke JJ, van Herk M, Belderbos JS, Rossi MM, Lebesque JV, Damen EM. Comparison of Different Strategies to Use Four-Dimensional Computed Tomography in Treatment Planning for Lung Cancer Patients. *International Journal of Radiation Oncology Biology Physics* 2008; 70:1229–1238.
- [103] de Boer HC, Heijmen BJ. eNAL: An Extension of the NAL Setup Correction Protocol for Effective Use of Weekly Follow-up Measurements. *International Journal of Radiation Oncology Biology Physics* 2007; 67:1586–1595.

- [104] Chen AM, Farwell DG, Luu Q, Donald PJ, Perks J, Purdy JA. Evaluation of the planning target volume in the treatment of head and neck cancer with intensity-modulated radiotherapy: What is the appropriate expansion margin in the setting of daily image guidance? *International Journal of Radiation Oncology Biology Physics* 2011; 81:943–949.
- [105] Oliveira FP, Tavares JMR. Medical image registration: A review. *Computer Methods in Biomechanics and Biomedical Engineering* 2014; 17:73–93.
- [106] Schultheiss TE, Tome WA, Orton CG. Point/counterpoint: it is not appropriate to "deform" dose along with deformable image registration in adaptive radiotherapy. *Medical physics* 2012; 39:6531–6533.
- [107] Bertelsen A, Hansen CR, Johansen J, Brink C. Single Arc Volumetric Modulated Arc Therapy of head and neck cancer. *Radiotherapy and Oncology* 2010; 95:142–148.
- [108] Oppelt A, Graumann R, Barfuss H, Fischer H, Hartl W, Schajor W. FISP, a novel, fast pulse sequence for nuclear magnetic resonance imaging. *Electromedia* 1986; pp. 15–18.
- [109] Scheffler K, Lehnhardt S. Principles and applications of balanced SSFP techniques. *European Radiology* 2003; 13:2409–2418.
- [110] Bieri O, Scheffler K. Fundamentals of balanced steady state free precession MRI, 2013.
- [111] Schmitt P, Griswold MA, Jakob PM, Kotas M, Gulani V, Flentje M, Haase A. Inversion Recovery TrueFISP: Quantification of T1, T2, and Spin Density. *Magnetic Resonance in Medicine* 2004; 51:661–667.
- [112] Ma D, Gulani V, Seiberlich N, Liu K, Sunshine JL, Duerk JL, Griswold MA. Magnetic resonance fingerprinting. *Nature* 2013; 495:187–192.
- [113] Jung BA, Hennig J, Scheffler K. Single-breathhold 3D-trueFISP cine cardiac imaging. *Magnetic Resonance in Medicine* 2002; 48:921–925.
- [114] Tsao J, Kozerke S, Boesiger P, Pruessmann KP. Optimizing spatiotemporal sampling for k-t BLAST and k-t SENSE: Application to high-resolution real-time cardiac steady-state free precession. *Magnetic Resonance in Medicine* 2005; 53:1372–1382.
- [115] Bieri O, Markl M, Scheffler K. Analysis and compensation of eddy currents in balanced SSFP. *Magnetic Resonance in Medicine* 2005; 54:129–137.
- [116] Bi X, Park J, Deshpande V, Simonetti O, Laub G, Li D. Reduction of flow- and eddy-currents-induced image artifacts in coronary magnetic resonance angiography using a linear centric-encoding SSFP sequence. *Magnetic Resonance Imaging* 2007; 25:1138–1147.
- [117] Spincemaille P, Nguyen TD, Wang Y. View ordering for magnetization prepared steady state free precession acquisition: Application in contrast-enhanced MR angiography. *Magnetic Resonance in Medicine* 2004; 52:461–466.
- [118] Nielsen JF, Nayak KS. Interleaved balanced SSFP imaging: Artifact reduction using gradient waveform grouping. *Journal of Magnetic Resonance Imaging* 2009; 29:745–750.
- [119] Markl M, Leupold J, Bieri O, Scheffler K, Hennig J. Double average parallel steady-state free precession imaging: Optimized eddy current and transient oscillation compensation. *Magnetic Resonance in Medicine* 2005; 54:965–974.
- [120] Piccini D, Littmann A, NIELLES-VALLESPIN S, ZENGE MO. Spiral phyllotaxis: The natural way to construct a 3D radial trajectory in MRI. *Magnetic Resonance in Medicine* 2011; 66:1049–1056.
- [121] Wundrak S, Paul J, Ulrici J, Hell E, Rasche V. A small surrogate for the golden angle in time-resolved radial MRI based on generalized fibonacci sequences. *IEEE Transactions on Medical Imaging* 2015; 34:1262–1269.
- [122] Usman M, Ruijsink B, Nazir MS, Cruz G, Prieto C. Free breathing whole-heart 3D CINE MRI with self-gated Cartesian trajectory. *Magnetic Resonance Imaging* 2017; 38:129–137.
- [123] Barmet C, De Zanche N, Pruessmann KP. Spatiotemporal magnetic field monitoring for MR. *Magnetic resonance in medicine* 2008; 60:187–97.
- [124] Fischer RF, Barmet C, Rudin M, Boesiger P, Pruessmann KP, Kozerke S. Monitoring and compensating phase imperfections in cine balanced steady-state free precession. *Magnetic Resonance in Medicine* 2013; 70:1567–1579.
- [125] Brodsky EK, Klaers JL, Samsonov AA, Kijowski R, Block WF. Rapid measurement and correction of phase errors from B0 eddy currents: Impact on image quality for non-cartesian imaging. *Magnetic Resonance in Medicine* 2013; 69:509–515.
- [126] Rahmer J, Mazurkewitz P, Börnert P, Nielsen T. Rapid acquisition of the 3D MRI gradient impulse response function using a simple phantom measurement. *Magnetic Resonance in Medicine* 2019; 82:2146–2159.
- [127] Cukur T. Accelerated phase-cycled SSFP imaging with compressed sensing. *IEEE Transactions on Medical Imaging* 2015; 34:107–115.

- [128] Biyik E, Ilıcak E, Çukur T. Reconstruction by calibration over tensors for multi-coil multi-acquisition balanced SSFP imaging. *Magnetic Resonance in Medicine* 2018; 79:2542–2554.
- [129] Borman PT, Tijssen RH, Bos C, Moonen CT, Raaymakers BW, Glitzner M. Characterization of imaging latency for real-time MRI-guided radiotherapy. *Physics in Medicine and Biology* 2018; 63.
- [130] Guo L, Derbyshire JA, Herzka DA. Pseudo-projection-driven, self-gated cardiac cine imaging using cartesian golden step phase encoding. *Magnetic Resonance in Medicine* 2016; 76:417–429.
- [131] Winkelmann S, Schaeffter T, Koehler T, Eggers H, Doessel O. An optimal radial profile order based on the golden ratio for time-resolved MRI. *IEEE Transactions on Medical Imaging* 2007; 26:68–76.
- [132] Stich M. Temperature-dependent Gradient System Transfer Function (GSTF). In: 27th Annu. Meet. ISMRM Montreal, 2019. p. 0443.
- [133] Wilm BJ, Dietrich BE, Reber J, Vannesjo SJ, Pruessmann KP. Gradient Response Harvesting for Continuous System Characterization During MR Sequences. *IEEE transactions on medical imaging* 2020; 39:806–815.
- [134] Sbrizzi A, van der Heide O, Cloos M, van der Toorn A, Hoogduin H, Luijten PR, van den Berg CA. Fast quantitative MRI as a nonlinear tomography problem. *Magnetic Resonance Imaging* 2018; 46:56–63.
- [135] Keall PJ, Barton M, Crozier S. The Australian Magnetic Resonance Imaging-Linac Program. *Seminars in Radiation Oncology* 2014; 24:203–206.
- [136] Fallone BG. The Rotating Biplanar Linac-Magnetic Resonance Imaging System, 2014.
- [137] Pandey A, Yoruk U, Keerthivasan M, Galons JP, Sharma P, Johnson K, Martin DR, Altbach MI, Bilgin A, Saranathan M. Multiresolution imaging using golden angle stack-of-stars and compressed sensing for dynamic MR urography. *Journal of Magnetic Resonance Imaging* 2017; 46:303–311.
- [138] Stemkens B, Tijssen RH, De Senneville BD, Lagendijk JJ, Van Den Berg CA. Image-driven, model-based 3D abdominal motion estimation for MR-guided radiotherapy. *Physics in Medicine and Biology* 2016; .
- [139] Spincemaille P, Liu J, Nguyen T, Prince MR, Wang Y. Z intensity-weighted position self-respiratory gating method for free-breathing 3D cardiac CINE imaging. *Magnetic Resonance Imaging* 2011; 29:861–868.
- [140] Johnson KM, Block WF, Reeder SB, Samsonov A. Improved least squares MR image reconstruction using estimates of k-Space data consistency. *Magnetic Resonance in Medicine* 2012; 67:1600–1608.
- [141] Cheng JY, Zhang T, Ruangwattanapaisarn N, Alley MT, Uecker M, Pauly JM, Lustig M, Vasanawala SS. Free-breathing pediatric MRI with nonrigid motion correction and acceleration. *Journal of Magnetic Resonance Imaging* 2015; 42:407–420.
- [142] Glover GH, Pauly JM. Projection Reconstruction Techniques for Reduction of Motion Effects in MRI. *Magnetic Resonance in Medicine* 1992; 28:275–289.
- [143] Moussavi A, Untenberger M, Uecker M, Frahm J. Correction of gradient-induced phase errors in radial MRI. *Magnetic Resonance in Medicine* 2014; 71:308–312.
- [144] CampbellWashburn A, Xue H, Lederman R, Faranesh A, Hansen M. Real-time distortion correction of spiral MRI using the gradient system impulse response function. *Magnetic Resonance in Medicine* 2014; 75:2278–2285.
- [145] Pang J, Bhat H, Sharif B, Fan Z, Thomson LE, Labounty T, Friedman JD, Min J, Berman DS, Li D. Whole-heart coronary MRA with 100% respiratory gating efficiency: Self-navigated three-dimensional retrospective image-based motion correction (TRIM). *Magnetic Resonance in Medicine* 2014; 71:67–74.
- [146] Fessler JA, Sutton BP. Nonuniform fast Fourier transforms using min-max interpolation. *IEEE Transactions on Signal Processing* 2003; 51:560–574.
- [147] Roemer PB, Edelstein WA, Hayes CE, Souza SP, Mueller OM. The NMR phased array. *Magnetic Resonance in Medicine* 1990; 16:192–225.
- [148] Uecker M, Lai P, Murphy MJ, Virtue P, Elad M, Pauly JM, Vasanawala SS, Lustig M. ESPIRiT - An eigenvalue approach to autocalibrating parallel MRI: Where SENSE meets GRAPPA. *Magnetic Resonance in Medicine* 2014; 71:990–1001.
- [149] Zhang T, Cheng JY, Potnick AG, Barth RA, Alley MT, Uecker M, Lustig M, Pauly JM, Vasanawala SS. Fast pediatric 3D free-breathing abdominal dynamic contrast enhanced MRI with high spatiotemporal resolution. *Journal of Magnetic Resonance Imaging* 2015; 41:460–473.

- [150] Weiger M, Börner P, Proksa R, Schäffter T, Haase A. Motion-adapted gating based on k-space weighting for reduction of respiratory motion artifacts. *Magnetic Resonance in Medicine* 1997; 38:322–333.
- [151] Segars WP, Sturgeon G, Mendonca S, Grimes J, Tsui BM. 4D XCAT phantom for multimodality imaging research. *Medical Physics* 2010; 37:4902–4915.
- [152] Heerkens HD, Reerink O, Intven MP, Hiensch RR, van den Berg CA, Crijs SP, van Vulpen M, Meijer GJ. Pancreatic tumor motion reduction by use of a custom abdominal corset. *Physics and Imaging in Radiation Oncology* 2017; 2:7–10.
- [153] Stam MK, van Vulpen M, Barendrecht MM, Zonnenberg BA, Intven M, Crijs SPM, Lagendijk JJW, Raaymakers BW. Kidney motion during free breathing and breath hold for MR-guided radiotherapy. *Physics in medicine and biology* 2013; 58:2235–2245.
- [154] GuizarSicairos M, Thurman ST, Fienup JR. Efficient subpixel image registration algorithms. *Optics Letters* 2008; 33:156.
- [155] Benkert T, Feng L, Sodickson DK, Chandarana H, Block KT. Free-breathing volumetric fat/water separation by combining radial sampling, compressed sensing, and parallel imaging. *Magnetic Resonance in Medicine* 2017; 78:565–576.
- [156] Stemkens B, Tijssen RHN, Denis de Senneville B, Heerkens HD, Vulpen MV, Lagendijk JJW, van den Berg CAT. Optimizing 4-Dimensional Magnetic Resonance Imaging Data Sampling for Respiratory Motion Analysis of Pancreatic Tumors. *Int. J. Radiat. Oncol. Biol. Phys.* 2015; 91:571–578.
- [157] Stemkens B, Benkert T, Chandarana H, Bittman ME, Van den Berg CA, Lagendijk JJ, Sodickson DK, Tijssen RH, Block KT. Adaptive bulk motion exclusion for improved robustness of abdominal magnetic resonance imaging. *NMR in Biomedicine* 2017; 30.
- [158] Zhang T, Cheng JY, Chen Y, Nishimura DG, Pauly JM, Vasanaawala SS. Robust self-navigated body MRI using dense coil arrays. *Magnetic Resonance in Medicine* 2016; 76:197–205.
- [159] Feng L, Grimm R, Block KT, Chandarana H, Kim S, Xu J, Axel L, Sodickson DK, Otazo R. Golden-angle radial sparse parallel MRI: combination of compressed sensing, parallel imaging, and golden-angle radial sampling for fast and flexible dynamic volumetric MRI. *Magnetic resonance in medicine* 2014; .
- [160] Feng L, Axel L, Chandarana H, Block KT, Sodickson DK, Otazo R. XD-GRASP: Golden-angle radial MRI with reconstruction of extra motion-state dimensions using compressed sensing. *Magnetic Resonance in Medicine* 2016; 75:775–788.
- [161] Batchelor PG, Atkinson D, Irrarazaval P, Hill DLG, Hajnal J, Larkman D. Matrix description of general motion correction applied to multishot images. *Magnetic Resonance in Medicine* 2005; 54:1273–1280.
- [162] Buerger C, Prieto C, Schaeffter T. Highly efficient 3D motion-compensated abdomen MRI from undersampled golden-RPE acquisitions. *Magnetic Resonance Materials in Physics, Biology and Medicine* 2013; 26:419–429.
- [163] Mugler JP. Optimized three-dimensional fast-spin-echo MRI. *Journal of Magnetic Resonance Imaging* 2014; 39:745–767.
- [164] Freedman JN, Collins DJ, GurneyChampion OJ, McClelland JR, Nill S, Oelfke U, Leach MO, Wetscherek A. Super-resolution T2-weighted 4D MRI for image guided radiotherapy. *Radiotherapy and Oncology* 2018; 129:486–493.
- [165] Watanabe Y, Nagayama M, Okumura A, Amoh Y, Katsube T, Suga T, Koyama S, Nakatani K, Dodo Y. MR Imaging of Acute Biliary Disorders. *RadioGraphics* 2007; 27:477–495.
- [166] Arizono S, Isoda H, Maetani YS, Hirokawa Y, Shimada K, Nakamoto Y, Togashi K. High-spatial-resolution three-dimensional MR cholangiography using a high-sampling-efficiency technique (SPACE) at 3T: Comparison with the conventional constant flip angle sequence in healthy volunteers. *Journal of Magnetic Resonance Imaging* 2008; 28:685–690.
- [167] Albiin N. MRI of Focal Liver Lesions. *Current medical imaging reviews* 2012; 8:107–116.
- [168] Benkert T, Mugler JP, Rigie DS, Sodickson DK, Chandarana H, Block KT. Hybrid T2 - and T1 -weighted radial acquisition for free-breathing abdominal examination. *Magnetic Resonance in Medicine* 2018; 80:1935–1948.
- [169] Song HK, Dougherty L. k-Space weighted image contrast (KWIC) for contrast manipulation in projection reconstruction MRI. *Magnetic Resonance in Medicine* 2000; 44:825–832.
- [170] Block KT, Uecker M, Frahm J. Model-based iterative reconstruction for radial fast spin-echo MRI. *IEEE Transactions on Medical Imaging* 2009; 28:1759–1769.
- [171] Rank CM, Heußner T, Buzan MT, Wetscherek A, Freitag MT, Dinkel J, Kachelrieß M. 4D respiratory motion-compensated image reconstruction of free-breathing radial MR data with very high undersampling. *Magnetic Resonance in Medicine* 2017; 77:1170–1183.

- [172] Prieto C, Doneva M, Usman M, Henningsson M, Greil G, Schaeffter T, Botnar RM. Highly efficient respiratory motion compensated free-breathing coronary MRA using golden-step Cartesian acquisition. *Journal of Magnetic Resonance Imaging* 2015; 41:738–746.
- [173] Greer JS, Wang X, Wang Y, Pinho MC, Maldjian JA, Pedrosa I, Madhuranthakam AJ. Robust pCASL perfusion imaging using a 3D Cartesian acquisition with spiral profile reordering (CASPR). *Magnetic Resonance in Medicine* 2019; 82:1713–1724.
- [174] Kolbitsch C, Neji R, Fenchel M, Mallia A, Marsden P, Schaeffter T. Fully integrated 3D high-resolution multicontrast abdominal PET-MR with high scan efficiency. *Magnetic Resonance in Medicine* 2018; 79:900–911.
- [175] Glitzner M, De Senneville BD, Lagendijk JJ, Raaymakers BW, Crijs SP. On-line 3D motion estimation using low resolution MRI. *Physics in Medicine and Biology* 2015; 60:N301–N310.
- [176] Zhu X, Chan M, Lustig M, Johnson KM, Larson PE. Iterative motion-compensation reconstruction ultra-short TE (iMoCo UTE) for high-resolution free-breathing pulmonary MRI. *Magnetic Resonance in Medicine* 2020; 83:1208–1221.
- [177] Cruz G, Atkinson D, Buerger C, Schaeffter T, Prieto C. Accelerated motion corrected three-dimensional abdominal MRI using total variation regularized SENSE reconstruction. *Magnetic Resonance in Medicine* 2016; 75:1484–1498.
- [178] McGee KP, Manduca A, Felmlee JP, Riederer SJ, Ehman RL. Image metric-based correction (Autocorrection) of motion effects: Analysis of image metrics. *Journal of Magnetic Resonance Imaging* 2000; 11:174–181.
- [179] Bruijnen T. [www.github.com/tombbruijnen/rcaspr-mcir](https://github.com/tombbruijnen/rcaspr-mcir), 2021.
- [180] Pruessmann KP, Weiger M, Scheidegger MB, Boesiger P. SENSE: Sensitivity encoding for fast MRI. *Magnetic Resonance in Medicine* 1999; 42:952–962.
- [181] Han F, Zhou Z, Cao M, Yang Y, Sheng K, Hu P. Respiratory motion-resolved, self-gated 4D-MRI using rotating cartesian k-space (ROCK). *Medical Physics* 2017; 44:1359–1368.
- [182] Jiang W, Ong F, Johnson KM, Nagle SK, Hope TA, Lustig M, Larson PEZ. Motion robust high resolution 3D free-breathing pulmonary MRI using dynamic 3D image self-navigator. *Magnetic resonance in medicine* 2018; 79:2954–2967.
- [183] Uecker M, Ong F, Tamir JI, Bahri D, Virtue P, Cheng J, Zhang T, Lustig M. Berkeley Advanced Reconstruction Tools. *Proc. Intl. Soc. Mag. Reson. Med.* 2015; 73:828–842.
- [184] Thirion JP. Image matching as a diffusion process: An analogy with Maxwell’s demons. *Medical Image Analysis* 1998; 2:243–260.
- [185] Vercauteren T, Pennec X, Perchant A, Ayache N. Diffeomorphic demons: efficient non-parametric image registration. *NeuroImage* 2009; 45:S61–S72.
- [186] Metz CT, Klein S, Schaap M, van Walsum T, Niessen WJ. Nonrigid registration of dynamic medical imaging data using nD+t B-splines and a groupwise optimization approach. *Medical Image Analysis* 2011; 15:238–249.
- [187] Yang D, Li H, Low DA, Deasy JO, Naqa IE. A fast inverse consistent deformable image registration method based on symmetric optical flow computation. *Physics in Medicine and Biology* 2008; 53:6143–6165.
- [188] Polak E, Ribiere G. Note sur la convergence de méthodes de directions conjuguées. *Revue française d’informatique et de recherche opérationnelle. Série rouge* 1969; 3:35–43.
- [189] Bruijnen T, Stemkens B, Lagendijk JJ, Van Den Berg CA, Tijssen RH. Multiresolution radial MRI to reduce IDLE time in pre-beam imaging on an MR-Linac (MR-RIDDLE). *Physics in Medicine and Biology* 2019; 64:055011.
- [190] Weigel M. Extended phase graphs: Dephasing, RF pulses, and echoes - Pure and simple, 2015.
- [191] Zachiu C, De Senneville BD, Raaymakers BW, Ries M. Biomechanical quality assurance criteria for deformable image registration algorithms used in radiotherapy guidance. *Physics in Medicine and Biology* 2020; 65.
- [192] Odille F, Vuissoz PA, Felblinger J, Atkinson D. Generalized Reconstruction by Inversion of Coupled Systems (GRICS) applied to parallel MRI. In: 2008 5th IEEE International Symposium on Biomedical Imaging: From Nano to Macro, Proceedings, ISBI, 2008. pp. 1019–1022.
- [193] Loktyushin A, Nickisch H, Pohmann R, Schölkopf B. Blind retrospective motion correction of MR images. *Magnetic Resonance in Medicine* 2013; 70:1608–1618.
- [194] Terpstra ML, Maspero M, D’Agata F, Stemkens B, Intven MP, Lagendijk JJ, Van Den Berg CA, Tijssen RH. Deep learning-based image reconstruction and motion estimation from undersampled radial k-space for real-time MRI-guided radiotherapy. *Physics in Medicine and Biology* 2020; 65:155015.

- [195] Rank CM, Heußer T, Wetscherek A, Freitag MT, Sedlaczek O, Schlemmer HP, Kachelrieß M. Respiratory motion compensation for simultaneous PET/MR based on highly undersampled MR data. *Medical Physics* 2016; 43:6234–6245.
- [196] Keall PJ, Mageras GS, Balter JM, Emery RS, Forster KM, Jiang SB, Kapatoes JM, Low DA, Murphy MJ, Murray BR, Ramsey CR, Van Herk MB, Vedam SS, Wong JW, Yorke E. The management of respiratory motion in radiation oncology report of AAPM Task Group 76. *Medical Physics* 2006; 33:3874–3900.
- [197] Murphy MJ, Martin D, Whyte R, Hai J, Ozhasoglu C, Le QT. The effectiveness of breath-holding to stabilize lung and pancreas tumors during radiosurgery. *International Journal of Radiation Oncology Biology Physics* 2002; .
- [198] De Muinck Keizer DM, Kontaxis C, Kerkmeijer LG, Van Der Voort Van Zyp JR, Van Den Berg CA, Raaymakers BW, Lagendijk JJ, De Boer JC. Dosimetric impact of soft-tissue based intrafraction motion from 3D cine-MR in prostate SBRT. *Physics in Medicine and Biology* 2020; 65.
- [199] Breuer K, Meyer CB, Breuer FA, Richter A, Exner F, Weng AM, Ströhle S, Polat B, Jakob PM, Sauer OA, Flentje M, Weick S. Stable and efficient retrospective 4D-MRI using non-uniformly distributed quasi-random numbers. *Physics in Medicine and Biology* 2018; 63.
- [200] Deng Z, Pang J, Yang W, Yue Y, Sharif B, Tuli R, Li D, Fraass B, Fan Z. Four-dimensional MRI using three-dimensional radial sampling with respiratory self-gating to characterize temporal phase-resolved respiratory motion in the abdomen. *Magnetic Resonance in Medicine* 2016; .
- [201] Cai J, Chang Z, Wang Z, Paul Segars W, Yin FF. Four-dimensional magnetic resonance imaging (4D-MRI) using image-based respiratory surrogate: A feasibility study. *Medical Physics* 2011; 38:6384–6394.
- [202] Paganelli C, Kipritidis J, Lee D, Baroni G, Keall P, Riboldi M. Image-based retrospective 4D MRI in external beam radiotherapy: A comparative study with a digital phantom. *Medical physics* 2018; 45:3161–3172.
- [203] Bjerre T, Crijns S, Rosenschöld PMA, Aznar M, Specht L, Larsen R, Keall P. Three-dimensional MRI-linac intra-fraction guidance using multiple orthogonal cine-MRI planes. *Physics in Medicine and Biology* 2013; 58:4943–4950.
- [204] Tryggestad E, Flammang A, HanOh S, Hales R, Herman J, McNutt T, Roland T, Shea SM, Wong J. Respiration-based sorting of dynamic MRI to derive representative 4D-MRI for radiotherapy planning. *Medical Physics* 2013; 40.
- [205] Brix L, Ringgaard S, Sørensen TS, Poulsen PR. Three-dimensional liver motion tracking using real-time two-dimensional MRI. *Medical Physics* 2014; 41.
- [206] Seregini M, Paganelli C, Lee D, Greer PB, Baroni G, Keall PJ, Riboldi M. Motion prediction in MRI-guided radiotherapy based on interleaved orthogonal cine-MRI. *Physics in Medicine and Biology* 2016; 61:872–887.
- [207] McClelland JR, Hawkes DJ, Schaeffter T, King AP. Respiratory motion models: A review. *Medical Image Analysis* 2013; 17:19–42.
- [208] McClelland JR, Modat M, Arridge S, Grimes H, D’Souza D, Thomas D, Connell DO, Low DA, Kaza E, Collins DJ, Leach MO, Hawkes DJ. A generalized framework unifying image registration and respiratory motion models and incorporating image reconstruction, for partial image data or full images. *Physics in medicine and biology* 2017; 62:4273–4292.
- [209] Griswold MA, Jakob PM, Heidemann RM, Nittka M, Jellus V, Wang J, Kiefer B, Haase A. Generalized Autocalibrating Partially Parallel Acquisitions (GRAPPA). *Magnetic Resonance in Medicine* 2002; 47:1202–1210.
- [210] Stemkens B, Tijssen RH, van den Berg CAT, Lagendijk JJW, Moonen CTW, Ries M, Denis de Senneville B. Optical flow MR analysis on undersampled radial acquisitions for real-time tracking of the pancreas in MR guided radiotherapy. In: *Proc. Int. Soc. Magn. Reson. Imaging*, 2013. p. 4325.
- [211] Roujol S, Ries M, Moonen C, Denis De Senneville B. Automatic nonrigid calibration of image registration for real time MR-guided HIFU ablations of mobile organs. *IEEE Transactions on Medical Imaging* 2011; 30:1737–1745.
- [212] Yuan J, Wong OL, Zhou Y, Chueng KY, Yu SK. A fast volumetric 4D-MRI with sub-second frame rate for abdominal motion monitoring and characterization in MRI-guided radiotherapy. *Quantitative imaging in medicine and surgery* 2019; 9:1303–1314.
- [213] Ong F, Zhu X, Cheng JY, Johnson KM, Larson PE, Vasanawala SS, Lustig M. Extreme MRI: Large-scale volumetric dynamic imaging from continuous non-gated acquisitions. *Magnetic Resonance in Medicine* 2020; pp. 1–18.

- [214] King AP, Buerger C, Tsoumpas C, Marsden PK, Schaeffter T. Thoracic respiratory motion estimation from MRI using a statistical model and a 2-D image navigator. *Medical Image Analysis* 2012; .
- [215] Fu M, Barlaz MS, Holtrop JL, Perry JL, Kuehn DP, Shosted RK, Liang ZP, Sutton BP. High-frame-rate full-vocal-tract 3D dynamic speech imaging. *Magnetic Resonance in Medicine* 2017; 77:1619–1629.
- [216] Burdumy M, Traser L, Burk F, Richter B, Echternach M, Korvink JG, Hennig J, Zaitsev M. One-second MRI of a three-dimensional vocal tract to measure dynamic articulator modifications. *Journal of Magnetic Resonance Imaging* 2017; 46:94–101.
- [217] Zhang Q, Pevsner A, Hertanto A, Hu YC, Rosenzweig KE, Ling CC, Mageras GS. A patient-specific respiratory model of anatomical motion for radiation treatment planning. *Medical Physics* 2007; 34:4772–4781.
- [218] Li R, Lewis JH, Jia X, Zhao T, Liu W, Wuenschel S, Lamb J, Yang D, Low DA, Jiang SB. On a PCA-based lung motion model. *Physics in Medicine and Biology* 2011; 56:6009–6030.
- [219] Mishra P, Li R, Mak RH, Rottmann J, Bryant JH, Williams CL, Berbeco RI, Lewis JH. An initial study on the estimation of time-varying volumetric treatment images and 3D tumor localization from single MV cine EPID images. *Medical Physics* 2014; .
- [220] Cai W, Hurwitz MH, Williams CL, Dhou S, Berbeco RI, Seco J, Mishra P, Lewis JH. 3D delivered dose assessment using a 4DCT-based motion model. *Medical Physics* 2015; 42:2897–2907.
- [221] Low DA, Parikh PJ, Lu W, Dempsey JF, Wahab SH, Hubenschmidt JP, Nystrom MM, Handoko M, Bradley JD. Novel breathing motion model for radiotherapy. *International Journal of Radiation Oncology Biology Physics* 2005; .
- [222] Huttinga N, Bruijnen T, van den Berg C, Luijten PR, Sbrizzi A. Prospective 3D+t non-rigid motion estimation at high frame-rate from highly undersampled k-space data: validation and preliminary in-vivo results. In: *roc. Int. Soc. Magn. Reson. Med.*, 2019. p. 1180.
- [223] Rueckert et al. D. Nonrigid Registration Using Free-Form Deformations: Application to Breast MR Images. *IEEE Transactions on Medical Imaging* 1999; 18:712–721.
- [224] Zachiu C, de Senneville BD, Moonen CTW, Raaymakers BW, Ries M. Anatomically plausible models and quality assurance criteria for online mono- and multi-modal medical image registration. *Physics in medicine and biology* 2018; 63:155016.
- [225] Rohlfing T, Maurer CRJ, Bluemke DA, Jacobs MA. Volume-preserving nonrigid registration of MR breast images using free-form deformation with an incompressibility constraint. *IEEE transactions on medical imaging* 2003; 22:730–741.
- [226] Liu DC, Nocedal J. On the limited memory BFGS method for large scale optimization. *Mathematical Programming* 1989; 45:503–528.
- [227] Becker S. L-BFGS-B, converted from Fortran to C, with Matlab wrapper, 2019.
- [228] Pipe JG, Menon P. Sampling density compensation in MRI: rationale and an iterative numerical solution. *Magnetic resonance in medicine* 1999; 41:179–186.
- [229] Pruessmann KP, Weiger M, Börnert P, Boesiger P. Advances in sensitivity encoding with arbitrary k-space trajectories. *Magnetic resonance in medicine* 2001; 46:638–651.
- [230] Feng L, Tyagi N, Otazo R. MRSIGMA: Magnetic Resonance SIGNature MAtching for real-time volumetric imaging. *Magnetic resonance in medicine* 2020; 84:1280–1292.
- [231] Jiang Y, Ma D, Keenan KE, Stupic KF, Gulani V, Griswold MA. Repeatability of magnetic resonance fingerprinting T1 and T2 estimates assessed using the ISMRM/NIST MRI system phantom. *Magnetic Resonance in Medicine* 2017; 78:1452–1457.
- [232] Sbrizzi A, Huttinga N, van den Berg C. Acquisition, reconstruction and uncertainty quantification of 3D non-rigid motion fields directly from k-space data at 100 Hz frame rate. In: *Proceedings 27th annual meeting ISMRM, Montreal, Canada, 2019.*
- [233] Huttinga NR, Bruijnen T, van den Berg CA, Sbrizzi A. Real-time 3D respiratory motion estimation for MR-guided radiotherapy using low-rank MR-MOTUS. In: *International Society for Magnetic Resonance in Medicine (ISMRM)*, 2020. p. 0598.
- [234] Lingala SG, Hu Y, DiBella E, Jacob M. Accelerated dynamic MRI exploiting sparsity and low-rank structure: k-t SLR. *IEEE transactions on medical imaging* 2011; 30:1042–1054.
- [235] Liang Z. SPATIOTEMPORAL IMAGING WITH PARTIALLY SEPARABLE FUNCTIONS. In: *2007 4th IEEE International Symposium on Biomedical Imaging: From Nano to Macro*, 2007. pp. 988–991.
- [236] Zhao B, Haldar JP, Christodoulou AG, Liang ZP. Image reconstruction from highly undersampled (k, t)-space data with joint partial separability and sparsity constraints. *IEEE transactions on medical imaging* 2012; 31:1809–1820.

- [237] Zhao B, Haldar JP, Brinegar C, Liang Z. Low rank matrix recovery for real-time cardiac MRI. In: 2010 IEEE International Symposium on Biomedical Imaging: From Nano to Macro, 2010. pp. 996–999.
- [238] Haldar JP, Liang Z. Spatiotemporal imaging with partially separable functions: A matrix recovery approach. In: 2010 IEEE International Symposium on Biomedical Imaging: From Nano to Macro, 2010. pp. 716–719.
- [239] Delmon V, Rit S, Pinho R, Sarrut D. Registration of sliding objects using direction dependent B-splines decomposition. *Physics in medicine and biology* 2013; 58:1303–1314.
- [240] Fu Y, Liu S, Li HH, Li H, Yang D. An adaptive motion regularization technique to support sliding motion in deformable image registration. *Medical physics* 2018; 45:735–747.
- [241] Kellman P, McVeigh ER. Image reconstruction in SNR units: A general method for SNR measurement. *Magnetic Resonance in Medicine* 2005; 54:1439–1447.
- [242] Eiben B, Bertholet J, Menten MJ, Nill S, Oelfke U, McClelland JR. Consistent and invertible deformation vector fields for a breathing anthropomorphic phantom: A post-processing framework for the XCAT phantom. *Physics in Medicine and Biology* 2020; 65.
- [243] van der Heide UA, Thorwarth D. Quantitative Imaging for Radiation Oncology. *International Journal of Radiation Oncology Biology Physics* 2018; 102:683–686.
- [244] Hall WA, Paulson ES, van der Heide UA, Fuller CD, Raaymakers BW, Lagendijk JJ, Li XA, Jaffray DA, Dawson LA, Erickson B, Verheij M, Harrington KJ, Sahgal A, Lee P, Parikh PJ, Bassetti MF, Robinson CG, Minsky BD, Choudhury A, Tersteeg RJ, Schultz CJ. The transformation of radiation oncology using real-time magnetic resonance guidance: A review. *European Journal of Cancer* 2019; 122:42–52.
- [245] Fram EK, Herfkens RJ, Johnson GA, Glover GH, Karis JP, Shimakawa A, Perkins TG, Pelc NJ. Rapid calculation of T1 using variable flip angle gradient refocused imaging. *Magnetic Resonance Imaging* 1987; 5:201–208.
- [246] Meiboom S, Gill D. Modified spin-echo method for measuring nuclear relaxation times. *Review of Scientific Instruments* 1958; 29:688–691.
- [247] Jiang Y, Ma D, Seiberlich N, Gulani V, Griswold MA. MR fingerprinting using fast imaging with steady state precession (FISP) with spiral readout. *Magnetic Resonance in Medicine* 2015; 74:1621–1631.
- [248] Ma D, Coppo S, Chen Y, McGivney DF, Jiang Y, Pahwa S, Gulani V, Griswold MA. Slice profile and B1 corrections in 2D magnetic resonance fingerprinting. *Magnetic Resonance in Medicine* 2017; 78:1781–1789.
- [249] Assländer J, Glaser SJ, Hennig J. Pseudo Steady-State Free Precession for MR-Fingerprinting. *Magnetic Resonance in Medicine* 2017; 77:1151–1161.
- [250] Badve C, Yu A, Dastmalchian S, Rogers M, Ma D, Jiang Y, Margevicius S, Pahwa S, Lu Z, Schluchter M, Sunshine XJ, Griswold M, Sloan A, Gulani V. MR fingerprinting of adult brain tumors: Initial experience. In: *American Journal of Neuroradiology*, mar 2017 pp. 492–499.
- [251] Rieger B, Akçakaya M, Pariente JC, Llufriu S, MartinezHeras E, Weingärtner S, Schad LR. Time efficient whole-brain coverage with MR Fingerprinting using slice-interleaved echo-planar-imaging. *Scientific Reports* 2018; 8.
- [252] Liao C, Wang K, Cao X, Li Y, Wu D, Ye H, Ding Q, He H, Zhong J. Detection of lesions in mesial temporal lobe epilepsy by using MR fingerprinting. *Radiology* 2018; 288:804–812.
- [253] Ma D, Jones SE, Deshmane A, Sakaie K, Pierre EY, Larvie M, McGivney D, Blümcke I, Krishnan B, Lowe M, Gulani V, Najm I, Griswold MA, Wang ZI. Development of high-resolution 3D MR fingerprinting for detection and characterization of epileptic lesions. *Journal of Magnetic Resonance Imaging* 2019; 49:1333–1346.
- [254] Yu AC, Badve C, Ponsky LE, Pahwa S, Dastmalchian S, Rogers M, Jiang Y, Margevicius S, Schluchter M, Tabayoyong W, Abouassaly R, McGivney D, Griswold MA, Gulani V. Development of a Combined MR Fingerprinting and Diffusion Examination for Prostate Cancer. *Radiology* 2017; 283:729–738.
- [255] Chen Y, Jiang Y, Pahwa S, Ma D, Lu L, Twieg MD, Wright KL, Seiberlich N, Griswold MA, Gulani V. MR fingerprinting for rapid quantitative abdominal imaging. *Radiology* 2016; 279:278–286.
- [256] Chen Y, Panda A, Pahwa S, Hamilton JI, Dastmalchian S, McGivney DF, Ma D, Batesole J, Seiberlich N, Griswold MA, Plecha D, Gulani V. Three-dimensional MR Fingerprinting for Quantitative Breast Imaging. *Radiology* 2019; 290:33–40.
- [257] Cavallo AU, Liu Y, Patterson A, AlKindi S, Hamilton J, Gilkeson R, Gulani V, Seiberlich N, Rajagopalan S. CMR Fingerprinting for Myocardial T1, T2, and ECV Quantification in Patients With Nonischemic Cardiomyopathy, aug 2019.

- [258] Cloos MA, Knoll F, Zhao T, Block KT, Bruno M, Wiggins GC, Sodickson DK. Multiparametric imaging with heterogeneous radiofrequency fields. *Nature Communications* 2016; 7.
- [259] Bruijnen T, Stemkens B, van den Berg CAT, Tijssen RHN. Prospective GIRF-based RF phase cycling to reduce eddy current-induced steady-state disruption in bSSFP imaging. *Magnetic Resonance in Medicine* 2020; 84:115–127.
- [260] Aszl ander J, Cloos MA, Knoll F, Sodickson DK, Hennig J, Lattanzi R. Low rank alternating direction method of multipliers reconstruction for MR fingerprinting. *Magnetic Resonance in Medicine* 2018; 79:83–96.
- [261] De Bazelaire CM, Duhamel GD, Rofsky NM, Alsop DC. MR Imaging Relaxation Times of Abdominal and Pelvic Tissues Measured in Vivo at 3.0 T: Preliminary Results. *Radiology* 2004; 230:652–659.
- [262] Deoni SC, Peters TM, Rutt BK. High-resolution T1 and T2 mapping of the brain in a clinically acceptable time with DESPOT1 and DESPOT2. *Magnetic Resonance in Medicine* 2005; 53:237–241.
- [263] Lu L, Chen Y, Shen C, Lian J, Das S, Marks L, Lin W, Zhu T. Initial assessment of 3D magnetic resonance fingerprinting (MRF) towards quantitative brain imaging for radiation therapy. *Medical Physics* 2020; 47:1199–1214.
- [264] Cruz G, Jaubert O, Qi H, Bustin A, Milotta G, Schneider T, Koken P, Doneva M, Botnar RM, Prieto C. 3D free-breathing cardiac magnetic resonance fingerprinting. *NMR in Biomedicine* 2020; 33:1–16.
- [265] Danet IM, Semelka RC, Leonardou P, Braga L, Vaidean G, Woosley JT, Kanematsu M. Spectrum of MRI appearances of untreated metastases of the liver. *American Journal of Roentgenology* 2003; 181:809–817.
- [266] Namasivayam S, Martin DR, Saini S. Imaging of liver metastases: MRI. *Cancer Imaging* 2007; 7:2–9.
- [267] Sbrizzi A, Hoogduin H, Hajnal JV, van den Berg CA, Luijten PR, Malik SJ. Optimal control design of turbo spin-echo sequences with applications to parallel-transmit systems. *Magnetic Resonance in Medicine* 2017; 77:361–373.
- [268] Fang P, Musall BC, Son JB, Moreno AC, Hobbs BP, Carter BW, Fellman BM, Mawlawi O, Ma J, Lin SH. Multimodal Imaging of Pathologic Response to Chemoradiation in Esophageal Cancer. *International Journal of Radiation Oncology Biology Physics* 2018; 102:996–1001.
- [269] van Schie MA, van Houdt PJ, Ghobadi G, Pos FJ, Walraven I, de Boer HC, van den Berg CA, Smeenk RJ, Kerkmeijer LG, van der Heide UA. Quantitative MRI Changes During Weekly Ultra-Hypofractionated Prostate Cancer Radiotherapy With Integrated Boost. *Frontiers in Oncology* 2019; 9.
- [270] Ling CC, Humm J, Larson S, Amols H, Fuks Z, Leibel S, Koutcher JA. Towards multidimensional radiotherapy (MD-CRT): Biological imaging and biological conformality. *International Journal of Radiation Oncology Biology Physics* 2000; 47:551–560.
- [271] Bentzen SM. Theragnostic imaging for radiation oncology: Dose-painting by numbers. *Lancet Oncology* 2005; 6:112–117.
- [272] Bruijnen T. “Quantifying head-and-neck tumor motion for personalized MRI guided radiotherapy”. PhD thesis, Eindhoven University of Technology, 2016.
- [273] Uecker M, Zhang S, Voit D, Karaus A, Merboldt KD, Frahm J. Real-time MRI at a resolution of 20 ms. *NMR in Biomedicine* 2010; 23:986–994.
- [274] Zhang S, Olthoff A, Frahm J. Real-time magnetic resonance imaging of normal swallowing. *Journal of Magnetic Resonance Imaging* 2012; 35:1372–1379.
- [275] Peters DC, Derbyshire JA, McVeigh ER. Centering the projection reconstruction trajectory: Reducing gradient delay errors. *Magnetic Resonance in Medicine* 2003; .
- [276] Brodsky EK, Samsonov AA, Block WF. Characterizing and correcting gradient errors in non-Cartesian imaging: Are gradient errors Linear Time-Invariant (LTI)? *Magnetic Resonance in Medicine* 2009; 62:1466–1476.
- [277] Buonincontri G, Methner C, Krieg T, Carpenter TA, Sawiak SJ. Trajectory correction for free-breathing radial cine MRI. *Magnetic Resonance Imaging* 2014; .
- [278] Vannesjo SJ, Graedel NN, Kasper L, Gross S, Busch J, Haeberlin M, Barmet C, Pruessmann KP. Image reconstruction using a gradient impulse response model for trajectory prediction. *Magnetic Resonance in Medicine* 2016; 76:45–58.
- [279] Stich M, Wech T, Slawig A, Ringler R, Dewdney A, Greiser A, Ruyters G, Bley TA, K ostler H. Gradient waveform pre-emphasis based on the gradient system transfer function. *Magnetic Resonance in Medicine* 2018; 80:1521–1532.

- [280] Herrmann KH, Krämer M, Reichenbach JR. Time efficient 3D radial UTE sampling with fully automatic delay compensation on a clinical 3T MR scanner. *PLoS ONE* 2016; .
- [281] Rosenzweig S, Holme HCM, Uecker M. Simple auto-calibrated gradient delay estimation from few spokes using Radial Intersections (RING). *Magnetic resonance in medicine* 2019; 81:1898–1906.
- [282] Mickevicius NJ, Paulson ES. Investigation of undersampling and reconstruction algorithm dependence on respiratory correlated 4D-MRI for online MR-guided radiation therapy. *Physics in Medicine and Biology* 2017; 62:2910–2921.
- [283] Paulson ES, Ahunbay E, Chen X, Mickevicius NJ, Chen GP, Schultz C, Erickson B, Straza M, Hall WA, Li XA. 4D-MRI driven MR-guided online adaptive radiotherapy for abdominal stereotactic body radiation therapy on a high field MR-Linac: Implementation and initial clinical experience. *Clinical and Translational Radiation Oncology* 2020; 23:72–79.
- [284] Doneva M, Stehning C, Nehrke K, Börnert P. Improving Scan Efficiency of Respiratory Gated Imaging Using Compressed Sensing with 3D Cartesian Golden Angle Sampling. *Proceedings 19th Scientific Meeting, International Society for Magnetic Resonance in Medicine* 2011; 19:641.
- [285] Otazo R, Candès E, Sodickson DK. Low-rank plus sparse matrix decomposition for accelerated dynamic MRI with separation of background and dynamic components. *Magnetic Resonance in Medicine* 2015; .
- [286] Biswas S, Aggarwal HK, Jacob M. Dynamic MRI using model-based deep learning and STORM priors: MoDL-STORM. *Magnetic Resonance in Medicine* 2019; 82:485–494.
- [287] Küstner T, Fuin N, Hammernik K, Bustin A, Qi H, Hajhosseiny R, Masci PG, Neji R, Rueckert D, Botnar RM, Prieto C. CINENet: deep learning-based 3D cardiac CINE MRI reconstruction with multi-coil complex-valued 4D spatio-temporal convolutions. *Scientific Reports* 2020; 10:1–13.
- [288] Sbrizzi A, Bruijnen T, van der Heide O, Luijten P, van den Berg CA. Dictionary-free MR fingerprinting reconstruction of balanced-GRE sequences, 2017.
- [289] Zhao B, Haldar JP, Liao C, Ma D, Jiang Y, Griswold MA, Setsompop K, Wald LL. Optimal experiment design for magnetic resonance fingerprinting: Cramér-rao bound meets spin dynamics. *IEEE Transactions on Medical Imaging* 2019; 38:844–861.
- [290] Winkelmann R, Börnert P, Nehrke K, Dössel O. Efficient foldover suppression using SENSE. *Magnetic Resonance Materials in Physics, Biology and Medicine* 2005; 18:63–68.
- [291] Murakami JW, Hayes CE, Weinberger E. Intensity correction of phased-array surface coil images. *Magnetic resonance in medicine* 1996; 35:585–590.
- [292] Borman PTS, Raaymakers BW, Glitznert M. ReconSocket: a low-latency raw data streaming interface for real-time MRI-guided radiotherapy. *Physics in medicine and biology* 2019; 64:185008.
- [293] Benkert T, Mugler JP, Rigie DS, Sodickson DK, Chandarana H, Block KT. Hybrid T 2 - and T 1 -weighted radial acquisition for free-breathing abdominal examination. *Magnetic Resonance in Medicine* 2018; 80:1935–1948.
- [294] Navest RJM, Mandija S, Andreychenko A, Raaijmakers AJE, Legendijk JJW, van den Berg CAT. Understanding the physical relations governing the noise navigator. *Magnetic resonance in medicine* 2019; 82:2236–2247.
- [295] Navest R, Mandija S, Zijlema S, Stemkens B, Andreychenko A, Legendijk J, van den Berg C. The noise navigator for MRI-guided radiotherapy: an independent method to detect physiological motion. *Physics in Medicine & Biology* 2020; 65(1).
- [296] Blasche M, “Gradient Performance and Gradient Amplifier Power”, 2017.
- [297] Hennig J, Welz AM, Schultz G, Korvink J, Liu Z, Speck O, Zaitsev M. Parallel imaging in non-bijective, curvilinear magnetic field gradients: A concept study. *Magnetic Resonance Materials in Physics, Biology and Medicine* 2008; 21:5–14.
- [298] Dispenza NL, Littin S, Zaitsev M, Constable RT, Galiana G. Clinical Potential of a New Approach to MRI Acceleration. *Scientific reports* 2019; 9:1912.
- [299] Shan S, Liney GP, Tang F, Li M, Wang Y, Ma H, Weber E, Walker A, Holloway L, Wang Q, Wang D, Liu F, Crozier S. Geometric distortion characterization and correction for the 1.0 T Australian MRI-linac system using an inverse electromagnetic method. *Medical physics* 2020; 47:1126–1138.
- [300] Zijlema SE, Tijssen RH, Malkov VN, Van Dijk L, Hackett SL, Kok JG, Legendijk JJ, Van Den Berg CA. Design and feasibility of a flexible, on-body, high impedance coil receive array for a 1.5 T MR-linac. *Physics in Medicine and Biology* 2019; 64.

- [301] Zijlema SE, Tijssen RHN, van Dijk L, Hackett SL, Wolthaus JWH, Breimer W, Legendijk JJW, van den Berg CAT. Improving the imaging performance of the 1.5 T MR-linac using a flexible, 32-channel, on-body receive array. *Physics in medicine and biology* 2020; 65:215008.
- [302] Maspero M, Savenije MHF, Dinkla AM, Seevinck PR, Intven MPW, JurgenliemkSchulz IM, Kerkmeijer LGW, van den Berg CAT. Dose evaluation of fast synthetic-CT generation using a generative adversarial network for general pelvis MR-only radiotherapy. *Physics in medicine and biology* 2018; 63:185001.
- [303] Maspero M, Bruijnen T, Savenije M, Kerkmeijer L, Seevinck P, van den Berg C. Golden angle radial undersampling to accelerate synthetic CT generation with generative adversarial networks for prostate MR-guided Radiotherapy. In: *Proc. ISMRM 27*, 2019. p. (Poster).
- [304] Maccioni F, Martinelli M, Al Ansari N, Kagarmanova A, De Marco V, Zippi M, Marini M. Magnetic resonance cholangiography: past, present and future: a review. *European review for medical and pharmacological sciences* 2010; 14:721–725.
- [305] Zytoon AA, Mohammed HH, Hosny DM. The Role of Magnetic Resonance Cholangiopancreatography in Diagnosis of Hepatobiliary Lesions. *Journal of Medical Imaging and Radiation Sciences* 2016; 47:66–73.
- [306] Morita S, Ueno E, Saito N, Suzuki K, Machida H, Fujimura M, Maruyama K, Onodera Y, Watanabe K, Suzuki T, Ohnishi T, Imura C, Mitsuhashi N. Frequency of common bile duct motion artifacts caused by inferior vena cava pulsation on magnetic resonance cholangiopancreatography. *Magnetic Resonance in Medical Sciences* 2008; 7:31–36.
- [307] Morita S, Saito N, Suzuki K, Mitsuhashi N. Common bile duct anteroposterior movement synchronized with inferior vena cava pulsation observed by cine magnetic resonance imaging. *Magnetic Resonance Imaging* 2008; 26:1232–1235.
- [308] Lohöfer FK, Kaissis GA, Rasper M, Katemann C, Hock A, Peeters JM, Schlag C, Rummeny EJ, Karampinos D, Braren RF. Magnetic resonance cholangiopancreatography at 3 Tesla: Image quality comparison between 3D compressed sensing and 2D single-shot acquisitions. *European Journal of Radiology* 2019; 115:53–58.
- [309] Pichler BJ, Kolb A, Nägele T, Schlemmer HP. PET/MRI: paving the way for the next generation of clinical multimodality imaging applications. *Journal of nuclear medicine : official publication, Society of Nuclear Medicine* 2010; 51:333–336.
- [310] Fendler WP, Czernin J, Herrmann K, Beyer T. Variations in PET/MRI Operations: Results from an International Survey Among 39 Active Sites. *Journal of nuclear medicine : official publication, Society of Nuclear Medicine* 2016; 57:2016–2021.
- [311] Würslin C, Schmidt H, Martirosian P, Brendle C, Boss A, Schwenzer NF, Stegger L. Respiratory motion correction in oncologic PET using T1-weighted MR imaging on a simultaneous whole-body PET/MR system. *Journal of Nuclear Medicine* 2013; 54:464–471.
- [312] Fayad H, Schmidt H, Wuerslin C, Visvikis D. Reconstruction-incorporated respiratory motion correction in clinical simultaneous PET/MR imaging for oncology applications. *Journal of Nuclear Medicine* 2015; 56:884–889.
- [313] Manber R, Thielemans K, Hutton BF, Wan S, Fraioli F, Barnes A, Ourselin S, Arridge S, Atkinson D. Clinical impact of respiratory motion correction in simultaneous PET/MR, using a joint PET/MR predictive motion model. *Journal of Nuclear Medicine* 2018; 59:1467–1473.
- [314] Palma DA, Salama JK, Lo SS, Senan S, Treasure T, Govindan R, Weichselbaum R. The oligometastatic state-separating truth from wishful thinking. *Nature Reviews Clinical Oncology* 2014; 11:549–557.
- [315] Palma DA, Olson R, Harrow S, Gaede S, Louie AV, Haasbeek C, Mulroy L, Lock M, Rodrigues GB, Yaremko BP, Schellenberg D, Ahmad B, Griffioen G, Senthil S, Swaminath A, Kopek N, Liu M, Moore K, Currie S, Bauman GS, Warner A, Senan S. Stereotactic ablative radiotherapy versus standard of care palliative treatment in patients with oligometastatic cancers (SABR-COMET): a randomised, phase 2, open-label trial. *The Lancet* 2019; 393:2051–2058.
- [316] Palma DA, Bauman GS, Rodrigues GB. Beyond Oligometastases. *International journal of radiation oncology, biology, physics* 2020; 107:253–256.
- [317] Shirvani SM, Huntzinger CJ, Melcher T, Olcott PD, Voronenko Y, BartlettRoberto J, Mazin S. Biology-guided radiotherapy: redefining the role of radiotherapy in metastatic cancer. *The British Journal of Radiology* 2020; p. 20200873.

List of Publications

Published papers:

Huttinga, N. R. F., **Bruijnen, T.**, van den Berg, C. A. T. and Sbrizzi, A. (2020). Nonrigid 3D motion estimation at high temporal resolution from prospectively undersampled k-space data using low-rank MR-MOTUS. *Magnetic Resonance in Medicine*.

Bruijnen, T., van der Heide, O., Intven, M. P. W., Mook, S., Lagendijk, J. J. W., van den Berg, C. A. T. and Tijssen, R. H. N. (2020). Technical feasibility of Magnetic Resonance Fingerprinting on a 1.5T MRI-Linac. *Physics in Medicine and Biology*. Navest, R. J. M., Mandija, S., **Bruijnen, T.**, Stemkens, B., Tijssen, R. H. N., Andreychenko, A., Lagendijk, J. J. W., and Van Den Berg, C. A. T. (2020). The noise navigator: a surrogate for respiratory-correlated 4D-MRI for motion characterization in radiotherapy. *Physics in Medicine and Biology*, 65(1).

Bruijnen, T., Stemkens, B., van den Berg, C. A. T., and Tijssen, R. H. N. (2020). Prospective GIRF-based RF phase cycling to reduce eddy current-induced steady-state disruption in bSSFP imaging. *Magnetic Resonance in Medicine*, 84(1), 115–127.

Stemkens, B., Prins, F. M., **Bruijnen, T.**, Kerkmeijer, L. G. W., Lagendijk, J. J. W., Van Den Berg, C. A. T., and Tijssen, R. H. N. (2019). A dual-purpose MRI acquisition to combine 4D-MRI and dynamic contrast-enhanced imaging for abdominal radiotherapy planning. *Physics in Medicine and Biology*, 64(6).

Bruijnen, T., Stemkens, B., Lagendijk, J. J. W., Van Den Berg, C. A. T., and Tijssen, R. H. N. (2019). Multiresolution radial MRI to reduce IDLE time in pre-beam imaging on an MR-Linac (MR-RIDDLE). *Physics in Medicine and Biology*, 64(5).

Bruijnen, T., Stemkens, B., Terhaard, C. H. J., Lagendijk, J. J. W., Raaijmakers, C. P. J., and Tijssen, R. H. N. (2019). Intrafraction motion quantification and planning target volume margin determination of head-and-neck tumors using cine magnetic resonance imaging. *Radiotherapy and Oncology*, 130.

Cruz, G., Schneider, **T.**, **Bruijnen, T.**, Gaspar, A. S., Botnar, R. M., and Prieto, C. (2018). Accelerated magnetic resonance fingerprinting using soft-weighted keyhole (MRF-SOHO). *PLoS ONE*, 13(8).

Sbrizzi, A., **Bruijnen, T.**, van der Heide, O., Luijten, P., and Berg, C. A. T. van den. (2017). Dictionary-free MR Fingerprinting reconstruction of balanced-GRE sequences. 1–11. arXiv:1711.08905

Submitted papers:

Zijlema, S.E., Breimer, W., Gosselink, W.J.M., **Bruijnen, T**, Arteaga de Castro, C.S., Tijssen, H.N., Philippens, M.E.P., Lagendijk, J.J.W and van den Berg, C.A.T. (2021). A mask-compatible, radiolucent, 8-channel head and neck receive array for MRI-guided radiotherapy treatments and pre-treatment simulation. Submitted to Physics in Medicine & Biology

Terpstra, M.L., Maspero, M, **Bruijnen, T**, Verhoeff, J.J.C., Lagendijk, J.J.W., van den Berg, C.A.T. (2021). Real-time 3D motion estimation from undersampled MRI using multi-resolution neural networks. Submitted to Medical Physics.

Bruijnen, T., Schakel, T., Akdag, O., Bruel, C. V. M., and Lagendijk, J. J. W. (2020). Free-breathing motion compensated 3D T2-weighted turbo spin-echo MRI for body imaging. Submitted to Magnetic Resonance in Medicine.

Conference Proceedings:

2021

Bruijnen, T, Borman, P.T.S., Schakel, T and Raaymakers, B.W. (2021). Parallel imaging stream for multi-purpose real-time adaptive MRI-guided prostate radiotherapy. Proc. AAPM, (Oral).

Bruijnen, T, Borman, P.T.S., Schakel, T, van den Berg, C.A.T. and Raaymakers, B.W. (2021). Parallel imaging stream for multi-purpose real-time adaptive MRI-guided prostate radiotherap. Proc. MRI in radiotherapy, (Oral, Young Investigator Award).

Bruijnen, T, Schakel, T, Lagendijk J.J.W., Geerts, L, Peeters, J.M. Johannes M. Peeters, Blanken, N, Veldhuis, W.B., and van den Berg, C.A.T. (2021). Free-breathing MRCP using motion compensated 3D Cartesian turbo spin-echo imaging. Proc. ISMRM 29 (poster).

2020

Bruijnen, T., Akdag, O., Bruel, C., Schakel, T., Lagendijk, J., van den Berg, C. and Tijssen, R. (2020). Free-breathing 3D T2-weighted TSE using Cartesian acquisition with rewinded spiral profile ordering (rCASPR) for abdominal radiotherapy. Proc. ISMRM Benelux 12, (Oral).

Huttinga, N., **Bruijnen, T.**, van den Berg, C., and Sbrizzi, A. (2020). Real-time 3D respiratory motion estimation for MR-guided radiotherapy using low-rank MR-MOTUS. Proc. ISMRM 28, (Oral, Summa Cum Laude).

Bruijnen, T., Akdag, O., Bruel, C., Stemkens, B., Schakel, T., Lagendijk, J. and van den Berg, CAT Tijssen, R. (2020). Free-breathing 3D T2-weighted TSE using Cartesian acquisition with rewinded spiral profile ordering (rCASPR) for abdominal radiotherapy. Proc. ISMRM 28, (Poster).

van der Heide, O., Sbrizzi, A., **Bruijnen, T.**, and van den Berg, C. (2020). Extension of MR-STAT to non-Cartesian and gradient-spoiled sequences. Proc. ISMRM 28, (Oral).

2019

Stemkens, B., Sital, C., Blokker, M., **Bruijnen, T.**, Lagendijk, J., Tijssen, R. and van den Berg, C. (2019). Deep residual learning of radial under sampling artefacts for real-time MR image guidance during radiotherapy. Proc. ISMRM 27, (Oral).

Maspero, M., **Bruijnen, T.**, Savenije, M., Kerkmeijer, L., Seevinck, P., and van den Berg, C. (2019). Golden angle radial undersampling to accelerate synthetic CT generation with generative adversarial networks for prostate MR-guided Radiotherapy. Proc. ISMRM 27, (Poster).

Huttinga, N., **Bruijnen, T.**, van den Berg, C., Luijten, P. and Sbrizzi, A. (2019). Prospective 3D+t non-rigid motion estimation at high frame-rate from highly undersampled k-space data: validation and preliminary in-vivo results. Proc. ISMRM 27, (Oral, Magna Cum Laude).

Bruijnen, T., Stemkens, B., Lagendijk, J., van den Berg, C., and Tijssen, R. (2019). Prospective GIRF-based RF phase cycling to prevent eddy current-induced steady-state disruption in balanced SSFP imaging. Proc. ISMRM 27, (Oral, Summa Cum Laude).

Stemkens, B., van Riel, M., **Bruijnen, T.**, Lagendijk, J., van den Berg, C. and Tijssen, R. (2019). Respiratory motion variability in 4D-MRI for MR-guided radiotherapy. Proc. ISMRM 27, (Poster).

Bruijnen, T., Borman, P., Lagendijk, J., Raaymakers, B., Berg, C. van den, Glitzner, M., and Tijssen, R. (2019). Real-time sliding window reconstruction of golden angle stack-of-stars acquisitions for continuous 3D tumor tracking. Proc. MR in RT 7, (Oral).

Slooten, E., **Bruijnen, T.**, Schakel, T., Akdag, O. and Tijssen, R. H. N. (2019). Do the standard free-breathing MRI protocols represent mid-position on the 1.5T Unity MR-Linac? Proc. NVKF, (Oral).

Bruijnen, T., Stemkens, B., Lagendijk, J., Berg, C. van den, and Tijssen, R. (2019). Prospective GIRF-based RF phase cycling to prevent eddy current-induced steady-state disruption in balanced SSFP imaging. Proc. ISMRM Benelux 11, (Oral).

2018

Bruijnen, T., Stemkens, B., Lagendijk, J., Berg, C. van den and Tijssen, R. (2018). Magnetic resonance fingerprinting on a 1.5T MRI-Linac for tumor response monitoring. Proc. ISMRM Cancer Study Group Workshop Dublin, (Oral, invited talk).

Bruijnen, T., Stemkens, B., Lagendijk, J., Berg, C. van den, and Tijssen, R. (2018). Multi-resolution radial MRI to reduce IDLE time in pre-beam imaging on a MR-Linac (MR-RIDDLE). Proc. NVKF Lustrum, (Oral).

Bruijnen, T., Stemkens, B., Lagendijk, J., Berg, C. van den and Tijssen, R. (2018). Multi-resolution radial MRI to reduce IDLE time in pre-beam imaging on a MR-Linac (MR-RIDDLE). Proc. MR in RT 6, (Oral, Young Investigator Award).

Blokker, M., Stemkens, B., **Bruijnen, T.**, Tijssen, R., and Berg, C. van den. (2018). Ultra fast image reconstruction for real time MRI-guided radiotherapy by removing undersampling artefacts using deep learning. Proc. MR in RT 6, (Oral).

Bruijnen, T., Stemkens, B., Lagendijk, J., Berg, C. van den and Tijssen, R. (2018). Magnetic resonance fingerprinting on a 1.5T MRI-Linac for tumor response monitoring. Proc. ISMRM 26, (Oral, best presentation award in the Cancer Study).

Bruijnen, T., Stemkens, B., Lagendijk, J., Berg, C. van den, and Tijssen, R. (2018). Gradient system characterization of a 1.5T MRI-Linac with application to UTE imaging. Proc. ISMRM 26, (Poster).

Navest, R., **Bruijnen, T.**, Lagendijk, J., Andreychenko, A. and van den Berg, C. (2019). Noise navigator based irregular motion detection and retrospective motion artifact removal. Proc ISMRM 26, (Oral, Magna Cum Laude).

Bruijnen, T., Stemkens, B., Lagendijk, J., Berg, C. van den, and Tijssen, R. (2018). Multi-resolution radial MRI to reduce IDLE time in pre-beam imaging on a MR-Linac (MR-RIDDLE). Proc. ESTRO 37, (Poster).

Stemkens, B., **Bruijnen, T.**, Lagendijk, J., Berg, C. van den and Tijssen, R. (2018). Optimizing Acquisition Speed and Contrast of Respiratory Correlated 4D-MRI on a 1.5T MRI-Linac. Proc. ESTRO 37, (Poster).

Bruijnen, T., Tijssen, R., Philippens, M., Terhaard, C., Schakel, T., Lagendijk, J., Raaijmakers, C., and Stemkens, B. (2018). MRI based radiotherapy: Intrafraction motion quantification of head-and-neck tumors using cine Magnetic Resonance Imaging. Proc. MDHNCs, (Poster).

Navest, R., **Bruijnen, T.**, Lagendijk, J., Andreychenko, A. and van den Berg, C. (2018). Noise navigator based irregular motion detection and retrospective motion artifact removal. Proc. ISMRM Benelux 10, (Poster).

Bruijnen, T., Stemkens, B., Lagendijk, J., Berg, C. van den, and Tijssen, R. (2018). Gradient system characterization of a 1.5T MRI-Linac with application to UTE imaging. Proc. ISMRM Benelux 10, (Poster).

2017

Stemkens, B., Berg, C. van den, **Bruijnen, T.**, Prins, F., Kerkmeijer, L., Lagendijk, J. and Tijssen, R. (2017). A dual-purpose MR acquisition for combined 4D-MRI and dynamic contrast enhanced imaging. Proc. AAPM 59, (Oral).

Sbrizzi, A., **Bruijnen, T.**, Luijten, P., and Berg, C. van den. (2017). Dictionary-free MR Fingerprinting with low-pass balanced-GRE sequences. Proc. ISMRM 25, (Oral).

Cruz, G., Gaspar, A., **Bruijnen, T.**, Botnar, R. and Prieto, C. (2017). Accelerated Magnetic Resonance Fingerprinting using Soft-weighted key-Hole (MRF-SOHO). Proc. ISMRM 25, (Power pitch).

Bruijnen, T., Stemkens, B., Lagendijk, J., Berg, C. van den, and Tijssen, R.

(2017). The efficacy of existing k-space corrections methods for 2D golden angle radial sampling on clinical 1.5T and 3T systems. Proc ISMRM 25, (Poster).

Bruijnen, T., Tijssen, R., Philippens, M., Terhaard, C., Schakel, T., Lagendijk, J., Raaijmakers, C. and Stemkens, B. (2018). Intra-fraction motion quantification of head-and-neck tumors using dynamic MRI. Proc. ESTRO 36, (Poster).

Bruijnen, T., Stemkens, B., Lagendijk, J., Berg, C. van den, and Tijssen, R. (2017). The efficacy of existing k-space corrections methods for 2D golden angle radial sampling on clinical 1.5T and 3T systems. Proc. ISMRM Benelux 9, (Poster).

Acknowledgements

Vooraf wil ik graag benadrukken dat dit proefschrift enkel tot stand is gekomen met behulp van de bijdragen van velen die ik hieronder wil bedanken. In alle waarschijnlijkheid ben ik hieronder een aantal personen vergeten. Voor deze personen wil ik graag de traditie van Matteo Maspero continueren en zijn jullie bij deze uitgenodigd voor een etentje bij ~~hem~~ mij thuis.

Mentoren

Rob, als mijn dagelijkse begeleider heb je de afgelopen jaren enorm veel voor mij betekend. Initieel heb je me voornamelijk geholpen op vaktechnisch gebied, maar de laatste jaren was het vooral de ondersteuning op persoonlijk vlak die me het meest is bijgebleven. Hierbij heb ik het ook zeer gewaardeerd dat je het laatste jaar nog steeds (wekelijks) tijd voor me hebt vrijgemaakt, ondanks je vertrek van onze afdeling. In het bijzonder is het volgende advies met betrekking tot tijdsmanagement mij altijd bijgebleven: *"Ja zeggen tegen de ene betekent dat je impliciet nee zegt tegen een ander"*. Rob, ik heb altijd bewondering gehad voor jouw toewijding aan de afdeling; ondanks het lange dagelijkse woon-werkverkeer leek jij altijd aanwezig te zijn. Wat mij betreft ben jij de belichaming van de ideale klinisch fysicus binnen een radiotherapie afdeling.

Bjorn, ik kan me het moment nog herinneren op de ISMRM benelux 2015 dat wij elkaar voor het eerst spraken en jij me wist te strikken voor een master project. In no-time had jij me geënthousiasmeerd voor de MRI-gestuurde radiotherapie waardoor ik nu inmiddels al 5 jaar op de afdeling werk. Ik heb altijd met veel plezier met jouw samengewerkt en ik hoop dat we in de toekomst nog contact zullen blijven houden en wellicht samen met Rob de langeverwachte ISMRM benelux zuid-oost editie kunnen organiseren.

Nico, tijdens mijn promotieonderzoek heb ik iedere 2-3 maanden korte perioden van een aantal dagen gehad waarin ik de relevantie van mijn werk sterk in twijfel trok. Deze perioden kwamen altijd meteen ten einde na een discussie met jou. Jouw enorme enthousiasme, passie en interesse in praktisch elk MRI-gerelateerd onderwerp is wat mij betreft ongeëvenaard. Vier jaar geleden heb ik exact deze zelfde eigenschap beschreven in *"the acknowledgements"* van mijn master thesis. Voor mij ben jij echt een enorme motivator en ideeën generator, twee eigenschappen waarvan ik hoop deze (voor een klein gedeelte) overgenomen te hebben.

Jan, jouw vastberadenheid en gedrevenheid om het concept van de MRI-versneller door te ontwikkelen is echt bewonderingswaardig. Die *"Just do it"* mentaliteit gekoppeld met jouw *"Blue Sky"* visie maakt je een enorm inspirerende promotor waar ik altijd tegenop heb gekeken. De komende tijd hoop ik veel bij te kun-

nen dragen aan die *Blue Sky* visie van een volledige autonoom robotisch MRI-versneller systeem.

Alessandro, tijdens de start van mijn promotie hebben wij samengewerkt aan het "*low-pass*" project (betreft de ouderwetse techniek van MR Fingerprinting ;). Ondanks dat het ons niet lukte om de peer review te passeren heb ik altijd met veel interesse en plezier met jou samengewerkt. Ik was altijd geïntrigeerd door jouw mathematisch perspectief op de probleemstelling en heb jou ook altijd als mentor beschouwd. Destijds heb ik zelfs een digitale lineaire algebra cursus gevolgd om zodoende een gedeelte van jouw denkwijzen over te kunnen nemen.

Aan de familie van **Klaas Nicolay**: de eerste paar jaar van mijn opleiding tot Biomedische Technoloog had ik sterk het gevoel dat ik niet op mijn plek zat. Het gevoel dat de acceptatie van mijn deelname aan de opleiding een fout was en dat ik minder (voor)kennis had dan mijn gelijken. Het derde jaar van de opleiding moesten we een minor kiezen waarbij ik, ten gevolge van willekeur, bij Klaas zijn Biomedical NMR groep terecht kwam. Hier mocht ik gedurende een half jaar een paar kleine projecten meedraaien onder begeleiding van Klaas. Deze kleine projecten waren uiteindelijk het hoogtepunt en keerpunt van mijn Bachelor. Tijdens deze periode kreeg ik een sterk gevoel van inclusiviteit en ontwikkelde ik in een zeer korte tijd een sterke interesse in wetenschappelijk onderzoek. Klaas, dit proefschrift was zonder jou toedoen nooit tot de stand gekomen en ik wil je nogmaals bedanken voor alles wat jij me meegegeven hebt.

Dear **Rene, Claudia and Markus**: while Klaas Nicolay was the one that initially sparked my interest in scientific research (explained in Dutch in the paragraph above), you three were certainly the ones that ignited my passion. My internship in London is a period of my life that I will never forget, where the dedicated supervision of you guys has to a large extent driven my personal and professional development to date. I hope that in the future you will continue to supervise students in the same way as I was privileged to experience.

PhD committee

Dear committee members, prof. dr. B.W. Raaymakers, prof. dr. C.T.W. Moonen, prof. dr. T. Leiner, prof. dr. P. Boernert, prof. dr. N.F. Ramsey, I am very grateful for your evaluation of this thesis, many thanks for your time investment.

Colleagues and Friends

Dank aan mijn kamergenoten in Q2.02.316 **Bjorn, Matteo** en **Mark**. Mede dankzij jullie toedoen ben ik iedere dag met plezier naar het werk gekomen. Zelfs in de hete zomer van 2018 zonder adequaat functionerende airconditioning, wat resulteerde in een onaangename mannenlucht, overwoog ik het zelfs niet om af en toe een dagje thuis te blijven. Matteo, bedankt dat jij, samen met mijn broer Bart, mijn paranimf wil zijn, dit betekent heel veel voor me.

Dank aan alle co-auteurs in volgorde van verschijning van de papers in deze thesis: Bjorn, Chris, Jan, Niels, Rob, Oscar, Martijn, Stella, Niek en Alessandro. Jullie bijdragen waren absoluut onmisbaar.

Niek, Tim en Pim, jullie zijn de personen waar ik de laatste jaren intensief mee heb samengewerkt. Niek, volgens mij hebben we de laatste 3 jaren minimaal 50 scan sessies uitgevoerd, verdeeld over praktisch alle MR systemen op de afdeling, om de golden mean cones/kooshball scans aan de praat te krijgen. Erop terugkijkend was het de tijdsinvestering meer dan waard, zeker nu ik continue weer nieuwe en verbeterde resultaten zie met de voorheen opgenomen datasets. Tim, de robuuste implementatie van de CASPR scan op MR21 gaat ons ooit nog lukken. Daarna gaan we uiteraard CASPR gebruiken voor praktisch alle applicaties (om onze tijdsinvestering te laten renderen), van multishot DWI tot MRCP tot free-breathing 3D T2-w scans. Pim, ons CASPR-ReconSocket werk is een van de meestbelovende en interessantste projecten binnen mijn portfolio. Ik hoop dat we beide in de nabije toekomst evenveel tijd blijven vinden om deze lijn door te ontwikkelen voor een klinisch prototype voor real-time imaging voor online adaptive radiotherapy.

Verder wil ik graag alle studenten, (A/O)IOs en andere onderzoekers bedanken waar ik de afgelopen jaren mee heb samengewerkt, koffie mee heb gedronken of mee heb getafelvoetbald. In alfabetische volgorde: Anna, Anneloes, Arjan, Bart, Bjorn, Carel, Casper, Charis, Christoph, Cornel, Daan, Dennis, Edwin, Ellis, Flavio, Luca, Federico, Fieke, Filipa, Gabrio, Georgios, Guus, Hanna, Hans, Hidde, Janot, Jean-Paul, Joao, Jorine, Joris, Katrinus, Maarten, Matteo, Mark, Markus, Martin, Maureen, Maxence, Michaela, Mick, Miha, Mike, Niek, Oscar, Peter, Pim, Priscilla, Robin, Sophie, Soraya, Stefan, Stefano, Steven, Thomas, Tim, Tristan en Yulia. Bas, Charlotte, Guus, Jorn, Maaïke en Osman, bedankt voor jullie enthousiasme en fanatieke inzet tijdens jullie bachelor of master thesis projecten. Ik heb veel van jullie geleerd en een aantal van deze projecten hebben de basis gevormd voor mijn verdere onderzoek.

Thanks to the Resolve team and the corresponding STW user committee: Gerald Schubert, Dave Fuller, Dennis Klomp, Martino Borgo, Catalina Arteaga, Shirley Baert and Margo Beukers.

Tevens wil ik alle artsen, laboranten, klinisch fysici, computer scientists en ICT-medewerkers bedanken voor hun ondersteuning, gezellige koffie-pauzes/borrels en natuurlijk de radio robbies voor de leuke voetbal wedstrijden. Vanuit de klinische fysica wil ik graag Astrid, Marielle en Niels in het bijzonder bedanken voor hun betrokkenheid bij een aantal (lopende) projecten.

Naast al mijn collega's wil ik ook graag mijn vriendengroep in Peel en Maas bedanken voor de mooie avonden, weekenden en vakanties de afgelopen jaren. Ook al hebben jullie niet direct bijgedragen aan dit proefschrift, toch waren deze sociale gelegenheden onmisbaar voor mijn dagelijks functioneren.

Family

While the term family is often used to describe blood relatives, I believe it also describes the household from the Lange Nieuwstraat. Anna, Casper, Carlo, Elena, Joao, Lisa, Matteo, Mirthe, Stefano and Soraya. Thank you very much for all the

incredible dinners, parties and casual cozy evenings in the house. You guys have taught me many many things about DOs and DONT's of the German, Greek and Italian (cuisinal) culture. The time at LN has truly been one of the best years of my life.

Mijn lieve ouders, Peter en Willemien. Inmiddels woon ik alweer bijna 8 jaar buitenshuis, maar toch voelt het nog iederen keer als "thuiskomen" wanneer ik de achterdeur in Beringe open. Jullie onvoorwaardelijke liefde en genegenheid jegens mij en Mirthe zou ik voor altijd blijven waarderen en pogen te retourneren. Ook wil ik mijn broer Bart en zijn vriendin Kristel bedanken voor jullie regelmatig interesse in mijn onderzoek, ook al is het vaak wat cryptisch waar ik nu precies mee bezig ben.

Mijn lieve schoonouders, Peter en Marion, en schoonbroer Pieter. Ik kom inmiddels al meer dan 10 jaar bij jullie over de vloer. De eerste aantal jaren voelde het als visite bij een goede kennis, maar de laatste jaren voelde het echt als een tweede thuis. Bedankt voor jullie onvoorwaardelijke gastvrijheid, oprechte interesse in mijn onderzoek en voor de volledige inclusiviteit binnen jullie familie. Marion†, jouw recent overlijden is voor mij ook een enorm gemis en ik zou onze gedeelde herinneringen voor altijd blijven koesteren. Rust zacht lieve Marion.

Lieve Mirthe, wij zijn nu ondertussen al ruim 10 jaar bij elkaar sinds 21 maart 2010. Tijdens deze jaren heb jij mij altijd geholpen met de grote keuzes des leven en altijd gesteund tijdens de momenten waarin ik het zwaar had. Wij hebben samen al veel gemaakt: van de lange afstandsrelatie toen ik in London woonde, tot de verre reis naar Maleisië, tot anderhalf jaar lang constant op elkaars lip zitten tijdens de COVID lockdown, tot het recent overlijden van jouw moeder Marion. Dat wij samen een goed team zijn na al deze gebeurtenissen lijkt mij wel duidelijk en ik ben er volledig van overtuigd dat wij in de toekomst samen ook alles aankunnen. Ik hoop dat we dit jaar (eindelijk) ons eigen huis kunnen kopen en zodoende kunnen bouwen aan onze gezamenlijke toekomst.

Curriculum vitae

Tom Bruijnen was born on July 17, 1992 in Beringe, the Netherlands. After primary school in Beringe he attended the Bouwens van der Boije College in Panningen, where he obtained his VWO diploma. In 2011, he enrolled at Eindhoven University of Technology and obtained his master degree (cum laude) in biomedical engineering in 2016. During this master he did an internship at the cardiac MRI group of King's College London on cardiac Magnetic Resonance Fingerprinting and subsequently conducted his master thesis at the department of radiotherapy at the University Medical Center Utrecht on the quantification of head-and-neck tumor motion using MRI. Fascinated by the use of MRI in radiotherapy he further pursued this topic with a PhD within the MR-linac project. The results of this research on the *"Technical developments for quantitative and motion resolved MR-guided radiotherapy"* are presented in this thesis.



Tom is currently a post-doctoral researcher at the Utrecht radiotherapy department. He continues his research and development for integrated MR imaging for MR-linac with a strong focus on the translation of research software to clinical prototypes.